Centro de Investigaciones Energéticas Medioambientales y Tecnológicas
(CIEMAT-Madrid)
•
Departamento de Física Atómica, Molecular y Nuclear
(Universidad Complutense de Madrid)

Search for Heavy W' Bosons Decaying into Muon and Neutrino in pp Collisions at $\sqrt{s}$=7 TeV in the CMS Experiment at the LHC

Tesis presentada por
Carmen Diez Pardos
para optar al grado de Doctor
(con mención europea)

Dirigida por
Dra. Begoña de la Cruz Martínez
Dra. María Isabel Josa Mutuberría

Madrid, Septiembre 2011

A mis padres y mis hermanas.

Contents

List of Figures

List of Tables

Chapter

1 Introduction

Particle physics studies the fundamental components of matter and their interactions. This quest to understand the basic components of nature has been pursued for many centuries. But it is in the last decades when impressive advancements in this field have been achieved. The variety of physics phenomena are explained in terms of four fundamental interactions between elementary particles. All of them, except the gravitational force, are combined into the Standard Model (SM) of particle physics, currently the universally accepted theory describing the building blocks of matter. This model has been successfully tested over the past 30 years, all the particles postulated by the SM have been observed with the exception of the Higgs boson, which has so far eluded discovery. However, such advancements have raised even more questions and highlighted the shortcomings of the theory. The SM cannot answer some of the observed features of our universe, such as the origin of dark matter and the predominance of matter over antimatter.

The Large Hadron Collider (LHC) and its four experiments have been built to shed light to the unsolved questions, going beyond the energy explored up to now, reaching the TeV energy scale, where most of the extensions of the SM predict the existence of new physics phenomena. Exploring this new energy regime will hopefully lead to the discovery of new particles and interactions to overcome the limitations of the Standard Model.

After twenty years of designing, building and commissioning the LHC, the first proton-proton collisions at a centre of mass energy of 7 TeV took place in March 2010. The data collected by the Compact Muon Solenoid (CMS) experiment up to November 2010, when a heavy ion (PbPb) run took place, was rapidly analysed. Standard Model processes were measured in the new energy regime and first searches of new particles were undertaken. Before the first collision data were delivered, several campaigns of cosmic ray muons data-taking were carried out with the CMS detector already in place and operational, in order to complete the commissioning of the whole experimental chain.

This thesis presents results from both, cosmic muon data and collision data. The focus of the work was first set on muon related studies, as any physics analysis requieres a good understanding of the objects involved. The studies presented here address various aspects of the muon detection, as triggering and offline reconstruction. Progressing in the way towards a physical measurement, a strong effort was made to develop an optimal method to evaluate the efficiency of selection processes involving single muons.

Finally, the acquired knowledge about muons and the developed tools were applied to the $W \to \mu\nu$ process cross section measurement and to the search for a new heavy charged gauge boson W' decaying into the same channel. Both of them were carried out with the data collected in 2010 amounting to an integrated luminosity of $\mathcal{L}$= 36 pb^{-1}.

Then, the first part of this thesis focuses on the trigger and the offline muon reconstruction as well as on the muon efficiency determination, in the second part the complete $W' \to \mu\nu$ analysis is presented. The content of each chapter is described in the following.

First, an overview of the status of particle physics and the motivation for the LHC physics program is given in Chapter 2, with the aim of setting the context of the work presented here. Some relevant results of the analysis of the first data collected will be highlighted. This is followed in Chapter 3.

The muon trigger and the offline muon reconstruction are described in Chapters 4 and 5, respectively. The Level 1 local muon trigger performance was studied with the cosmic data sample collected during 2008. The results obtained and the comparison with the performance with collision data are reported. Regarding the High Level Trigger, the whole trigger chain is reviewed, concentrating on the L2 step. Chapter 5 deals with the offline muon reconstruction, first the standard muon reconstruction in CMS is presented, to focus later on the performance of the algorithms specifically developed to improve the reconstruction of high momentum muons.

Chapter 6 presents the method developed to evaluate the single muon efficiency, with control data samples. To validate the method, the results are cross checked with the Monte Carlo efficiency. The studies carried out to assess the robustness of the method and estimate the systematic uncertainty associated are described. Finally, to illustrate its application to a particular physics analysis, the efficiencies are obtained in the scope of the $W \to \mu\nu$ cross section measurement. The study of W bosons is relevant by itself, but here also as it is the main background in the W' searches.

The remaining chapters are devoted to the W' boson search in its muonic decay channel carried out by the CMS collaboration. The physics analysis was performed within a specialised working group covering all the steps of the measurement. The most relevant contributions of the work presented here to the common effort are as aforesaid all the aspects involving the muons, which will be carefully explained.

W' bosons would appear as an excess of observed events compared to the Standard Model prediction in the tail of the transverse mass spectrum of the reconstructed muon-neutrino pair. This implies that one looks for events with high transverse momentum muons. Therefore the key pieces of the analysis are a good understanding of the background events and a competent muon reconstruction in the mentioned range. All the relevant aspects of the search will be addressed. A brief introduction to the theoretical motivation for the existence of new bosons and the W' production and decay mechanism is given in Chapter 7. The simulation of background processes and the expected signal as well as its properties are outlined in the same chapter. Special attention was paid to the determination of the background, as it is fundamental in a search. Thus, the discussion of the different background sources and the estimation of the background yields are reported in Chapter 8. The chapter deals also with the corrections applied to the simulation to model adequately the data, due to the fact that certain characteristics of the simulation differ from the behaviour observed in data. The efficiency determination employing the method previously described is presented as well. Finally, the estimation of the uncertainties of the number of signal and background events is provided. To conclude, the results are discussed in Chapter 9. They are obtained profiting from the software and tools already in place, developed by the W' working group. In this thesis, the search is extended to the case of a W' decaying to a heavy neutrino.

The conclusions of this dissertation are summarised in Chapter 10. A summary in Spanish of the most relevant aspects is included as an appendix.

Chapter

2

An Overview of Particle Physics

Elementary particle physics is the quest for understanding the smallest constituents of matter and their interactions. Over the last 60 years, great breakthroughs have been accomplished in this field as a result of a fruitful interplay between improved experimental data-taking and theoretical insights. In the 1960s Sheldon Glasgow, Steven Weinberg and Abdus Salam proposed a model of particle physics, currently known as the Standard Model [1, 2, 3, 4] which predicted many quantities that were later experimentally confirmed to a high level of accuracy. As modern particle colliders were increasing their accelerating power most of the particles predicted by the Standard Model were observed. It is remarkable the discovery of the electroweak bosons W and Z in 1983, and the observation in 1995 of heaviest quark, the top quark and in 2000 the τ neutrino.

In this chapter a brief introduction to the Model, its caveats and other models proposed to address the unresolved questions, will be given in the context of the physics program in the LHC complex.

2.1 Brief Introduction to the Standard Model

The Standard Model (SM) describes the strong, weak, and electromagnetic forces between the fundamental particles of ordinary matter. An introduction to the SM can be found in [5, 6]. Despite its success in describing most of the experimental data, the SM is not an ultimate theory of fundamental interactions, primarily because it does not describe the gravitational force and leaves several questions unresolved. An overview of its main shortcomings, which indicate a more comprising theory should exist, is given later on.

The fundamental components of nature are two basic types of particles, fermionic and bosonic particles. All matter is built from only twelve fermions which are up to now not known to have substructure. They all have spin -1/2, which means they obey the Pauli exclusion principle. Each of these fermions has its anti-particle, which has the same mass, but opposite quantum numbers. The twelve fermions comprise three generations of leptons: the electron, the muon and the tau particles, with their counterpart neutrinos; and quarks, with different flavours: up and down, strange and charm, and top and bottom. Each extra generation is an exact copy of the first one, apart from the increasing particle mass. An overview of all fermions, leptons and quarks, is given in Table 2.1.

quark	**mass (GeV/c^2)**	**charge (q$_e$)**	**lepton**	**mass (GeV/c^2)**	**charge (q$_e$)**
down, d	0.005	-1/3	electron, e	0.0005	-1
up, u	0.003	2/3	neutrino ν_e	<2×10^{-6}	0
strange, s	0.1	-1/3	muon, μ	0.106	-1
charm, c	1.3	2/3	neutrino ν_μ	<0.002	0
bottom, b	4.3	-1/3	tau, τ	1.8	-1
top, t	175	2/3	neutrino ν_e	<0.015	0

Table 2.1: Fundamental fermions of the Standard Model [7].

Forces in nature are transmitted through the interchange of particles: photons for the electromagnetic force, the Z and W bosons for the weak force, and gluons (g) for the strong force. All these bosons of the Standard Model are listed in table 2.2. In addition, a new particle, known as Higgs boson, also included in the table, was predicted as part of the mechanism that allows the rest of the particles to acquire mass. It has not been observed, and its discovery is a major goal of the LHC experiments. For completeness the gravitons, mediators of the gravitational interaction, are listed in the table, although they are not included in the SM and they have neither been experimentally observed. The relative strengths of the strong, electromagnetic, weak and gravitational forces are of the order (1, 1/137, 10^{-6}, 10^{-39}).

Interaction	**boson**	**spin**	**mass (GeV/c^2)**	**charge(q$_e$)**
Electromagnetic	photon, γ	1	0	0
Weak	W$^\pm$	1	80.4	±1
	Z	1	91.2	0
Strong	gluon, g	1	0	0
	Higgs, H	0	> 114 (?)	0
Gravity	graviton, G	2	0	0

Table 2.2: Fundamental bosons of the Standard Model. The table also includes the predicted Higgs boson and the graviton (not described by the SM).

The SM is a quantum field theory, the underlying symmetry group is $\mathrm{SU}(3)_C \times \mathrm{SU}(2)_L \times \mathrm{U}(1)_Y$. All these terms are gauge theories, coupling fermions to intermediate bosons.

- The $\mathrm{SU}(3)_C$ symmetry term describes Quantum Chromodynamics (QCD), the strong interaction; a theory of the interactions of particles which carry colour charge, the quarks and gluons. The latter are the eight massless particles mediators of the interaction.

- $\mathrm{SU}(2)_L \times \mathrm{U}(1)_Y$ describes the unification of the weak and the electromagnetic interactions. Before electroweak-symmetry breaking, $SU(2)$ is mediated by three weak isospin, massless bosons W^μ, and $U(1)$ by a weak hypercharge massless boson, B^0. The latter, weak hypercharge, relates the electrical charge and the third component of the weak isospin. After electroweak symmetry breaking, these gauge bosons are recombined and give raise to the massive carriers of weak force (W^+, W^-, Z) and the massless photon γ, carrier of the electromagnetic interaction. This process requires the introduction in the model of a scalar field, the Higgs field, and its elementary scalar (spin-0) the Higgs boson. Otherwise, for reasons of invariance, it is not possible to include mass terms for the gauge fields or the fermions.

The SM agrees with high precision with the current experimental data, being the deviations between the predictions and the measurements of precision observables below the 3σ level, see figure 2.1.

Nevertheless, there are hints that the Standard Model is not the ultimate theory due to several unresolved problems, for instance some of the questions are:

- The reason why there are only three fermion families is unknown.

- It does not include the gravitational interaction.

- It contains a large number of free parameters, including particle masses and coupling constants, that cannot be calculated using the model itself.

- The nature of neutrinos, whether they are Dirac or Majorana particles, is unknown as well as the mechanism of mass generation and the reason why the masses are so small compared to the charged leptons.

- It does not explain the so-called hierarchy problem, which refers to the orders of magnitude existing between the electroweak scale ($\approx$ 100 GeV, unification of weak and electromagnetic forces) and the Planck scale ($\approx 10^{19}$ GeV, grand unification scale).

- The origin of Charge-Parity violation, responsible of the matter-antimatter asymmetry in the universe.

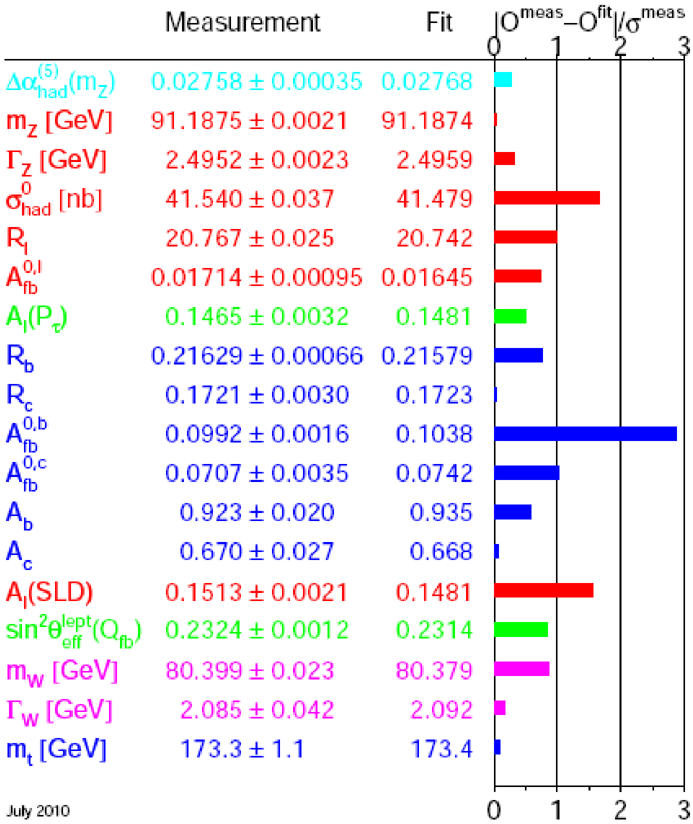

Figure 2.1: Observables of the Standard Model [8].

Thus, extensions have to be constructed so that the SM is embedded or contained as a low-energy effective theory. The discovery of new particles or interactions would be a milestone of the physics program at the LHC.

2.2 LHC Scientific Scope

The physics program of the LHC comprises two general objectives, first, to perform precision measurements, like measurements of the W and top quark masses or triple gauge boson couplings, and second, as a discovery machine in a new energy regime. With the data recorded during 2010 no sign of new physics has been found, but many search analyses have set up more stringent limits to the existence of new particles as leptoquarks, heavy stable particles or the scale of compositeness, for example. All the results already published by the CMS experiment can be found in [9].

The cross sections of some processes that are studied in the LHC are shown in Figure 2.2, as a function of the centre of mass energy of the collision. The high production rate of many SM phenomena ensures that most measurements will have small statistical uncertainty. Moreover it allows to perform accurate studies on the detector response, resulting in a precise understanding of associated systematic uncertainties.

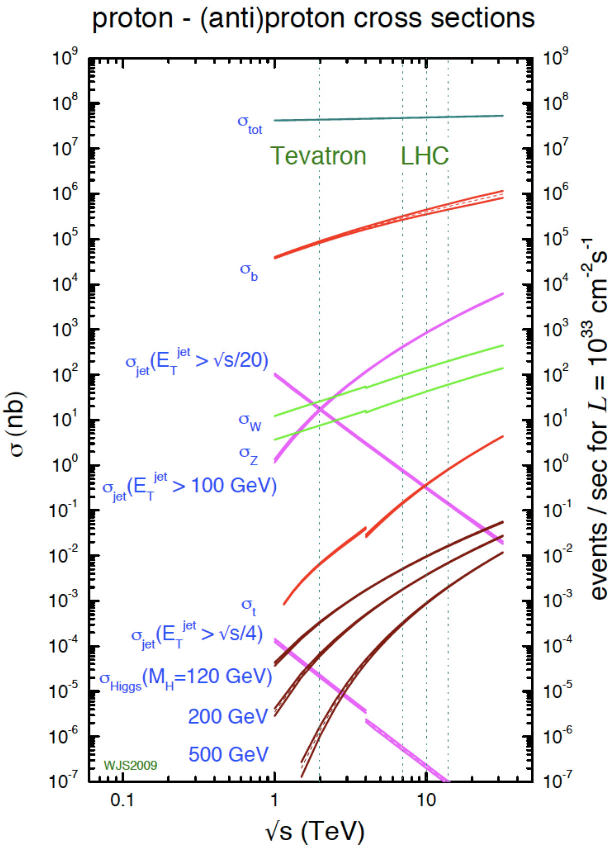

Figure 2.2: Cross-section of production of several physics processes.

The production of W and Z bosons has a large cross section and is theoretically well understood. Hence these reactions are useful for many purposes, including a precise luminosity monitor, a high-statistics detector calibration tool and to demonstrate the performance of the CMS experiment. These processes have been among the first ones measured at the LHC. Already with the data collected during 2010 CMS provided a large number of results: the precise measurements of inclusive cross sections with boson decays into leptons (electrons, muons and even taus), studies of differential cross sections in Drell-Yan production, precise measurements of different observables (asymmetries, W polarisation), including a first measurement of the weak mixing angle, detailed studies of the associated jet production and the observation of diboson final states: WW, Wγ, Zγ. A summary of the electroweak measurements obtained with the 2010 data sample is presented in Figure 2.3.

Top-quark processes are studied for the first time in multi-TeV proton-proton collisions. The measurements of top quark properties are a fundamental part of the LHC program (the $t\bar{t}$ production rate will be up to 5 orders of magnitude higher than in the Tevatron), due to its importance both as a precise test of the SM predictions and as a background source to many searches. These precision measurements include the

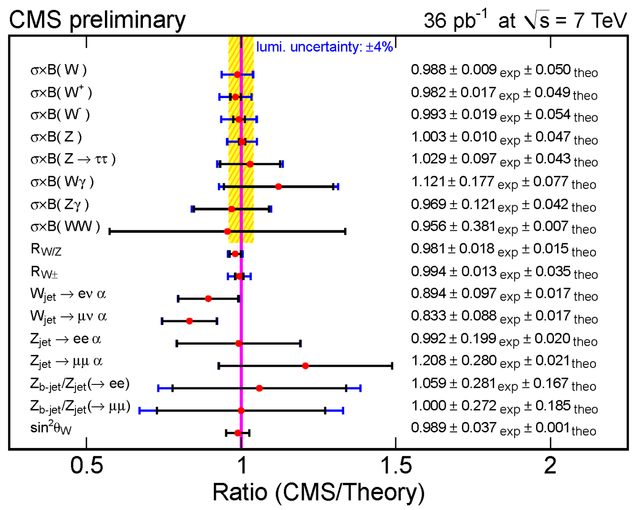

Figure 2.3: Summary of the EWK physics measurements with 2010 data, the ratio between the value measured with CMS is compared to the theory prediction.

cross-section for top quark-top antiquark pairs, see Figure 2.4 left where a summary of the results is shown. The top mass measurement is expected to reach, combining the various decay modes, a precision of less than 1 GeV/c^2 at the LHC. CMS has already published the first measurements of the top mass reconstructed in various channels. An example of the result obtained in the dilepton channel ($t \to Wb \to l\nu b$) is presented in Figure 2.4 right. Together with the improvements expected in the W sector, the top mass measurement will allow to further tighten the bounds on the Higgs mass with respect to the current value, establishing a very stringent constraint on the SM in the case the Higgs is not found in the expected mass range.

Another example of SM measurements is related to the field of b-physics. The main interest are the decays of neutral B mesons to study the CP violation, where the LHC will benefit from a very large $b\bar{b}$ production cross section. .

The Higgs is related to various open problems of particle physics, hence the detection of this particle was a primary design consideration for CMS. The theory predicts all of the SM Higgs properties except its mass, which is the only remaining free parameter of the Standard Model. Theoretically the Higgs boson mass is bounded to be M$_H$ $<$ 1 TeV/c^2 for unitarity reasons (preventing WW scattering to be divergent). Experimental data have set as well mass limits, indirect bounds based on precision electroweak measurements [11] favour low Higgs masses, in the range of 100–200 GeV/c^2. LEP direct search [8, 12] set a lower mass limit at 114 GeV/c^2. ATLAS and CMS have recently excluded the existence of a Higgs over most of the mass region from 145 to 466 GeV/c^2 with 95% certainty. The expected exclusion limit (dashed line, green and yellow error bands) is shown together with the observed one (solid line) in Figure 2.5.

If no trace of the Standard Model Higgs boson is found at the LHC, the model will have to be revised. There are already different theories available which extend the

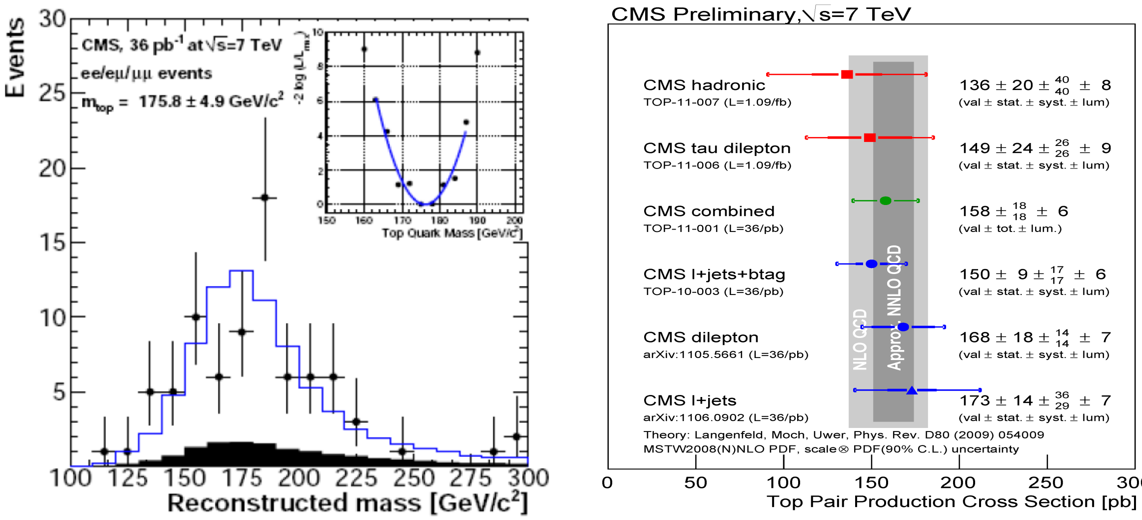

Figure 2.4: Measurement of the top mass in the dilepton channel [10] with 2010 data in CMS (left) and summary of the top pair cross section measurements obtained by analysis different channels (right).

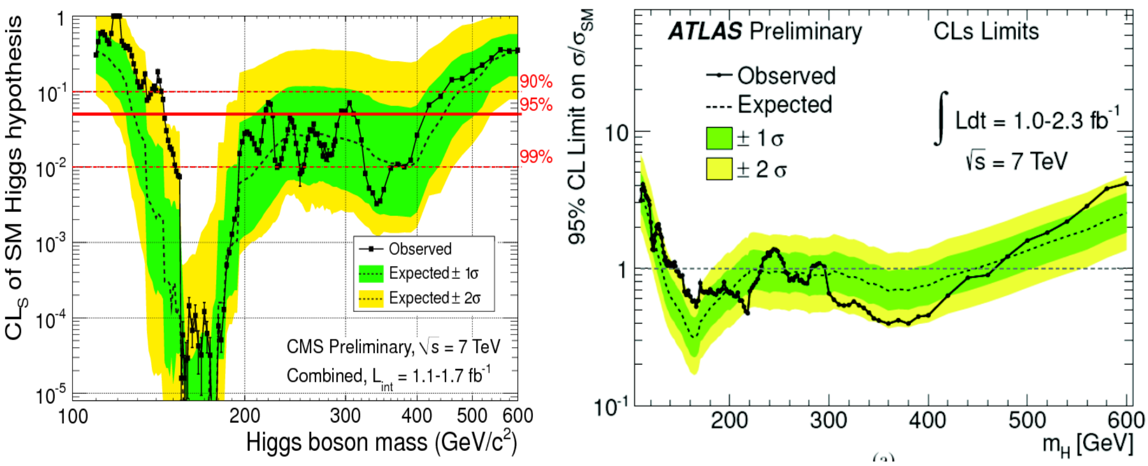

Figure 2.5: Higgs exclusion plot prepared by the CMS (left) and ATLAS (right) collaborations, with integrated luminosities up to 2 fb^{-1}. The existence of a Higgs over most of the mass region from 145 to 466 GeV/c^2 with 95% certainty is excluded.

model, allowing for different models of electroweak symmetry breaking, while still in agreement with the current experimental data.

One of the most popular extensions of the Standard Model is Supersymmetry, see for instance [13]. Sypersymmetry (SUSY) is one proposed solution to the hierarchy problem, ensuring a finite Higgs boson mass by loop cancellation. It doubles the number of elementary particles in nature: it postulates that there are new particles with similar mass and equal couplings to those in the SM. The SUSY and the SM particles are related by an operator Q, such that Q$|$fermion$\rangle$ = $|$boson$\rangle$ and Q$|$boson$\rangle$ = $|$fermion$\rangle$, and therefore the superpartners differ from their standard model counterparts by a half-unit of spin. Thus, all fermions have bosonic SUSY partners, and vice-versa. The electroweak symmetry breaking problem is still solved through a Higgs mechanism, though in this case instead of a single Higgs scalar field, at least two Higgs doublets have to be introduced. Experimental signatures of these supersymmetric particles should be observed at the energies that the LHC will reach. The limits obtained in some SUSY parameters from several 2011 CMS SUSY searches are shown in Figure 2.6.

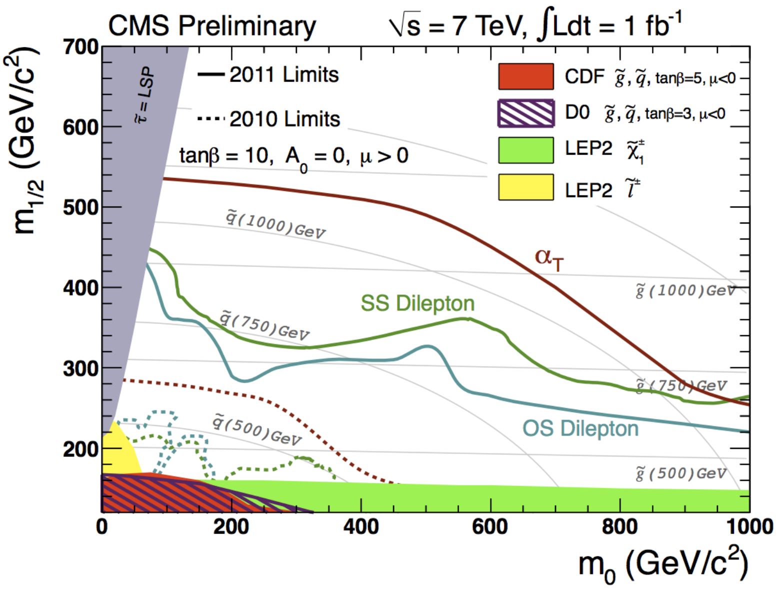

Figure 2.6: Observed limits from several 2011 CMS SUSY searches plotted in the CMSSM $(m_0, m_{1/2})$ plane. Supersymmetric Standard Model CMSSM is often used as a benchmark model for presenting the search results. The parameters of this model are $m_{1/2}$ and m_0, the universal gaugino mass and scalar mass at GUT scale, tanβ, the vacuum expected value ratio for the two Higgs doublets, A_0 is the trilinear coupling and the and the sign of Higgs mixing parameter μ.

Another extension of the SM are Grand Unified Theories (GUTs) describing the symmetry in the Standard Model $(\mathrm{SU}(3)_C \times \mathrm{SU}(2)_L \times \mathrm{U}(1)_Y)$ as if it would be originated from a larger symmetry group relating quarks and leptons. This addresses the unification problem: the symmetry is unbroken at some higher energy where all interactions are described by a local gauge theory with one running coupling. A general problem with most GUT theories is the prediction of proton decay, which has not yet been observed.

Also the existence of Extra Dimensions is considered. In the ADD model the SM fields are confined to a four-dimensional membrane in a higher-dimensional space. Gravity travels in additional spatial dimensions, making it seem much weaker than the other fundamental forces in four dimensions. The theory thus offers a solution to the hierarchy problem. It also contributes with a Dark Matter candidate: the graviton travels in all the spatial dimensions, giving rise to several Kaluza-Klein resonances on the four-dimensional brane.

Compositeness is a possible explanation for the source of the mass hierarchy of quarks and leptons. It proposes a composite structure for them and postulates the existence of excited fermions. Many different models of excited fermions and fermion substructure studies via contact interactions have been carried out but till now none of the experiments have found any evidence. An example of these searches in CMS is the search for excited leptons (μ^*, e^*), where a limit on the contact scale, Λ, is set, as illustrated in Figure 2.7.

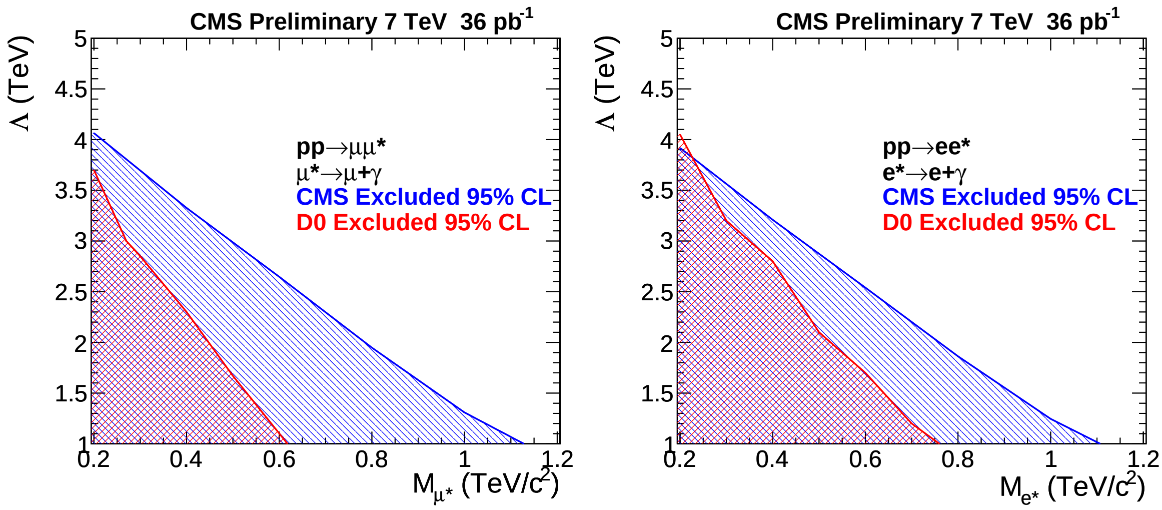

Figure 2.7: Exclusion limit to the compositeness scale as a function of the excited lepton mass [14].

Additional heavy gauge bosons (W' and Z') are predicted in many superstring-inspired models and grand unified theories (GUTs), as well as in dynamical symmetry breaking and little Higgs models. The description of the W' bosons will be addressed in chapter 7.

In this scenario, the discovery of new particles or interactions would be a milestone of the physics program at the LHC, contributing to disentangle which are the correct models among all proposed ones.

Chapter

3

The Large Hadron Collider and the Compact Muon Solenoid

Hadron colliders are suitable machines to explore new domains of energy. In particular, the LHC was designed to provide proton beams with an energy of 7 TeV yielding an energy of 14 TeV in the centre of mass reference and with a luminosity of $10^{34}\text{s}^{-1}\text{cm}^{-2}$ providing parton-parton collisions up to energies of about 1 TeV, and with a very high collision rate in order to favour the study of the production of rare particles. For the early running phase, 2010-2012, the energy in the centre of mass is 7 TeV. The LHC has also the functionality of accelerating nuclei of heavy atoms instead of protons, producing collisions with a centre of mass energy 30 times higher than in previous experiments. This feature allows the LHC to have a complete program in heavy-ion collisions to include studies about the hot nuclear matter.

In this chapter a concise overview of both the LHC accelerator and the CMS detector will be given, with the aim of setting the context of the work presented in this thesis. First the main features of the accelerator are presented.

3.1 The LHC Machine

The Large Hadron Collider, LHC, [15, 16, 17] is a two ring superconducting hadron accelerator and collider located at CERN near Geneva in the existing 26.7 km tunnel built for the LEP accelerator in the border between Switzerland and France about 100 m underground. There are four experiments installed in the caverns along the ring:

two high luminosity experiments ATLAS (A Toroidal LHC ApparatuS) [18] and CMS (Compact Muon Solenoid) [19] [20], the LHCb (Large Hadron Collider beauty) [21], dedicated to B physics, and ALICE (A Large Ion Collider Experiment) [22], devoted to study heavy ion collions. Other two smaller experiments, LHCf (Large Hadron Collider forward) and TOTEM (TOTal Elastic and diffractive cross-section Measurement), are situated in the tunnel, near ATLAS and CMS respectively. They focus on forward physics.

3.1.1 Overview of the Accelerator Chain

An schematic view of the accelerator complex with the injection chain is shown in Figure 3.1. To supply the LHC with pre-accelerated protons the existing CERN facilities have been upgraded. The process to obtain the protons and accelerate them to the injection energy goes as follows: protons are initially obtained by ionising gaseous hydrogen and then accelerated in bunches to the linear accelerator (LINAC2) to an energy of 50 MeV. Afterwards they are injected into the Proton Synchrotron Booster (PSB), and boosted to an energy of 1.4 GeV before being accelerated in the Proton Synchrotron (PS) to 26 GeV. Finally, the beams are pushed up to the injection energy of 450 GeV in the Super Proton Synchrotron (SPS).

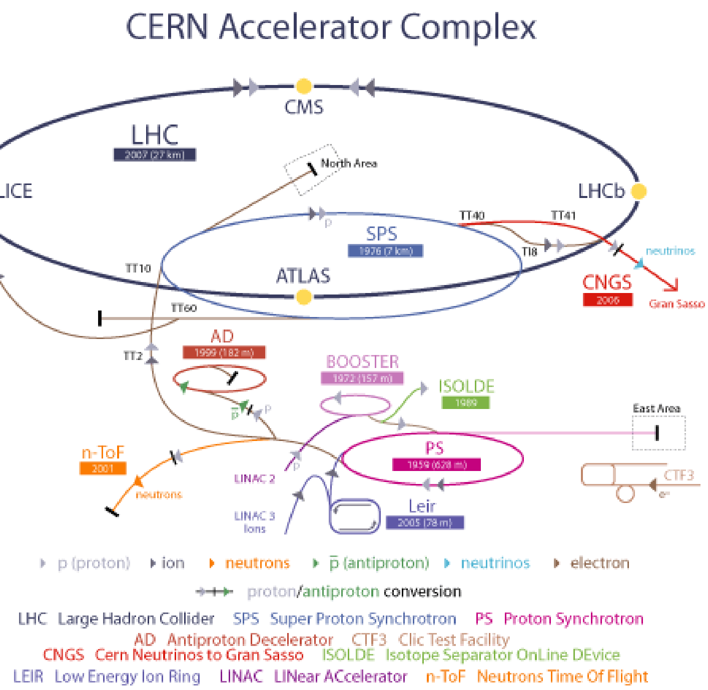

Figure 3.1: CERN accelerator complex.

Once they are injected into the LHC, the beams are accelerated up to collision energy (nominal $\sqrt{s}$ = 14 TeV, during its first phase 2010-2012 $\sqrt{s}$ =7 TeV). A total number of 1232 superconducting dipole magnets, which provide a magnetic field of

8.3 TeV, are needed to keep the protons on the orbit during the acceleration. Additional 392 quadrupole magnets are used to keep the beams focused. Further corrections are obtained by means of other magnets, up to dodecapoles. The superconducting magnets are cooled using liquid helium at a temperature of 1.9 K.

The need for a high beam intensity, not reachable with anti-proton beams, made necessary to have independent magnetic cavities, one for each proton beam.

3.1.2 Luminosity Measurement

The number of events per time unit of a given process generated in pp collisions at the LHC is given by:

$$N_{event} = \mathcal{L}\sigma_{event} \tag{3.1}$$

where σ_{event} is the cross section for the physics process under study and $\mathcal{L}$ is the machine luminosity, which depends only on the beam parameters. It can be written for a Gaussian transverse beam profile distribution as:

$$\mathcal{L} = \frac{N_b^2 n_b f_{rev} \gamma_r}{4\pi\epsilon_n\beta^*} \tag{3.2}$$

where

- N_b is the number of particles per bunch,
- n_b the number of bunches per beam,
- f_{rev} the revolution frequency,
- γ_r the relativistic gamma factor,
- ϵ_n is the normalised transverse beam emittance, defined as the product of the RMS of the particles positions distribution, σ, times the RMS of the particle momenta distribution, σ'. It gives an idea of the spatial and the momentum dispersion of the beam. This parameter is constant for all the beam life and the goal of the injection procedure is to introduce a beam with the lowest beam emittance in the collider. The design value was 3.75 μm, however in 2010 it was already smaller than 2.5 μm.
- β^*, the beta function at the collision point, defined as the ratio σ/σ'. Contrary to ϵ, β^* can be reduced along the ring length, with dedicated magnetic optics which squeezes the beams in the Interaction Point (IP). Note that a lower β^* means a higher spread in the particle momenta.
- F is the geometric luminosity reduction factor due to the crossing angle at the interaction point.

The above expression assumes round beams with equal beam parameters for both proton beams. The exploration of rare events in the LHC collisions requires both high beam energies and high beam intensities. All these parameters and other design characteristics of the accelerator are summarised in Table 3.1.

Under nominal operating conditions, LHC will have 2808 bunches in each beam, with around 10^{11} protons per bunch. During 2010, the highest number of bunches was 368, while the number of protons per bunch was already at design level. The size of the bunch at the interaction points is approximately 16 μm which increases the probability of proton-proton collisions. The design luminosity is 10^{34} cm^{-2}s^{-1}, being 10^{32} cm^{-2}s^{-1} at the end of the 2010 data taking.

Design Parameters	
Circumference Length	26659 m
Depth	50 - 175 m
Total number of magnets	9600
Number of main Dipoles	1232
Time between collisions	25 ns
Bunch Crossing Rate f_{rev}	40.08 MHz
Temperature	1.9 K (-271.3C)
Injection energy	450 GeV
Dipole field	8.33 T
Nominal proton energy	7 TeV
Centre-of-mass energy $\sqrt{s}$	14 TeV
Number of bunches per proton beam	2808
Protons per bunch	1.1×10^{11}
Bunch spacing	25 ns
ϵ_n Norm. transverse emittance	3.75 μm
Transverse beam size at IP5	16.7 μm
$\beta^\star$ IP5 beta value	0.55 m
Crossing angle	285 μrad
E_{stored} Stored energy	362 MJ
Design instantaneous luminosity	10^{34} cm^{-2}s^{-1}
Average number of collisions per crossing	20

Table 3.1: Design parameters of the Large Hadron Collider.

3.2 The Compact Muon Solenoid Experiment

The CMS experiment is a general purpose detector installed 100 m underground at the LHC interaction point 5 (P5) near the village of Cessy in France. The design of the detector is driven by the challenges of a physics experiment in the LHC environment: many of the physics benchmark channels have a small cross section and the background from QCD production is overwhelmingly dominant. A high rejection power with an optimal efficiency for rare channels has to be achieved. The detector requirements for CMS to meet the goals of the LHC physics program comprise an excellent identification and resolution for the reconstruction of lepton signatures as well as good missing transverse energy and jet energy resolution. Moreover, a precise measurement of secondary vertices and impact parameter is necessary to efficiently identify heavy flavour and τ-lepton decays.

The short bunch crossing separation and the high event rate at the LHC imposes further challenges. At design luminosity about 20 inelastic interactions per bunch crossing will occur on average, a phenomenon known as pile-up [1]: products from other interactions can be confused with the ones from the interaction under study. Its effect can be reduced by using high-granularity detectors resulting in low occupancy. This requires a large number of detector channels and an excellent synchronisation among them. In addition, a good time resolution is needed to discriminate the interaction of interest from the interactions occurring in neighbouring bunch crossings. Another difficulty arises from the large flux of particles near the interaction point which leads to high radiation levels and the need of radiation hard materials in the detectors and front-end electronics.

The CMS detector, illustrated in Figure 3.2, consists of a silicon tracking system, an electromagnetic and a hadronic calorimeter and a muon system. A magnetic field of 3.8 T parallel to the beam axis is provided by a superconducting solenoid magnet. It is 21.6 m long, has a diameter of 14.6 m and a weight of 12.5 T.

The coordinate system adopted by CMS has the origin centred at the nominal collision point, the *x-axis* points inward, towards the centre of the LHC, the *y-axis* points vertically upwards and the *z-axis* is in the direction of the beam, completing the right-handed coordinate system. In cylindrical coordinates, the azimuthal angle ϕ is measured from the *x-axis* in the *xy plane*, the radial coordinate in this plane is r. The polar angle θ is defined in the *r-z plane* with respect to the *z-axis* and the pseudorapidity is $\eta = \ln(\tan(\theta/2))$. In CMS, the projections in the transverse plane of momentum and energy $p_T = p \cdot sin(\theta) = \sqrt{p_x^2 + p_y^2}$, $E_T = \sqrt{E_x^2 + E_y^2}$ are commonly used instead of momentum p and energy E because the magnetic field curves the trajectory in that plane and because E_z cannot be measured due to the energy losses in the region of the beam pipe.

3.2.1 Superconducting Solenoid

The superconducting solenoid magnet reaches a maximum magnetic field of 3.8 T in the positive z direction in the inner detectors. This magnetic field provides a large bending power in the transverse plane for charged particles, which makes possible to measure precisely their momentum from the curvature radius.

The magnet is 12.5 m long, has an inner radius of 4.9 m and is composed by a four-layers winding of NbTi conductor stabilised and reinforced by aluminium. It is

[1] The mean number of pile-up events in the data collected in 2010 was 2.7.

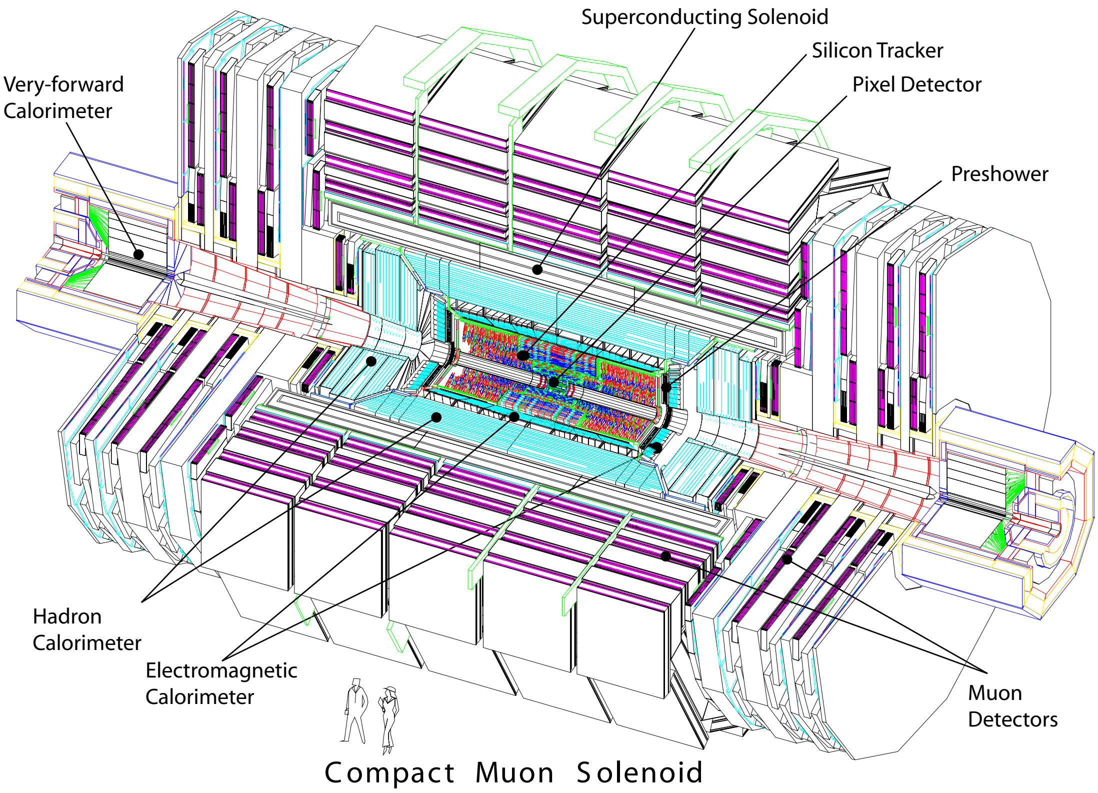

Figure 3.2: Layout of the CMS detector.

the largest superconducting magnet ever built, with the capacity to store an energy of 2.6 GJ at full current. The magnetic flux is returned through an iron yoke formed by five iron wheels and two endcaps (1000 ton in total), in which the muon spectrometer stations are integrated. In this part of the detector the magnetic field is saturated at 2 T. The field in the tracker volume has been mapped with an accuracy better than 0.1%. In the CMS yoke it is estimated to be accurate to better than 3% in the steel of the three central barrel wheels, and to about 8% in the steel of the two outermost barrel wheels [23].

3.2.2 Central Tracking Detectors

The central tracking system of CMS [20, 24] is designed to provide an efficient measurement of the trajectories of charged particles emerging from the LHC collisions, as well as a precise reconstruction of secondary vertices. By design its requirements were a reconstruction efficiency higher than 95% for isolated tracks and 90% for tracks within jets in a pseudorapidity range -2.5 $< \eta <$ 2.5, full ϕ coverage, and a charged particle momentum resolution better than $\Delta p_T / p_T = 10\%$ up to the TeV/c scale. CMS innermost detector is its all silicon tracker with a total active area of 200 m^2. The tracking detector is divided into a pixel detector close to the interaction region and a strip detector covering radii from 0.2 m to 1.1 m.

At the design luminosity there will be on average ~1000 charged particles from more than 20 overlapping proton-proton interactions traversing the tracker at each bunch crossing. Accordingly a very high granularity is needed to identify the different trajectories and a very fast response in order to assign them to the correct bunch crossing. These features imply a high power density of the on–detector electronics which requires efficient cooling; in direct conflict with the aim of keeping to the minimum the amount of material to limit multiple scattering, bremsstrahlung, photon conversion and nuclear interactions. Hence a compromise had to be found in this respect. In addition, the material of the tracker has to be specifically designed to resist radiation. These requirements on granularity, speed and radiation hardness lead to a tracker design entirely based on silicon detector technology.

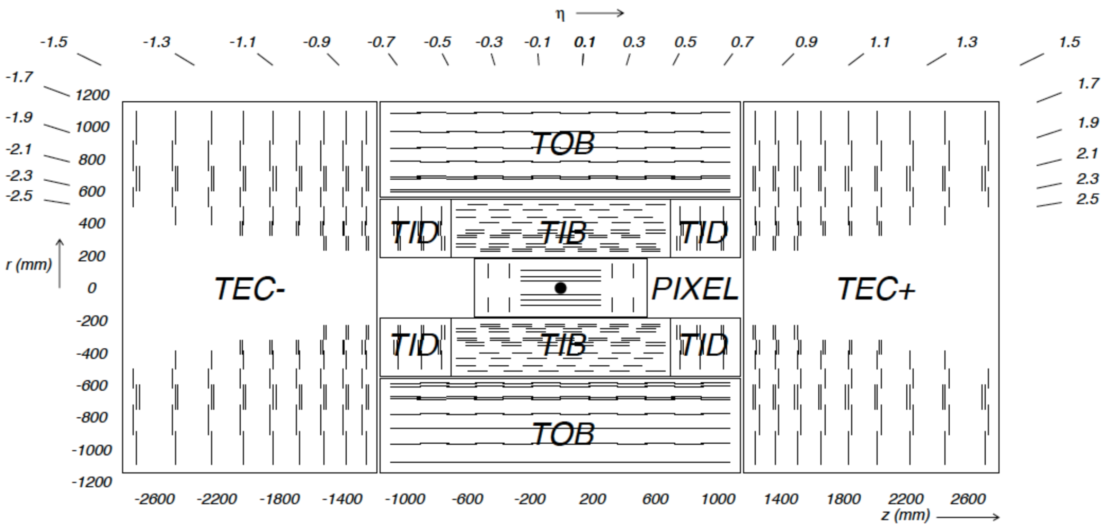

Figure 3.3: General layout of the silicon tracker. Each line represents a detector module. Double lines indicate back-to-back modules which deliver stereo hits.

A general view of the silicon tracker is shown in Figure 3.3. The **pixel detector** is built from 3 barrel layers, at radii of 4.4, 7.3 and 10.2 cm and two end disks on each side at a distance of $z = \pm 34.5$ and ± 46.5 cm from the interaction point. It consists of 1440 segmented silicon sensor modules with a total of 66 million readout channels. The sensor surface of the barrel modules is parallel to the magnetic field, while the modules in the forward detectors are tilted by 20°. Each pixel is 125×125 μm^2, and a spatial resolution of ≈ 10 μm in the $r - \phi$ projection and $\approx 15 - 20$ μm in the *z-axis* is achieved.

The **silicon strip tracker** is at the radial region between 20 cm and 116 cm. It is composed of silicon microstrips, from 320 to 550 μm of width, depending on their localisation. They are organised in modules (15148 in total) providing a measurement in two dimensions of the position of the particle. This is done by calculating the centre of the charge distribution in the different strips, detected through the ionisation produced by the particles traversing the detector. The silicon strip tracker is composed of three different subsystems: the Tracker Inner Barrel (TIB) and the Tracker Inner Disks (TID) which are composed of 4 barrel layers up to R = 55 cm, supplemented by 3 disks at each end. The TIB/TID is surrounded by the Tracker Outer Barrel (TOB). It has an outer radius of 116 cm and consists of 6 barrel layers, extending until $z = \pm 118$ cm. Beyond this z range the Tracker EndCaps (TEC+ and TEC-) cover the region 124 cm $<| z |<$ 282 cm and 22.5 cm $<| r |<$ 113.5 cm. Each TEC is composed of 9 disks.

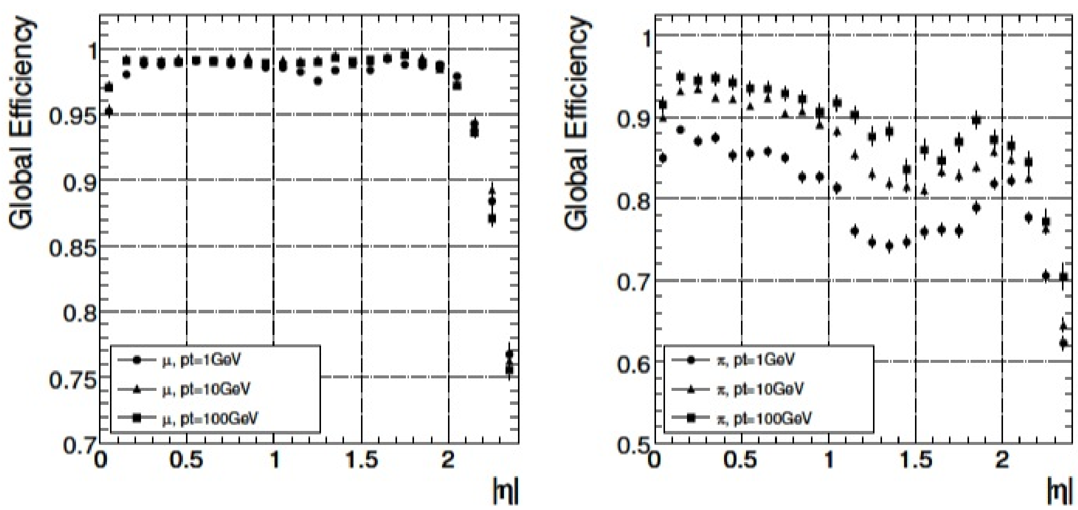

Figure 3.4: Global track reconstruction efficiency for simulated muons (left panel) and pions (right panel) of transverse momenta of 1, 10 and 100 GeV/c.

The expected performance of the track reconstruction is shown in Figure 3.4 for muons and pions. The track reconstruction efficiency for high energy muons is about 99% and drops at $|\eta| > 2.1$, due to the reduced coverage of the forward pixel detector. For pions and hadrons the efficiency is in general lower because of interactions with the material in the tracker.

The granularity of CMS tracker ensures excellent intrinsic momentum resolution. Figure 3.5 shows the material budget of the CMS tracker in units of radiation length[2]. It increases from 0.4 X_0 at $\eta \approx 0$ to about 1.8 X_0 at $|\eta| \approx 1.4$, beyond which it falls to about 1 X_0 at $|\eta| \approx 2.5$.

In order to compute the intrinsic error in the measurement of the transverse momentum it is necessary to take into account the error due to the determination of the position of the particle in the sensor, multiple scattering and energy losses due

[2]The radiation length X_0 is a characteristic of the material, related to the energy loss of high energy electrons in the material. It is defined as $\frac{716.4 \cdot A}{Z(Z+1)\cdot \ln \frac{287}{\sqrt{Z}}}$ (gcm^{-2}), where Z is the atomic number and A is mass number of the nucleus.

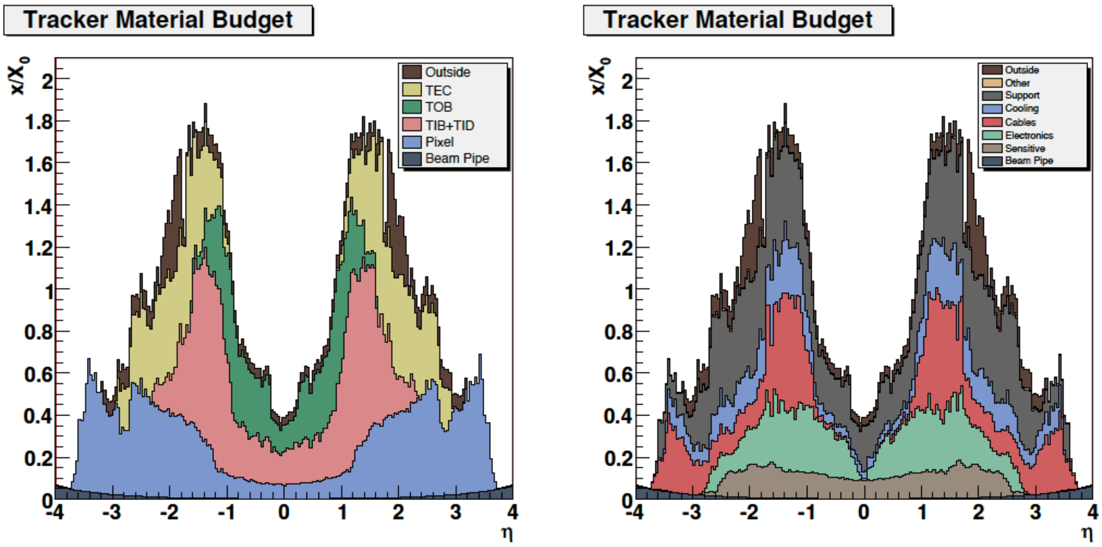

Figure 3.5: Material budget in units of radiation length as a function of pseudorapidity for the different CMS tracker sub-detectors, left, and split into the functional contributions.

to ionisation which add non-Gaussian tails to the measurement. Other material effects are bremmstrahlung, relevant at high momenta, delta rays and other backgrounds. Another source of uncertainty comes from deviations from the ideal modelling of the detector such as misalignment. Therefore the error results in a dependence of the form:

$$\frac{\Delta p_T}{p_T} = kp_T \oplus \beta \oplus \frac{\gamma}{p_T}$$

In Figure 3.6 the transverse momentum resolution and the impact parameter one for muon tracks with $p_T = 1$, 10 and 100 GeV/c are shown. At high momenta the resolution is around 1-2% up to $|\eta| \approx 1.6$, beyond which it degrades due to the reduced lever arm. The material of the tracker accounts for 20-30% of the transverse momentum resolution. At lower momenta the resolution is dominated by multiple scattering. Concerning the transverse impact parameter, d_0, it is constant at high momentum and dominated by the hit resolution in the first pixel layer, while at lower momentum it is degraded by multiple scattering, similarly for the longitudinal impact parameter, z_0. The improvement of the z_0 resolution up to $|\eta| \approx 0.5$ is due to the charge sharing effects among neighbouring pixels.

An example of the resolution of the track impact parameter measured with 2010 collision data at a centre of mass of 7 TeV is displayed in Figure 3.7, the agreement between the measured resolutions and the predictions from simulation is within 2-3% [25].

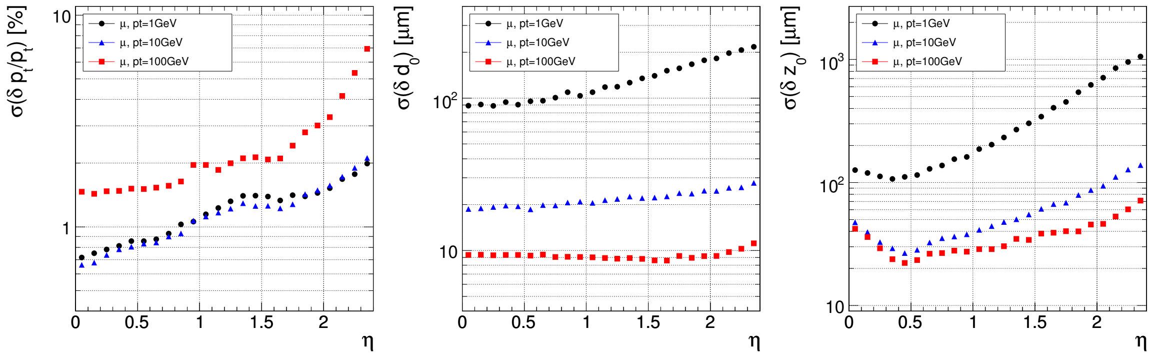

Figure 3.6: Resolution of several track parameters for single muons simulated with transverse momenta of 1, 10 and 100 GeV/c: transverse momentum (left panel), transverse impact parameter (middle panel), and longitudinal impact parameter (right panel) [19].

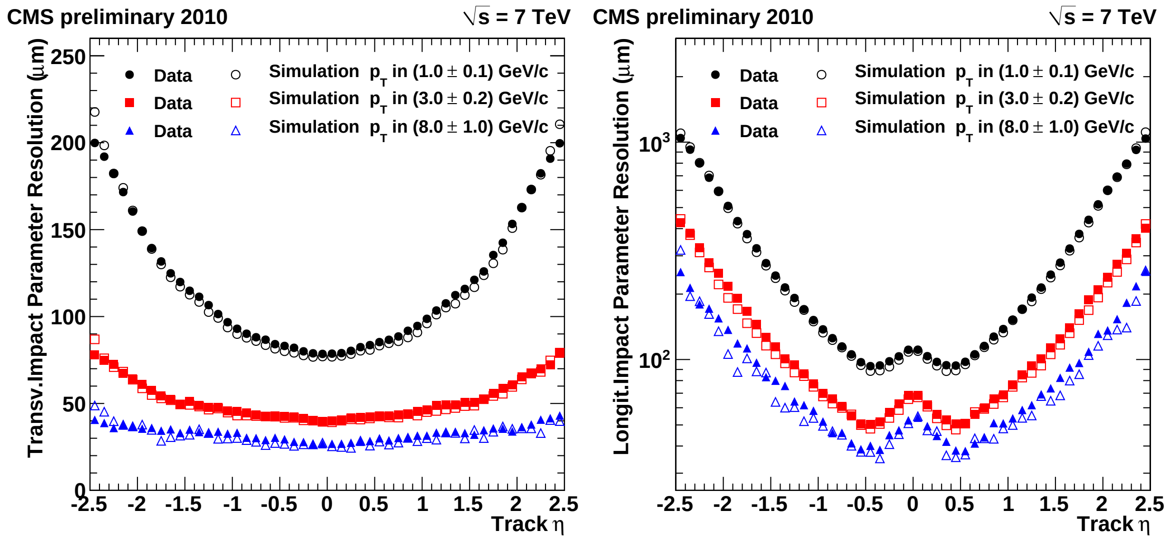

Figure 3.7: Measured resolution with 2010 collision data [25] of the track transverse (left) and longitudinal (right) impact parameter as a function of the track η for transverse momenta in 1.0±0.1 GeV/c (circles), in 3.0±0.2 GeV/c (squares) and in 8.0±1.0 GeV/c (triangles). Filled and open symbols correspond to results from data and simulation, respectively.

3.2.3 Calorimetry: Electromagnetic Calorimeter

The electromagnetic calorimeter (ECAL) [26, 27] is an hermetic and homogeneous detector with a large pseudorapidity coverage, $|\eta| < 3.0$. The ECAL is divided into barrel and endcap detectors as illustrated in figure 3.8. It is composed of scintillation crystals from lead tungstate ($PbWO_4$), 61200 in the barrel and 7324 in each endcap, to measure mainly the energy and position of photons and electrons. The choice of that material is motivated by its fast response and high radiation resistance and its very good resolution.

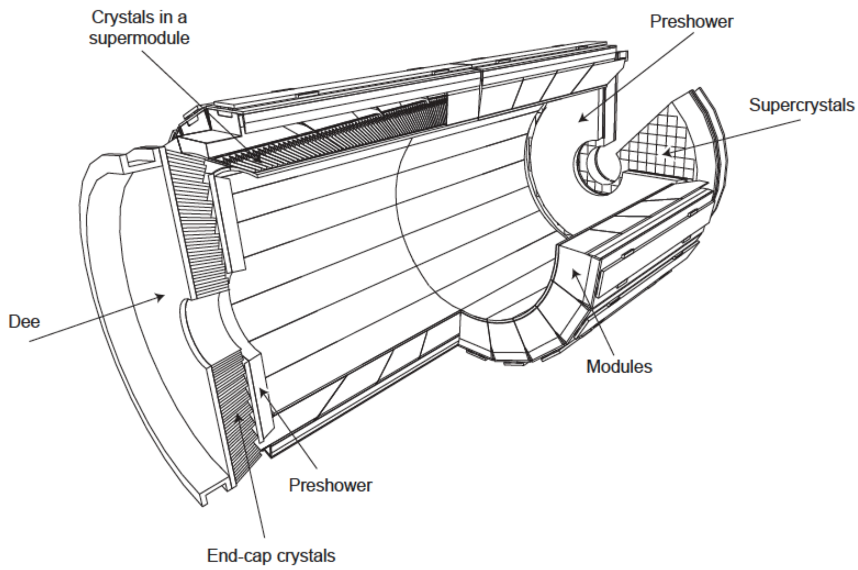

Figure 3.8: Layout of the CMS electromagnetic calorimeter showing the arrangement of crystal modules, supermodules and endcaps, with the preshower in front.

The crystals have tapered shape and are mounted in a quasi-projective geometry. The crystal front face is 22×22 mm^2 in the barrel and 28.6×28.6 mm^2 in the endcaps, ensuring a fine granularity. The length of a barrel crystal is 23 cm, corresponding to 25.8 radiation lengths, and of an endcap crystal is 22 cm, 24.7 radiation lengths. This values matched the requirement that the electromagnetic shower must be fully contained in the calorimeter. The presence of a preshower detector, two layers of lead each followed by a silicon strip detector, in front of the endcaps with a thickness of $3X_0$, reduces this required length and improves the position determination of electrons and photons, as well as the identification of neutral pion decays.

The ECAL barrel (EB) has a volume of 8.14 m^3 and its front face is at a radial distance of 1.29 m from the interaction point. It has 360-fold azimuthal segmentation and two times 85-fold segmentation in pseudorapidity. The two ECAL endcaps (EE) cover the rapidity range $1.479 < |\eta| < 3.0$ and they are situated at a longitudinal distance of 3.15 m from the interaction point, with a total volume of 2.90 m^3.

Electrons and photons deposit their energy in the form of electromagnetic cascades in the crystals. The scintillation light is read out by avalanche photodiodes (APDs) in the barrel and vacuum phototriodes (VPTs) in the endcaps. The light output and the amplification have a strong temperature dependence, being the nominal operating temperature 18^{o}C, which has to be kept stable to a precision of $\pm$0.05^{o}C.

For energies below about 500 GeV, the energy value at which shower leakage from the rear of the calorimeter starts to become significant, the energy resolution can be parametrised by the following expression:

$$\left(\frac{\sigma_E}{E}\right)^2 = \left(\frac{S}{\sqrt{E}}\right)^2 + \left(\frac{N}{E}\right)^2 + C^2$$

where S is the stochastic term, N the noise term, and C the constant term. The individual contributions are shown in Figure 3.9. The stochastic term includes fluctuations in the shower containment as well as a contribution from photostatistics. The noise term contains the contributions from electronic noise, important at low energy, and pile-up noise, negligible at low luminosity. The values of the parameters were determined by an electron test beam measurement, resulting S = 0.028 GeV$^{1/2}$, N = 0.12 GeV and C = 0.003. The curve labelled 'intrinsic" includes the shower containment and a constant term of 0.55%. Terms representing the degradation of the energy resolution at extremely high energies have not been included. This result with beam test demonstrates that the goal for energy resolution of better than 0.5% above 100 GeV is achieved.

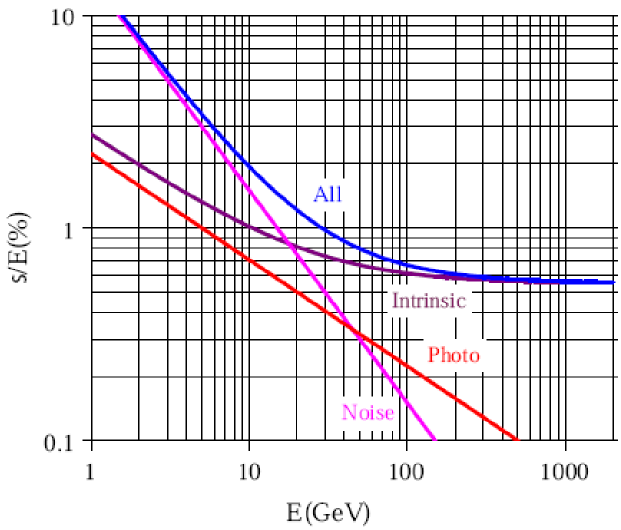

Figure 3.9: Different contributions to the energy resolution of the $PbWO_4$ calorimeter.

3.2.4 Hadronic Calorimeter

In the CMS detector the energy measurement of the ECAL is complemented by the hadronic calorimeter (HCAL) [28, 27]. The hadronic calorimeters are particularly important for the measurement of hadron jets and missing transverse energy due to neutrinos or exotic particles as they require a hermetic detector coverage. The HCAL is a sampling calorimeter built from alternating layers of massive absorbing brass plates and plastic scintillator tiles arranged in trays. The quality of the energy measurement depends on the fraction of the hadronic shower detected in the calorimeter. Consequently, the thickness of the material in the tray has to be large enough to absorb the major part of the shower. The barrel part of the HCAL, HB, occupies the volume between the ECAL (r = 1.77 m) and the magnetic coil (r = 2.95 m). Thus, the HB is supplemented by an outer hadronic calorimeter (HO) located between the solenoid and the muon chambers. The latter uses the solenoid as an additional absorbing material and provides sufficient containment for hadronic showers with a thickness of 11.8 interaction lengths (λ_l). This part of the subdetector covers up to $|\eta|$ <1.3, the endcap hadronic calorimeter (HE) covers from that η value to $|\eta|$ <3.0. Beyond that region, the forward hadron calorimeter (HF) placed at 11.2 m from the interaction point extends the pseudorapidity coverage up to $|\eta| < 5.2$. An scheme of the hadronic calorimeter is depicted in Figure 3.10

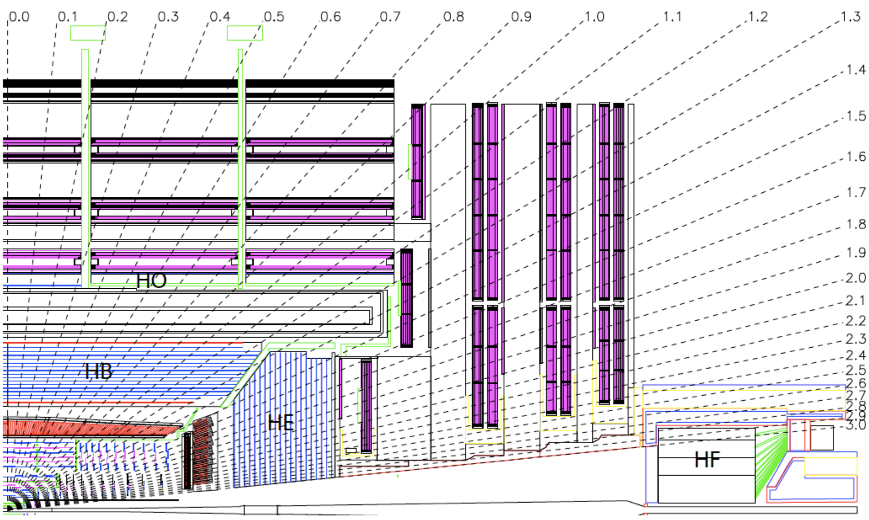

Figure 3.10: Longitudinal cut of a quarter of CMS showing the location of the different components of the hadronic calorimeter. The HB and HE components surround the ECAL calorimeter, the HO is located at the central wheels and outside the solenoid and the HF is behind the last station of the muon system.

The HB is mounted inside the 3.8 T field. The plastic scintillator is divided into 16 η sectors, resulting in a segmentation ($\Delta\eta$, $\Delta\phi$) = (0.087, 0.087). It consists of 36 identical azimuthal wedges which form the two half–barrels (HB+ and HB-). Each wedge is a 20 degree stack. The HO is divided into 5 rings in η, to fit with the muon system. The central ring has two layers of 1.49 cm scintillating tiles, whereas the layers of the remaining ones have only one. The segmentation is designed to mirror that of the HB such that consistent hadronic towers can be constructed.

The endcap calorimeters, HEs, are attached to the muon endcaps and have about 10 interaction lengths. They are approximately 1.8 m thick, with an inner radius of 40 cm and outer radius of about 3 m. The granularity obtained is identical to the one in the barrel up to $|\eta| < 1.6$ and increases to $(\Delta\eta, \Delta\phi) = (0.17, 0.17)$ for larger pseudorapidities. There are 19 layers of scintillator. The absorber plates are staggered to ensure all incident particles will shower.

The HF, at $3 <| \eta |< 5.2$ resides in a very high radiation area and cannot be constructed of conventional scintillator and wave-shifter materials. Consequently it is made of iron and quartz fibres as active media. Hadronic showers are sampled at various depths by the quartz fibres, of selected lengths, which are inserted into the absorber plates. The energy of jets is measured from the Čerenkov light signals produced as charged particles pass through the quartz fibres. These signals result mainly from the electromagnetic component of showers, which results in excellent directional information for jet reconstruction. Fiber optics transport the Čerenkov signals to photomultiplier tubes located in radiation shielded zones to the side and behind each calorimeter.

The transverse energy resolution of each subdetector is shown in Figure 3.11, it is typically of the order of 10% for jets with high transverse energy.

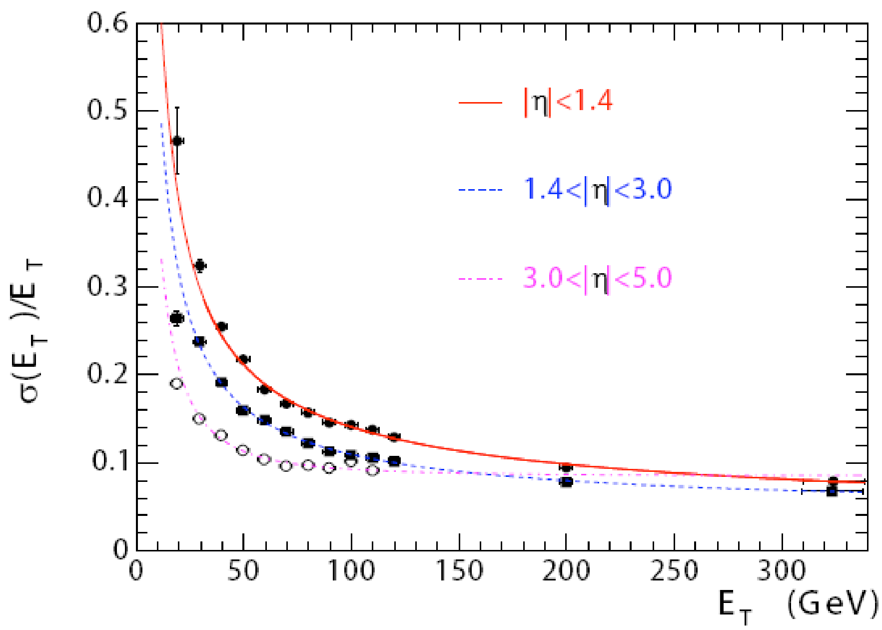

Figure 3.11: Evolution of the HCAL jet energy resolution as a function of the transverse energy for the different subdetectors [28].

3.2.5 Muon System

One of the main design objectives of the Compact Muon Solenoid detector was to obtain a high precision muon momentum measurement, for its key role both in new physics searches and in Standard Model measurements. In particular, it is relevant for the analysis presented in this thesis, as the selection is based on a well reconstructed high p_T muon. Hence a robust and redundant muon spectrometer is needed to provide precise muon identification, good resolution of high p_T measurements and effective trigger capabilities. In comparison with other observables, muons are characterised by their simplicity in identification: between the interaction point and the muon chambers there is a big amount of material that absorbs practically all other particles. Only muons and neutrinos are able to reach the muon chambers.

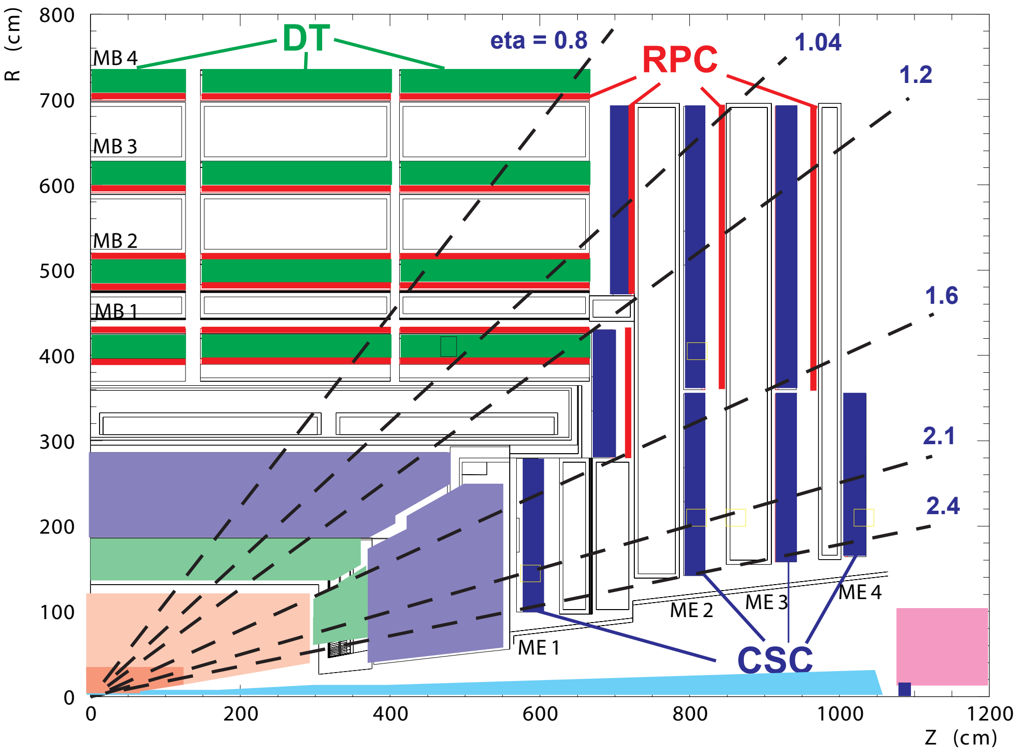

Figure 3.12: Layout of the different subdetectors of which the Muon Spectrometer is composed.

The muon system [29, 27] is the outermost group of subdetectors of the CMS experiment, covering an $|\eta|$ region up to 2.4. Its layout is shown in Figure 3.12. It consists of three different types of gaseous detectors, whose design is driven by the differences in the radiation environment and magnetic field at different η regions. Drift Tubes Chambers (DTs) are used in the barrel, up to $|\eta| < 1.2$, where both the muon rate and residual magnetic field are low. The endcaps, $0.8 < |\eta| < 2.4$, are instead equipped with Cathode Strip Chambers (CSCs), chosen to cope with the high particle flux and non uniformity of the magnetic field. In order to ensure redundancy and improve trigger capabilities, Resistive Plate Chambers (RPCs) complement DT and CSC based detectors, both in barrel and endcaps. RPCs allow only coarse spatial resolution measurements, however they are characterised by fast response and excellent time resolution.

- **Drift Tubes**

  The Barrel Detector consists of 4 concentric stations of 250 chambers inside the magnet return yoke of CMS. It follows the yoke segmentation and consists of 5 iron wheels composed of 12 azimuthal sectors, each one covering an angular region of 30°. Every wheel consists of four concentric rings of chambers, called stations and named respectively MB1/2/3/4, where MB stands for Muon Barrel. Each station is formed by 12 DT chambers with the exception of MB4 which consists of 14 of them.

  The basic detector element is a rectangular drift tube cell with a transverse size of 4.2 cm × 1.3 cm. Cells are filled with a 85%/15% Ar/CO_2 gas mixture and are grouped parallely to form detection layers. Groups of four layers are assembled to form a superlayer and a block of two superlayers (SL) measuring the ϕ coordinate plus one measuring the z one finally forms a DT chamber. The only exception to this rule applies to the MB4 stations where only the two ϕ superlayer are present. A schematic layout of a single DT chamber is shown in Figure 3.13.

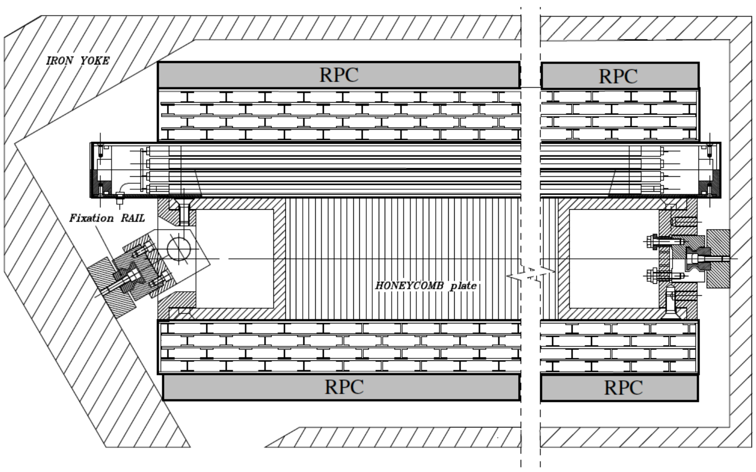

Figure 3.13: $(r - \phi)$ plane view of a DT chamber layout in position inside the iron yoke. The 2 SLs with wires along the beam direction and the other perpendicular to it are shown. In between is a honeycomb plate with supports attached to the iron yoke. The RPCs are attached to the DT chambers via support plates glued to the bottom and/or top faces, depending on chamber type.

The chamber design guarantees redundancy, since the muon crosses more cells than geometrically needed to define the track. A muon coming from the interaction point first encounters a ϕ–measuring SL, passes through the honeycomb plate, then crosses the z-measuring SL and the second ϕ-measuring

SL. The target chamber resolution is 100 μm in the r-ϕ plane and 150 μm in the z direction. This is achieved by 8 track points measured in the two (r-ϕ) SL, provided the maximum deviation from linearity of the cell space-time relation be less than 100-150 μm and the wire resolution be better than 250 μm.

- **Cathode Strip Chambers**

  The muon endcaps are composed of a total of 468 CSCs. Each Endcap consists of 4 stations of chambers, mounted on the disks enclosing the CMS magnet, perpendicular to the beam direction. In each disk the chambers are divided into 2 concentric rings around the beam axis (3 for the innermost chambers).

  Each CSC is trapezoidal in shape and consists of 6 gas gaps, each gap having a plane of radial cathode strips and a plane of anode wires running almost perpendicularly to the strips. All CSCs, except those in the innermost station, are overlapped in ϕ to avoid gaps in the muon acceptance. There are 36 chambers in each ring of a muon station, except for the innermost (highest η) rings starting from the second station which have 18 chambers. The CSCs are gaseous ionisation detectors working in avalanche mode and characterised by a short drift length. Information about the position of the incoming particle is collected both in the anode wire and on a group of finely segmented cathode strips. The latter allows to perform centre of gravity measurements ensuring high position resolution, while the former is characterised by a fast signal suitable for trigger purposes.

  The resolution measurements with the strips varies from $\sim$70 μm for the innermost stations to $\sim$150 μm for the outermost ones, while r can be determined with a precision of $\sim$0.5 cm.

- **Resistive Plate Chambers**

  A total of 6 layers of RPCs are embedded in the barrel muon system, 2 in each of the first 2 stations, and 1 in each of the last 2 stations. The redundancy in the first 2 stations guarantees that the trigger algorithm works even for low-p_T tracks, that may stop before reaching the outer 2 stations. In the endcap region, there is a plane of RPCs in each of the first 3 stations in order for the trigger to use the coincidences between stations to reduce background, to improve the time resolution for bunch crossing identification, and to achieve a good p_T resolution at trigger level. Time tagging capabilities of RPCs is better than 25 ns (LHC bunch crossing time).

  The CMS RPC basic double-gap module consists of 2 gaps, referred as up and down gaps, operated in avalanche mode with common pick-up readout strips in between. The total induced signal is the sum of the 2 single-gap signals. When an ionizing particle traverses a RPC, a cluster of electrons starts an avalanche multiplication. The drift of the charge towards the anode induces a fast charge on the pick–up electrode, which represents the useful signal of the RPC.

Figure 3.14 shows the total muon p_T resolution distribution and the one obtained using only information coming from the tracker or the muon system only. It can be seen that, at low transverse momentum, tracker precision dominates, while at higher p_T (p_T>200 GeV/c) the combination of the two systems improves the overall resolution. Given the relevance for the work presented in this thesis, the muon reconstruction will be described in detail in chapter 5.1.

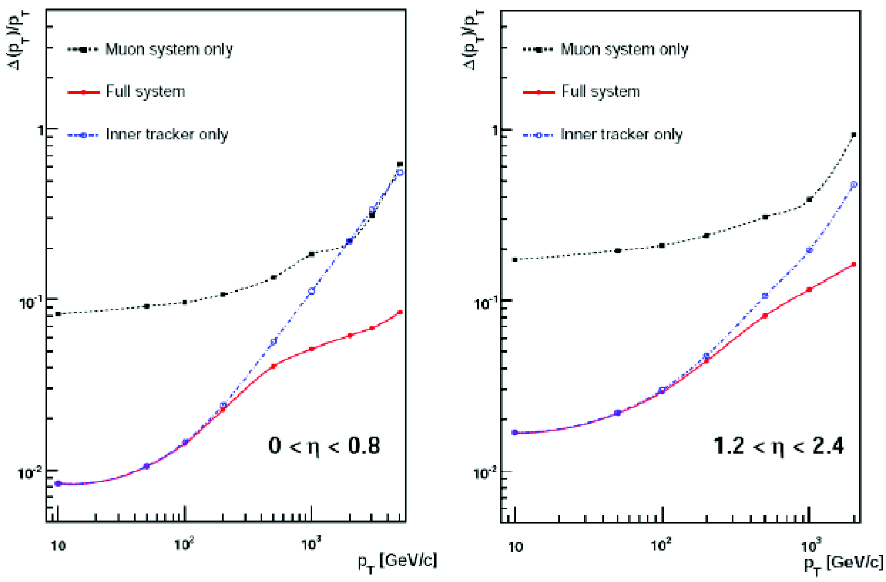

Figure 3.14: Muon transverse momentum resolution as a function of p_T in the barrel (left) and endcap (right) region obtained using only the tracker or the muon system information and combination of both.

3.2.6 CMS Trigger and Data Acquisition System

The CMS trigger system is designed to cope with an unprecedent high luminosity and interactions rates. It ensures high data recording efficiency for a wide range of physics objects and events topologies, while applying online selective requirements to reduce the incoming 40 MHz event rate to an output rate of about 100 Hz, allowing the permanent storage of the events.

The CMS trigger system reduces the event rate in two steps called Level 1 (L1) [30] and High Level Trigger (HLT) [31]. The former is designed to achieve a maximum output rate of 100 kHz and consists of custom-designed, programmable electronics while the HLT is based on software algorithms running on a large cluster of commercial processors, the event filter farm.

The L1 trigger system uses only coarsely segmented data from the muon system and the calorimeters while the full granularity data are stored in the detector front-end electronics waiting for the L1 decision. This has to be taken within a latency time of 3.2 μs, that is, after 128 bunch crossings and is based on the decision of local, regional and global trigger components. It also depends on the readiness of the other subdetectors and the Data Acquisition System (DAQ) which is supervised by the Trigger Control System. The trigger architecture is displayed in Figure 3.15. The HLT has access to the complete read-out data and can perform complex calculations similar to those made in the offline analysis software.

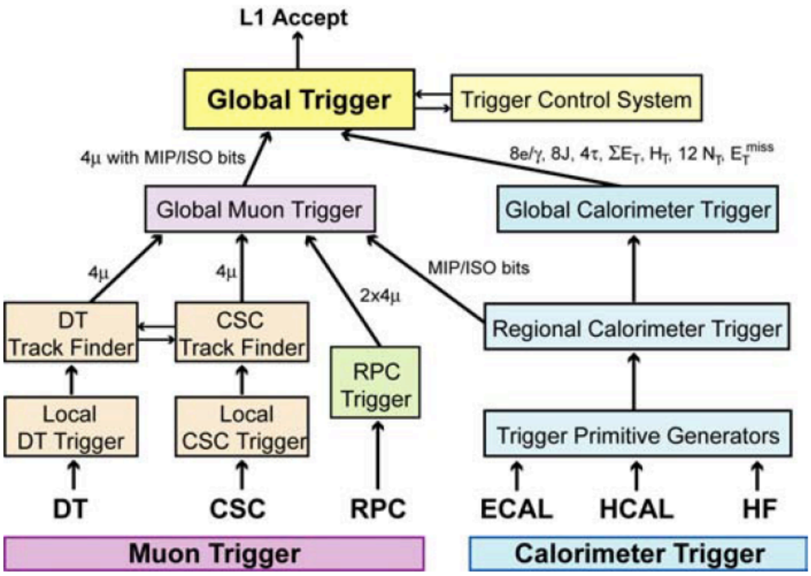

Figure 3.15: Architecture of the Level-1 Trigger.

The Local Triggers or Trigger Primitive Generators (TPG) are based on energy deposits from calorimeter trigger towers and track segments or hit patterns in muon chambers, respectively. Regional Triggers combine their information and use pattern logic to determine ranked and sorted trigger objects, for instance electron, photon, jets or muon candidates in limited spatial regions. The rank is determined as a function of energy or momentum and quality. The latter reflects the level of confidence attributed to the L1 parameter measurements, based on detailed knowledge of the detectors and trigger electronics and on the amount of information available. The Global Calorimeter and Global Muon Triggers determine the highest-rank calorimeter and muon objects across the entire experiment and transfer them to the Global Trigger, which takes the decision to reject an event or to accept it and distributes it to the subdetectors. The decision is based on the results of algorithms which for example apply momentum thresholds to single objects or require objects multiplicities to exceed predefined values. This information consists of classified candidates as electrons, photons, muons and central and forward hadronic jets as well as global quantities like total and missing transverse energy, the sum of transverse energies over a programmable threshold and twelve, threshold dependent, jet multiplicities. Up to 128 algorithms can be executed in parallel.

If an event is accepted by the L1 trigger, the full detector information (∼1 MB) is read out by the Data Acquisition (DAQ) system at a rate of up to 100 kHz, passed to the event filter farm and used as input for the HLT. The HLT algorithms are implemented in the same software as used for offline reconstruction and analysis and consist of subsequent reconstruction and selection steps. The framework uses a modular architecture and the modules to be executed are defined at runtime by means of configuration files. The HLT menu is composed of a set of trigger paths, each path addressing a specific physics object selection. The execution of a path is interrupted if the processed event does not fulfil the conditions imposed by a given filter module.

3.3 Data in CMS

The LHC proton-proton collision start-up was the 23th November 2009, but well before that, the CMS experiment was already installed in the cavern and commissioned. During 2008 and 2009 two major cosmic data-taken campaigns took place, recording more than 300 million cosmic muons in each of them. CMS exploited these cosmic muon campaigns as a calibration and commissioning tool for the data-taking chain and the performance of the detectors. In addition, more than a million beam halo muons were recorded during the commissioning of the LHC accelerator during 2008-2010.

The analyses performed using these cosmic and halo muons events was a valuable tool to establish the alignment of the detector to the level previously foreseen to be reached after the analysis of the first 10 pb^{-1} [32, 33] of data and to improve the modelling of the magnetic field [23], apart from testing the response of the different components of the detector. The calibration obtained with the cosmic data analysis was incorporated in the reconstruction software for the first collision data taken.

In particular, the determination of the momentum resolution of cosmic muons gave a handle on the performance of the muon with high transverse momentum, which has been used to estimate the expected reconstruction efficiency and resolution of muons from proton-proton collisions. Otherwise, one would have to rely only on the predictions by the simulation.

3.3.1 2010 Collision Data

The first p collisions took place at the end of 2009, as stated above, starting by a pilot commissioning run with collisions at centre of mass energy, $\sqrt{s}$, of 900 GeV and 2.36 TeV in November and December. Finally, the LHC operation at $\sqrt{s}$= 7 TeV started on March 30th, 2010. LHC operated proton-proton collision mode until the beginning of November 2010, when the heavy ion run started.

The 2010 Run can be divided into three periods: an initial commissioning period in which the integrated luminosity recorded was few nb^{-1} and two longer periods, henceforth called Run2010A and Run2010B where approximately 3.3 pb^{-1} and 40 pb^{-1} were recorded by CMS, respectively. To have an approximate idea of the number of events produced, at the centre of mass energy, 7 TeV, the total inelastic cross section corresponds to 60 mb, which means that 60 million particles are produced per nb^{-1}. Electroweak processes have a much lower cross section, see Figure 2.2, for instance only around 100 W bosons are expected per nb^{-1} (10^5 per pb^{-1}).

These long two periods, Run2010A and Run2010B, correspond to the data analysed in this thesis. Between each period there was a relatively long technical stop of the LHC operation, aimed to increase the instantaneous luminosity. This was achieved by reducing the beam size (β^*), increasing the number of particles per bunch and the number of colliding bunches, see equation 3.2.

The LHC machine performed smoothly during the whole 7 TeV operation in 2010 increasing progressively the instantaneous luminosity up to $\mathcal{L} = 2 \times 10^{32}\text{cm}^{-2}\text{s}^{-1}$ reached in October 2010 (see Figure 3.16). The filling scheme evolved frequently and at the beginning of November 2010 it was 248 bunches, with a spacing of 150 ns. The LHC beam parameters at the end of both periods are listed in Table 3.2.

Parameter	Design	End of Run2010A	End of Run2010B
$\sqrt{s}$	7 TeV/c	3.5 TeV/c	
Dipole field B	8.33 T	4.17 T	
Protons per bunch	1.15×10^{11}		
ϵ_n Norm. transverse emittance	3.75μm		2.5μm
$\beta^\star$ IP5 beta value	0.55 m	3.5m	
Number of bunches per beam	2808	50	368
E_{stored} Stored energy	362 MJ	2.8MJ	28 MJ
collisions per crossing	20	1.5	2.7
Luminosity	10^{34} cm^{-2}s^{-1}	10^{31} cm^{-2}s^{-1}	10^{32} cm^{-2}s^{-1}

Table 3.2: LHC Beam Parameters at the end of the two main periods of data taken in 2010, compared to nominal values.

In summary, the proton-proton integrated luminosity delivered by LHC until the winter shut down was around 47 pb^{-1} and the one recorded by CMS was approximately 43 pb^{-1}. This means that the overall data taking efficiency of CMS during 2010 was 91.72%. Figure 3.17 shows the integrated luminosity delivered by LHC in 2010 for the proton-proton collision period.

The quality of the data used in all CMS analyses is guaranteed by the Data Quality Monitoring (DQM) system, which controls the detector conditions and the reconstruction chain and objects. It consists of a catalogue of one and two dimensional histograms that allows to have access to information from the performance of the hardware to high level objects variables. This information is scrutinised by experts to asses the quality of the data recorded and to certify its goodness to be analysed. According to these quality tests, 36 pb^{-1} of data were certified as optimal out of the 43 pb^{-1} total recorded during 2010 for the physics analysis discussed in this dissertation. Thus that is the data sample employed.

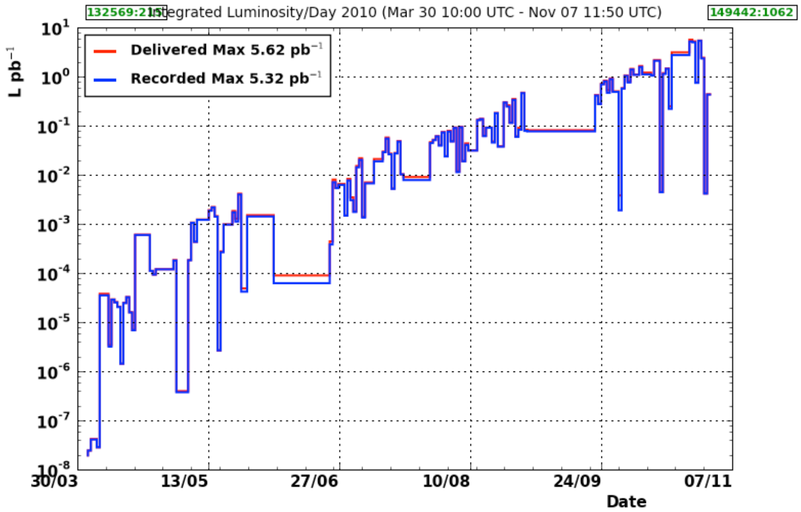

Figure 3.16: Maximum instantaneous luminosity per day delivered to CMS (red) and recorded (blue) during stable beams at 7 TeV centre-of-mass energy.

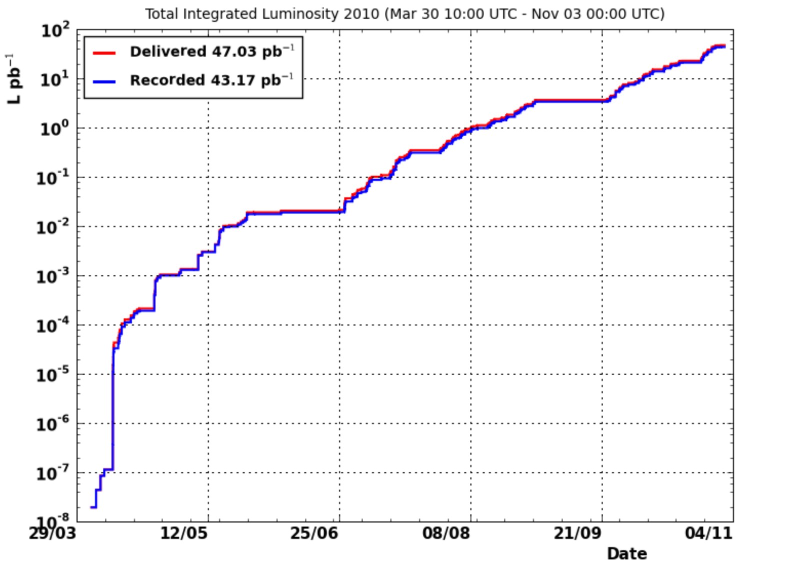

Figure 3.17: Integrated luminosity versus time delivered to (red), and recorded by CMS (blue) during stable beams at 7 TeV centre-of-mass energy in 2010.

The data-taking was resumed in March 2011, at the same energy as in 2010. More than 2 fb^{-1} were already recorded at the beginning of August. It is foreseen that this new campaign will follow until the end of 2012 with the goal of recording an integrated luminosity of 5-10 fb^{-1}. Afterwards a long shutdown, not shorter than a year, is planned to commission the LHC to reach the designed centre of mass energy of 14 TeV.

Chapter

4

Muon Trigger Reconstruction

Several of the new physics processes searched for in hadron collision events are characterised by muons in the final state. For instance, they provide a clean signature in a large background of jets, allowing for the identification of rare signal events. Thus it is crucial for CMS to be able to detect them efficiently and with an excellent momentum resolution in a wide p_T range. The spectrum of inclusive muons produced in proton-proton collisions falls rapidly with transverse momentum. The low p_T region is populated mostly by muons coming from minimum bias processes while the sources of muons at high momentum are mainly decays of heavy flavour ($b\bar{b}$) and electroweak ($W \to l\nu$, $Z \to ll$, $t\bar{t}$) processes. These physical sources of muons coming from the proton-proton interaction are accompanied by misidentified objects as fake muons, cosmic muons, hadron punch-through or decays in flight of pions and kaons.

Apart from the well known processes, many interesting physical processes foreseen to occur at the LHC are characterised by final states containing high p_T muons, therefore a muon spectrometer able to perform precise measurements is needed, in order to carry out effective standalone track reconstruction. Moreover, due to the high interaction rate, a high-performance Level-1 muon trigger system is required, to operate fast identification of the relevant events.

In this chapter a more detailed description of the muon trigger system in CMS is presented, focusing on the aspects studied, namely the performance of the DT local trigger (L1 trigger) and the Level 2 step of the High Level Trigger. For completeness an overview of the remaining elements of the trigger will be briefly presented.

4.1 L1 Muon Trigger

The Level 1 Muon Trigger is devoted to identify the existence of a muon in an event and assign it spatial information and p_T as well as the identification of the bunch crossing, BX, when the particle was produced. All the three subsystems described in section 3.2.5 take part in the trigger process, providing robustness and redundancy to the system. CSC and DT based triggers ensure good spatial resolution, whereas excellent time resolution is obtained from RPCs information. These complementary detector technologies are also sensitive to different types of backgrounds, thus leading to good noise rejection capabilities. Prior to the performance of the muon barrel subdetector local trigger, a succinct summary of the whole L1 muon trigger is presented in the following.

The Level 1 Trigger in the DT chambers provides track segments in the ϕ projection and hit pattern in the η one, while the CSC determine three-dimensional track segments. CSC and DT triggers operate using a two-level logic, based on Trigger Primitive Generators (TPGs) which creates initial trajectory segments inside a muon chamber starting from the detector signals, hits, and Regional Triggers, consisting on Track Finders (TF), which join them afterwards to form complete tracks and assign physical parameters to them.

On a first processing phase the information coming from every single DT/CSC chamber is elaborated by on-board DT/CSC-TPGs, which operate reconstruction algorithms on the detector signals. They are in charge of BX assignment, trigger segment position/direction estimation, and computation of a system dependent quality bit.

Information coming from different stations is then passed to the DT and CSC Track Finders (DTTF - CSCTF) whose mission is to build full muon tracks on the basis of local reconstructed primitives, assign them their charge and estimate their transverse momentum using tabulated values. They also deliver information about the quality of the track based on the number of stations used for reconstruction and coded in terms of a quality bit. In the η region where muons coming from the interaction point cross both the DT and CSC subsystems, the so called overlap region, exchange of information between the DTTF and the CSCTF is performed in order to improve regional track reconstruction.

The RPCs deliver an independent measurement derived from regional hit patterns, it does not perform a two step (local-regional) reconstruction. After synchronisation and cluster reduction, hits from all the stations are collected by a Pattern Comparator Trigger (PACT) that looks for space-time correlations in order to perform matching among them and p_T assignment. Pattern identification is carried out when at least three of the four stations are involved in the reconstruction process.

The Global Muon Trigger (GMT) receives up to four candidates (the ones with highest p_T) from each subsystem (DT, barrel RPC, CSC and endcap RPC) together with the isolation information from the global calorimeter trigger. If different subsystems share a muon, their parameters are combined to reach a better precision.

The GMT selects from all the muon subtrigger candidates a maximum of four and determines their momentum, charge, position and quality. The resulting list of trigger objects is then forwarded to the GT system for final processing. More in depth description of the CSC and RPC trigger systems can be found in [30], while a more exhaustive analysis of the DT local trigger is given in the next section.

4.1.1 DT L1 Local Trigger

As mentioned, before the first collisions took place in CMS, several periods of cosmic data taking were carried out. Even though the topology and timing are different for cosmic muons than for collision muons, these data was invaluable for the commissioning of the offline reconstruction in the muon chambers and of the muon local trigger. In this section the performance of the Level 1 local muon trigger is studied compared to the offline reconstruction of muon segments at the chamber level [34, 35] using cosmic data. The results are compared with collision data collected during 2010, see section 3.3.1. First of all, a description of the structure of this subdetector and its working mode will be reviewed.

The barrel muon system of the CMS detector covers the pseudorapidity region $|\eta| < 1.2$. It consists of four stations integrated in the return yoke of the magnet, divided into 5 wheels along the beam pipe direction. Each wheel is divided into 12 sectors, each one covering 30° in the $r - \phi$ plane, see Figure 4.1.

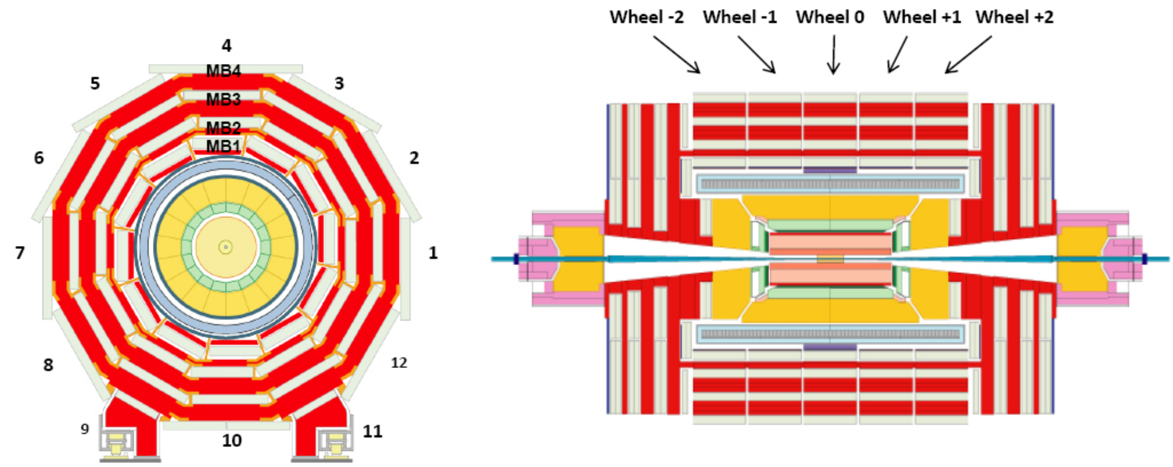

Figure 4.1: Left: schematic view of one of the five wheels of the muon barrel system of the CMS experiment, in the x-y plane. Right: the five wheels are visible in the longitudinal view of the CMS detector [35].

Every chamber is formed by twelve planes of drift tubes, organised in three independent subunits called Super Layers (SL) made up of four planes with parallel wires. Two SLs measure the coordinate in the bending plane (ϕ-SL), the third one measures the track coordinate along the beam axis (z-SL).

The segment reconstruction in a chamber is done independently for the $r-\phi$ and $r-z$ projections, only at the end of the procedure both projections are combined to build a three dimensional segment. The reconstruction is performed in three steps. First a segment candidate is built from a set of aligned hits inside a SL, this step begins with the selection of 2 hits in different layers, starting from the most separated ones. The pair is kept if the bending angle of the segment is compatible with a track pointing to the nominal interaction point. For each pair, additional hits are looked for in all layers. A linear fit is performed using the hit position and error for each collection of hits. The second step consists in selecting the best segments among those sharing hits, solving conflicts and suppressing hits, on the basis of the number of hits and the χ^2 of the segment. Finally the hits from the leftover candidates are updated, taking into account the incidence angle as reconstructed by the segment, and the linear fit is eventually redone using the updated hits. Segments must have at least three hits.

The DT Level-1 local muon trigger [27], see Figure 4.2, consists of several components: the Bunch and Track Identifier (BTI), the Track Correlator (TRACO) and the Trigger Server (TS). The BTIs are the DT trigger front-end device, they search for track segment candidates made of three or four aligned DT hits within a superlayer, for every bunch crossing. A quality bit used to discriminate *low* and *high* quality segments is also computed on the basis of the number of layers involved in the track identification, 3 or 4 respectively. The geometric layout of a single BTI is shown in Figure 4.2 top. Each BTI is connected to 9 cells of a single SL and adjacent BTIs partially overlap (having 5 cells in common) in order to avoid geometrical inefficiencies. BTIs are identical in the ϕ-view and θ-view SLs, the number of BTIs per SL depends on the chamber size.

The Track Correlator (TRACO) combines the segments from two ϕ-superlayers in a chamber. It attempts correlation between BTI segments coming from inner and outer SLs and links the information between them, improving track parameter determination. Each TRACO is connected to 4 BTIs in the inner SL and 12 BTI in the outer SL and adjacent TRACOs overlap only in the outer one. After this step there are two types of segments, uncorrelated and correlated ones. An uncorrelated segment is reconstructed only from hits in one SL, with either 3 hits (L, low quality) or 4 hits (H, high quality). The correlated one is a reconstructed segment with at least three hits in each of the two ϕ-layers of the chamber. Its quality can be HH, HL or LL, depending on the quality of the original segments in both superlayers.

The Trigger Server selects, in each chamber and at every bunch crossing, the two segments with the highest quality and the smallest angular distance with respect to the radial direction from the vertex (i.e. with the highest p_T) as the input of the DT Track Finder (DTTF). It also performs ghost track reduction on the fake tracks generated by adjacent TRACOs on the basis of configurable rejection algorithms.

The DTTF is divided into sectors, each of them covering an azimuthal angle, ϕ, of 30°. It builds tracks from segments in different stations and it assigns them a quality flag, p_T and ϕ and η coordinates using memory based look-up tables (LUTs). More details about the DTTF, part of the Regional Trigger, are given in section 4.1.3.

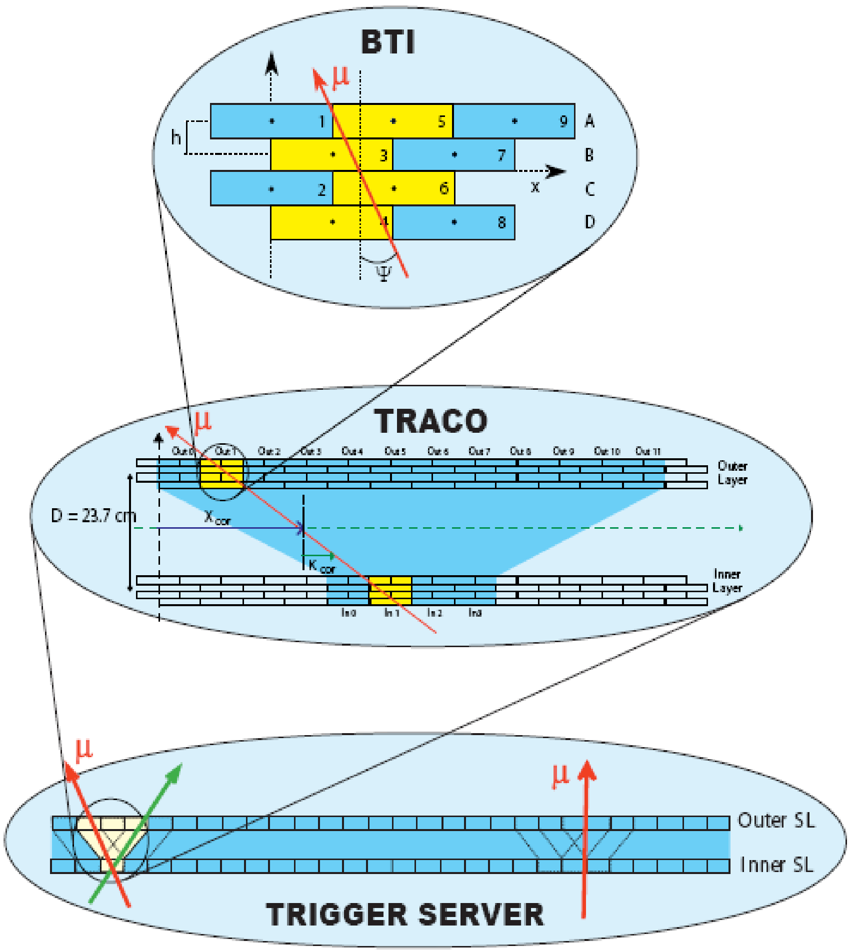

Figure 4.2: The main components of the DT Local Trigger in the ϕ view of a muon chamber. The BTIs detect hit alignments within each superlayer, the TRACOs search for a proper matching between superlayers, and the Trigger Server selects the best two candidates in the chamber and applies a ghost-suppression algorithm.

The aim of this chapter, as already mentioned, is to compare the offline segment reconstruction with the output of the local (at chamber level) L1 trigger reconstruction, i.e. the TRACO output, which is the input of the DTTF.

This study was performed using real data from cosmic muon global runs, corresponding to two different periods in 2008, when the detector was already installed in the cavern. Those periods are called CRUZET3 (Cosmic RUn at Zero Tesla) and CRAFT (Cosmic Run At Four Tesla). The former (7 - 14 July 2008) was the first global run with cosmic muons with large statistics from the trigger readout cards. At that time there was no magnetic field. In the latter (13 October - 10 November 2008), the magnetic field was raised to 3.8 T.

The analysis of CRUZET3 data was restricted to top sectors, in particular 3, 4 and 5, see Figure 4.1, where both the information from the chambers and the DTTF were available, whereas for CRAFT data the analysis was extended to all sectors as the DTTF information was recorded for all of them for the first time. In the majority of cases the results for CRUZET3 and CRAFT are compatible, meaning no difference in the trigger performance in the absence/presence of magnetic field, thus only CRAFT results are presented. During that data campaign some runs were taken without magnetic field, a comparison of the results from these runs and those taken with the solenoid on, as well with results from the collision data taken during 2010 are presented.

The collision data used correspond to the certified Run2010B data, with an integrated luminosity of approximately 33 pb^{-1}. In particular the analysis was done over a selected sample containing candidate events of W and Z bosons decaying to muons. These events were required to pass a selection to ensure that they contain offline reconstructed muons and muon trigger candidates. This selection required the event to be fired by a single muon trigger with certain p_T thresholds. The offline reconstructed muon must have been reconstructed in the tracker and the muon chambers to be accepted. Additionally, acceptance requirements in transverse momentum (p_T>20 GeV/c) and pseudorapidity (η <2.1) were also applied. A threshold in the transverse impact parameter with respect to the collision point was set to reduce the contamination from cosmic data in this collision data sample, which have different timing than collision muons.

The condition to trigger a muon in the DT system was to have at least two chambers fired in a sector. Within a chamber, the triggering condition relied on having either a correlated segment or a high quality segment in a ϕ-superlayer plus any kind of segment in a θ-superlayer.

4.1.2 DT Local Trigger Performance

This section is organised as follows: first, the selection of the muon segments studied is introduced. Second, the information obtained at trigger level, position and direction, is compared with the one from the offline reconstruction. Finally the comparison between the results of the data taken with and without magnetic field during the CRAFT period is shown.

The performance in all wheels and stations was studied, comparing only the position and direction corresponding to the $r-\phi$ plane, as there was no available information about the θ coordinate in the DTTF at that time. The information about the trigger and the offline reconstruction at this level is:

- Trigger: bunch crossing, wheel, sector and station which give the trigger, radial and bending angle (from which the local position and direction are derived) and quality code.
- Offline segments reconstructed in a given chamber, characterised by local position and direction.

The same primary information, the recorded hits, is used as starting point for both trigger and offline reconstruction, which then follow different processes. The comparison of the DT local trigger output with the information from the DT local muon reconstruction is done on a selected sample of good quality segments. Figure 4.3 shows the distribution of the number of segments reconstructed per event for the cosmic run (left) and collision data (right). The difference between both figures is a consequence of the different topology of cosmic muon and collision data. The former traverse the detector in general from top to bottom, so they can be reconstructed in its two halves, while the latter are produced in the centre of the detector and travel outwards, crossing only once the muon spectrometer. That is the origin of the small bump around 8 segments in Figure 4.3 left, corresponding to cosmic muons reconstructed in the whole detector, which can be measured in eight chambers. The distribution corresponding to the trigger information differs from the offline segments one because usually there is only one segment firing the local L1 trigger in a chamber while there could be more muon segments reconstructed per chamber in the same event.

Figure 4.4 presents the number of offline segments per chamber as a function of the sector number. The distribution in ϕ is homogeneous in collision data (right plot), that is, the population is similar in every sector, while cosmic muons (left plot) are concentrated on the top sectors (3, 4 and 5 according to Figure 4.1 left). As CMS is located 100 meters underground, the angular distribution of cosmic ray muons that traverse the detector is strongly peaked in the vertical direction and they are easier detected in sectors with the chambers more perpendicular to its trajectory. If the muon is parallel to the chamber it traverses, it may not cross enough layers to reach the minimun number of hits to create the segment. Bottom sectors (from 9 to 11) have lower occupancy compared to the top ones, because only the most energetic muons can cross the whole detector, so a large number of muons reconstructed on the upper part of the detector stops before reaching the lower half of the muon spectrometer. Due to the magnetic field, the muon trajectories bend in such a way that muons crossing the whole spectrometer are deflected into tilted sectors with respect to the vertical direction in the lower half (for instance sectors 8 or 11).

Around 10% of the cosmic muon events analysed contains more than one segment reconstructed in a chamber, see Figure 4.4 left, whereas by construction there is only one trigger segment, as mentioned above. Then to avoid double counting trigger segments only the cases where there was a unique segment reconstructed in the chamber were taken into account, which corresponds to the expected situation in collisions, where the number of muons per buch crossing per chamber is not expected to be often greater than one.

In Figure 4.5 left, the quality of the segments given by the trigger is compared to the number of hits of the reconstructed segment with CRAFT data. A good correlation is observed between the number of hits used for the reconstruction of the segment by the local trigger and the offline reconstruction. For example, most of the trigger segments with quality code HH are also reconstructed offline with 8 hits. In general terms, the offline reconstruction provides segments with equal or larger number of hits than the corresponding triggering segment. The distribution obtained with collision data is shown, see Figure 4.5 right plot, the correlation is similar.

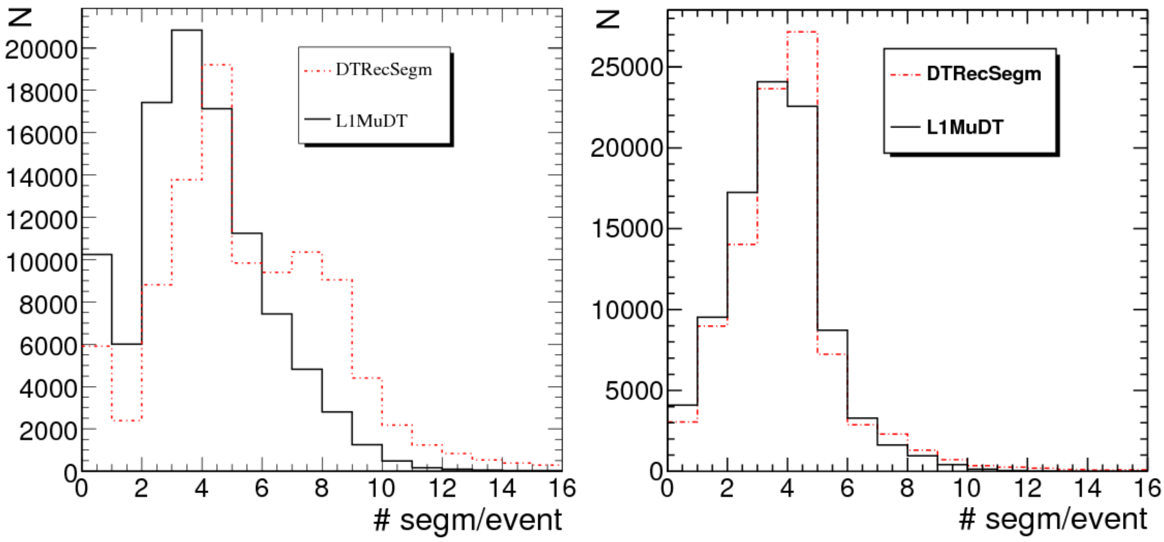

Figure 4.3: Number of segments per event given by the local L1 trigger and the offline reconstruction, for cosmic data (left) and collision data (right).

Once the samples are characterised, the comparison of the position and the direction of the segments given by the local trigger and the offline reconstruction is addressed. For that purpose segments were selected in the following way: for each reconstructed DT segment with 6 to 8 hits, the segment given by the trigger in the same chamber (same wheel, sector and station) with bunch crossing zero, BX=0, was chosen. The only additional condition applied was that the segment given by the trigger had to be a correlated one, i.e. its quality being HH, HL or LL. No restriction in the muon incidence angle was applied.

The L1 local mu trigger and the offline reco provide the information in term of different magnitudes and related to different coordinate systems. The local position, x, and direction, dx/dz, of the segment in the chamber is given with respect to a Cartesian coordinate system, whose origin is the geometrical centre of the chamber. The $x - axis$ $(y - axis)$ is parallel to the wires in the θ SL (ϕ-SLs), see Figure 4.6, left. The variables delivered by the trigger are a radial angle, ϕ, and a bending angle, ϕ_B, see Figure 4.6, right. The angle ϕ is defined as the angle between the position in x where the segment is reconstructed and the perpendicular line from the centre of coordinates of CMS to the chamber. The bending one measures the angle between the direction of the segment and ϕ.

In order to compare them, the radial angle, ϕ, is translated to the position x with respect to the centre of the chamber and the bending angle, ϕ_B, to the angle with respect to the normal to the chamber plane, $\psi = \text{atan}(dx/dz)$. According to Figure 4.6

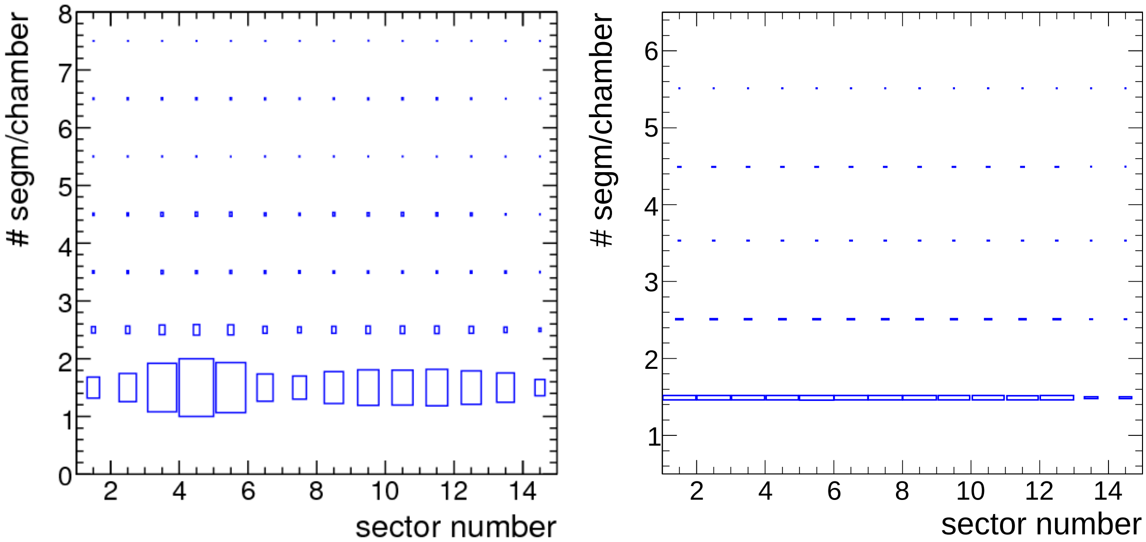

Figure 4.4: Number of segments per event reconstructed offline in a chamber as a function of sector number, for cosmic data (left) and collision data (right).

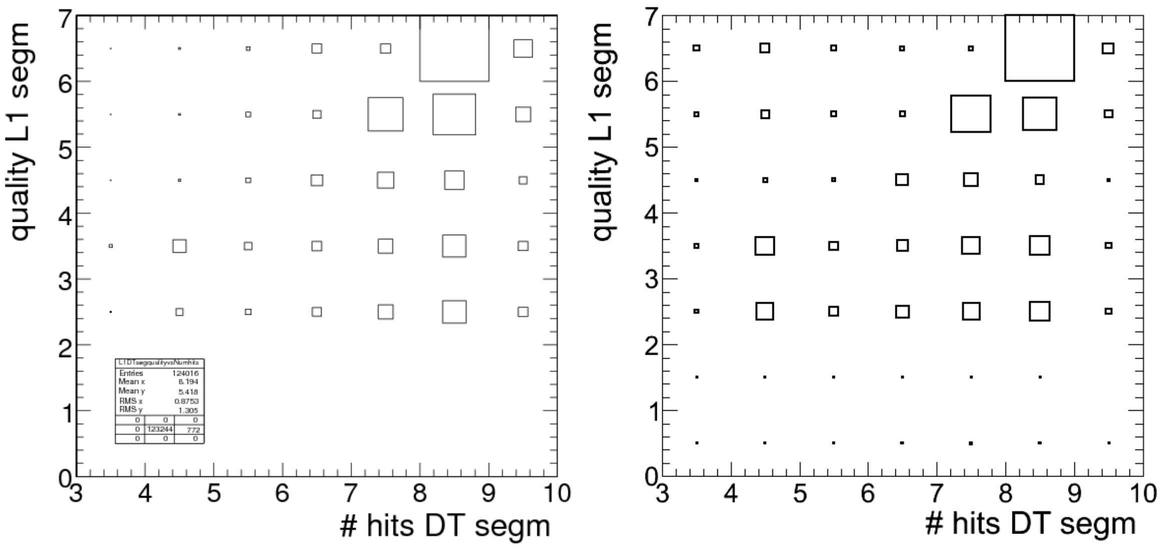

Figure 4.5: Quality of the L1 segment versus number of hits from the offline reconstruction (only for cases with just one reconstructed segment in the chamber) with cosmic data, left, and collision data, right. Quality code: 1=L_i, 2=L_o, 3=H_i, 4=H_o, 5=LL, 6=HL, 7=HH with subindices i, o meaning that the segment reconstructed in the innermost or outermost superlayer.

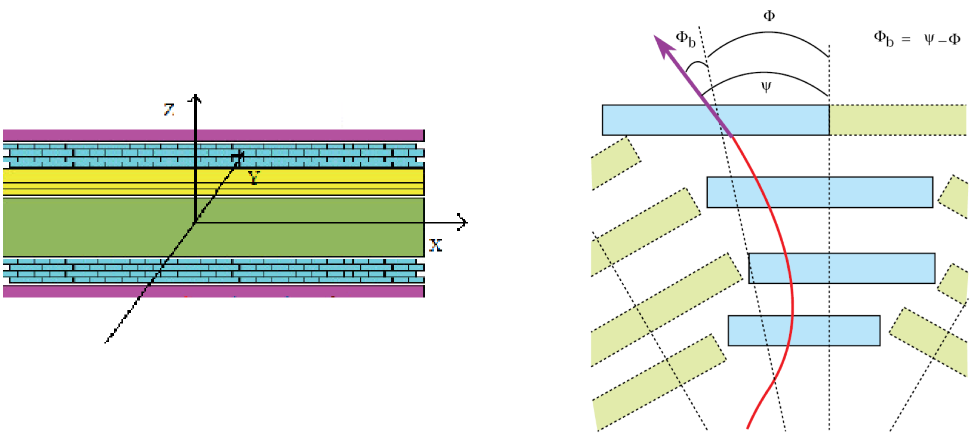

Figure 4.6: Local coordinate system of the chamber (left) and variables given by the trigger (right) for an example of a muon triggering in the fourth station.

the transformations are given by

$$x_{L1} = yshift + radius \cdot \tan\phi, \qquad \mathrm{atan}(dx/dz) = \psi = \phi + \phi_B \tag{4.1}$$

where *yshift* is the distance between the centre of the chamber in x-coordinate and the perpendicular from the origin of coordinates to the chamber ($\phi = 0$) and *radius* is the distance from the centre of CMS to the middle position of the chamber supposing $\phi = 0$. The values of *yshift* and *radius* are different for every station, although uniform with sector numbers, due to the designed disposition of the stations in a wheel. For the fourth station, MB4, *yshift* varies also among the sectors because of their different size. The values used, making use of the CMS geometry, are listed in Table 4.1.

Station	$radius$ (cm)	$yshift$ (cm)
MB1	431.1	−39.12
MB2	512.5	21.43
MB3	617.8	−22.08
MB4 Feet: S9, S11	720.2	0
MB4 Bottom: S10 (S14)	720.2	(−)136.7
MB4 Top: S4, (S13)	720.2	(−)160.7
MB4 Big: S1, S2, S3 (S5, S6, S7)	720.2	(−)98.89
MB4 Small: S12 (S8)	720.2	(−)98.89

Table 4.1: Distance from the centre of CMS to the middle position of the chamber with ϕ= 0, first column, and distance between the centre of the chamber in x and the perpendicular from the origin of coordinates to the chamber, second column, for all stations.

The TRACO z local coordinate, whose origin lies in the mean plane in between the two ϕ-SLs, differs with respect to the centre of the chamber, used as a reference for the segment x coordinates, by ~1.8 cm for MB3 and MB4 chambers. This comes from the fact that the centre of the chamber is computed on the basis of the DT and RPC dimensions, therefore, there is a shift where only one RPC chamber is present for every DT chamber. This is not the case for the MB1 and MB2 chambers, where two RPCs are positioned on top and bottom of a single DT chamber. Thus, for the outermost stations the parameter describing the distance between the interaction point and the mid-plane between ϕ-SLs, *radius*, has to be corrected and the x coordinate has to be propagated to the centre of the chamber along the segment direction. The orientation of the chambers, positive or negative depending on the situation of the Frontend and High Voltage sides with respect to the interaction point, has to be also taken into account. This means introducing the appropriate sign in the reconstructed and/or trigger magnitudes to adapt them to a common reference system. Chambers with positive (negative) orientation are in wheels in the $+z$ ($-z$) coordinate axis, see scheme in Figure 4.1 right. Chambers in Wheel 0 are alternated, changing the orientation every two sectors.

In the following the information from the L1 trigger and the offline reconstruction, position and direction, are analysed presenting the most significant results.

Position in the Chamber

In this section the segment position given by the DT local trigger is compared to the one from the offline reconstruction in the chambers. The study is done per station, distinguishing between positive and negative chamber orientations. The results for the MB1 station using CRAFT data are presented separately and superimposed for chambers with negative (YB-) and positive (YB+) orientation[1], see Figure 4.7. The distributions correspond in particular to top sectors (3, 4 and 5). The plots on the left show the position given by the trigger versus the position of the reconstructed segment. A very good correlation between both positions is observed. On the right side, the difference of these positions on a segment by segment basis is presented, $\Delta x = x_{L1} - x_{DT}$. There is a systematic shift, ~2 cm, in the distribution corresponding to YB- chambers. This feature was due to a problem in the configuration of the look-up-tables and adequately corrected for the following data campaigns, see Figure 4.8, where the equivalent plots with 2010 collision data are shown. The distributions are not perfectly centred at zero because the official reconstruction includes the internal alignment while the LUTs computation does not take it into account.

The width of the Gaussian fit to the Δx distributions with cosmic data is about 1 mm for both positively and negatively oriented chambers and about 0.8 mm for collision data. The spatial resolution of the offline reconstruction is much better than the resolution of the trigger reconstruction. Then, the measured width would correspond to the resolution achieved by the trigger, which is approximately the expected nominal resolution, in agreement with test beam studies [36]. The results obtained with other chambers are similar.

[1]YB stands for Yoke Barrel.

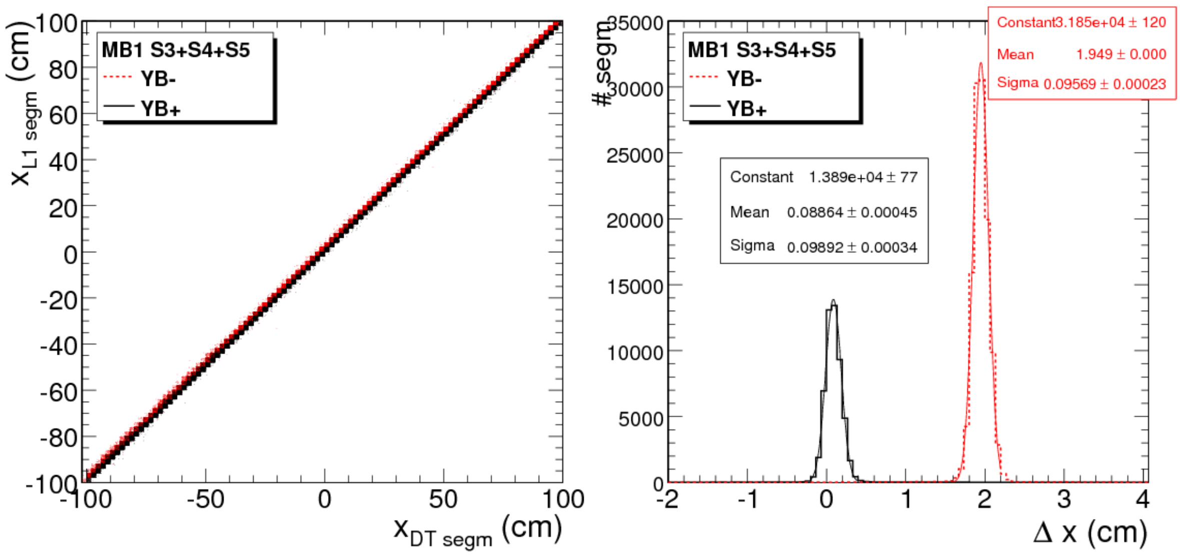

Figure 4.7: Cosmic data (CRAFT): MB1, position given by the trigger (y axis) versus position from the offline reconstruction (x axis), the black dots correspond to chambers with positive orientation, YB+, and the red ones to chambers with negative orientation, YB-, for the top sectors. The segment by segment difference in position, $\Delta x = x_{L1} - x_{DT}$, is shown in the right plot.

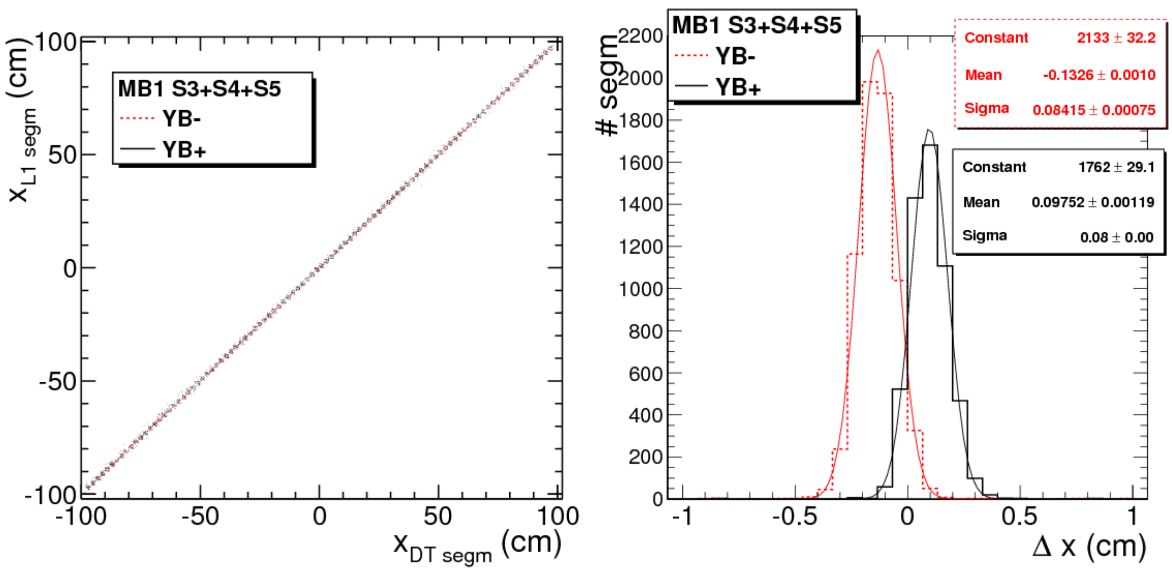

Figure 4.8: Collision data: MB1, position given by the trigger (y axis) versus position from the offline reconstruction (x axis), the black dots correspond to chambers with positive orientation, YB+, and the red ones to chambers with negative orientation, YB-, for the top sectors. The segment by segment difference in position, $\Delta x = x_{L1} - x_{DT}$, is shown in the right plot.

Direction of the Segments

The muon local trigger also provides the direction of the incident muon, as described previously. In this section this incidence angle, $\mathrm{atan}(dx/dz) = \psi = \phi + \phi_B$, is compared with the information from the offline reconstruction, obtained from the slope of the reconstructed segment. The study is not done for the MB3 station because the bending angle is not defined there. The reason is the insensitivity of the bending to the p_T, due to the direction of the magnetic field with respect to the trajectory.

The results for the top sectors are presented in Figure 4.9. The correlation is very good for all angles, including larger angles than the expected ones for muons coming from the interaction point in pp collisions which reach angles up to $\pm 35°$, see Figure 4.10 left, where the same distribution is presented for collision data. Here most of the segments concentrate in the range $|\psi| < 0.2$ (roughly $\pm 12°$) with fewer muons going up to $|\psi| \sim 0.6$ ($\sim 35°$). The residual distributions are also shown, in the right plots of Figures 4.9 and 4.10. They are well described by a Gaussian fit with a width, σ, around 4 mrad for chambers with negative and positive orientation. There is a small shift, of the order of few miliradians, in the mean value for distributions from chambers in both orientations, which disappeared in the distributions with collision data as the aforementioned LUTs configuration problem had been solved. The resolution achieved with the collision data is slightly better, in line with the test beam results. There were no remarkable differences within chambers in other muon stations.

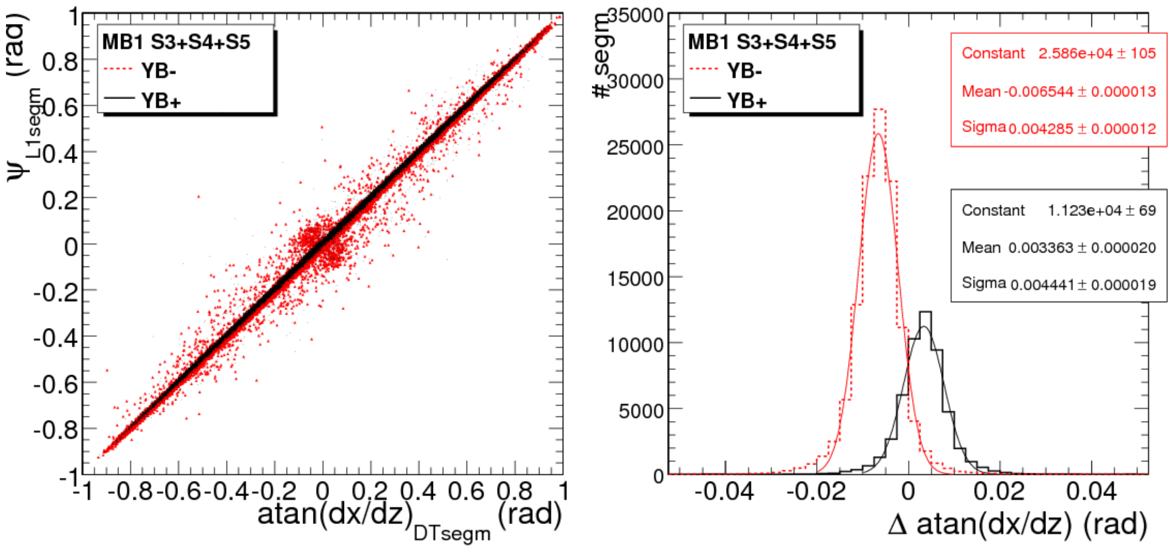

Figure 4.9: Cosmic muon data: MB1, muon incidence angle given by the trigger, $\psi = \phi + \phi_B$, (y axis) versus the angle from the offline reconstruction, $\mathrm{atan}(dx/dz)$ (x axis). Notice that the apparent cloud of points is not a real effect, but an artefact whose origin is the way that the figure is depicted. On the right hand side the difference between both quantities, $\psi - \mathrm{atan}(dx/dz)$, is plotted, in red for YB- chambers and black for YB+ chambers. The parameters of the Gaussian fits are listed.

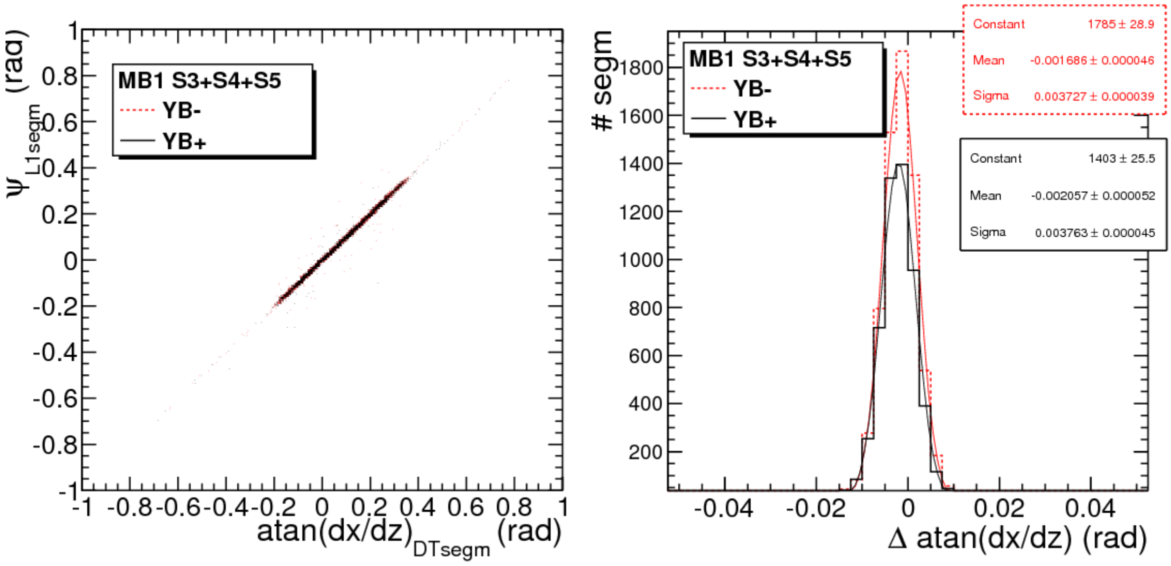

Figure 4.10: Collision data: MB1, muon incidence angle given by the trigger, $\psi = \phi + \phi_B$, (y axis) versus the angle from the offline reconstruction, $\text{atan}(dx/dz)$ (x axis). On the right hand side the difference between both quantities, $\psi - \text{atan}(dx/dz)$, is plotted, in red for YB- chambers and black for YB+ chambers. The parameters of the Gaussian fits are listed.

Comparison between Runs with and without Magnetic Field

During the CRAFT data taking period there were also some runs taken with the CMS solenoid switched-off, which allowed to study the effect of the magnetic field. The main conclusion is the similarity between the distributions with or without magnetic field, although some small effects can be seen. As an example, in Figure 4.11 left the Δx distributions for sector 3 in the MB1 station for negatively oriented chambers (YB-) is shown. The distributions without magnetic field are normalised to the area of the distributions with magnetic field. Finally, the effect of the magnetic field in the angular distributions can be seen in Figure 4.11 right. In these particular runs analysed, the resolution in angle is slightly better without magnetic field, around 0.2 mrad for the MB2 for the chosen sector. The remaining sectors exhibit a similar behaviour.

Conclusions

Some runs from the cosmic ray data collected during 2008 have been analysed. The main conclusion drawn is the good correlation in position and direction between the information provided by the L1 DT local trigger and the offline reconstruction in the DT chambers, both in the presence or absence of magnetic field. The mean trigger resolution achieved in position is around 1 mm, whereas the resolution in the bending angle is of the order of 5 mrad for all stations and sectors. Those values are of the order of the nominal resolution.

Some problems were spotted during from the analysis of the cosmic data, such as

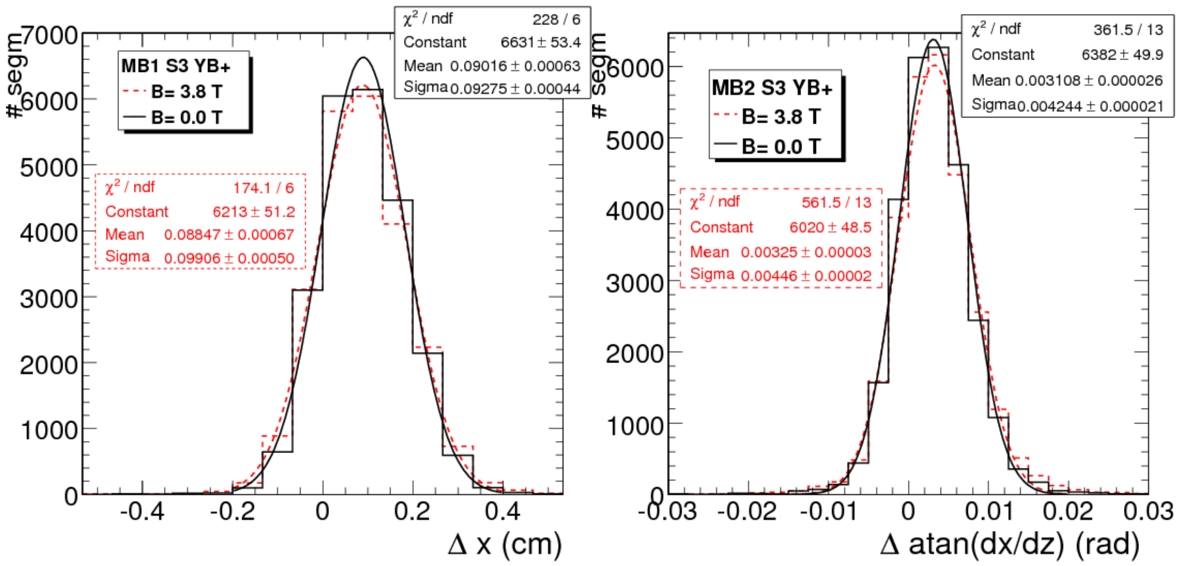

Figure 4.11: CRAFT data: difference in position, Δx, for positively oriented chambers in sector 3, MB1 station (left) and angular difference, $\Delta\psi$, MB2 station (right). The black solid histogram corresponds to data taken without magnetic field (normalised to number of events of the data with the field on) and the red dashed one to data with a magnetic field of 3.8 T.

the shift shown in positive oriented chambers due to a problem with the configuration of the LUTs. They have been solved and its correction implemented in subsequent data taking periods.

This study provided some suggestion for data quality monitoring plots to check the trigger data quality and similar plots to the ones presented here are now implemented in the DT offline data analysis code. In CMS, the Data Quality Monitoring (DQM) system, briefly discussed in section 3.3.1, refers to an archive of information of each run taken, consisting of a catalogue of one and two dimensional histograms that allows to have access to information to control the detector performance *online* and also the first data delivered to the *offline* analysis. This is done centrally for the whole detector, but there is also specific analysis code to check in more detail the quality of the data in different subdetectors, like in the case of the DTs. In this particular analysis code is where the performance plots showing the correlation between the trigger and the local offline reconstruction are implemented.

4.1.3 DT Regional Trigger and Global Muon Trigger

Once the local segments are available, the next step in the trigger chain, the DT Regional Trigger, performs correlation between track segments in order to build full muon tracks. Those segments are forwarded by the Sector Collector which collects track segments coming from one DT sector, selected by the Trigger Server (TS), the last on-board component of the DT Local Trigger logic. The TS selects the two best trigger candidates (in terms of quality and transverse momentum) among the track segments selected by all the TRACOs of a muon chamber. Track segments in the regional trigger are processed independently by the ϕ and η components of the DT Track Finder (DTTF) system, named respectively Phi Track Finder (PHTF) and Eta Track Finder (ETTF).

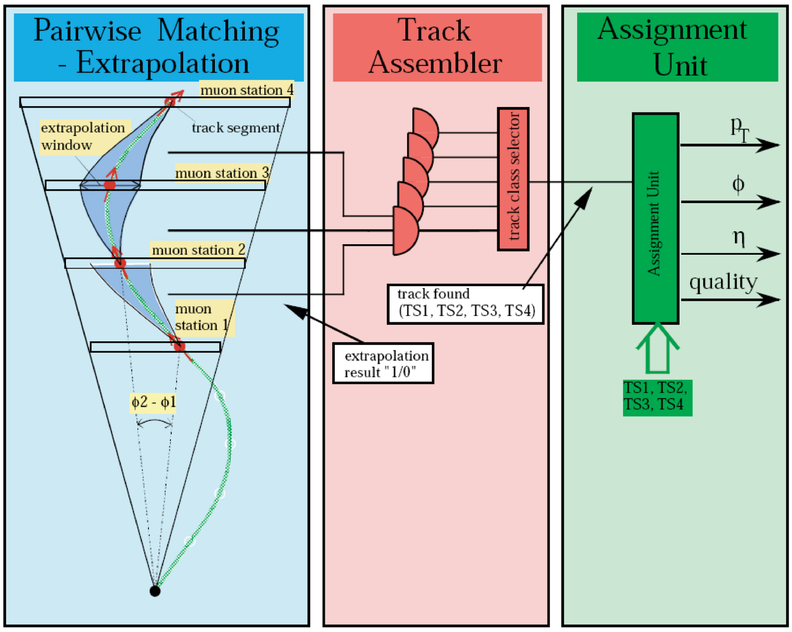

Figure 4.12: Overview of the PHTF algorithm.

An scheme of the PHTF is shown in Figure 4.12, where its three logic steps are drawn. Initially segments from all stations within a sector are considered, and matched among each other taking into account the local trigger position and direction. For that, tracks are propagated outwards, with the exception of tracks in the MB4 station that are propagated inwards to MB3 stations due to the low sensitivity of the particle bending to p_T in this region. This is, from MB1 to MB2, from MB2 to MB3 and from MB4 to MB3, so the bending angle for the third station is never used. In a second step, a Track Assembling (TA) unit matches segments selected by the EU to form a full track and assign it a quality word related to the number and type of stations involved in the reconstruction. A matching between at least two segments is necessary to generate a track. Finally, an Assignment Unit assigns muon physical parameters to the two reconstructed tracks with best quality codes. The tabulated p_T information is computed using the $\Delta\phi$ from the two innermost stations involved in the matching. In the case of the η coordinate assignment (ETTF) the information coming from the different groups of BTIs from the θ-view is matched to reconstruct a straight line, on the basis of a predefined set of patterns.

Afterwards, the best track candidates are selected by the Muon Sorter and passed to the Global Muon Trigger. The Global Muon Trigger attempts to correlate the DT and CSC muon candidates with the RPC candidates. Matching candidates are merged according to configurable criteria and their quality coefficient is increased. In the barrel-endcap overlap regions, the GMT eliminates duplicate candidates detected by both subsystems. Information delivered by the calorimeter trigger is used to determine whether these muons are isolated. The final ensemble of muons is sorted based on their quality and p_T, and the four best muons are then transmitted to the Global Trigger, which requires the candidates to pass certain transverse momentum thresholds and quality requisites.

Summarising, the Level-1 muon trigger returns the reconstructed p_T at the interaction point of the four best muons in discrete momentum bins. It also returns the global position of the segment which made the L1 decision at the second muon station and a quality code for each muon. It provides as well event timing and assigns events to a particular bunch crossing.

4.2 Muon High Level Trigger

Once the L1 muon trigger has been fired signalling the presence of a muon of certain characteristics in the event, the next step in the trigger chain is the High Level Trigger. It is structured in two levels, Level 2 (L2) and Level 3 (L3) implemented in software. It integrates the information from the muon, calorimeter and silicon tracking systems. Within the Muon HLT, the L2 uses information from the muon spectrometer (parameters from the L1 muon candidates converted into seeds) to perform a *standalone* reconstruction, providing a muon p_T measurement with a precision of about 15%. The L2 reconstruction follows closely the offline standalone reconstruction using Kalman-filter techniques [37], which will be described in section 5.1 in more detail, with the only difference being the seed to initiate the process. A separate module computes the isolation of each muon candidate using calorimeter information.

Finally, the L3 adds information from the inner tracker, by performing track reconstruction in the silicon tracker (strips and pixels) using L2 candidates as seeds. This reconstruction is regional, it performs pattern recognition and track fitting only in a small η-ϕ slice of the tracker, to keep execution time low. Trajectories are then reconstructed using like in the L2 case Kalman-filter techniques. Level 3 provides a much more precise p_T measurement (1% - 2% in the barrel region) than Level 2, as well as the ability to select on the basis of the track impact parameter with respect to the beam spot. A L3 isolation algorithm uses information from nearby pixel detector hits.

In the next section the performance of the L2 seeding and reconstruction will be addressed, it is not an exhaustive description of the HLT, the focus is put on the relevant aspects and optimisation studies treated during the work developed for this thesis. For a description of the remaining aspects (also concerning L3) see [38].

4.2.1 Level 2 Muon Trigger

The L2 muon trigger algorithm is presented in this section, it consists of two main steps:

1. Seeding of L2 tracks in the muon chambers starting from the L1 information.

2. Track finding (pattern recognition and fitting) in the muon system.

Level 2 Seeding

The Kalman filter based reconstruction algorithm requires a state vector with the definition of a starting position, direction and p_T value. In the general case during offline reconstruction this vector is obtained combining segments reconstructed in the muon detector. In the case of the HLT, muon candidates from L1 are used as the *external seed* with a significant reduction of seeding time. A L2 seed is built for each L1 Muon object promoted by the GMT to the HLT. There is at most one seed per L1 object and no information of the reconstructed hits is attached to the L2 seed, which is state vector seed. The L2 is seeded with the L1 muon candidate taking its p_T, direction and position. The L2 seed can be rejected if the L1 candidate fails some configurable p_T, η or quality requirements.

As explained in the previous section, the L1 muon objects provide an estimation of the transverse momentum at the interaction point and the global position of the hit which made the L1 decision at the second muon station.

A trajectory state vector of an helix, the L2 seed, is created from the global position of the L1 hit at the second muon station surface. The propagation is then done using steps along the helix defined by the initial state vector. The momentum and direction of this initial state are taken in the same direction as the global position vector with the constraint that p_T equals the estimate given by L1 at the interaction point. This description has the bias in the p_T of the Level 2 seeding, coming from the significant energy loss of the muon between the interaction point, where the p_T value is given, and the second muon station, where the state is defined. This can be seen in Figure 4.13, left, where the difference between the momentum given in the vertex and the second muon station is shown. These distributions (and all the rest in this section) are obtained with a simulation sample of $Z \to \mu\mu$ events. The Δp_T distributions peak at 2 GeV/c, if the muon is reconstructed with the DTs, or 3 GeV/c, if it is reconstructed at higher η values, in the CSCs, for muons with p_T ~40-50 GeV/c (the average p_T of muons from Z decays). The effect of correcting the seed momentum to account for this energy loss was checked by evaluating the momentum resolution and pulls, defined as:

$$R(q/p_T) = \frac{(q/p_T)_{L2} - (q/p_T)_{sim}}{(q/p_T)_{sim}}, \qquad P(q/p_T) = \frac{(q/p_T)_{L2} - (q/p_T)_{sim}}{\Delta(q/p_T)_{L2}}. \tag{4.2}$$

The distributions were obtained with the default seed and with a seed with the p_T estimate corrected by the observed difference of 2 GeV/c or 3 GeV/c depending on η.

The variation in the resolution and the pull was negligible and therefore no change in the algorithm was implemented. The difference in the incidence angle is also presented in Figure 4.13, right, to illustrate how also angular values change, however as ϕ is taken as given in the second station there is no bias.

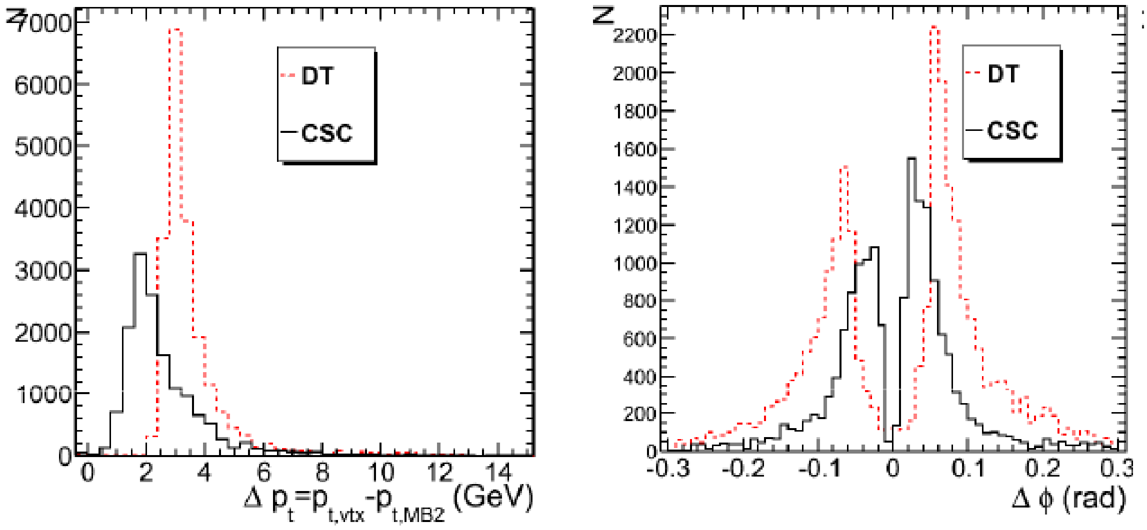

Figure 4.13: Comparison of the muon p_T (left) and ϕ (right) distributions between the simulated value in the interaction point and the L2 seed estimate in the second station.

To perform a reliable reconstruction is mandatory to have a good estimate of the errors associated to the parameters defining the vector state which describes a helix in space. The errors on the initial state of the L2 seed are set according to Table 4.2, where the parameters are the charged inverse of the transverse momentum (q/p_T), the position in the transverse plane (x_T, y_T), the azimuthal angle ϕ and λ, defined as the angle between the tangent to the trajectory with respect to the magnetic field. The accuracy of these values was checked and whether varying them could improve the L2 resolution was studied. In practice, the resolution of the L1 trigger (equivalent to the L2 seed) was obtained using the simulated information at generator level. The results for the first two parameters in the table (q/p_T and λ) are presented as an example in Figure 4.14. The RMS of the Gaussian fits to the (q/p_T) residual distribution is similar to the initial error associated to that track parameter in the Barrel region and 1.5 times smaller in the Endcap region. The error assigned to λ is twice the observed resolution. The resolution of the final L2 candidates was evaluated assigning the measured values as the errors to the initial state of the L1 candidates. No significant improvement was observed.

The Level 2 Seeding step is close to be 100% efficient in Monte Carlo samples, see Figure 4.15, as it is only a reparametrization of the L1 variables, except in the border detector regions, in which the limited resolution of the Level 1 hardware makes more difficult the seeding in the muon system, see Figure 4.15. The efficiency is defined as the ratio of the number of L2 muon seeds over the total L1 candidates.

Parameter Error	Value
$\sigma(q/p_T)$	$0.25/p_T$ (Barrel), $0.4/p_T$ (EndCap) $(\mathrm{GeV/c})^{-1}$
$\sigma(\lambda)$	0.05 rad
$\sigma(\varphi)$	0.2 rad
$\sigma(x_T)$	20 cm
$\sigma(y_T)$	20 cm

Table 4.2: Initial errors on the L2 trajectory seed from the L1 muon parameters.

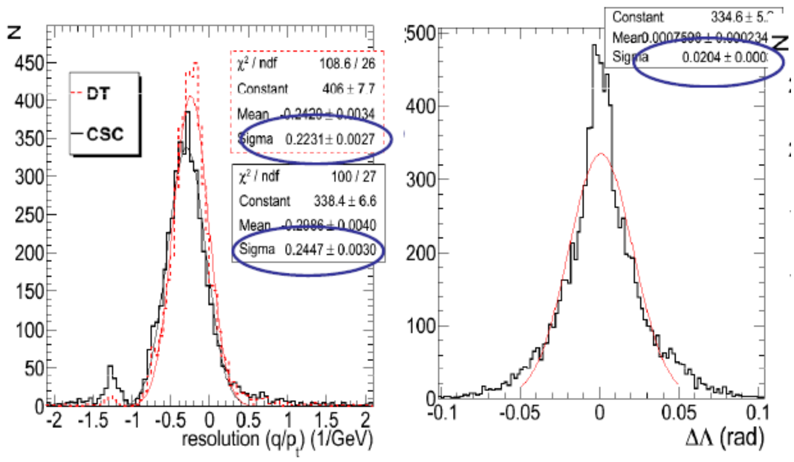

Figure 4.14: Resolution of the Level 1 algorithm with respect to the simulated objects, as a function of muon p_T and λ.

The resolution of the L2 seed parameters is illustrated in Figure 4.16 in terms of the kinematic variables p_T (for all η ranges), η and ϕ. The L2 seed parameters, that are defined on the innermost muon detector compatible with the L1 object, are propagated to the vertex and compared with the muon simulated track variables. A Gaussian fit is performed to each of the distributions.

The shift of the mean value of the Gaussian fit (~ 0.332) in the p_T distribution is due to the use of the L1 p_T value evaluated at the track point of closest approach to build the seed on the innermost muon detector. The rest of the distributions are well centred at zero, with a similar width value for η and ϕ (σ ~0.03).

Level 2 Muon Trajectory Building

The pattern recognition in the muon system is performed in the following steps:

1. Forward Kalman Filtering on the reconstructed segments (Forward Pattern Recognition): the estimated track parameters from the seeds are first propagated to the innermost reachable muon system layer. From there, they are propagated to the next reachable muon chamber, navigating outwards. The most compatible measurement is searched in terms of the best χ^2. Then the track parameters are updated with the 3D information of the best measurement only if a tight

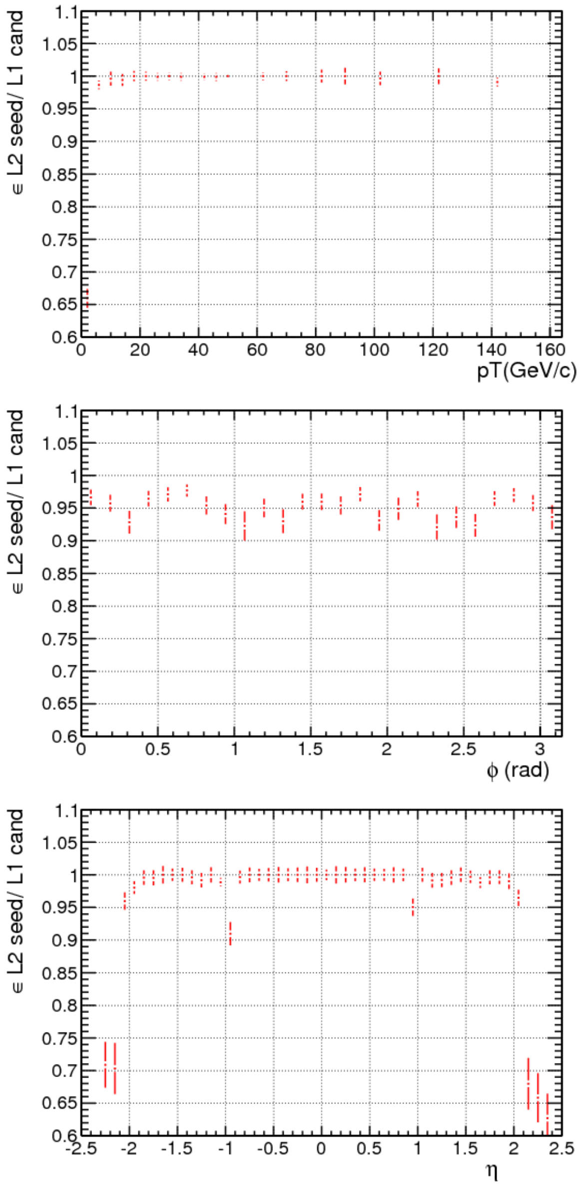

Figure 4.15: Efficiency of the Level 2 seeding algorithm with respect to L1 objects, as a function of muon p_T, ϕ and η, from top to bottom.

requirement in χ^2 is satisfied. Otherwise the compatible segment or hit is recorded in the trajectory but not used for the update. The updated track parameters are propagated to the next reachable chamber and the same procedure is repeated until the last reachable chamber. If no compatible measurements are found in at least two muon chambers, one being a DT or CSC chamber, the track is not produced.

2. Backward Kalman Filtering, the parameters obtained in the previous step are used as input for the backward pattern recognition, which works in the same manner but navigating inward.

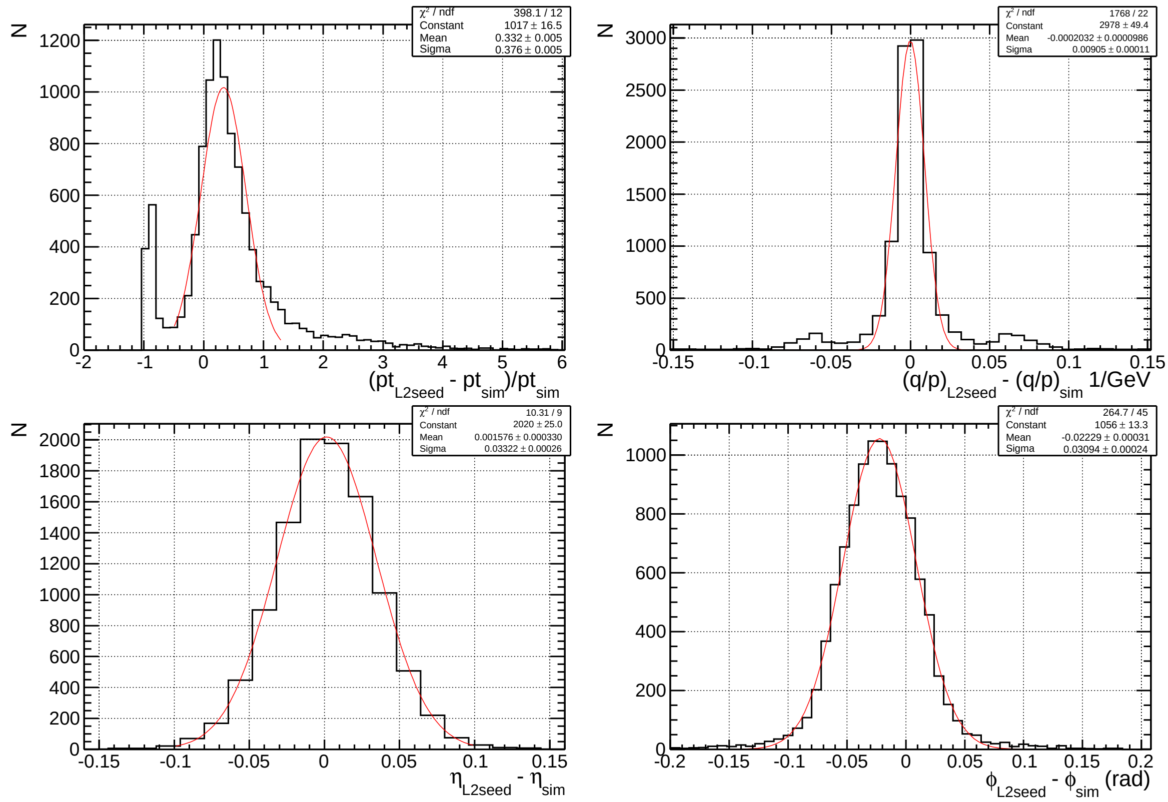

Figure 4.16: Residual distributions of the Level 2 seeds parameters in terms of the muon variables p_T, q/p, η and ϕ, from left to right and from top to bottom, with a Monte Carlo sample of $Z \to \mu\mu$.

3. Final fitting of the L2 track parameters to the collected fits, which is currently not used.

4. Cleaning of the track candidates in order to remove possible duplicates.

5. Constraint of the track parameters to the interaction region by means of the beam spot position. Two collections of L2 tracks are produced, one without this constraint and the second including the tracks compatible with the vertex constraint.

After the track finding step, the muon p_T is not anymore a discrete quantity estimate, but an actual measurement. The comparison of the p_T distributions from the L1 muon and the L2 is displayed in figure 4.17. While the L1 reconstructed p_T is a discrete quantity, with the spacing between reconstructed momenta increasing as a function of p_T with a maximum reconstructed p_T value at 140 GeV/c , the L2 p_T distribution is continuous, showing the expected spectrum of muons from Z decays.

Figure 4.18 presents the resolution of the L2 muon candidates for a simulated $Z \to \mu\mu$ sample in the kinematic variables p_T, q/p, η and ϕ. The width of the Gaussian fit to the residual distribution is around 1.3% with respect to the simulated ϕ and slightly better in η, ~0.8%. The resolution depends on the momentum range, the one

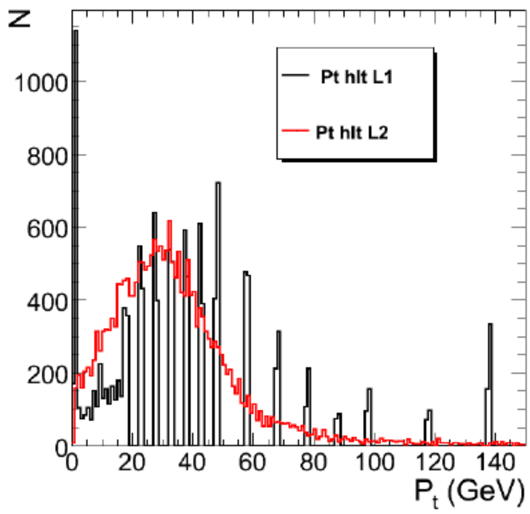

Figure 4.17: Transverse momentum distributions of the Level 2 seeds (L1 muon) and the L2 muon candidates from a simulated sample of $Z \rightarrow \mu\mu$ events.

obtained with medium p_T muons is close to 20%. The L2 track collection chosen had no constraint to the interaction region, thus the resolution is worse than the expected 15% mentioned before, which was referred to the tracks compatible with the vertex constraint.

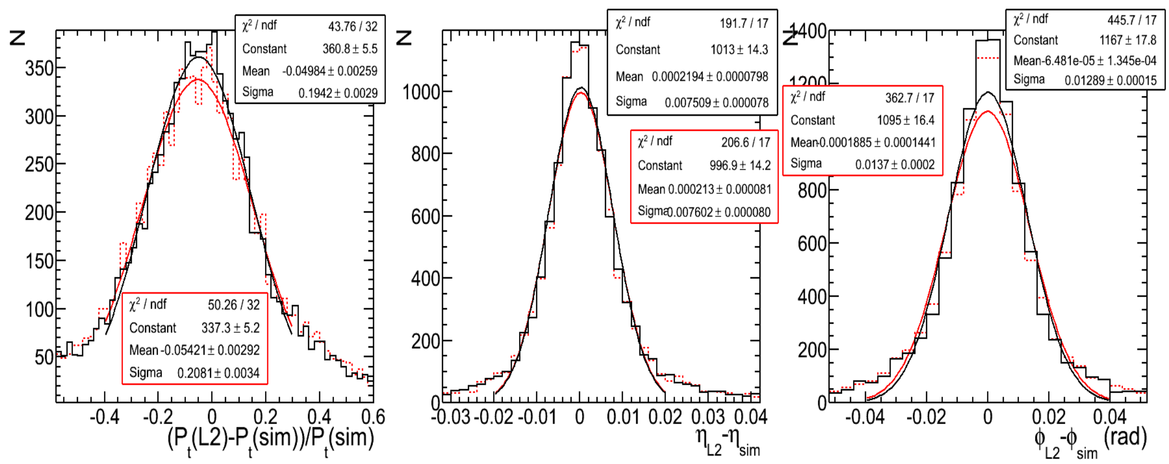

Figure 4.18: Residual distributions of the Level 2 muon candidates in terms of the variables p_T, η and ϕ, from left to right. The solid black histogram corresponds to the current L2 implementation and the dotted red one to a different propagator algorithm studied for optimisation. The simulated sample corresponds to $Z \rightarrow \mu\mu$ events.

The final step of the L2 trigger is the reconstruction of isolated muon candidates. The HLT uses the same algorithm as the offline reconstruction to calculate the muon isolation with information from the calorimeters. The calorimeter energy deposits above a certain threshold are summed in a cone of ΔR <0.24 centred on the direction of the L2 muon track, with the update at vertex applied. The sum of energy in a veto cone, centred around the state of the L2 muon propagated to the inner ECAL surface, is subtracted. A L2 muon is tagged as isolated if the weighted sum is lower than an η-dependent threshold.

Once the L2 candidates are reconstructed, the final step of the HLT, the Level 3, takes place combining L2 muons and charged particle tracks reconstructed in the tracker. Track parameters of the L2 muon, constrained to the interaction region, define a η-ϕ region where a seed for the L3 reconstruction is found. A relaxed beamspot constraint is applied to track candidates above a given transverse momentum threshold to obtain the initial values of the trajectory parameters. Trajectories are then reconstructed using Kalman-filter techniques. Finally, isolation requirements are applied using the number of pixel tracks instead of calorimetric information.

Chapter

5

Muon Reconstruction in CMS: Momentum Assignment and Resolution

As discussed in the previous chapter, it is crucial for CMS to be able to detect muons with high efficiency, low fake-rate from backgrounds, and excellent momentum resolution. This implies not only to have a solid trigger but also to be able to perform an optimal offline muon reconstruction.

In this chapter, an overview of the offline muon reconstruction in CMS is presented, focusing on the muon momentum assignment and the resolution. Muons are reconstructed as tracks both in the silicon inner detector, like any other charged particle, and in the muon detectors in an independent way, where they are identified unequivocally. Combining the information provided by muon spectrometers and tracker, a very precise measurement of the muon momentum and trajectory is obtained. In addition to the *standard* muon reconstruction in CMS, the different algorithms developed to improve the reconstruction of high p_T muons are described.

5.1 Muon Reconstruction in CMS

CMS aims for an excellent muon reconstruction in a wide p_T range: low momentum muons for b-physics studies (peaking at transverse momenta lower than 10 GeV/c), relatively energetic muons such as the ones coming from electroweak processes (p_T~40 GeV/c) and very high momentum muons, of the order of the TeV/c, a distinctive signature expected by some new physics models, as the heavy vector bosons W' decaying into muons, the process described later on in this thesis. Various algorithms are especially developed to the momentum measurement of those TeV-muons, see section 5.2.1.

In the standard CMS reconstruction for *pp* collisions [27, 39], tracks are first reconstructed independently in the silicon tracker, *tracker tracks*, and in the muon spectrometer, *standalone muon tracks*, and their associated giving rise to *global tracks*, giving an estimate of the muon charge, momentum and production vertex. The next sections are devoted to their description.

5.1.1 Muon Reconstruction in the Muon Specrometer

Muon reconstruction starts with the track segments from the muon chambers obtained by the local reconstruction. The seed consists on position and direction vectors and an estimate of the muon transverse momentum associated with the segments found in the innermost chambers. The seed trajectory state parameters are propagated to the innermost compatible muon detector layer, by identifying for each point the detectors that most probably contain the next hit to be included in the trajectory as described for the L2 algorithm. The predicted state vector at the next measurement surface is compared with existing measurement points and updated accordingly. In the DT chambers, reconstructed track segments are used as measurements in the Kalman-filter procedure [37]. In the endcap CSC chambers, where the magnetic field is inhomogeneous, the three-dimensional hits of the segments are used instead of track segments. Reconstructed hits from the RPC chambers are also included in the filter procedure. A cut in χ^2 (variable) is applied to reject bad hits, mostly due to showering, delta rays and pair production. If no matching hits (or segments) are found for example due to detector inefficiencies, geometrical cracks, or hard showering, the search is continued in the next station. The state is propagated from one station to the next one taking into account the muon energy loss in the material, the effect of multiple scattering and the nonuniform magnetic field in the muon system. The track parameters and the corresponding errors are updated at each step. The procedure is iterated until the outermost measurement surface of the muon system is reached. A backward Kalman filter is then applied, going inward up to the innermost muon station, where the track parameters are defined.

5.1.2 Muon Reconstruction in the Tracker

As in the muon system, the reconstruction process starts locally with the seed finding. While in the muon system the trajectory is built during the pattern recognition, in the tracker the pattern recognition and the final fit are performed separately.

The algorithm developed is the Combinatorial Kalman Filter (CKF). It uses the capability of the Kalman Filter for simultaneous pattern recognition and track fitting.

Starting from an initial estimate of the track parameters from the innermost layers of the tracking system, the algorithm iterates through the tracker layers and builds a combinatorial tree of track candidates. The seeds are made out of a hit pair and a loose beam-spot constraint or out of a hit triplet. The starting parameters of the trajectory are calculated from a helix passing through the three points. Recalling, the track parameters describe a helix in space parametrised by the position where the momentum is defined, λ, which is the angle between the tangent of the trajectory makes and the magnetic field, and the charged inverse of the momentum (q/p_T). The selected hits must be pointing towards the interaction point and a minimum transverse momentum threshold (configurable) is applied. From each seed the propagation to the next surface is attempted. Hits are identified in a window whose width is related to the precision of the track parameters. If a hit is found within the window, it is added to the candidate trajectory and the track parameters are updated. Candidates are sorted according to quality which is based on the χ^2 and the number of hits. The best ones are retained for further propagation. The result is a collection of tracker tracks.

The reconstruction in the tracker has better resolution than the one in the muon chambers, see Figure 3.14 previously presented. An example of the comparison of the algorithm behaviour with data is shown in Figure 5.1, where the transverse momentum of muons coming from $Z \rightarrow \mu\mu$ decays as measured in the tracker and the muon spectrometer is presented, left plot. The peak given by the standalone reconstruction is broader due to its worse resolution. The right plot corresponds to the difference between the momentum as given by both algorithms ($p_T^{SA} - p_T^{Tr}$), the width of the distribution comes mainly from the resolution of the standalone algorithm. It corresponds to ~5.5 GeV/c, taking into account that the muon p_T distribution from Z events peaks at 40 GeV/c, this number translates into the expected ~15% resolution in q/p_T of the standalone muons. This implies that for muons with transverse momentum below ~ 250 GeV/c adding information only marginally improves the momentum resolution given by the tracker reconstruction.

5.1.3 Track Matching: Global Reconstruction

The global muon reconstruction aims to combine tracks in the muon spectrometer and the tracker in a unique muon track. The process starts with the muon trajectories, extending it to include hits in the silicon tracker. The track in the muon spectrometer is used to define a region of interest in the tracker. The determination of this region is based on the track parameters and their corresponding uncertainties of the extrapolated muon trajectory, obtained with the assumption that the muon originates from the interaction point.

The track matching is performed by propagating the muon and the tracker tracks onto the same plane and looking for the best χ^2 value from the comparison of track parameters. If there is a suitable match between the tracker track and the standalone muon track, the hits from the tracker and the stand-alone muon track are combined in one collection and a final fit is performed over all hits, leading to the global muon.

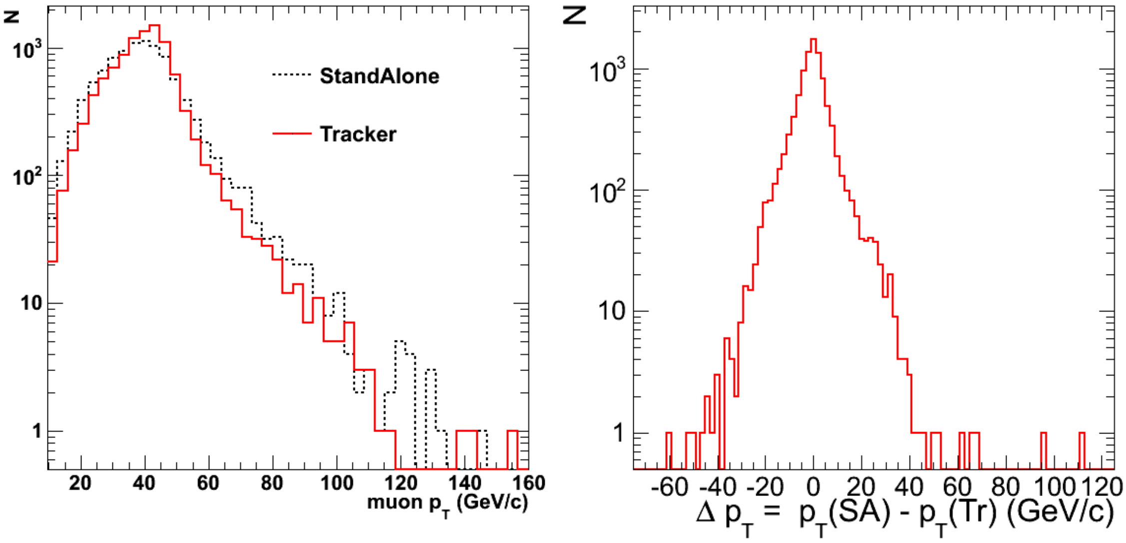

Figure 5.1: Transverse momentum distribution for muons from the Z decay, reconstructed in the muon spectrometer (dotted black histogram) and tracker system (solid red histogram), left, and difference between both algorithms, right.

The reconstruction of the muons ends with the matching of the global muon track and the energy deposits in the calorimeters.

The momentum assignment to the global muon in CMS is done according to the so called *sigma switch*. It chooses the global fit if both the global and the tracker-only fit estimate the muon transverse momentum to be above 200 GeV/c and the fit for q/p agrees to within two sigma of the tracker-only fit, otherwise it chooses the tracker-only fit.

5.2 Reconstruction Algorithms for High p_T Muons

5.2.1 Description of the Algorithms

As the muon passes through the iron of the magnet return yoke, multiple scattering and radiative processes can alter its trajectory. The former is not so important for high-momentum muons from high-mass Drell-Yan decays or possible new physics processes. However, the energy loss due to the latter, as well as the extra hits produced in the muon chambers from the resulting electromagnetic showers, can drop the track fit. In that case the resulting estimate of the muon momentum at the production vertex is significantly different from the true value.

Therefore, several different strategies on how to include information from the muon system have been developed. Here only the ones which were implemented and employed for the measurement of the transverse momentum in the analysis are described:

- The *tracker-plus-first-muon-station* (TPFMS) fit, starts with the list of hits used in the global track, but uses only hits from the first muon station having any, with the goal of being insensitive to the stations farther along the muon trajectory past more iron yoke that are possibly contaminated by showers.

- The *Picky* fit, again starts with the global track hit list, but, in chambers appearing to have hits from showers (determined by the hit occupancy of the chamber), requires the hits used in the fit to have χ^2 with respect to the trajectory to be below a certain threshold.

To further improve the resolution, especially with the intent to reduce the tails of the momentum resolution distribution, *cocktails* of the above described algorithms including the tracker and global can be used: on a muon-by-muon basis, these *cocktails* select between the global, tracker-only, TPFMS, and Picky fits. There are several choices for the cocktail algorithm as the *sigma-switch*, already mentioned, *truncated muon reconstructor* and, the selected one for the analysis, referred as *Tune P*.

- The *truncated muon reconstructor*, TMR, chooses between the tracker-only and TPFMS fits as discussed above: if the tail probability of the χ^2 of the TPFMS fit is significantly worse than that of the tracker-only fit, tracker-only is chosen, but TPFMS otherwise.

- *Tune P* chooses between the tracker-only, TPFMS, and Picky fits similarly to TMR. The algorithm starts with the Picky fit, then switches to tracker-only if the tail probability of the latter is significantly better. Finally it compares the tail probability of the chosen track with the one of TPFMS; TPFMS is chosen if it is found to be better.

The *Tune P* cocktail (hereafter referred simply as *cocktail*) was found to have the best resolution among the individual refits in cosmic ray studies [40, 41]. For this reason it was the algorithm recommended for the high p_T muon reconstruction for the 2010 analysis, thus used for many muonic searches, in particular for the heavy vector boson W' and Z' searches. The performance of this algorithm was tested with the available cosmic data from 2010 and with simulation samples to confirm the previous results. This is described in the next section, in the scope of the W' study.

5.2.2 Momentum Assignment of the Cocktail Algorithm

For the analysis presented in this thesis, the search of heavy W' discussed later, one looks for signatures with one high p_T muon in the final state. And as it was just mentioned, it makes use of the measurement given by the cocktail algorithm to determine the muon momentum, optimised with cosmic muons. One caveat to the cosmic studies is that they are restricted to the barrel region of the muon detector besides the topological differences with respect to collision muons, described in section 4.1.1. Therefore, the resolution of this algorithm was studied in comparison with each individual algorithm to confirm that the *tune*, ie. the way it selects the algorithms, yields better results than using one of the muon reconstructors.

Taking into account the lack of high p_T muons in 2010 collision data, the study is carried out first with simulated samples, used for the $W' \to \mu\nu$ study described later on, and cross checked with results obtained with cosmic muon data collected during 2010. In particular, the simulated samples chosen were a W' signal of mass $M_{W'}$=1500 GeV/c^2 for the high p_T region and $W \to \mu\nu$ sample, which is the most important background source for the search. A detailed description of the samples is given in chapter 7.2, where the W' analysis is discussed.

To perform the study, the focus was set on the muon momentum resolution of the cocktail algorithm measurement compared to the other algorithms considered in the cocktail choice. First, good muon candidates are selected, which must be identified as *tracker* and *global* muon and, to ensure a good reconstruction, a minimum number of hits in each of the subdetectors involved is required, see section 6.1 for more details. The χ^2 of a track determines the quality of the fit and it is usually used in the selection, nevertheless here its value is not constraint as it the discriminating variable in the cocktail choice.

The algorithms between the ones the cocktail chooses are TPFMS, Picky, tracker only and global reconstruction by means of the χ^2 of each fit. By definition, the cocktail algorithm always assigns a valid muon momentum by selecting the measurement of one of the algorithms involved in the refit, so there is no efficiency loose by using this algorithm instead of the global muon. The momentum given by the global algorithm is in practice never taken in the samples considered (both simulation and cosmic data), as it is only selected if the conditions on all the three other algorithms fail, which does not happen. Then, cocktail muons are a combination of Picky, TPMFS and tracker muons. The first two reconstructors are the dominant contributions, with around one half of the total measurements given by each of them, being the contribution of tracker only of few percent.

The p_T distributions for the different algorithms are displayed in Figure 5.2 for the W' MC sample to illustrate the p_T region of interest. The distributions given by the TPFMS and Picky algorithms are similar. In the case of the tracker muon, the resolution worsens at high p_T values and the peak is shifted. On the right hand side of the figure the p_T spectra obtained with cosmic muons is shown, although the distribution reaches high p_T values, it falls steeply as a function of p_T, so the statistics is limited at high momentum. Note the very different momentum distribution between both samples, which is relevant for the results presented in the following.

The tranverse momentum residuals of the simulated samples, defined as

$$R(q/p_T) = \frac{(\frac{q}{p_T})^{gen} - (\frac{q}{p_T})^{reco}}{(\frac{q}{p_T})^{gen}} \tag{5.1}$$

were obtained with the different algorithms employed by the cocktail refit. The results are illustrated in Figure 5.3 for the W' sample. The resolution of the two specialised TeV algorithms is similar while the resolution of the tracker-only algorithm is clearly

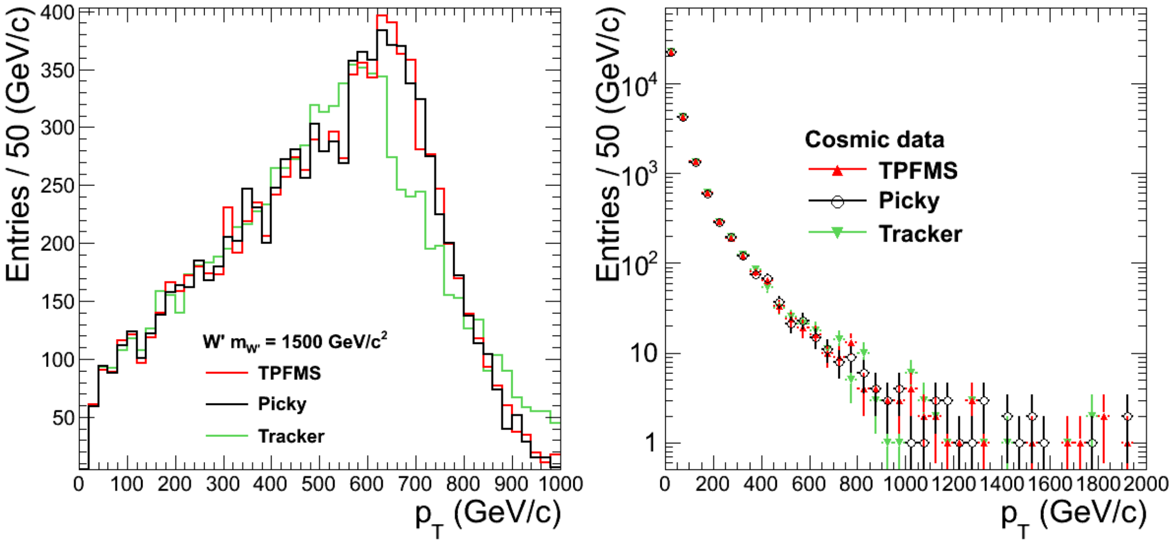

Figure 5.2: Transverse momentum distributions as measured by the tracker only (green inverted triangles), TPFMS (red triangles), and Picky (open circles) reconstructors for muons from a simulated W' signal, left, and cosmic data, right.

worse in the high p_T range from the W' decay muons. A Gaussian fit was performed to each distribution, in the range $(-1.5 \cdot \sigma + \text{mean}, 1.5 \cdot \sigma + \text{mean})$, the parameters of the fits are shown in the figure as well (and listed in Table 5.1, discussed later). Simulated muons and data are reconstructed following the same procedure and with the same alignment conditions, so it can be expected that the algorithms behave similarly in both samples.

Keeping in mind that for the analysis we look for signatures with high p_T muons, two aspects must be taken into account concerning the resolution: the size of the tails of the distributions and the core of the resolution. If tails are small, only a reduced number of muons is reconstructed with a much higher p_T than the real one. This kind of events, where a low p_T muon is misreconstructed in the high p_T region, could fake a signal event. Second, it is relevant that the core of the resolution for high p_T muons is not spread outside a reasonable range considering the capabilities of the detector. This would again imply big shifts in p_T and, thus, either to have an extra muon reconstructed in the signal region or to loose the muon to lower p_T where only background events are expected.

The mean and width of the Gaussian fits to the momentum residual distributions for the W' and W samples as given by the different algorithms are listed in Table 5.1. (Notice that all numbers are multiplied by a factor 100.) The results for the W sample are split into two p_T regions, $p_T < 100$ GeV/c and higher p_T to evaluate the behaviour for different p_T ranges. The last row for each sample corresponds to the far-off tail where the reconstructed information is much larger than the simulated one (left tail), defined as the proportion of events with resolution higher than $3 \cdot \sigma$ over the total number of

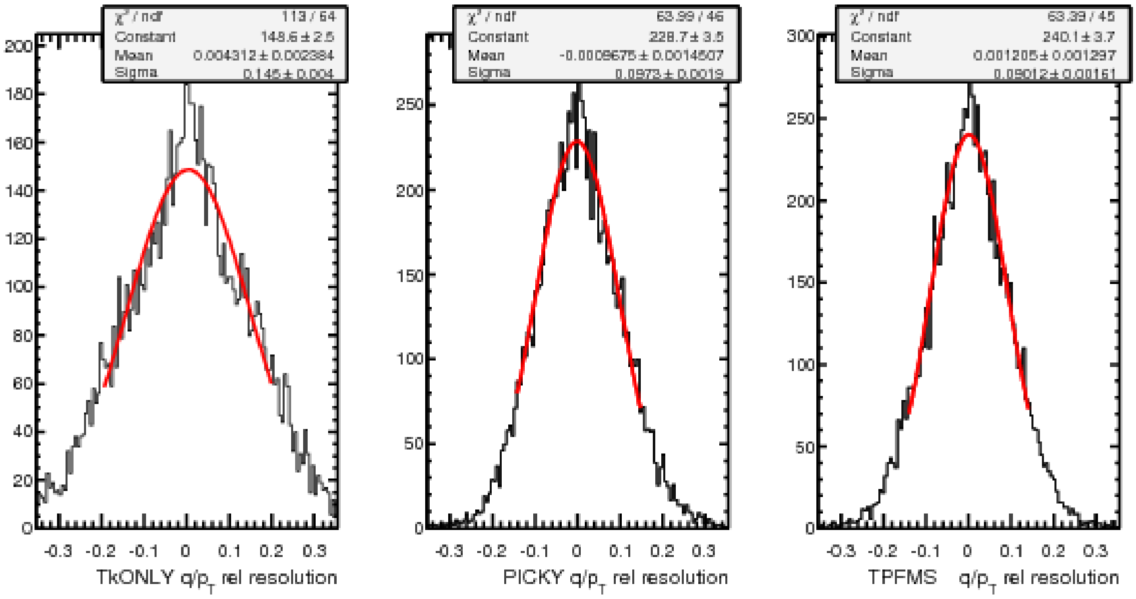

Figure 5.3: Resolution residuals for a sample of W' of $M_{W'}$=1500 GeV/c^2 using the three algorithms selected by the cocktail reconstructor, from left to right, tracker, Picky and TPFMS. A Gaussian function in the range $(-1.5 \cdot \sigma, 1.5 \cdot \sigma)$ if fitted to each distribution.

events.

The width of the distributions is similar for all algorithms considered at low and medium p_T. At low p_T, up to 200 GeV/c, the muon momentum measurement is dominated by the precision of the silicon tracker, so one already has the best performance by using the tracker only fit for that range. The fact that results obtained with the dedicated TeV algorithms are similar indicates that it is safe to use the cocktail value also in that p_T region. The results for the tracker only algorithm are worse at high p_T, as already seen, when the more selective cocktail fit manages to perform better (and also better than the global algorithm by itself [42]). The same conclusion applies to the far-off tails. The tail of the fit to the distribution given by the cocktail algorithm is the smallest. Regarding the mean values of the fits for the W' sample, the values of the dedicated TeV algorithms are compatible with zero, while there is a certain discrepancy in the case of the tracker reconstructor, which points out a global shift of the distribution, already seen in Figure 5.2.

Figure 5.4 shows the mean and the width of the fits respectively presented in the table as a function of p_T for the W' mass point chosen as a reference, to illustrate the previous results.

In Table 5.2 the previous table is split into the cases where the TPFMS and the Picky algorithms are selected or rejected by the cocktail fitter. The resolution given by the latter is listed in the last column of the table. The values for the tracker are not given for simplicity due to its small impact on the final cocktail resolution, as it is

(Value×100)	Tracker	Picky	TPFMS	Cocktail
W' $M_{W'}$ =1500 GeV/c^2				
Mean	0.43 ± 0.24	0.097 ± 0.145	0.12 ± 0.13	0.15 ± 0.13
Width	14.5± 0.4	9.73± 0.19	9.12± 0.16	9.14 ± 0.17
Tail < $\frac{\#(-3.0\cdot\sigma)}{\text{Total}}$	1.02	0.55	0.84	0.56
W p_T^μ >100 GeV/c				
Mean	-0.50 ± 0.05	-0.039 ± 0.05	-0.48 ± 0.05	-0.45 ± 0.05
Width	4.37± 0.04	4.08± 0.04	3.94 ± 0.04	3.98 ± 0.04
Tail < $\frac{\#(-3.0\cdot\sigma)}{\text{Total}}$	3.65	4.01	5.11	2.50
W 100> p_T^μ >25 GeV/c				
Mean	-0.018 ± 0.003	0.013 ± 0.003	0.003 ± 0.003	-0.005 ± 0.003
Width	2.019± 0.003	1.997± 0.003	1.996± 0.003	1.99± 0.03
Tail < $\frac{\#(-3.0\cdot\sigma)}{\text{Total}}$	1.23	1.10	1.18	1.12

Table 5.1: Summary of W' and W Monte Carlo p_T resolution plots for tracker only, Picky, TPFMS and cocktail reconstruction algorithms. The mean, width and the number of events in the far-off tails (defined as #(-3.0·σ)/Total) are shown, all number are multiplied by a factor 100.

only chosen in a few cases, consistent with the observation of its worse resolution. For all samples and all p_T ranges, the width of the resolution with the Picky reconstructor is better when the algorithm is selected than when it is rejected. Moreover, the far-off tails are also smaller. This would indicate that the cocktail choice in this case is adequate. The core of the resolution with the TPFMS algorithm in both cases (selected and rejected) is very similar, however the tails are considerably reduced when the algorithm is selected, being the effect more remarkable for higher p_T values.

As mentioned these results cannot be directly compared with collision data, but it is feasible to use cosmic muons reconstructed in both halves of the detector, that is, the two legs of a single muon are reconstructed. The momentum of both legs of the muon should be the same, as it is just a muon. One of the legs can be used as a reference to estimate the muon q/p_T resolution, in a similar way as the simulated information in the case of MC, and the other one plays the role of the reconstructed information. Then, a good estimator for the resolution is defined as:

$$R(q/p_T) = \frac{(\frac{q}{p_T})^{upper} - (\frac{q}{p_T})^{lower}}{\sqrt{2}\cdot(\frac{q}{p_T})^{lower}} \tag{5.2}$$

where *upper* and *lower* refer to the results of the fits in the two halves of CMS, and the factor $\sqrt{2}$ accounts for the fact that the two reconstructions are independent.

To select cosmic muon events in which the muons are most similar to those produced in collision events, only pairs of tracks passing close to the interaction point are employed. The condition applied was that at least one hit from the pixel detector must be used in each of the pairs of tracks. To keep only good quality tracks, eight

(Value×100)	Picky selected	TPFMS selected	Picky rejected	TPFMS rejected	Cocktail
W' $M_{W'}$ =1500 GeV/c^2					
Mean	0.26 ± 0.22	0.05 ± 0.17	-0.29 ± 0.20	0.28 ± 0.21	0.15 ± 0.13
Width	9.01± 0.28	9.09± 0.21	10.17± 0.27	8.92 ± 0.26	9.14 ± 0.17
Tail < $\frac{\#(-1.5\cdot\sigma)}{\text{Total}}$	6.73	6.83	5.97	8.35	7.14
Tail < $\frac{\#(-3.0\cdot\sigma)}{\text{Total}}$	0.45	0.45	0.60	1.45	0.56
W, p_T^{μ} >100 GeV/c					
Mean	-0.34 ± 0.07	-0.048 ± 0.06	-0.42 ± 0.06	-0.46 ± 0.07	-0.45 ± 0.05
Width	3.77± 0.06	4.02± 0.06	4.27± 0.06	3.78 ± 0.06	3.98 ± 0.04
Tail< $\frac{\#(-1.5\cdot\sigma)}{\text{Total}}$	6.3	7.0	9.1	12.2	7.1
Tail< $\frac{\#(-3.0\cdot\sigma)}{\text{Total}}$	2.67	2.39	4.81	9.12	2.50
W, 100> p_T^{μ} >25 GeV/c					
Mean	0.015 ± 0.005	-0.025 ± 0.004	0.012 ± 0.005	0.006 ± 0.005	-0.005 ± 0.003
Width	1.91± 0.04	2.02± 0.04	2.08± 0.04	1.91 ± 0.04	1.99 ± 0.03
Tail< $\frac{\#(-1.5\cdot\sigma)}{\text{Total}}$	3.17	4.16	4.10	3.47	4.11
Tail < $\frac{\#(-3.0\cdot\sigma)}{\text{Total}}$	0.91	1.21	1.09	1.07	1.12

Table 5.2: Summary of W' and W Monte Carlo p_T resolution plots for Picky and TPFMS reconstruction algorithms and the cocktail fitter. The mean, width and number of events it the tails outside 1.5σ and 3.0 σ are shown. Notice that all numbers are multiplied by a factor 100.

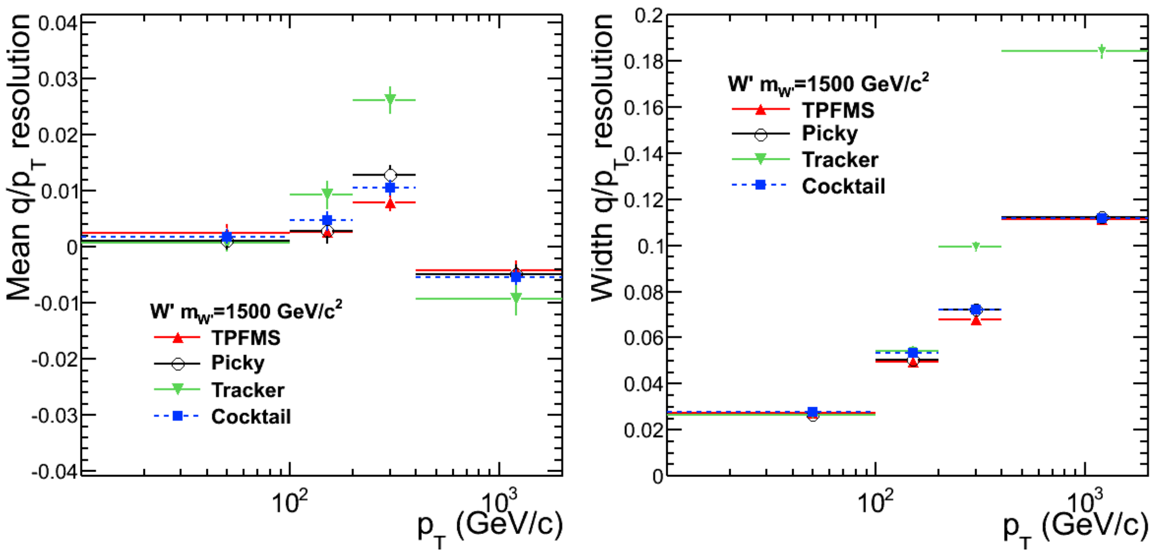

Figure 5.4: Mean and width of the Gaussian fits in the range $(-2.0\cdot\sigma, 2.0\cdot\sigma)$ to the muon q/p_T resolution residuals as a function of p_T using the three algorithms actually selected by the cocktail reconstructor, tracker, Picky and TPFMS and the cocktail itself, for a W' simulated sample of $M_{W'}$=1500 GeV/c^2.

strip layers hits were required to each track. Only events with exactly two global muons for which all the refits exist for both legs are kept. To ensure that both legs correspond to the same muon, an angular matching was performed requiring $\Delta\phi$ <0.1 and $\Delta\theta$ <0.05.

Figure 5.5 shows the relative resolution as measured by the Gaussian mean and width for the studied algorithms as a function of the p_T of the muon. The results given by the tracker are remarkably worse at high p_T. It is important to stress that muons are not equally distributed as a function of p_T, as presented in Figure 5.2. In each bin, the majority of the muons accumulates at the lowest values for the cosmic sample, while muons from W' tend to higher values. In other words, the average p_T value in a certain bin is higher in the latter and consequently the σ reflects that difference. Thus, the comparison between the resolution for the different algorithms for the two samples focus on the trend and not on the exact value of the width of the resolution, which is similar.

From this collection of plots and the previous one (Figure 5.4), the improvement in the resolution by using the dedicated TeV algorithms at high p_T is clear. Comparing the results with the simulation, one sees the goodness of the performance of the cocktail algorithm. Even if the resolution of the other two algorithms does not differ considerable, it was seen with the simulated samples that the resolution distribution with the cocktail choice has less tails. This was probed in cosmic data as well: there are no muons reconstructed at $|R(q/p_T)|$ >1 for the highest p_T bin considered, while there are few outsiders with the TPFMS or Picky reconstructors.

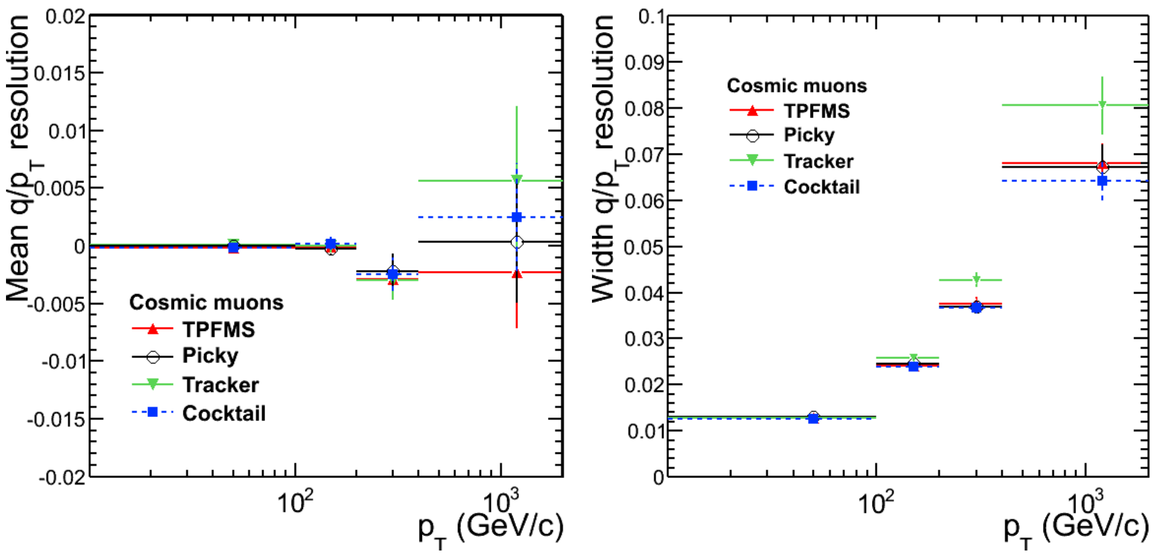

Figure 5.5: Mean and width of the Gaussian fits to the distributions of the muon q/p_T resolution residuals as a function of p_T for the cosmic sample gathered during 2010 using the three algorithms selected by the cocktail reconstructor: tracker, Picky and TPFMS, and the cocktail itself.

Summarising, the performance of the cocktail fit, as it was the recommended algorithm, was studied in the scope of the $W' \to \mu\nu$ searches. The dedicated TeV algorithms perform well, better than the standard reconstruction for the p_T signal region. The selected cocktail tune, previously optimised with cosmic data, did perform as expected, reducing the tail of the resolution distributions for instance. The study was carried out with the simulated samples used to compare with the data in the W' analysis (in particular, W' of $M_{W'} = 1500$ GeV/c^2 and W, the main background) and cross checked with 2010 cosmic data. In both cases, the core of the resolution is at least as good as the one obtained with the other algorithms and the tails of the resolution are smaller, which implies that p_T muons are not misreconstructed with a much higher p_T, which could fake signal events. In the light of this results, the goodness of cocktail was probed and its adequacy for the analysis.

Chapter

6

Measurement of the Single Muon Efficiency

A fundamental piece of any physics analysis is the determination of the efficiency of the reconstruction, trigger and selection of the objects involved. This chapter is dedicated to the description of a method developed to determine the single muon efficiency, based on real data. The evaluation of the efficiency directly from data avoids depending on Monte Carlo and introducing biases due to detector behaviour mismodelling.

Efficiency measurements are closely related to physics analysis as they depend on the particular selection chosen. This means that efficiencies are not absolute values applicable to any study. In this case, the analysis for which the efficiency determination is aimed is $W' \to \mu\nu$ searches and $W \to \mu\nu$ cross section measurement. The expected signature of that process is an isolated high p_T muon and, therefore, the aim is to measure the efficiency for that kind of muons. To estimate it with the data collected in 2010 electroweak processes, whose decay muons have similar characteristics, can be used for this purpose. Moreover, $W \to \mu\nu$ events constitute the largest background to the W', so it is crucial to accurately measure the muon reconstruction and selection efficiency. The measurement was not only applied to the W', see section 8.3, but also to the $W \to \mu\nu$ cross section measurement [43], shown in this chapter.

Several studies were performed to optimise the reconstruction and selection of muons, the recommended selection, described in the next section, was established as the reference one adopted by different analyses, in particular the W and Z cross section measurement and W' search, and it is then the efficiency to determine.

The method is based on dimuon events from a known resonance, where one muon is required to pass stringent criteria to select the event and the second one is used to determine the efficiency. This kind of methods are commonly referred to as "Tag and Probe" methods. To study the low muon p_T spectrum J/Ψ or Υ resonances decaying to muon pairs are the adequate candidates. For the electroweak analysis (W, Z decays) the focus is set on medium p_T muons, around 40 GeV/c. The method exploits the clear selection of $Z \to \mu\mu$ candidates and takes into account the possible presence of background processes remaining in the selected event sample. Muons coming from W decays are kinematically similar to those arising from Z boson decays, so the latter are well suited for muon efficiency measurement in electroweak studies in general, not only for Z decays.

The chapter is structured as follows: first, the definition of the single muon efficiency is introduced and the samples used for the analysis are described. Second the *MC truth* efficiency is calculated, to compare it with the one from the data based method. Third, this Tag and Probe method is detailed and the results are shown. Finally a thorough description of the systematic errors associated to the measurement andthe various checks carried out to asses the validity of the method are presented. To conclude, the results obtained with this method to determine the efficiency for the $W \to \mu\nu$ cross section measurement are summarised.

6.1 Single Muon Efficiency Calculation

In order to guarantee a correct reconstruction, the muon is required to fire the muon triggers, and to be reconstructed offline as a global muon. In addition, instrumental background, badly reconstructed muons and muons coming from decays in flight are suppressed by examining the quality of the fits, their distance from the vertex and their penetration in the muon system. Moreover, the selection should include specific criteria, involving the characteristics that differenciate muons from signal events and background processes, to further reject the latter. The optimal required criteria are then:

1. **Muon identification**: it must be identified as *global* and *tracker* muon, see Chapter 5, to ensure good consistency between the inner detector and the muon spectrometer reconstructions, which guarantees good momentum measurement and additionally reduces the contamination from muons from decays in flight of hadrons and from punch-through.

2. **Quality cuts related to the muon track** (inner and global):

    - The number of hits in the silicon tracker has to be larger than 10. Generally tracks with small number of hits give a wrong p_T estimate. In addition, decays in flight give rise in many cases to lower hit occupancy in the tracker.

- There should be at least one pixel hit in the tracker track of the muon. The innermost part of the tracker is an important handle to discard non-prompt muons.
- The global muon fit should contain at least one good muon chamber hit and have crossed at least two chambers. This implies that the muon has penetrated deeply enough in the muon system. In general good muons will cross the whole detector due to their high momentum, so punch-through candidates are suppressed.
- Bad fits are rejected by requiring reasonable global muon fit quality in terms of its normalised χ^2: $\chi^2/ndof < 10$, where $ndof$ is the number of degrees of freedom of the fit. For instance, if there was a decay in flight inside the tracking volume, the trajectory could contain a sizeable *kink*, resulting in a poor χ^2.

3. The transverse impact parameter of the track measured in the transverse plane with respect to the beam-spot must fulfil $|d_0| < 0.2$ cm. This is meant to reject cosmic muon background.

4. **Isolation**: Isolation is extremely useful to discriminate between different physical processes in terms of the amount of energy or momentum surrounding the muon. Objects coming from electroweak processes are expected to be isolated in the detector while high p_T muons from hadronic processes typically have a much higher track and calorimeter occupancy, and produce a larger number of low momentum jets. The muon is hence surrounded by other tracks and energy deposits in the calorimeter. The basic element to quantify the isolation is the activity in a cone $R = \sqrt{\Delta\phi^2 + \Delta\eta^2}$ around the muon, in this case $R <0.3$.

   Every reconstructed muon is assigned track, electromagnetic and hadronic calorimeter isolation, defined respectively as the sum of the momentum of all reconstructed tracks, the transverse energy deposits in the electromagnetic calorimeter and in the hadron calorimeter, all measured around the muon track direction. The momentum and the energy deposits in the calorimeter of the muon itself are excluded from the computation.

   Combining information from the tracker and the calorimeters demonstrates a higher rejection power against hadronic events, leaving the signal efficiency intact, compared to track-only isolation, in the lower part of the momentum spectra where hadronic background is concentrated. Frequently, muons originating from background processes tend to have lower p_T than those from the signal. So the separation between signal and background muons is improved by normalising the isolation energy to the p_T of the muon, giving the relative isolation variable. All this considerations lead to a final combined, relative variable:

$$I^{rel}_{comb} = \frac{\sum_{\text{tracks}} p_T + \sum_{\text{Cal}} E_T}{p_T^{\mu}}$$

The efficiencies were calculated for different thresholds, $I^{rel}_{comb} < 0.10 - 0.15$, for the first data collected.

5. **Trigger selection:** The basic trigger strategy is to use a single muon trigger that was set unprescaled in any given run. Due to the rapid increase in luminosity during the 2010 run, the p_T threshold changed several times to keep the trigger rate at a low level, from 9 GeV/c to 11 GeV/c and 15 GeV/c. This corresponds to three triggers for 2010: `HLT_Mu9`, `HLT_Mu11` and `HLT_Mu15`. All these triggers have the same L1 seed, with a p_T cut in 7 GeV/c. In particular, the criterion consists on requiring the offline muon to be associated to a high level trigger muon corresponding to one of the three trigger paths mentioned. Both muons must be separated by an angular distance of $R = \sqrt{\Delta\phi^2 + \Delta\eta^2}$ <0.2.

The single muon efficiency calculation defines the efficiency of all these steps involved in the muon reconstruction and selection: triggering, reconstructing and tracking it in the muon and in the central silicon detectors and computing its degree of isolation.

So the single muon efficiency, ϵ_μ, can be written as

$$\epsilon_\mu \equiv \epsilon_{track} \cdot \epsilon_{rec} \cdot \epsilon_{isol} \cdot \epsilon_{trig} = \epsilon_{track} \cdot \epsilon_{global}$$

where

- ϵ_{track} stands for the reconstruction efficiency in the central tracker,
- ϵ_{rec} involves the steps of reconstructing a good quality muon, passing specific criteria in the tracker and muon detectors,
- ϵ_{isol} is the isolation efficiency, accounting for the amount of particle activity in the neighbourhood of the lepton as described,
- ϵ_{trig} corresponds to the efficiency of a muon to fire the high level trigger

In the method presented here, the efficiency is computed as a global value, except from ϵ_{track}, which is factorised from the rest of the terms (reconstruction, isolation, trigger) included in ϵ_{global}. The study focuses on the determination of ϵ_{global}, comprising globally the efficiency of obtaining a muon with certain quality criteria, without decomposing the different terms. This approach is based on the interest of obtaining a final value for the analysis, it is not a particularity of the method. In section 8.3 the various terms are computed individually.

The term ϵ_{track}, involving only the central silicon detector, is also evaluated with a dedicated Tag and Probe exercise. It is expected to be close to 100% in the whole tracker acceptance region.

For a correct muon identification efficiency measurement it is important to subtract the remaining background, not coming from the resonance under study, from the total dimuon pair sample gathered after applying a stringent quality criteria on one muon and the dimuon mass constraint. This is the key aspect of the measurement and it will be carefully described along this chapter.

6.2 Data and Simulation Samples

The data samples used in this study correspond to the proton-proton collision data at 7 TeV centre of mass energy of the LHC recorded between April and October 2010, the Run2010A and Run2010B. Only data which was certified as *good* by CMS is employed, which means that the performance of all subdetectors involved in the reconstruction of the interesting objects for the analysis was correct, discussed in section 3.3.1. The total integrated luminosity amounts to 36 pb^{-1} according to the final luminosity measurement in CMS [44]. Data periods, depending on the lowest p_T threshold trigger, and accumulated luminosity of each of them are reported in Table 6.1.

Muon Data	Trigger	Luminosity (pb^{-1})
Run2010A	HLT_Mu9	3.1
Run2010B	HLT_Mu9	5.0
	HLT_Mu11	9.4
	HLT_Mu15	18.3

Table 6.1: Summary of the datasets used in the analysis and accumulated luminosity.

Simulated Monte Carlo samples were used to develop the method to measure the efficiency and establish its validity. A brief description of the generators employed for the simulation of the Monte Carlo sample is presented. Event generators are general purpose tools designed to describe a variety of processes, allowing theoretical and experimental studies of complex multiparticle physics. They randomly generate events similar to those produced in particle accelerators, including the kinematics of the products of the hard collision and the evolution of the underlying event. Generated events are processed through the full `GEANT4` [45, 46] detector simulation, trigger emulation and event reconstruction chain of the CMS experiment.

- PYTHIA [47] is a general purpose event generator commonly used in High Energy Physics. It provides predictions at leading order (LO) with higher order effects approximated via parton showers (PS) and matrix elements (ME) corrections. It is used as the standard LO event generator for QCD processes. (From the samples used here, also $t\bar{t}$ and diboson samples were generated with Pythia.)
- POWHEG ("Positive Weight Hardest Emission Generator") [48, 49, 50] includes full next-to-leading order (NLO) matrix elements, however it relies on parton showering to account for higher order soft QCD effects. It is the standard NLO event generator used by CMS for simulating electroweak physics, used here for the production of W and Z events decaying into muons or taus, interfaced with the PYTHIA parton-shower generator.

See Table 6.2 for the complete list of samples used. These samples include the simulation of ad-hoc additional interactions (pile-up events).

Generator	Process	Kinematic cuts (in GeV, $c = 1$)	σ_{LO} (pb)	σ_{NNLO} (pb)	# of events	PDF set
POWHEG	$Z \rightarrow \mu\mu$	$m_{\mu\mu} > 20$	1300	1666	~2M	CT10
POWHEG	$W^+ \rightarrow \mu^+\nu_\mu$	no cuts	5775	6152	~2M	CT10
POWHEG	$W^- \rightarrow \mu^-\nu_\mu$	no cuts	3944	4286	~2M	CT10
POWHEG	$W \rightarrow \tau\nu_\tau$	no cuts	7899	10438	~5M	CT10
POWHEG	$Z \rightarrow \tau\tau$	$m_{\tau\tau} > 20$	1300	1666	~2M	CT10
PYTHIA	$t\bar{t}$	no cuts	94	157.5 (NLO)	~1M	CTEQ6L
PYTHIA	Inclusive μ QCD	$\hat{p}_T > 20$, $p_T^\mu > 15$, $\lvert\eta_\mu\rvert < 2.5$	84679	84679	~30M	CTEQ6L
PYTHIA	WW	no cuts	28	43	100k	CTEQ6L
PYTHIA	WZ	no cuts	10.4	18	100k	CTEQ6L
PYTHIA	ZZ	no cuts	4.3	5.9	100k	CTEQ6L

Table 6.2: Summary of the Monte Carlo samples used to model the signal and the various background processes. More information about the samples can be found in [51].

6.3 Single Muon Efficiency with Monte Carlo

In this section, the estimation of the MC truth efficiency for identifying and selecting (trigger, reconstruction and isolation) single muons in a Z→ $\mu\mu$ sample and a W→ $\mu\nu$ is presented. These results will be used to validate the developed Tag and Probe method to determine the efficiency with data, introduced later.

The selection starts by requiring at least one muon with ${p_T}^{gen}$ >25 GeV/c and $|\eta^{gen}| < 2.1$, at generator level. The single muon efficiency is calculated as the ratio of the number of generated muons associated to a reconstructed muon fulfilling the criteria over the number of preselected muons in the defined generated phase space. The generated and reconstructed muons are associated by the angular requirement: $R = \sqrt{\Delta\phi^2 + \Delta\eta^2} < 0.5$.

Table 6.3 shows the cumulative efficiency after each selection step and, in parentheses, the efficiency with respect to the previous requirement for the $Z \rightarrow \mu\mu$ sample and the $W \rightarrow \mu\nu$. The W efficiencies correspond to the combined efficiency from the W$^+$ and W$^-$ samples, taking into account the different cross section of each process, see Table 6.2.

The single muon efficiency is expected to be very similar no matter whether it is computed on a W→ $\mu\nu$ or a Z→ $\mu\mu$ sample due to the similar kinematic region of the produced muons. The results for both are presented in Figure 6.1 as a function of the generated muon p_T, η. They are obtained with all MC statistics available ($\sim$ 2 million events) for each chosen sample. The errors reflect the statistical fluctuations appear. There is no significant dependence with respect to p_T from $p_T\sim$ 30 GeV/c up to 100 GeV/c, where the statistics are significant. However, the efficiency varies as a function of η, being lower in the η regions corresponding to the overlap zone between the EndCap and Barrel muon detectors ($|\eta| \sim 1.2$) and in the regions between wheels.

The average efficiencies on both samples are:

Selection step	Efficiency (Z sample)	Efficiency (W sample)
Good quality reco. muon	97.20%	97.39%
d_0, χ^2 requirements	96.84% (99.64%)	97.06% (99.66%)
Isolation	94.05% (97.11%)	94.21% (97.07%)
Associated to trigger muon	89.22% (94.87%)	89.26% (94.75%)

Table 6.3: Single muon efficiencies determined on $Z \to \mu\mu$ and $W \to \mu\nu$ samples for each of the selection steps, with respect to the number of generated muons in the kinematic range $|\eta| < 2.1$ and $p_T > 25$ GeV/c. In parentheses, the efficiency values with respect to the previous requirement are given. The errors associated to these numbers reflect the statistics analysed and amount to 0.03%.

- Z$\to \mu\mu$: $\epsilon = 0.8922 \pm 0.0003$
- W$\to \mu\nu$: $\epsilon = 0.8926 \pm 0.0003$

confirming that the results for both electroweak channels are very close, as expected, due to the similarities of the decay muons (isolated, medium p_T range, etc.). In the following sections, the focus is set on the data based method for the efficiency measurement.

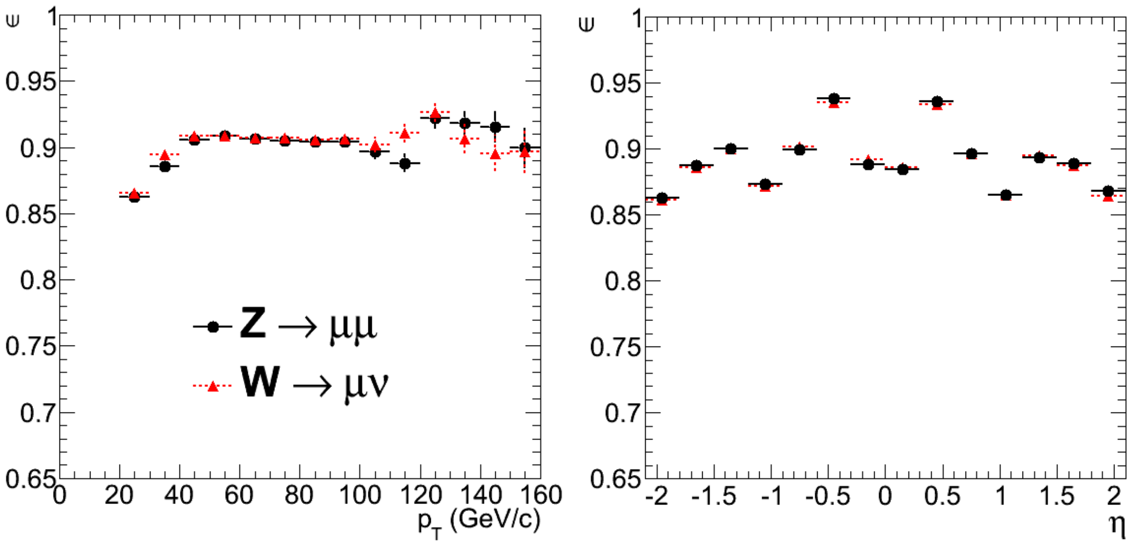

Figure 6.1: Single muon efficiencies from MC truth information obtained with a simulated Z$\to \mu\mu$ sample (black dots), with an equivalent luminosity of $\mathcal{L}_{\rm int} \sim$1238 pb^{-1}, and a simulated W$\to \mu\nu$ (red triangles) sample, with an statistics equivalent to $\mathcal{L}_{\rm int} \sim$325 pb^{-1}. Efficiency dependence versus muon p_T (left) and η (right) is shown.

6.4 Single Muon Efficiency: Tag and Probe Method

Tag and probe techniques rely on the selection of a clean and with high purity Z→ $\mu\mu$ sample, making use of the Z boson mass constraint, on which the muon selection efficiency is determined in an unbiased way. Candidate events are selected with strict selection requirements on one muon, referred to as the *tag* muon, which ensures a good preselection of events, and with looser criteria on the other muon, the *probe* muon. The efficiency under study is then defined as the fraction of *probe* muons that satisfy certain criteria.

Candidate events from Z boson decays are preselected as those containing two opposite signed tracks measured in the central tracker, with kinematics cuts p_T>25 GeV/c and $|\eta| < 2.1$, which give an invariant mass in the range $60 < M_{\mu\mu} <$ 120 GeV/c^2.

In these events, one of the tracks, the *tag*, must pass all the muon identification criteria described in section 6.1. The association between the preselected muon track, in inner tracker, and its corresponding global muon is done using the reference to the track contained in the muon object, which provides univoque correspondence. The second track is considered the *probe*, the one to be tested for the set of criteria depending on the efficiency under study. In this case, the requirements are the ones the *tag* muon fulfils. Only events with a single *probe* candidate per *tag* muon are considered. In case of multiple possible *probe* tracks for a *tag* muon, the event is rejected. Measuring the efficiency with this technique the *probe* muons are tracks reconstructed using only the inner tracker, so there is no bias from the muon detectors.

6.4.1 Tag and Probe Efficiencies with Monte Carlo

The start up point is the calculation of the results with the same $Z \to \mu\mu$ MC sample as in the previous section, to compare it with the MC truth efficiency. The efficiency is obtained as the ratio of the number of *probe* muons fulfilling the selection cuts with respect to the total number of *probe* muons, resulting $\epsilon = 0.8942 \pm 0.0004$. This result is not directly comparable to the pure MC one, as the tracking efficiency factor is not included. However, the first conclusion is that the Tag and Probe result differs by less than 0.002 from the MC truth one. The efficiency as a function of the kinematic variables p_T and η is presented in Figure 6.2. The distributions follow the same pattern as the plots in Figure 6.1.

6.4.2 Tag and Probe Efficiencies with Data

After applying the criteria to select the muon pairs, about 22000 *tag* muons survive in the whole data sample. Figure 6.3 shows the dimuon invariant mass distribution from *tag-probe* muon pairs, before and after requiring any criteria to the probe track. The lowest $M_{\mu\mu}$ values correspond to the region where the relative amount of selected muons is lower compared to the number of *probes*, there are more *failing probes*. The

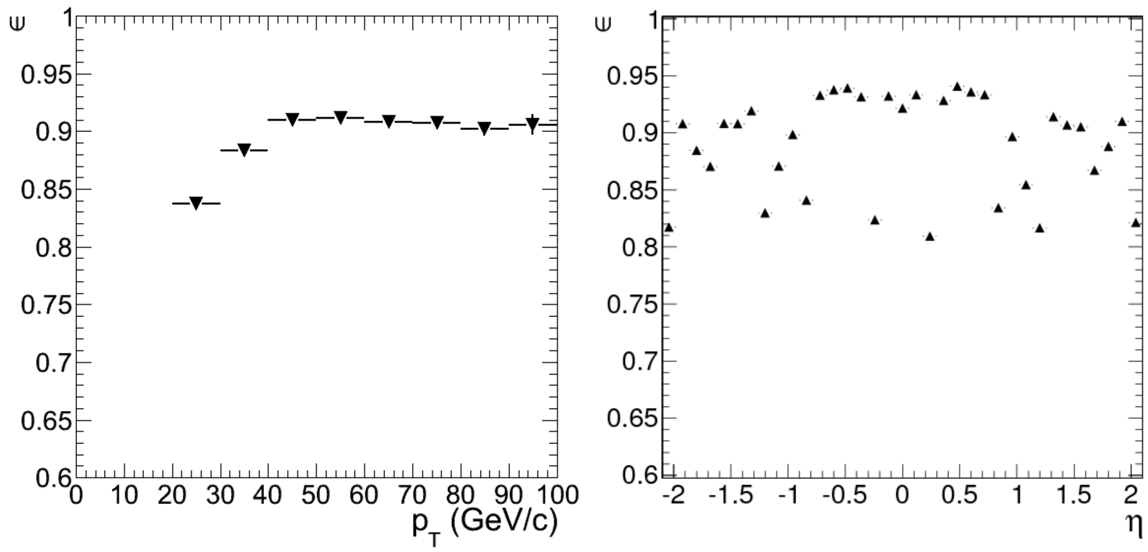

Figure 6.2: Single muon efficiencies with Tag and Probe obtained with a high statistics MC Z→ $\mu\mu$ as a function of muon p_T (left) and η (right).

corresponding distributions of the *probe* muon kinematic variables are presented in Figure 6.4. These figures illustrate how the selection criteria to the *probe* muon rejects them uniformly as a function of ϕ, being both distributions roughly flat. In η the global shape before and after the selection is similar in general terms, while less muons pass the whole selection criteria for lower p_T values, so the distribution after requirements shows a sharper peak around 40 GeV/c (smaller tail before that value) than the distribution with all *tag-probe* pairs.

The selected $Z \to \mu\mu$ candidate data sample, consisting on pairs of a good muon and a high p_T track, contains a certain contamination from other physical processes which generate muons with a similar topology. Thus, the single muon efficiency can only be computed as the ratio of the number of *probe* muons fulfilling the selection requisites with respect to the total number of *probe* muons accompanying a *tag* muon, once the background contamination is taken into account, which is described in the following. Assuming that one has the dimuon invariant mass distribution with N bins and that in each bin i there are μ_i *probes*, the number of muons satisfying the selection criteria in a bin, $\mu_i^{passing}$, would be

$$\mu_i^{passing} = \mu_i \xi_i = \mu_i(\omega_i \epsilon + \omega_{Bi}\epsilon_B) \tag{6.1}$$

where ξ_i can be interpreted as an effective efficiency in bin i; ω_i is the probability of each muon of being signal, hence of coming from a $Z \to \mu\mu$ event; ω_B is the probability of that muon of being background; ϵ_B is the probability that a background *probe* satisfies the selection and ϵ is the signal efficiency, the quantity to determine. The only hypothesis in the previous equation is that both the signal efficiency and the background efficiency do not depend on the mass bin i the muon contributes to. To

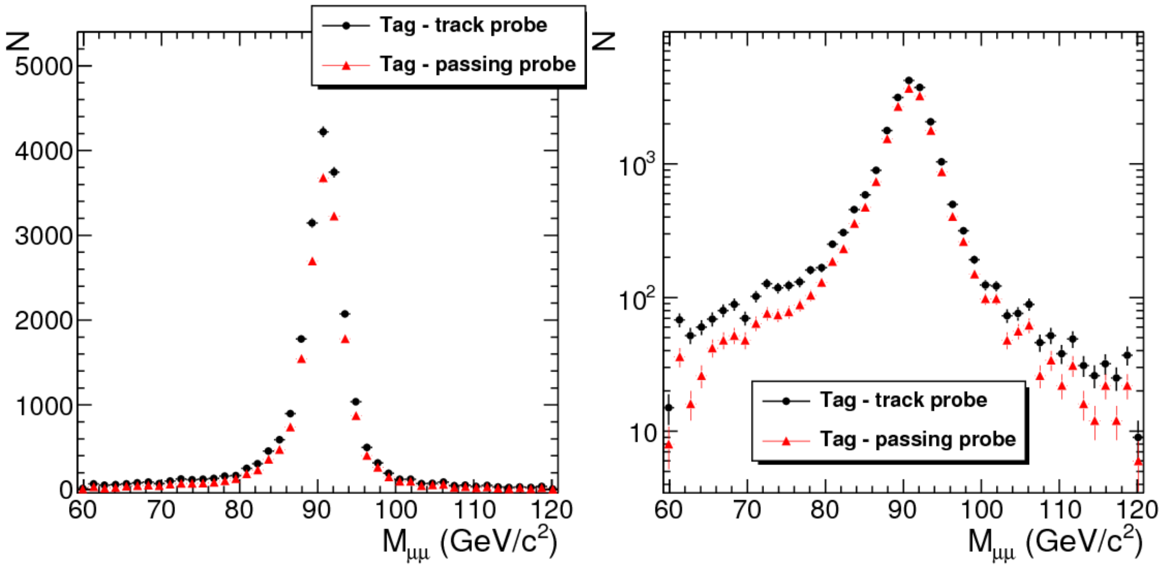

Figure 6.3: Dimuon invariant mass distribution from *tag-probe* muon pairs with data, before requiring any criteria to the *probe* track, black dots, and pairs where the *probe* muon satisfies all requirements, red triangles, in linear (left) and logarithm (right) scale.

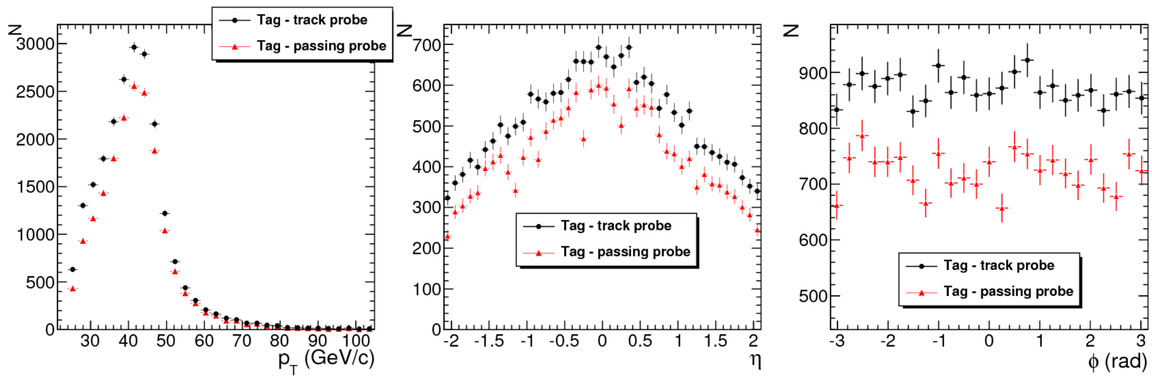

Figure 6.4: *Probe* muon kinematic variables, p_T, η, ϕ from all data associated to a *tag* muon, black dots, and *probe* muons satisfying all requirements, red triangles.

extract ϵ, it is first necessary to estimate the terms involving the background in the previous equation, ω_B, ϵ_B.

This estimation of the background contamination in data is obtained from the Monte Carlo simulation, with a high statistics $Z \to \mu\mu$ sample and the corresponding background sources, see table 6.2 for the complete list of samples used. The background processes considered are

- pp $\to \mu$X
- pp$\to$ t$\bar{\text{t}}$X
- pp$\to$ZX$\to \tau\tau$X
- pp$\to$WX$\to \mu\nu$X
- pp$\to$WX$\to \tau\nu$X
- diboson decays (WW, WZ, ZZ events)

These background processes are expected to have lower efficiency than the considered signal events, for instance muons from QCD processes are less isolated. Therefore, in this situation the ratio between passing *probes* over all *probes* does not correspond to the single muon efficiency under study, yielding a lower efficiency, and it is necessary to subtract the background contribution from the calculation.

After the event preselection, requiring the presence of a *tag* muon in the event, the sample gathered (normalised to the luminosity in data) consists of 2.2×10^4 Z$\to \mu\mu$ events and about 1080 background events, being $W \to \mu\nu$ and $t\bar{t}$ the dominant contributions and from which ~30 muons come from diboson events, see Table 6.4. This implies that the expected contamination of background in the *tag* and *probe* initial sample, the "denominator", is ~4.7%, which must be taken into account. Once the selection for the *probe* is applied, the number of muons from background events satisfying the selection criteria corresponds roughly to $\epsilon_B\omega_B$ ~0.27% from the total of muons surviving the selection. One important remark is that approximately half of the muons from background processes contributing to the "numerator" are diboson events with Z bosons decaying to muons. Those events are a source of background in terms of the analysis, however they are reconstructed and identified as efficiently as muons from $Z \to \mu\mu$ so their presence does not bias the measurement as they behave like signal events. Then the contribution of the rest of the background has a negligible effect in ϵ in the scope of the precision reachable with the actual statistics.

Thus, the efficiency, neglecting $\epsilon_B\omega_B$, can be computed as

$$\epsilon = \frac{\sum^{Npass} \mu_i^{passing}}{\sum^{Nprobes} \omega_i \mu_i} \tag{6.2}$$

summing all the *probe* muons. This means that effectively each *probe* muon is reweighted by the probability of coming from a $Z \to \mu\mu$ event, the way to calculate

Sample	Muons preselected	Muons selected
Z→ $\mu\mu$	21868	19582
pp→ μX	73.9	0.0
$\mathrm{t\bar{t}}$	117.0	17.1
W→ $\mu\nu$	719.6	0.22
W→ $\tau\nu$	61.0	0.0
Z→ $\tau\tau$	75.3	15.3
WW	13.0	4.0
WZ, ZZ	19.3	15.8

Table 6.4: Expected number of preselected and selected events from signal and background processes corresponding to $\mathcal{L}_{\text{int}} = 36\ \text{pb}^{-1}$, according to the MC prediction.

the weight is one of the particularities of this method: in order to obtain it one relies on variables with different behaviour for signal and background events. The variables considered are:

- Dimuon invariant mass, see Figure 6.5, where the MC distributions in the range $60 < M_{\mu\mu} < 120$ GeV/c^2 are displayed from the expected Z→ $\mu\mu$ events and the background in the sample. From this plot, it is clear that the proportion of background in the tails is much higher than in the peak region.

- Transverse momentum of the *probe* muon, p_T, shown in Figure 6.6 for muons from background processes (blue dashed line) and for muons from Z boson decays (solid line). Muons from background processes have a lower p_T spectrum than muons from Z decays, most of the contribution concentrates at p_T<35 GeV/c. Notice that in the figure both contributions are normalised to unity.

6.4.3 Background Extraction

The procedure to extract the weight consists in fitting the experimental reconstructed invariant mass to a function composed of two contributions: the dimuon invariant mass of Z→ $\mu\mu$ events obtained from the simulation and a function accounting for the background in the mass range considered. Then the total number of events selected in each mass bin can be written as the sum of the number of events from Z→ $\mu\mu$ decays plus the number of background events. That is, $\mathrm{N}^{sel} = \mathrm{N}^{sel}_{Z\mu\mu} + \mathrm{N}^{sel}_{Bkgd}$. In fact, two different mass distributions are considered, one for *probe* muons with $p_T < 35$ GeV/c, where most of the background muons are present, and the second one for *probe* muons with $p_T \geq 35$ GeV/c, clearly dominated by Z→ $\mu\mu$ muons according to Figure 6.6. In other words, two sets of weights are computed, one for each p_T region. The choice of separating in two p_T bins is a compromise between accounting properly the dependence on p_T and keeping the statistical error of the fit as small as possible.

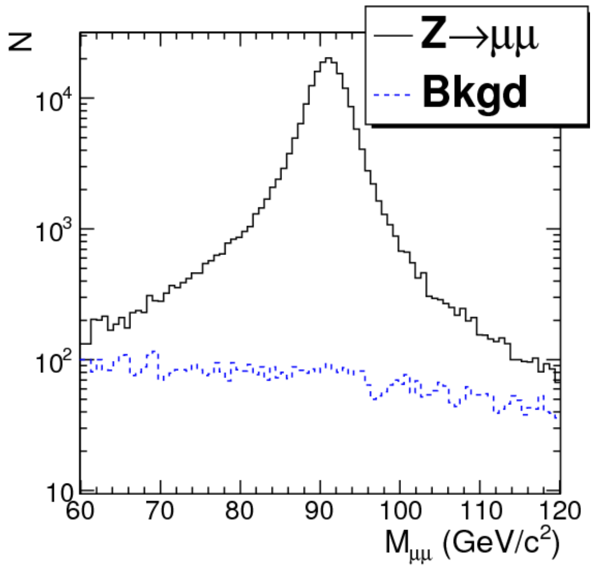

Figure 6.5: Dimuon invariant mass from muon pairs for a high luminosity MC sample, for Z→ $\mu\mu$ events (solid line) and contribution from background events (blue dashed line).

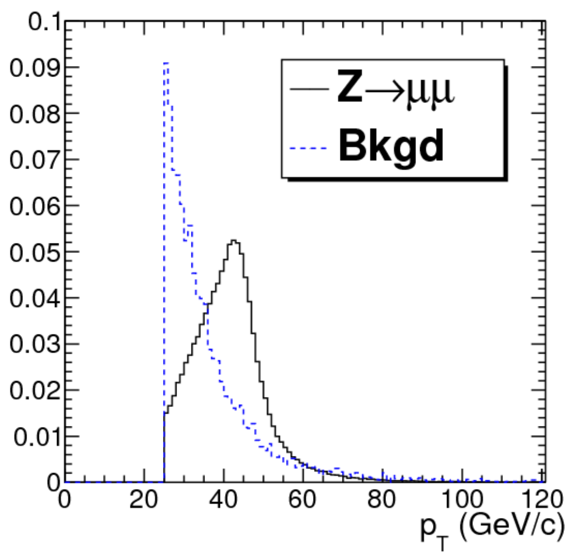

Figure 6.6: Transverse momentum distributions for *probe* muon (before passing the criteria) separately shown for muons from background processes (blue dashed line) and for muons from Z boson decays (black solid line). Both histograms are normalised to unity.

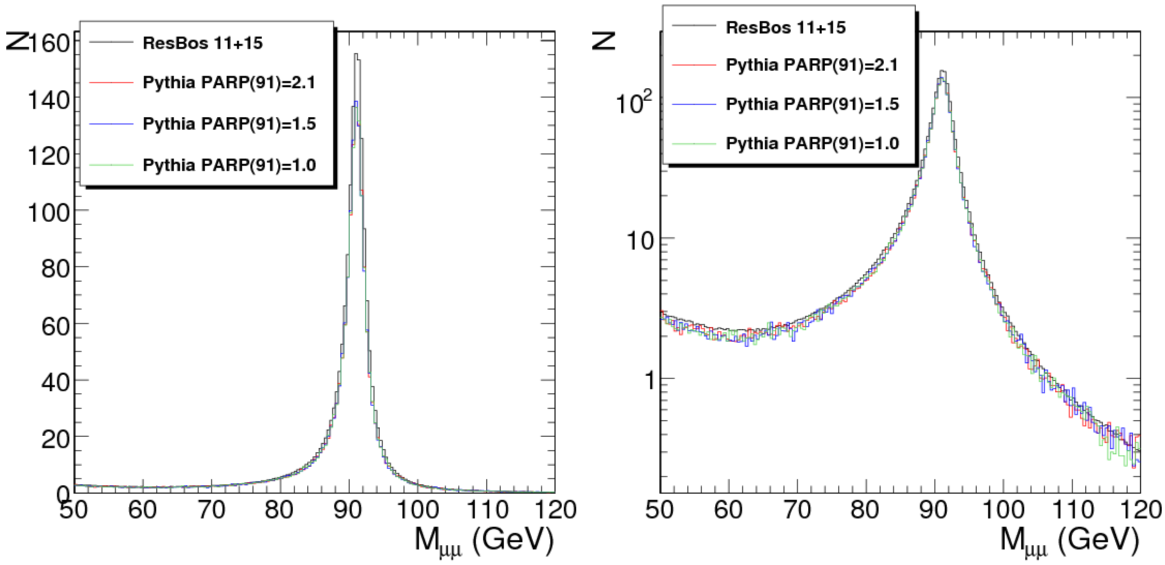

Figure 6.7: MC dimuon invariant mass obtained with several tunings of PYTHIA and ResBos, at generator level, in linear (left) and logarithmic scale (right). The parameter PARP(91) is related to the the intrinsic k_T distribution, which is the primordial transverse momentum associated to the shower initiator parton in the event generation with PYTHIA.

The shape of the Z boson mass distribution is robustly described by several MC generators, as illustrated in Figure 6.7, where the invariant mass of the dimuon system at generator level obtained with different PYTHIA tunings is compared with the predictions from ResBos [52, 53]. ResBos is an integrator for hadron collisions that resumes the effect of initial state multiple soft-gluon emission to predict the distribution of the leptons from the decay of Z produced.

Therefore, the invariant mass is taken directly from the Monte Carlo simulation instead of modelling it with analytical functions, as most of the experimental effects, like resolution, are already included in the Monte Carlo simulation. In this case the Monte Carlo used as reference is POWHEG.

For simplicity, the function chosen to fit the background contribution is a linear shape in $M_{\mu\mu}$, however other functions, see section 6.6.6, were also considered. The effect of varying the function had no impact on the final result.

A function formed by the Z mass distribution from the simulation sample, with a normalisation constant, plus a linear function to describe the background is fitted to the reconstructed invariant mass. Both contributions are left free, without any constraint in their relative normalisation, to allow for adjustment to the real analysed luminosity. In this way,

$$M_{\mu\mu}^{\text{model}}(K, a, b) = K M_{Z-MC} + ax + b \tag{6.3}$$

with x between 60 and 120 GeV/c^2, K is the normalisation constant for the Z$\rightarrow$ $\mu\mu$ events contribution to the real sample and a and b are the parameters describing the distribution of background events in terms of the dimuon mass. In practice, one has two sets of parameters, one for each p_T region.

	Muon p_T<35 GeV/c	Muon $p_T\geq$35 GeV/c
Parameter	Fitted value	Fitted value
Normalization, K (Z$\rightarrow$ $\mu\mu$)	0.967 $\pm$ 0.021	1.005 $\pm$ 0.012
Slope, a (Bkgd)	-0.205 $\pm$ 0.026	-0.028 $\pm$ 0.034
Constant, b (Bkgd)	26.26 $\pm$ 2.90	5.96 $\pm$ 2.98

Table 6.5: Results from the dimuon invariant mass fit to a Z$\rightarrow$ $\mu\mu$ plus background contribution, for the two regions in muon transverse momenta considered.

The fitting procedure was done minimising the distribution of a binned log-likelihood function, derived from a Poissonian distribution

$$-\log L = \sum[M_i^{\text{model}}(K,a,b) - M_i^{data} \times \log M_i^{\text{model}}(K,a,b)] \tag{6.4}$$

where M_i is the number of muons in the i bin of the mass distribution. The MINUIT [54] package for minimization was used. The results for the fit parameters, for both muon transverse momentum ranges (p_T < 35 GeV/c and $p_T \geq$ 35 GeV/c), are listed in Table 6.5. Approximately 1/4 of the whole statistics (21761 *probe* muons) corresponds to *probes* in the lower p_T range, 5463 compared to 16298 in the higher p_T bin. The invariant mass distributions for both p_T ranges, the result of the fit and the signal and background contribution are shown in Figure 6.8. The fit describes correctly the behaviour in data in both p_T regions, overlaying the data distributions. From these distributions, the much larger contribution of the background to the sample with p_T< 35 GeV than to the higher p_T is seen. The global distribution is illustrated in Figure 6.9, showing a good agreement between the resulting fit and the data.

Once the Z$\rightarrow$ $\mu\mu$ component and the background contribution are quantified in terms of the dimuon mass and the muon p_T, the set of weights is computed, on a bin by bin basis, as the fraction of the fitted Z$\rightarrow$ $\mu\mu$ contribution to the total fitted function, for each of the two muon p_T ranges considered. That is

$$\omega = \frac{K \cdot M_{Z-MC}}{K \cdot M_{Z-MC} + a \cdot x + b} \tag{6.5}$$

where K, a and b are the experimentally fitted values, in each p_T range. Figure 6.10 shows the weight distribution as a function of the dimuon mass, for both p_T regions. The weight tends to be close to unity at the nominal Z boson mass (91.2 GeV/c^2), decreasing towards the tails of the distribution, being smaller for the p_T < 35 GeV/c range, where the background is mostly concentrated.

After applying these sets of weights to the selected muons from data, the resulting muon momenta and η distributions resemble that of the Z$\rightarrow$ $\mu\mu$ (no background present) sample from Monte Carlo, see Figure 6.11, in solid black line for the clean Z boson MC sample and in red triangles for the reweighted data. The distributions in black dots, shown for comparison, are the sames as in Figure 6.4, the original data.

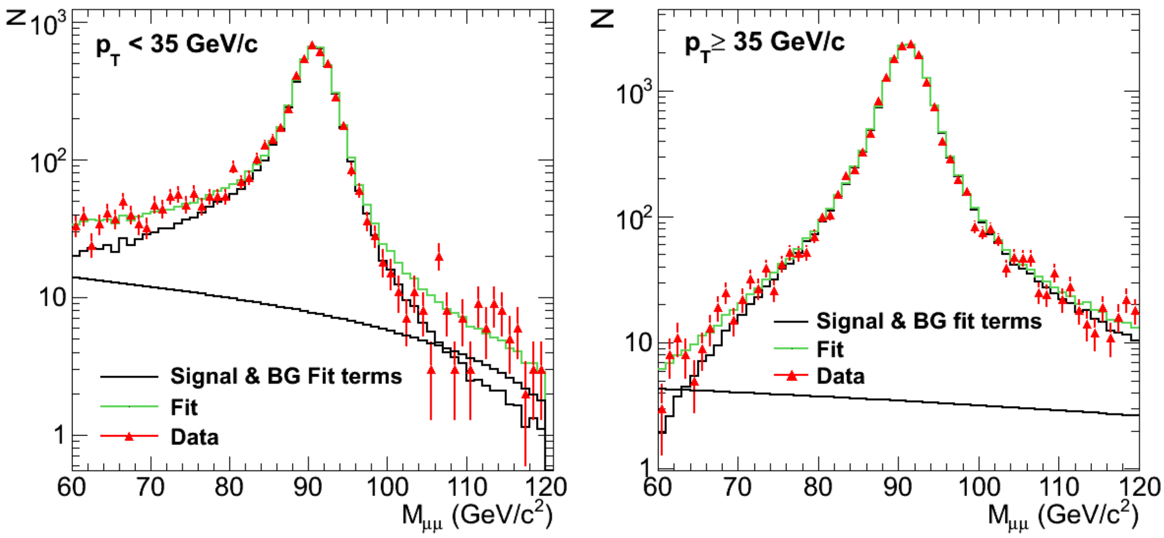

Figure 6.8: Invariant mass distribution for the *tag-probe* pair, for probe muons with p_T< 35 GeV/c, left plot, and with $p_T \geq$35 GeV/c, right plot. Data is shown as red triangles, the fit function is the light green solid line. The black histograms correspond to the signal and background terms of the fit function.

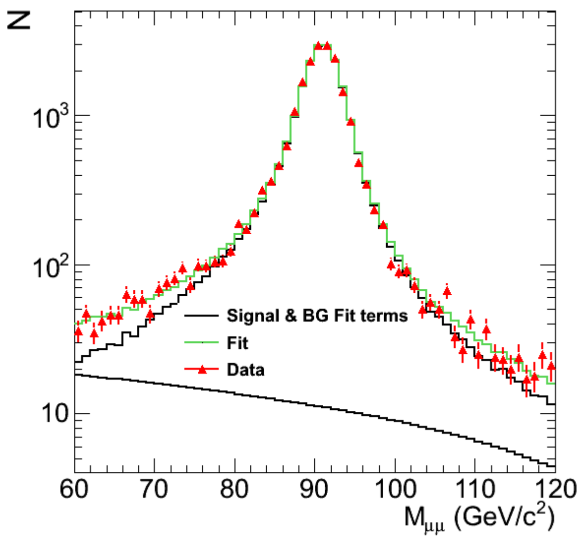

Figure 6.9: Invariant mass distribution for the data *tag-probe* muon pairs for all p_T regions, red triangles, the sum of the fits for the two p_T ranges is shown superimposed, as well as the background and signal individual contributions.

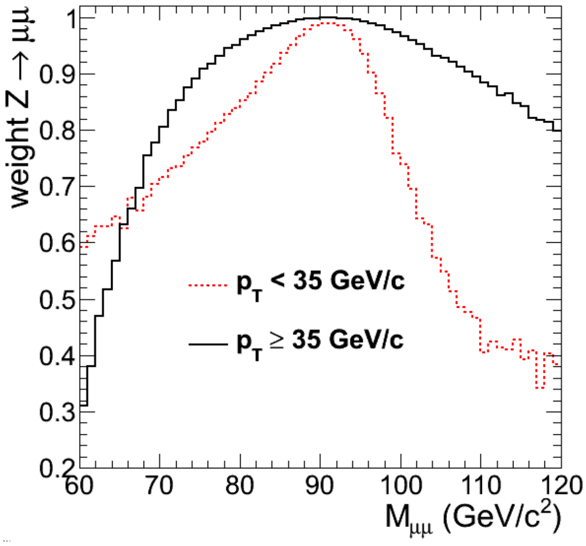

Figure 6.10: Weights applied to muons as a function of the dimuon invariant mass in the event, for the two p_T ranges, to account for the background events in the selected sample.

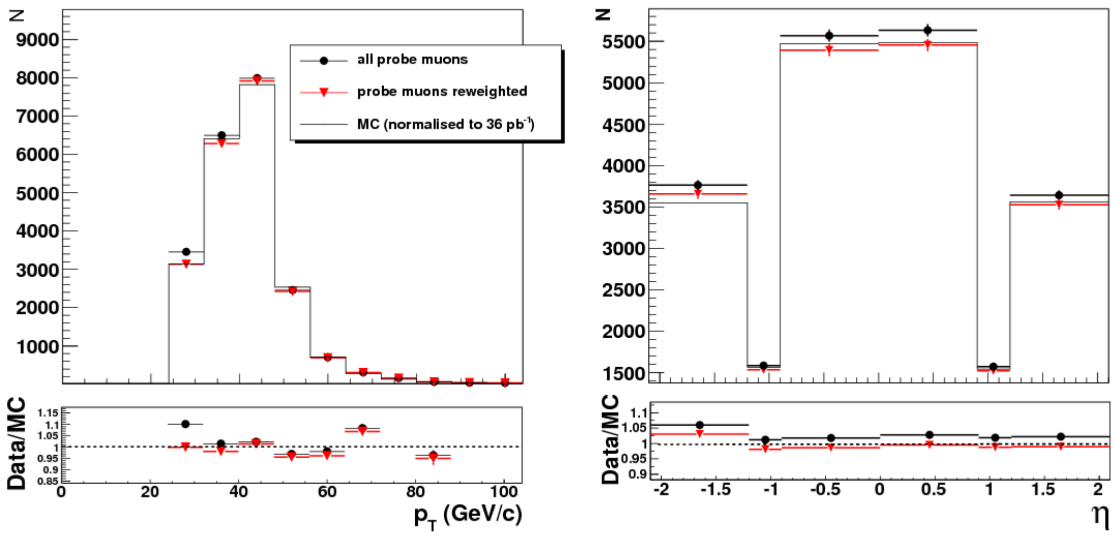

Figure 6.11: *Probe* data muon p_T, left, and η, right, before (black dots) and after (red triangles) applying the weighting factor. The distributions are compared to thethe $Z \to \mu\mu$ Monte Carlo sample one (solid line) normalised to the luminosity from data, 36 pb^{-1}.

This provides a first check that the background present in the selected sample has been accounted for correctly.

The efficiency, calculated as the ratio between *probe* muons passing all selection over all weighted *probes*, as defined in 6.2, results

$$\epsilon_{gl} = \epsilon_{reco} \cdot \epsilon_{iso} \cdot \epsilon_{trig} = 0.8565 \pm 0.0027.$$

The error is only the statistical one, the systematic error associated to the measurement is described later on. The efficiency as a function of the *probe* muon p_T and η is shown in Figure 6.12. The highest efficiency is measured in the central region of η, while it is 7-8% lower in the overlap region and 3-4% lower in the EndCaps. Regarding the distribution in p_T, it is lower in the first p_T bin (25,30) GeV/c and approximately constant in the region considered, up to 100 GeV/c. Qualitatively, the pattern in both variables is similar to the results in MC, nevertheless the latter yields higher values. A more detailed discussion of the results is given in section 6.5, after the tracking efficiency term is calculated and included to obtain the final efficiency.

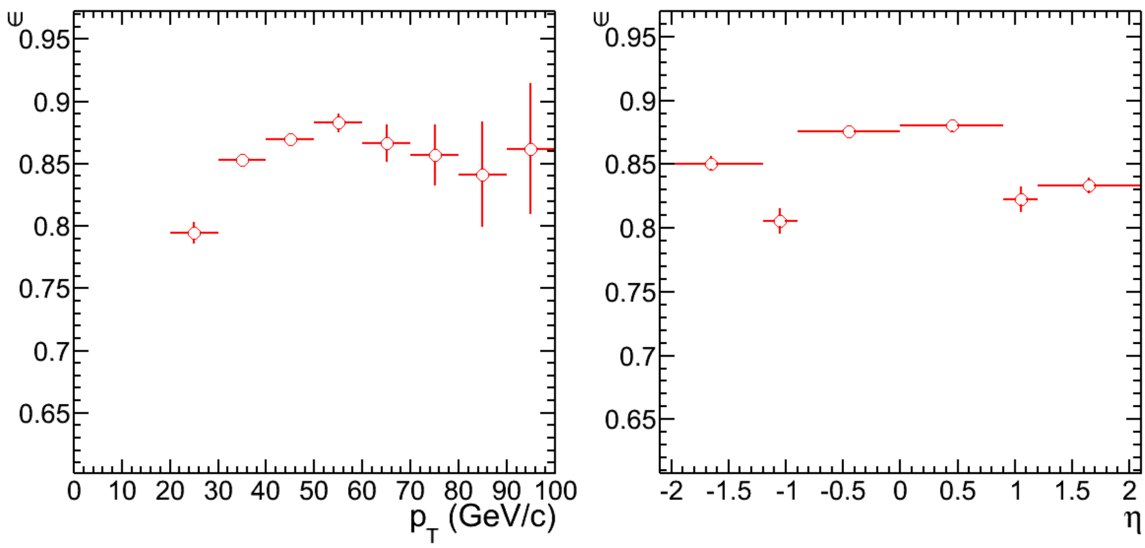

Figure 6.12: Single muon efficiency as a function of muon p_T (left) and η (right) obtained with the 36 pb^{-1} data.

6.4.4 Tracking Efficiency

The single muon efficiency was factorised in two terms: $\epsilon_\mu = \epsilon_{track} \cdot \epsilon_{global}$, the term concerning the reconstruction in the central tracker detector (ϵ_{track}) is addressed in this section.

This efficiency is obtained also with a Tag and Probe approach, considering isolated Standalone muon pairs in the data sample, with invariant mass in the same range used along the chapter, $60 < M_{\mu\mu} < 120$ GeV/c^2 and the same kinematic region,

p_T> 25 GeV/c and $|\eta|$ < 2.1. From this preselected sample, events with *tag* muons are selected as those fulfilling the same criteria as in section 6.1, while the condition to be fulfilled by the *probe* muons to estimate the tracker efficiency is to have a matching track in the central tracker. The association between the Standalone muon and the track in the central tracker is done by means of the reference to the track contained in the muon object, as described before.

The tracking efficiency is found to be 0.9981±0.0003 (stat). The efficiency obtained with the high statistics $Z \rightarrow \mu\mu$ Monte Carlo sample is slightly higher, being 0.99889±0.00004. The dependence with the *probe* muon kinematic variables p_T and η is shown in Figure 6.13. The distributions are roughly flat as a function of both variables. The efficiency between 50-60 GeV/c in data is a bit lower, however it is likely just a statistical fluctuation: the errors in the plot are computed as the 68% CL intervals, if instead the 95% CL interval is given the efficiency of that bin lays within the interval. The small fluctuations in η for data are at the 0.1-0.2% level, compatible with the statistical errors.

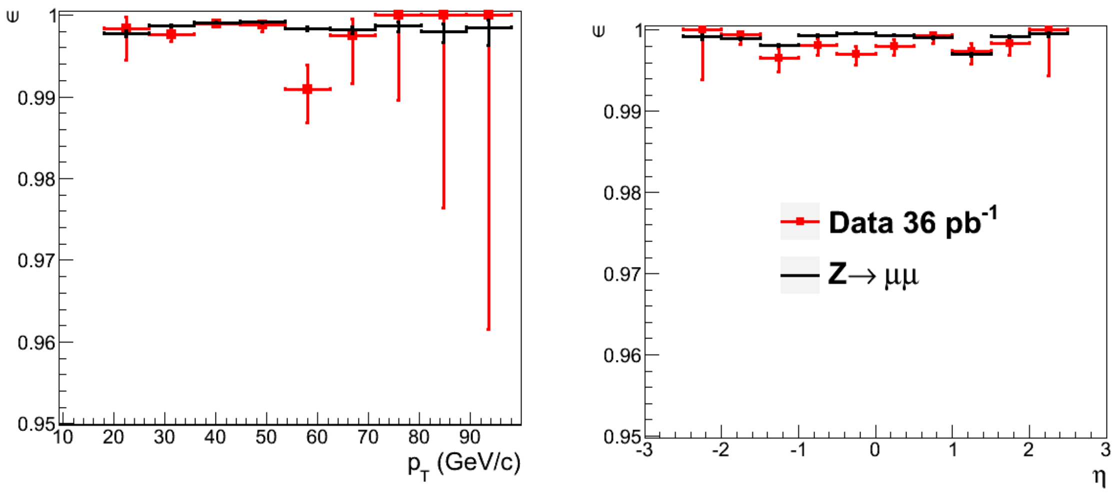

Figure 6.13: Tracking efficiency from a Tag and Probe method as a function of muon p_T and η for data, (red squares) and a $Z \rightarrow \mu\mu$ Monte Carlo sample. The errors are obtained as 68% Confidence level Clopper-Pearson intervals [55].

6.5 Final Efficiencies

Finally the two efficiency factors studied separately are combined. The efficiencies have been computed as a function of muon pseudorapidity and transverse momentum, to better reproduce the real detector performance. These results, including already the tracking efficiency obtained in section 6.4.4, are shown in Figure 6.14 for the whole data sample. For comparison purposes, the single muon efficiencies previously calculated with this Tag and Probe method on the MC Z→ $\mu\mu$ sample are superimposed. The efficiency is systematically lower in data than in the signal Monte Carlo sample. The efficiency in data follows essentially the same pattern as in MC as a function of p_T, in other words, the ratio is approximately constant. The efficiency pattern in η is similar as well, though the drop in efficiency is larger in certain regions, which correspond to the areas between the different wheels that conform the muon detector.

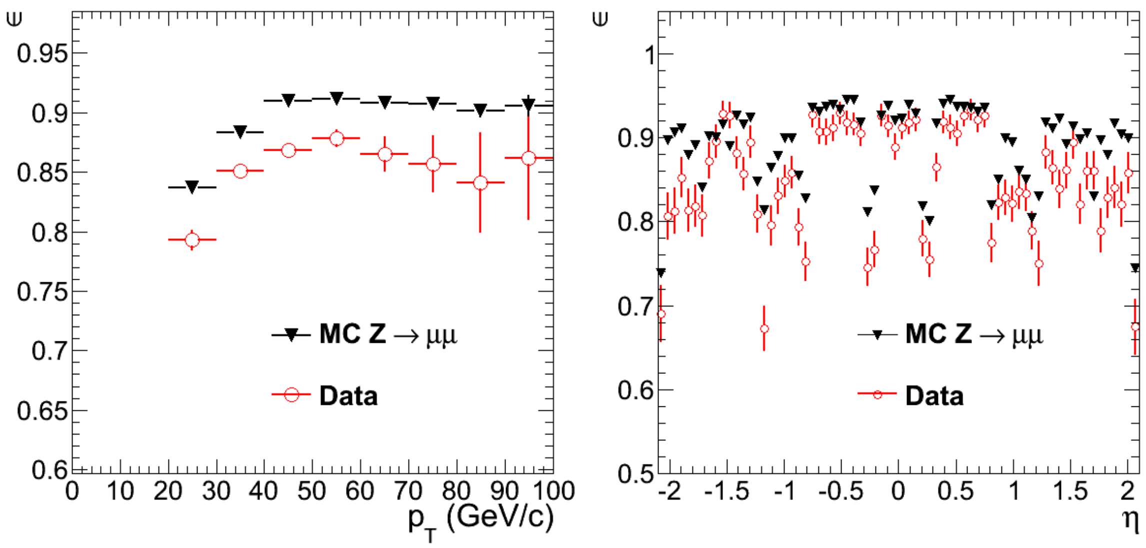

Figure 6.14: Final single muon efficiency ($\epsilon_{global} \cdot \epsilon_{track}$) as a function of p_T and η for data, open circles, compared to a Monte Carlo sample of $Z \to \mu\mu$, triangles.

The average efficiency is 0.8548±0.0027(stat.)±0.0024(stat. fit), compared with the Monte Carlo results $\epsilon_{MC} = 0.8932 \pm 0.0004$. The MC result can be compared as well to the MC truth one for the $Z \to \mu\mu$ sample (0.8922 ± 0.0003). Both agree within 0.1%, indicating that there is no bias in the Tag and Probe calculation and it gives the correct answer. The 0.0024 error in data comes from the propagation of the fit parameter uncertainties listed in Table 6.5. It is obtained as the quadratic sum of the difference between the efficiency and the result obtained by computing it modifying one by one the parameters by its error (and the rest accordingly taking into account the correlation between the parameters).

Finally, the efficiency was determined separately for positive and negative charged muons. It was observed that the efficiency in data was slightly different between μ^+ and μ^- while both kind of muons behave similarly in MC. This can be seen in Figure 6.15, where the ratio between data and MC efficiencies are depicted. Most of the difference comes from the negative η region. The global average efficiency for data and MC for all the sample and divided into positive and negative muons are listed in Table 6.6, the error encompasses only the statistical ones.

The various terms involving the efficiency calculation were studied individually to find the source of the difference, however, there is not a clear answer to explain it, see Figure 6.16. The larger differences between ϵ_{μ^+} and ϵ_{μ^-} seem to arise from the isolation

	$\mu^{\pm}$	μ^{+}	μ^{-}
Data TP efficiency	0.8548±0.0027	0.8598±0.38	0.8500±0.0036
MC TP efficiency	0.8932±0.0004	0.8925±0.0005	0.8938±0.0005

Table 6.6: Tag and Probe efficiencies for positive and negative muons for data and a sample of $Z \to \mu\mu$ MC.

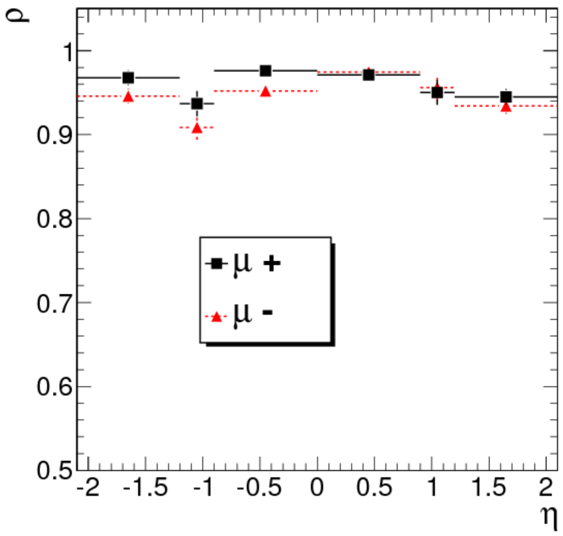

Figure 6.15: Data/Simulation efficiency ratio as a function of η split into negative (triangles, dotted line) and positive charged *probe* muons (squares, solid line).

and reconstruction steps, though this result may be not be conclusive, as most of the differences are consistent once the systematic errors (described later on) are considered.

6.6 Systematic Studies for the Efficiency

In this section a detailed description of the studies carried out to assess the validity of the method and estimate the systematic uncertainty associated to the efficiency is presented. The various checks can be done with MC or with data. The former ones allow to evaluate the absolute effect on the efficiency and whether the result is closer to the MC truth value and the latter let study the relative effect and whether modifying parameters as the p_T binning, mass range, etc. has a sizable effect in the efficiency determination.

The aspects considered can be summarised in several categories: a *closure test* with MC to asses the validity of the method, studies related to the $Z \to \mu\mu$ shape from MC used to model (influence of the PDFs employed for the generation of the MC or muon resolution effects not properly accounted for in the simulation) and dependence on the p_T binning, mass range, chosen function to model the background.

At the end of the section, the most relevant outcome from the different terms studies

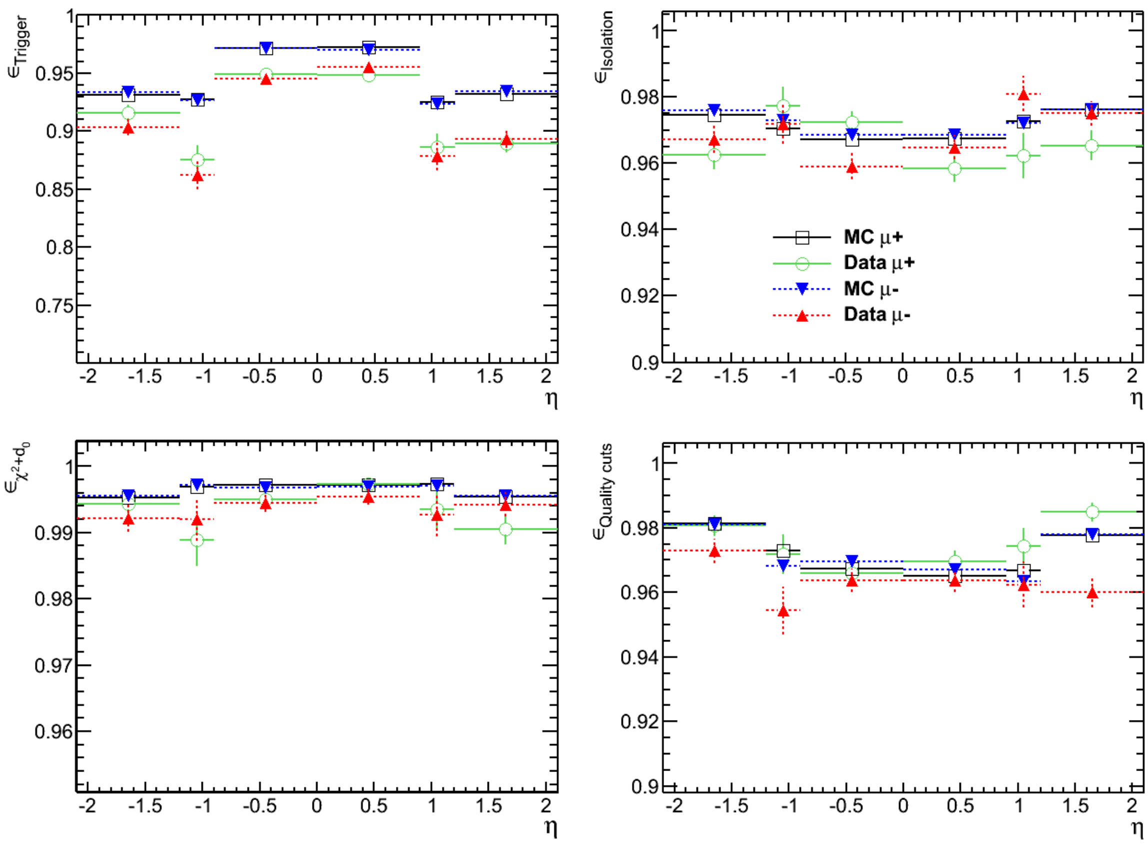

Figure 6.16: Data and simulation efficiency as a function of η split into negative and positive charged *probe* muons. The efficiency is divided into four factors: trigger (top left), isolation (top right), passing d_0 and χ^2 requirements (bottom left) and reconstruction including all track quality requisites (bottom right).

are summarised.

6.6.1 Closure Test: Efficiencies with MC

The same efficiency determination method was applied to a set of high statistics *fake data* (from simulated $Z \rightarrow \mu\mu$ and background samples in the correct proportions) to estimate if the efficiency obtained with the pure $Z \rightarrow \mu\mu$ sample is completely recovered. The samples used are listed in Table 6.2. The efficiency with the *fake data* is lower, being the ratio $\epsilon_{\text{Fakedata}}/\epsilon_{\text{Signal}} = 0.992$. Most of the difference comes from the low p_T region, see Figure 6.17.

6.6.2 Isolated Template for $Z \rightarrow \mu\mu$ Shape

Signal and background events have very different isolation distribution. Then the possibility of using isolation as a discriminating variable to identify background events was considered, in a similar way as it was done with the p_T regions.

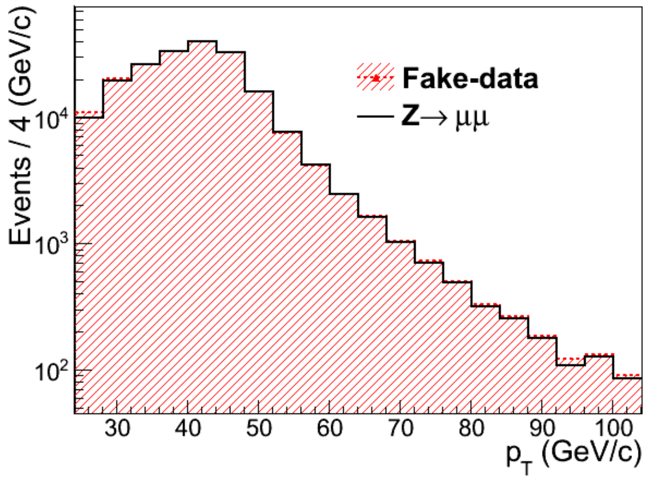

Figure 6.17: *Probe* muon p_T distribution from a high statistics $Z \to \mu\mu$ sample (solid line) and a *fake data* sample ($Z \to \mu\mu$ plus background simulated samples) corrected to account for the background (full histogram).

Two tests were carried out regarding this issue, employing the same MC samples as before:

- The Z peak shape from MC was taken including only muon pairs where the *probe* muon is isolated (relIso ≤ 0.1) instead of all *tag-probe* pairs. A fit with the whole *fake-data*, keeping the two p_T ranges, was performed.
- Two Z templates from MC were employed, one with all isolated *probe* muons and the second with non-isolated muons. Then, two fits to the *fake-data*, separating into isolated and non-isolated cases, were done. Effectively there were four ranges with the two p_T bins.

In both cases the ratio $\epsilon_{\text{Fakedata}}/\epsilon_{Signal}$ is similar, being 0.1% higher than the result of the closure test, described in section 6.6.1. Taking into account the statistics of the 2010 data sample, such a change in the efficiency is covered by the statistical error of the fit (which would be larger if one splits into four regions). Therefore, this was finally not implemented in the method.

6.6.3 Computing the Efficiency for Positive and Negative Muons Independently

One interesting observation of this study is the fact that the efficiency for negative and positive charged muons is slightly different, obtained calculating a single weight function for all muons. In this section, the efficiencies are obtained splitting the sample into positive charged and negative charged *probe* muons and the correction to account for the background is calculated independently. In Figure 6.18 the weight distributions

Efficiency	Fit μ^+	Fit μ^-	Fit for all muons
$\epsilon(\mu^-)$	-	0.8558±0.0039	0.8522±0.0039
$\epsilon(\mu^+)$	0.8657±0.0038	-	0.8670±0.0038

Table 6.7: Single muon efficiency for positive and negative charged muons, obtained with an independent fit and weight for μ^+ and μ^-. The last column correspond to the result when the weight is calculated for all muons. The exercise was carried out with a data sample of 28 pb^{-1}, the errors are only statistical.

are presented, for all muons and for μ^+, μ^- only, for the two p_T regions studied. The distributions are similar for muons with p_T< 35 GeV/c, while the weights are lower for μ^- for higher p_T values and higher for μ^+. The efficiency for $\mu^\pm$ calculated in both ways, with a weight for all muons and with a weight depending on the charge is listed in Table 6.7. In both cases the difference between the efficiency for negative and positive charged muons is well covered by the statistical error. Dividing into μ^- and μ^+ to obtain the weights yields a slightly higher efficiency, ~0.1% averaging to all muons, a difference compatible with the statistical error.

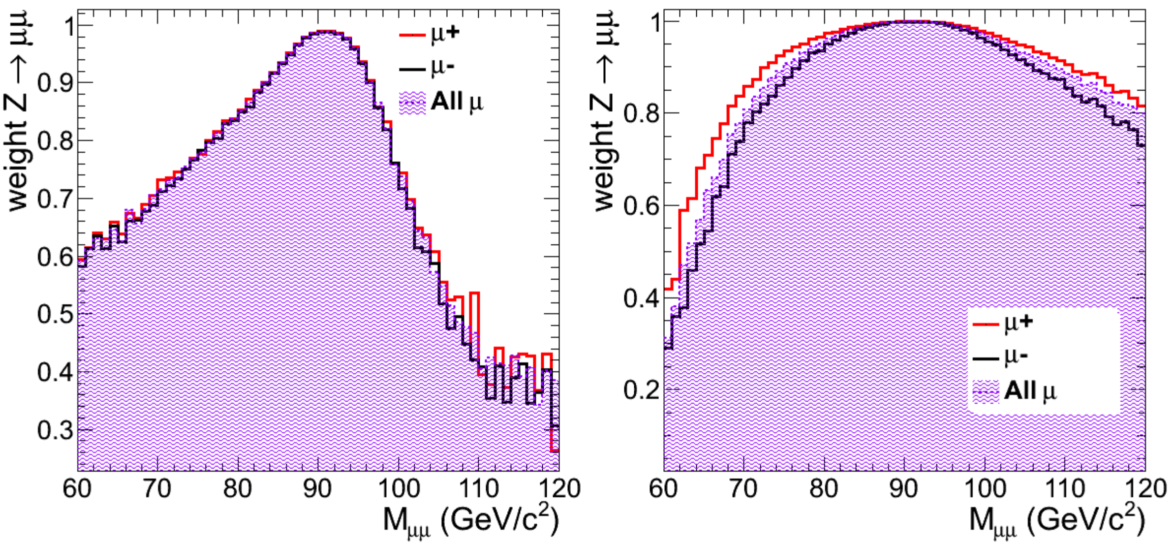

Figure 6.18: Weight distributions as a function of the dimuon invariant mass in the event, obtained with all muons (full histogram) and with μ^+ (red line) and μ^- (black line). Left plot: p_T< 35 GeV/c, right plot: p_T≥ 35 GeV.

6.6.4 Muon Momentum Resolution and Scale

Several methods have been developed within CMS to evaluate with great precision the momentum scale and resolution of the muon. One of them, the SIDRA [56, 42] method compares the data with the full simulation of the Z decay to two muons in the

CMS detector and provides a way to directly modify the simulation to better match the data.

According to the results obtained with this method with the 2010 data, the reconstructed transverse momentum p_T has to be modified to reach an optimal agreement with data as follows, starting from the reconstructed p_T of the muon in the simulation, $p_{T,sim}$:

$$\frac{1}{p_T} = \frac{1}{p_{T,sim}} + \delta_{\kappa_T}(q,\phi,\eta) + \sigma_{\kappa_T}(q,\phi,\eta)\ \mathrm{Gauss}(0,1) \tag{6.6}$$

where δ_{κ_T} and σ_{κ_T} are the parameters controlling the muon momentum scale shifts and the resolution distortions, respectively. Gauss$(0,1)$ denotes a sampling following a Gaussian of zero mean and unit variance. This ansatz is adequate for cases presenting slightly worse resolutions in data than in simulation, and therefore well suited for the present study. It assumes that all remaining corrections with respect to the simulation are due to misalignment, with relative effects that increase with p_T. This is justified by the excellent agreement between data and simulation for low-mass dimuon resonances. The data behaviour, comparing the experimental dimuon mass with MC prediction, suggests angular dependencies of the type:

$$\delta_{\kappa_T}(q,\phi,\eta) = A + B\eta^2 + q\ C\ \sin(\phi-\phi_0) \tag{6.7}$$

$$\sigma_{\kappa_T}(q,\phi,\eta) = A' + B'\eta^2 \tag{6.8}$$

where the parameters are obtained from the fit. The values obtained with the 36 pb^{-1} of collected data are:

$$A = 0.236\ (\mathrm{TeV/c})^{-1} \tag{6.9}$$

$$B = -0.135\ (\mathrm{TeV/c})^{-1} \tag{6.10}$$

$$C = 0.282\ (\mathrm{TeV/c})^{-1} \tag{6.11}$$

$$\phi_0 = 1.337 \tag{6.12}$$

$$A' = 0.0155\ (\mathrm{TeV/c})^{-1} \tag{6.13}$$

$$B' = -0.0055\ (\mathrm{TeV/c})^{-1} \tag{6.14}$$

To determine the effect in the efficiency, the p_T of both muons, *tag* and *probe*, are modified accordingly. Then the *corrected* invariant mass distribution is reconstructed and used as the new template for the signal in the fit, see Figure 6.19. The default invariant mass is shown superimposed to the distribution where the p_T has been modified, the distributions are normalised to the luminosity of data. The mean value of the position of the $M_{\mu\mu}$ peak changes by less than 0.1% and the width around 0.25%, being both of them greatly similar.

Following the same procedure as described, the resulting efficiency compared to the original one is: $\epsilon_{modified}/\epsilon_{original} = 1.001 \pm 0.007$ (only statistical error), the effect is at the per mil level, well covered by the statistical error.

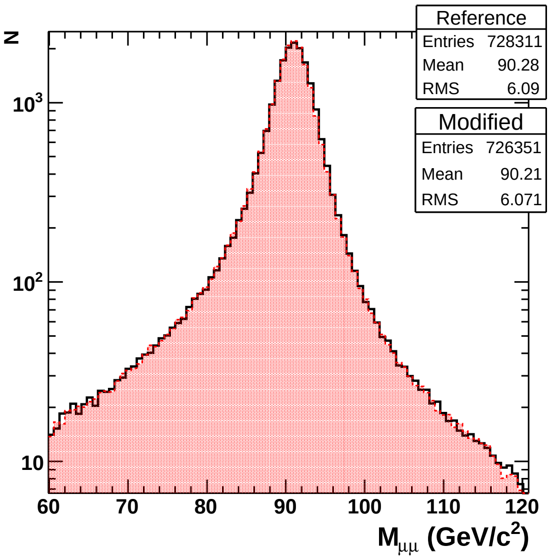

Figure 6.19: Invariant mass distribution of the *tag-probe* muon pairs with a high statistics Monte Carlo sample, normalised to the luminosity of data, the black histogram correspond to the reference simulation and the dashed line full histogram to the optimised one, using the SIDRA results.

6.6.5 Effect of the PDF Chosen to Generate the Z Events

The effect due to the uncertainty on the modelling of the parton distribution functions is expected to be negligible as it enters both in the numerator and the denominator of the efficiency computation. The PDF used for the generation of the Drell-Yan sample employed to derive the template to model the signal was CT10 [57]. The change in efficiency coming from using an alternative set of proton PDF's for the Z MC generation was evaluated.

To obtain the efficiency with another PDF, the procedure is as follows: each event is weighted by the ratio of the default PDF and the central value (or another element of the set) of a different PDF. In particular the comparison here was done with NNPDF [58]. In Figure 6.20 the efficiency calculated with CT10 is compared to the one obtained with every element of the set of NNPDF, resulting in the thin green band. The highest and lowest efficiency values obtained with the NNPDF set differ by less than 0.07%. The central value of the two PDF sets was compared, the absolute variation of the efficiency obtained with the central values among them is as small as $6.8{\cdot}10^{-5}$, this is a 0.008% relative difference.

6.6.6 Dependence on the Function to Model the Background

The function selected to model the background contamination in the *probe* muons was a linear one, the main motivation was to employ the simplest function which described correctly the dimuon invariant mass distribution of the background processes.

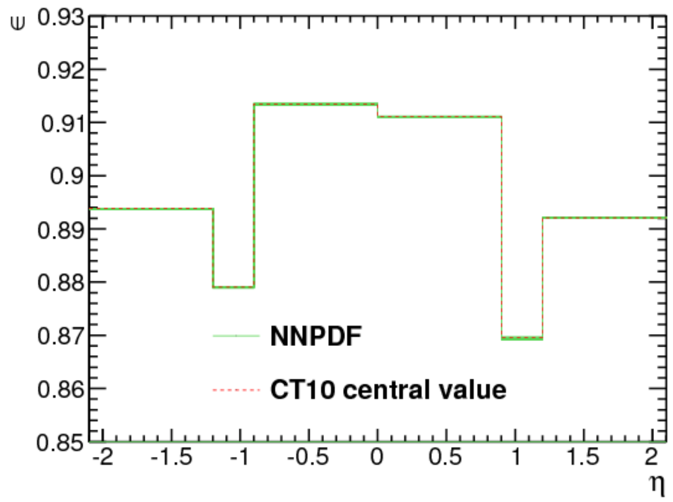

Figure 6.20: Monte Carlo efficiency calculated with the central value of CT10, red dashed histogram, and the set of elements of NNPDF, represented by the green band.

The first check was done using the Monte Carlo simulation: a linear function, a second order polynomial and an exponential function were fitted to the expected background distribution. In all cases the fitting procedure gives similar results in terms of the expected number of background events estimated by each of them. The integral of the first one gives the closest value to the number of muons, though all of them underestimate the background by a small amount, 1.1-1.2%. From the three functions checked the worst results were obtained with the second order polynomial function, whose integral is smaller than the linear one by 0.1%. This would indicate that the selected linear function is indeed the most adequate one.

However, one of the hypothesis of this method is that one does not rely on the Monte Carlo description of the background, then the exercise of comparing the efficiency with another function was carried out in data to probe that what the simulation yields is also valid in data. In particular the exponential function was selected.

The outcome with the two functions checked is:

- Using an exponential function ($e^{a \cdot M_{\mu\mu}+b}$) for both ranges, the efficiency compared to the original one results $\frac{\Delta\epsilon}{\epsilon_{original}} = 7.1 \cdot 10^{-4}$, a 0.05% higher efficiency in absolute terms.

- Using an exponential function for the first p_T bin, where the contribution of background concentrates predominantly at lower values of the invariant mass, and the lineal function for the second bin, $p_T \geq 35$ GeV/c, for which the background falls less deeply with the growing invariant mass, the result is also 0.05% higher than with the linear function.

This result shows the robustness of the method in this regard, allowing to establish a systematic error associated of <0.1%.

6.6.7 Dependence on the p_T Binning

The sample was divided into two p_T regions because the background concentrates mainly at low p_T. The cut was fixed at the p_T value where the tendency changed, see Figure 6.6. The goodness of that choice was checked in two ways, first the p_T value where the cut is set was changed and second, instead of using two p_T bins, the efficiency was calculated using three ranges. The results are:

- Moving the threshold from 35 GeV/c to 32 GeV/c. The latter value was a compromise between varying the cut enough to appreciate the change and keeping reasonable statistics in the first bin. The efficiency varies by $\frac{\Delta\epsilon}{\epsilon_{original}} = 1.06 \cdot 10^{-4}$, being higher in the second case. Again this can be considered negligible taking into account the statistical error (± 0.0027).

- Division into three p_T regions: the first bin was divided into two regions, p_T<30 GeV/c and 30<p_T<35 GeV/c while the second bin was left unchanged, $p_T \geq$ 35 GeV/c. The idea lying behind this binning is to recover better the efficiency in the first bin, where the proportion of background is higher. However, the net result is the opposite, the average efficiency is lower than the obtained with two p_T bins, by the same amount ~0.1%, which is in any case not very significant.

6.6.8 Dependence on the Mass Window

The single muon efficiency was expected to be independent of the invariant mass range, nevertheless, the robustness of the result changing the range was checked. First, the invariant mass range for the fit was set to (50, 120) GeV/c^2 while the efficiency was calculated in the usual range, (60,120) GeV/c^2. The relative difference with the default efficiency is 0.08%.

Secondly, the efficiency was obtained in a more restricted range, 65< $M_{\mu\mu}$ <115 GeV/c^2 while keeping the original range for the fit, 60< $M_{\mu\mu}$ <120 GeV/c^2, in this case there is no remarkable change in the efficiency either, ~0.05% which is five times smaller than the statistical error.

Table 6.8 summarises all the effects analysed and their impact on the final efficiency. The most relevant factor is the error associated to the MC test, which yields an error in the efficiency of 0.8%. The rest of the terms have much lower impact on the final efficiency, being smaller than the statistical error in any case.

6.7 Application to an Analysis: $W \rightarrow \mu\nu$ Cross Section Measurement

In this section the single muon efficiency extraction is applied to the specific case of the $W \rightarrow \mu\nu$ cross section measurement [43]. As a reminder, this calculation covers the

Source of systematic error	Impact on efficiency (%)
Closure test	0.81
Muon momentum scale & resolution	0.1
PDF choice	0.01
Dependence on p_T range	0.1
Dependence on mass window	0.08
Function modelling the BG	0.05
Total (for analysis)	0.82

Table 6.8: Systematic uncertainties and their impact on the efficiency.

efficiency of all the selection steps of the analysis: triggering the muon, reconstructing it in the muon and central silicon detectors, applying the quality selection and the isolation cut.

For analysis purposes, a correction factor defined as the ratio between the efficiency obtained in data and in the Monte Carlo sample with the same method is computed:

$$\rho = \frac{\epsilon_{data}(\text{TnP})}{\epsilon_{MC}(\text{TnP})}$$

This is incorporated to the cross section measurement, as a correction to the MC selection efficiency:

$$\sigma_W \times \text{BR}(W \to \mu\nu) = \frac{N^{obs} - N^{bckg}}{A_W \epsilon_\mu \int Ldt}.$$

where N^{obs} are the observed events, N^{bckg} is the estimated number of background events, A_W is the acceptance and ϵ_μ is the selection efficiency from MC corrected with the ρ factor to account for the difference between the efficiency in data and MC: $\epsilon_\mu = \rho \cdot \epsilon_{MC}$.

The average ratio is $\rho = 0.957 \pm 0.009$, the error includes the statistical and systematics effects, described previously, summed in quadrature. This error is propagated to the error of the $W \to \mu\nu$ cross section measurement and thus considered as one of the final sources of systematical errors of the measurement. In Table 6.9 the global efficiencies and correction factors for all muons and split by charge including the statistical and systematical error are listed.

TP efficiency	$\mu^\pm$	μ^+	μ^-
Data	0.8548±0.0027±0.0074	0.8598±0.0038±0.74	0.8500±0.0036±0.0074
MC	0.8932±0.0004	0.8925±0.0005	0.8938±0.0005
Ratio, ρ_{eff}	0.9570±0.0030±0.0083	0.9633±0.0043±0.0083	0.9509±0.0040±0.0083

Table 6.9: Tag and Probe efficiencies for positive and negative muons for data and a sample of $Z \to \mu\mu$ MC. The last row corresponds to the correction factor between the data and MC efficiencies.

The correction factor as a function of p_T and η is presented in Figure 6.21. It can be taken approximately as a constant up to p_T= 100 GeV/c, and so was done for the analysis. Nonetheless, the efficiency shows a clear dependence as a function of η due to the different regions covered by distinct muon detectors. Therefore the binning was adequated to reproduce the physical effects of the detector, while keeping a reasonable statistical samples to evaluate the efficiency in every bin. For the measurement the correction factor was further split into μ^+ and μ^-, due to the difference observed.

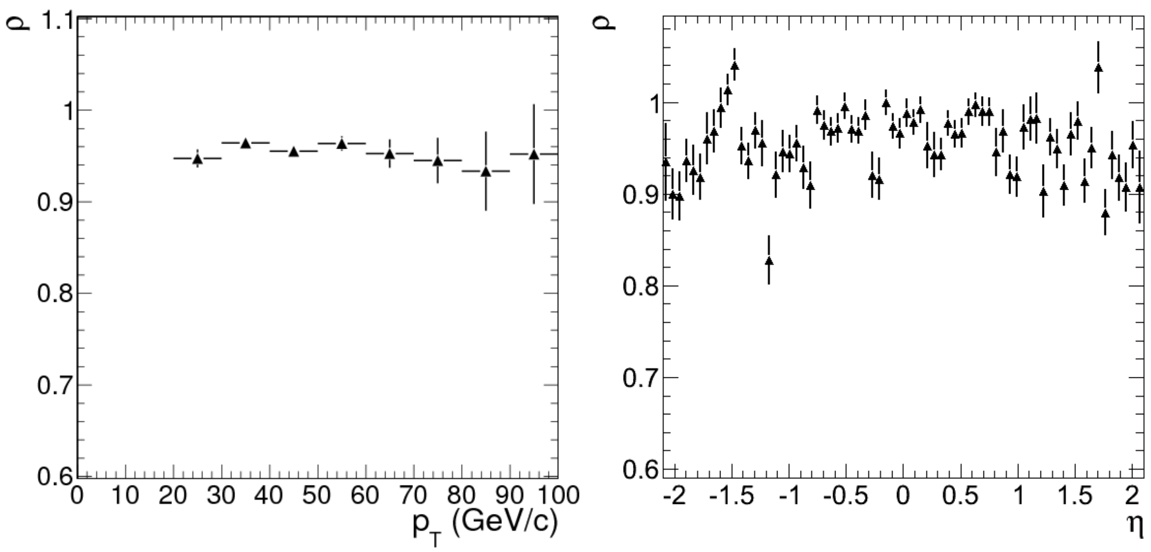

Figure 6.21: Single muon efficiency ratio between data and $Z \to \mu\mu$ Monte Carlo as a function of p_T (left) and η (right).

In order to illustrate the effect of applying the correction factor with the appropriate binning, the distribution for the selected muons in the W analysis obtained with the fine binning, compared to the result using only six bins is shown in Figure 6.22. The chosen six regions correspond to the central region covered by the barrel detector, the overlap region, where muons cross the DT and CSC, and the Endcap further dividing in positive and negative η. It is clear from the excellent agreement between data and simulation that all the needed effects are considered. For the measurement of the total cross section, this agreement in η is not essential, nevertheless, it is fundamental for other analysis such as the extraction of the differential cross section or for charge asymmetry studies.

The η-dependent correction factor has been applied in the analysis and ensures that muons, either coming from Z or W decays, are treated correctly, without requiring any other correction due to the slight difference in muon kinematic distributions of leptons originating from W or Z bosons. Figure 6.23 shows the generated p_T and η distributions of muons coming from Z and W boson decays. Muons originated by Z bosons tend to have higher values of transverse momentum and are produced at slightly higher angles with respect to the beam line (smaller η), than muons from W decays.

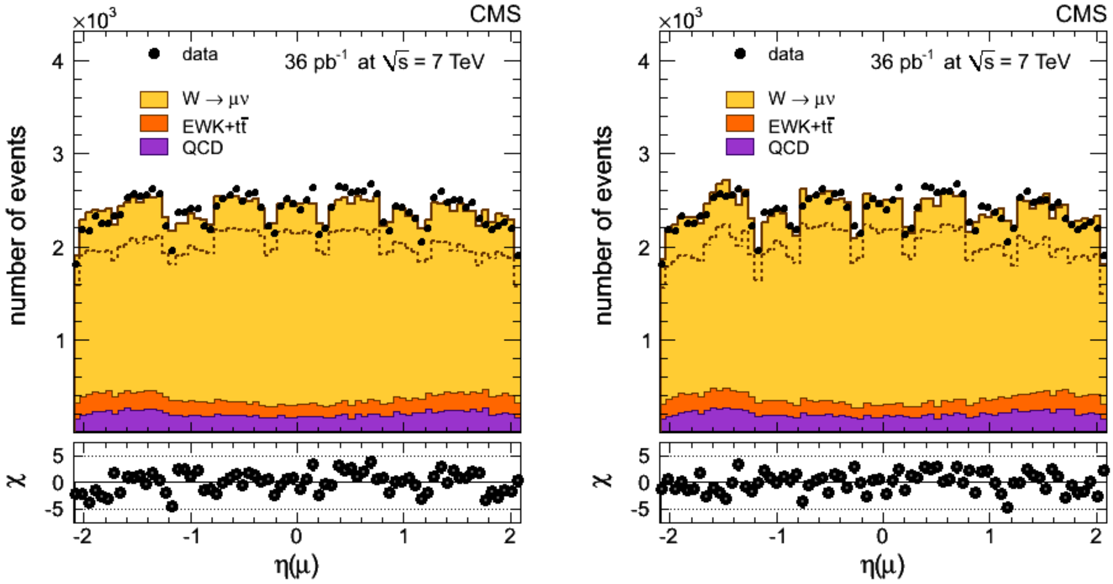

Figure 6.22: η distribution of the muons passing the selection criteria for the W cross-section measurement, for data (dots) compared to the Monte Carlo prediction including the signal and background processes, normalised to the luminosity of the data. $W \to \mu\nu$ simulation is corrected by the efficiency ratio split in 6 η bins (left) and 70 bins (right).

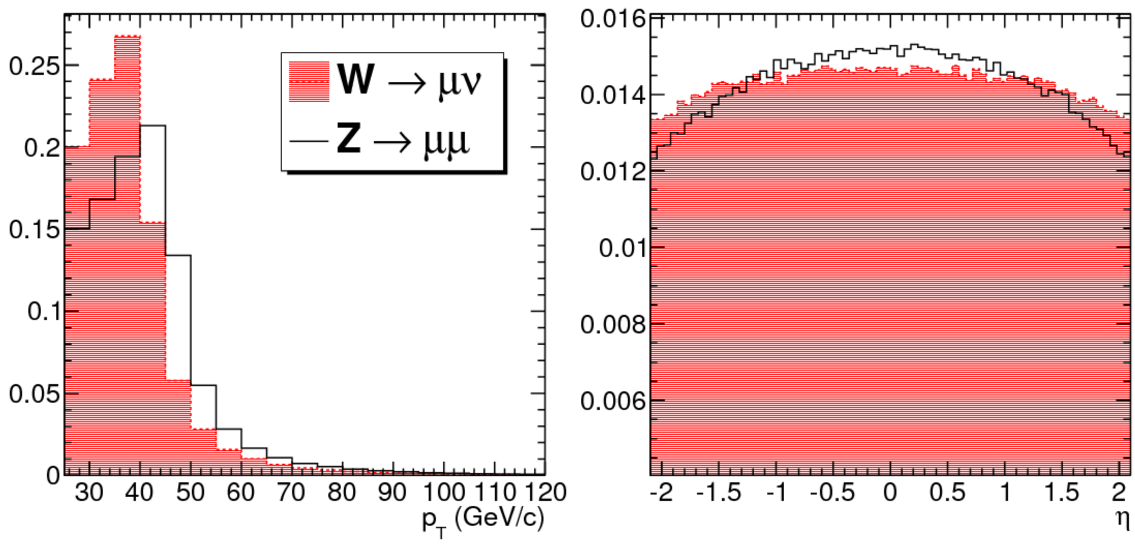

Figure 6.23: Generated muon p_T (left) and η (right) distributions from the processes W$\to \mu\nu$ (solid red histogram) and Z$\to \mu\mu$ (black histogram), normalised to area, in order to compare shapes.

To obtain the average single muon efficiency value determined from Z boson muons and apply it to those muons from W decays, the differences in (η,p_T) need to be taken into account. Hence a reweighting procedure has been devised for the first kind of muons in such a way that they resemble the (η, p_T) distributions of muons from the $W \to \mu\nu$ process. It consists in computing a matrix of weights, where each element is computed as the ratio of the bidimensional (η, p_T) distributions, normalised to unity, of muons from W with respect to those from Z boson. The projections of the weight matrix along either p_T or η axis are presented on Figure 6.24 left and right plot, respectively. The weights are calculated at generator level, with muons in the phase space used through the chapter (p_T> 25. GeV/c and $|\eta| < 2.1$).

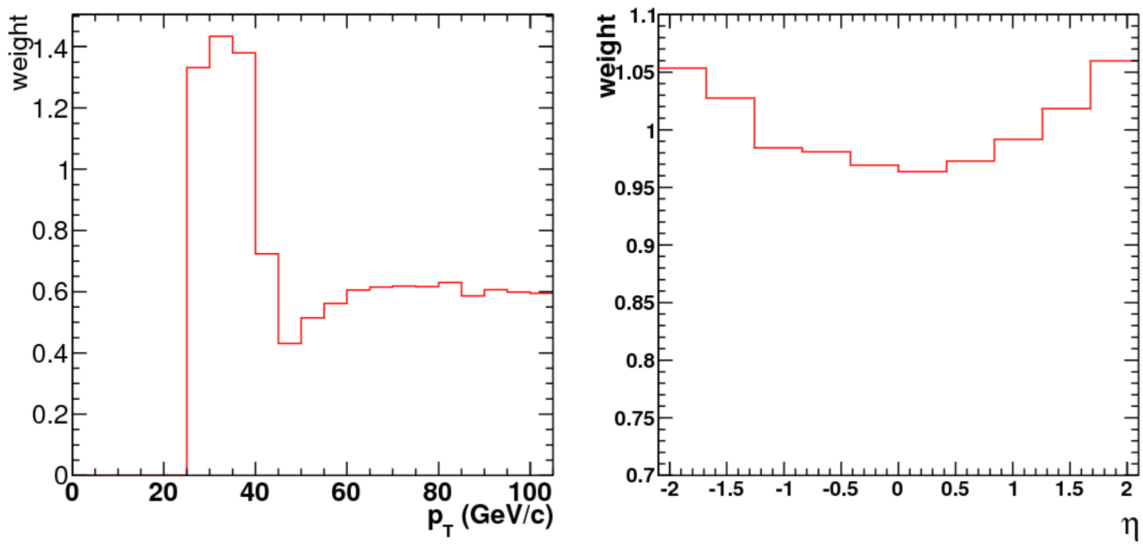

Figure 6.24: Projections of the bidimensional (η, p_T) weight on to the p_T (left) and η (right) axis. The weights are applied to muons from Z decays, to take into account differences in Z and W kinematics.

The weights are applied to all *probe* muons, so the average efficiency results:

$$\epsilon_W = \frac{\sum \rho(p_T, \eta) \cdot \mu_i^{pass}}{\sum \rho(p_T, \eta) \cdot \mu_i}$$

The net effect of the Z→W correction is to decrease the muon efficiency from $\epsilon = 0.8548 \pm 0.0079$ (before reweighting) to $\epsilon = 0.8484 \pm 0.0079$ (after reweighting), that is a 0.6% decrease. As stated before, for the $W \to \mu\nu$ cross section measurement [59] the selection efficiency was employed binned in η, therefore this correction is only needed to obtain the global value for W decay muons.

6.8 Conclusions

A Tag and Probe method to measure single muon efficiency has been developed and applied to extract the efficiency on a $Z \to \mu\mu$ sample for a luminosity $\mathcal{L}_{\text{int}} \sim$36

pb^{-1} corresponding to the certificated data in 2010. The contribution of background processes to the preselected $Z \to \mu\mu$ sample is considered in order to obtain an unbiased efficiency. In practice, this means that muons are reweighted by the probability of coming from a signal event, which depends on the dimuon invariant mass and also on the muon momentum range considered, as most of the background concentrates at low transverse momenta values, $p_T < 35$ GeV/c. This efficiency is factorised in two terms, one involving tracking in the central Si-tracker and the other comprising muon triggering, reconstruction, selection with certain quality criteria and isolation. The efficiency was studied as a function of the muon kinematic variables p_T and η, showing a constant behaviour with muon p_T in the range 30 GeV/c$< p_T <$ 100 GeV/c, where the muon statistics is significant. As a function of η, the efficiency decreases in the transition region between the Barrel and the EndCap domains, moreover it shows variations along the whole η range due to real effects of the detector. Another important feature is the difference in efficiency found between positive and negative charged muons.

The method was developed in the context of the electroweak processes due to the affinity of muons from W and the expected W' decays, to obtain the efficiencies for the optimal muon reconstruction and selection criteria defined in 2010. Finally the result of the efficiency calculation was applied to the $W \to \mu\nu$ cross section measurement, illustrated in this chapter (for the W' analysis it will be described later on), as a correction factor between the MC efficiency and the efficiency measured in data.

Chapter

7

W′ Searches

In this chapter and the following ones the $W' \to \mu\nu$ analysis is detailed. The search for the W' signal is accomplished comparing the data with simulated events from the expected signal process and the background processes, that contribute to the inclusive final state, to determine whether the distributions are compatible with the background only hypothesis or with the presence of a W' of a given mass. The latter would be reflected in an excess of events at high transverse mass values.

The background sources are due to the Standard Model processes and cosmic muons. The event selection is optimised taking into account the characteristics of the potential signal events. An excellent understanding of the data, which translates into a good description with the MC samples, is fundamental to distinguish a hint of new physics from background processes. After the selection and with that purpose the simulation will be corrected, if necessary, to account for possible effects seen in data not included in the MC prediction.

The cosmic muon contamination, which is not described by MC, has to be evaluated independently. These steps of the analysis are reviewed in Chapter 8. Also a careful evaluation of the systematic uncertainty associated to the final numbers of background and signal events is presented. Afterwards, the comparison can be carried out to extract the final result, which is presented in Chapter 9.

Here, a brief motivation for this particular search is presented. Later in the chapter the data and simulation samples used in the analysis are described, focusing on the W' signature, and a description of the analysis objects is reported.

7.1 New Charged Gauge Bosons beyond the SM

The Standard Model, as outlined in Chapter 2, agrees well with the current experimental data. However, there are several unsolved questions and problems that indicate that the SM is not the ultimate theory. Therefore, extensions have to be constructed so that the Standard Model is contained as an effective low-energy theory. Beyond the Standard Model (BSM) theories often involve the existence of new particles which must be heavy and/or weakly interacting as they have not yet been observed. The experimental search for these new particles will allow to confirm or rule out a theory. One of them would be the heavy bosons, charged (W') or neutral (Z'), are predicted.

W' gauge bosons are attractive candidates for an early discovery at the LHC, as a W' with a TeV scale mass can easily be produced via an s-channel resonance from quark anti-quark initial state at the LHC. Generically, W' bosons have significant branching fractions to leptons, and these decay modes lead to a clean signature in the final state.

7.1.1 Left-Right Symmetric Models

Beside the theories predicting an additional charged bosons with W' -behaviour such as Kaluza-Klein excitations in models with extra dimensions [60] or Technicolor [61], the most common theories of new physics with W' bosons are the extensions of the SM with enlarged gauge groups.

The left-right (LR) symmetric extensions [62, 63, 64, 65], are among the most popular models. This kind of models naturally explains the parity violation seen in weak interactions as a result of spontaneously broken parity. In the LR models, an enlarged $SU(2)_L \times SU(2)_R \times U(1)_{B-L}$ (where B and L correspond to baryon and lepton numbers) replaces the SM $SU(2)_L \times U(1)$ symmetry. The Standard Model fermions with left-handed helicity couple to W transforming as doublets under $SU(2)_L$, as described in the SM, and the right-handed ones transforming as doublets under $SU(2)_R$. In the same way as in the SM the gauge group $SU(2)_L$ is associated to the $W^{\pm}$ and Z, $SU(2)_R$ in the LR symmetric models is also associated with the new gauge bosons $W_R^{\pm}$ and Z'. In this model the W' couples primarily to the right-handed fermions, its coupling to left-handed fermions arises solely due to $W - W'$ mixing.

The lagrangian is required to be invariant under the discrete symmetry operation $R \longleftrightarrow L$, the interchange between left- and right-handed fields. In the models known as *manifest and pseudo-manifest* Left-Right symmetric models the symmetry is exact. Thus the gauge couplings g_L and g_R corresponding to the $SU(2)_L$ and $SU(2)_R$ gauge group respectively are predicted to be both equal to the usual weak gauge coupling, g. Furthermore, the *manifest LR symmetric model* assumes that the right-handed Cabibbo-Kobayashi-Maskawa (CKM) matrix is identical to the SM one. The CKM is a unitary matrix which contains information on the strength of flavour-changing weak decays. There are other models with no exact LR symmetry for which the previous conditions are not required.

The LR symmetry is broken spontaneously in a similar way as the Higgs mechanism in the standard electroweak theory, although the Higgs content in the former is more complex, containing charged Higgs bosons. First, the symmetry is broken down to the symmetry of the SM, which gives mass to the W_R and Z_R. The subsequent stage of the symmetry breaking at a lower energy scale (the known SM one) gives mass to the W_L and Z_L bosons which are equivalent to the standard model W and Z bosons. The fact that parity is violated in electroweak interactions at the energies probed so far, implies that the RH bosons must be much heavier than their LH partners, this justifies the assumption that the mixing is negligible due to the large mass difference.

The hypercharge is modified so that the quantum number is identical for left and right handed particles. The charge formula of the SM, $Q = I_3 + \frac{Y}{2}$, is replaced by $Q = I_3^L + I_3^R + \frac{Y}{2}$, where the weak hypercharge chosen to give the correct charge to all particles is changed by the baryon and lepton number difference. I_3^L and I_3^R are the weak isospin components of the fields.

A further interesting feature of the LR symmetric models is that they provide small masses to the standard neutrinos because they incorporate the seesaw mechanism, for which there is no explanation in the SM. In the LR models, the breaking of the left-right symmetry gives a large Majorana[1] mass to the right-handed neutrinos. The breaking of $SU(2)_L \times U(1)_Y$ symmetry relates the masses of the LH and RH neutrinos in such a way that the LH neutrino gets a light mass.

7.1.2 The W' Reference Model

Due to the variety of models, experimental searches usually consider a more general approach, known as the *Reference Model* [66]. This is not an actual 'Beyond the SM' model, but rather a benchmark model to evaluate the discovery potential. In this model the new gauge boson W' is a heavier version of the SM W boson. The couplings of the W' boson to quarks and leptons are identical to the Standard Model ones. In principle, the new decay channel $W' \to WZ$ would be dominant for high masses ($M_{W'} > 2M_Z$), however in the LR symmetric models this is suppressed by a mixing angle, while in the Reference Model this suppression is introduced by hand. Then, the W' boson does not interact with other bosons (or the hypothetical Z').

With these basic prerequisites, the production cross section of the potential W' signal and its branching ratio can be calculated as it is done for the SM particles. First, the production cross section in *pp* collisions is briefly discussed.

At the LHC, the colliding particles are not elementary, protons consist of three valence quarks and additional quark-antiquark pairs (sea quarks) and gluons. Then the interaction between two colliding protons is really an interaction between their constituent partons.

In the case of the W' boson, the production mechanism, at leading order, with no gluon emission, is a quark-antiquark annihilation as shown in Figure 7.1, in the same

[1] A Majorana nature indicates that the particle is its own antiparticle.

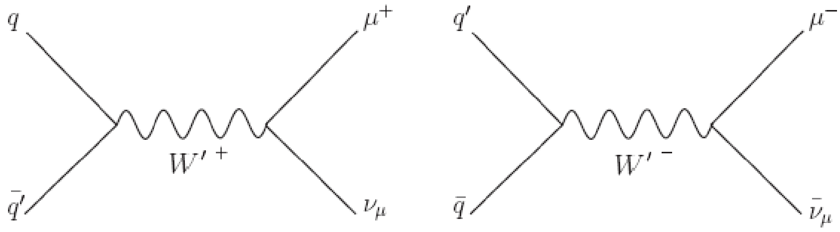

Figure 7.1: Feynman diagram for the W' production at leading order in pp collisions and decay into a muon and a neutrino.

way as the SM bosons are produced. Charge conservation requires an up-type and a down-type quark to interact. The two partons (valence quarks, sea quarks, gluons) that enter the hard interaction do not carry the total beam momentum, but only the fractions x_1 and x_2 respectively of the proton momentum. Formally, this fraction of the momentum carried by a given parton is expressed as a probability distribution, called a parton distribution function, PDF [7]. Note that the probability functions $f(x, Q^2)$ depend on the momentum transfer between the particles, Q. The squared invariant mass of the two partons is defined as $\hat{s} = \sqrt{Q^2} = x_1 \cdot x_2 \cdot s$, where $\sqrt{s}$ is the centre of mass energy of the colliding particles.

The production cross section of any particle at a hadron collider can be determined in general from the convolution of the hard scattering cross section of the intervening partons a and b, $\hat{\sigma}_{ab\to X}$, and the PDFs of the hadron, $f_a(x_1, Q^2)$ and $f_b(x_2, Q^2)$ at a given energy scale, summed over all possible initial partonic states, for momentum fractions x_1 and x_2 and momentum transfer Q^2.

The production cross section of a hypothetical W' could be written as

$$\sigma(pp \to W' + X) = \sum_{a,b} \int\int dx_1 dx_2 f_a(x_1, Q^2) f_b(x_2, Q^2) \hat{\sigma}_{ab\to W'+X} \tag{7.1}$$

The cross section for the parton interaction, $\hat{\sigma}$, is obtained applying the Feynman rules:

$$\hat{\sigma}(q_i\bar{q}_j \to W') = \frac{\pi |V_{ij}|^2}{4} g^2 \delta(\hat{s} - M_{W'}^2) \tag{7.2}$$

where g is the coupling constant, $\hat{s}$ is the centre of mass of the partonic system and V_{ij} represents the CKM matrix element. One can see that the difference between the W and W' production comes from the propagator, which depends on the boson mass. The coupling constant and the Fermi constant are related as follows:

$$\frac{G_F}{\sqrt{2}} = \frac{g^2}{8M_W^2} \tag{7.3}$$

The total cross section for the scattering process $\sigma(pp \to W' + X \to \mu\nu + X)$ can be determined by the multiplication of the production one by the corresponding branching fraction

$$\sigma(pp \to W' + X \to \mu\nu + X) = \sigma(pp \to W' + X) \times BR(W' \to \mu\nu) \quad (7.4)$$

$$BR(W' \to \mu\nu) = \frac{\Gamma(W' \to \mu\nu)}{\Gamma_{W'}} \quad (7.5)$$

The partial width into fermion pairs is

$$\Gamma(W' \to f_i\bar{f}_j) = \frac{N_C G_F M_W^2 M_{W'}}{6\pi\sqrt{2}} \quad \text{with} \quad \mathrm{N_C} = \begin{cases} 3 \cdot |V_{ij}| & \text{for quarks} \\ 1 & \text{for leptons} \end{cases} \quad (7.6)$$

where N_C is the color factor and $|V_{ij}|$ represent the quark mixing (CKM) matrix elements. The previous equation can be expressed as a function of the W boson partial width,

$$\Gamma(W' \to f_i\bar{f}_j) = \Gamma(W \to f_i\bar{f}_j)\frac{M_{W'}}{M_W} \quad (7.7)$$

The decay channel into the third quark family, $W' \to tb$, opens for masses beyond the kinematic threshold which is approximately $m_t + m_b \approx 180$ GeV/c^2, well below the W' masses already excluded. Hence $\mathrm{N}_C \simeq 12$ (for lower masses would be $\mathrm{N}_C \simeq 9$) and the total width of the heavy gauge boson is approximately given by

$$\Gamma(W') = \frac{4}{3} \cdot \Gamma(W)\frac{M_{W'}}{M_W}. \quad (7.8)$$

The width increases linearly with the mass of the heavy boson. The branching fraction to the muon channel, taking into account the decay to quarks and leptons and that there are three families, corresponds to 1/12=0.0833. Finally, including the W' decay in the calculation, the cross section results:

$$\hat{\sigma}(q_i\bar{q}_j \to W' + X \to \mu\nu) = \frac{V_{ij}^2}{3\pi}\left(\frac{G_F M_W^2}{\sqrt{2}}\right)^2 \frac{\hat{s}}{(\hat{s} - M_{W'}^2)^2 + (\Gamma_{W'} M_{W'})^2} \quad (7.9)$$

Here, the δ-distribution is replaced by the relativistic Breit-Wigner function which takes into account the finite lifetime of the intermediate gauge boson. The convolution with the Breit-Wigner shape has various effects: the overall resonance is asymmetric, the low mass tail is enhanced, a long tail appears, and the high-mass one is suppressed, as it is later presented on in this chapter, see Figure 7.3.

The previous equations hold not only for left-handed, but also for right-handed charged currents. So if right-handed neutrinos from boson decays are light ($m_\nu << M_{W'}$) and stable, the results presented here can be reinterpreted in the generic model since the kinematics of the left- and right-handed W' bosons do not differ. In other words, the W' bosons in the Reference Model sense can be either left- or right-handed.

Summarising, the analysis presented in this thesis is based on the Reference Model, which can be seen as an extension of the *manifest* LR symmetric Model, with light right handed neutrinos. The production of a W' and subsequent decay into a muon and a light, non-detectable neutrino is searched for. This channel provides a clean final state containing a highly energetic muon. Experimentally, the muon is triggered and well reconstructed by CMS, as the necessary tools are in place and validated.

7.1.3 Experimental Constraints on the W' Mass

The W' boson has been previously searched for in high energy physics experiments using final state signatures such as leptons, jets, and/or missing energy. The most stringent constraints to the W' boson existence, previous to the searches at the LHC, were the limits established by the Tevatron experiments, D0 and CDF, which excluded W' with masses below 1.0 TeV/c^2 [67] and 1.1 TeV/c^2 [68], respectively, with the direct search for the boson in the electronic channel. The CDF experiment previously set limits on the cross section times branching fraction in the decay mode $W' \to tb$ and excluded a W' boson with a mass below 800 GeV/c^2 [69]. These mass limits assume as well that the couplings between the new vector boson and the fermionic final states are the same as in the Standard Model.

The properties of the W' bosons are also constrained by measurements of processes at energies much below the $M_{W'}$ mass, for instance studying the kaon sector: if the W' couplings to quarks are not suppressed, the box diagrams involving W and W' would contribute to neutral meson $K_L - K_S$ mixing. Also if right-handed neutrinos have Majorana masses, then the tree level contributions to neutrinoless double-beta decays, and a limit on $M_{W'}$ as a function of the neutrino mass can be derived [70, 71].

7.2 Collision and Monte Carlo Data

The search for the W' signal, as aforementioned, is based on the comparison between the relevant experimental distributions from the data and the ones from the expected signal and the known Standard Model processes (background events), that contribute to the inclusive final state. This section presents the data set used, already described in previous chapters, along with the Monte Carlo samples, to describe the signal and the background events.

7.2.1 The 2010 Data Set

This analysis is performed, recalling from the previous chapter, with the whole proton-proton collision data at 7 TeV centre of mass energy of the LHC certified as *good* by CMS, amounting to an integrated luminosity of 36 pb^{-1} (Run2010A and Run2010B data).

7.2.2 Simulation of Monte Carlo Samples

Here the discussion of the Standard Model backgrounds simulated to reproduce the data is presented together with the description of the simulated signal samples, focusing on the characteristics of the signal events.

Simulation of Background Events

The Monte Carlo (MC) simulated samples are used in this analysis to evaluate signal and background efficiencies, when they cannot be extracted directly from data, and to validate the analysis techniques deployed.

The main sources of background contributing to the inclusive final state are the Standard Model W-boson, with the decay channels $W \to \mu\nu$ and $W \to \tau\nu$, multi-jets events (referred to hereafter as QCD), $t\bar{t}$, Drell-Yan ($Z \to \mu\mu$ and $Z \to \tau\tau$) and diboson processes with muons in the final state. Due to the close affinity to the signal process and the high cross section the irreducible background from $W \to \mu\nu$ is the most significant one. Besides those processes where the missing transverse energy is produced by one or more neutrinos, there is another source of instrumental background if for instance one muon from a $Z \to \mu\mu$ is lost or misreconstructed. This kind of background is also irreducible as a consequence of its similarity to signal events.

The background simulated samples considered as a reference set for this analysis, used for all computations and plots, are listed in Table 7.1. The reference samples of electroweak processes for $W \to \mu\nu$ and $Z \to \mu\mu$ used for the analysis are produced with POWHEG [48, 49, 50] interfaced with PYTHIA [47]. For $W \to \tau\nu$ and $Z \to \tau\tau$ only PYTHIA samples have been considered. QCD events with a muon in the final state are also simulated with PYTHIA. This inclusive muon sample includes decays-in-flight, but no punch-through. For $t\bar{t}$ events a Madgraph [72] sample combined with PYTHIA for showering and hadronization is taken by default.

The NNLO (NLO for $t\bar{t}$) cross sections [73] are reported in the table. They are used for normalisation in plots and computations.

Generator	Process	Kinematic cuts	σ_{NNLO} (pb)	# of events	PDF set
Samples used as reference					
`POWHEG`	$W^+ \to \mu^+\nu_\mu$	no cuts	6152	∼2M	CT10
`POWHEG`	$W^- \to \mu^-\nu_\mu$	no cuts	4286	∼2M	CT10
`PYTHIA`	$W \to \tau\nu_\tau$	no cuts	10438	∼5M	CTEQ6L
`POWHEG`	$Z \to \mu\mu$	$m_{\mu\mu} > 20$ GeV/c^2	1666	∼2M	CT10
`PYTHIA`	$Z \to \tau\tau$	$m_{\tau\tau} > 20$ GeV/c^2	1666	∼2M	CTEQ6L
`Madgraph`	$t\bar{t}$	no cuts	157.5 (NLO)	∼1M	CTEQ6L
`PYTHIA`	Inclusive μ QCD	$\hat{p}_T > 20$ GeV/c, $p_T^\mu > 15$ GeV/c, $\lvert\eta_\mu\rvert < 2.5$	84679 (LO)	∼30M	CTEQ6L
`PYTHIA`	WW	no cuts	43	100k	CTEQ6L
`PYTHIA`	WZ	no cuts	18	100k	CTEQ6L
`PYTHIA`	ZZ	no cuts	5.9	100k	CTEQ6L

Table 7.1: Summary of analysed Monte Carlo samples for various background processes. The information listed comprises the generator employed, the cuts applied at generator level, the NNLO cross section (except for the $t\bar{t}$ and the QCD sample for which the NLO cross-section and the LO respectively are given), the number of events generated and the PDF set.

Simulation of signal events: W'

Signal samples for W' decaying into a muon and a neutrino for the range of W' masses between $M_{W'}$ = 600 GeV/c^2 to $M_{W'}$ = 1500 GeV/c^2 were generated[2] in steps of 100 GeV/c^2 along with a sample of heavier W' boson with $M_{W'} = 2$ TeV/c^2. A total of 11000 events per mass point was generated with the full simulation chain using the PYTHIA 6.4.9 generator, based on a leading order approach. The specific parameters to generate the W' samples are listed in Table 7.2.

Pythia Parameter	Meaning
MSUB(142)	Switch W' production
PMAS(34,1)	W' mass
PMAS(34,2)	W' width
MDME(328,1)	decay into $\mu\nu$

Table 7.2: Parameters to generate W' with PYTHIA event generator

The parameters in PYTHIA are set according to the Reference Model discussed previously with the following assumptions:

1. The new charged gauge boson W' couples to fermions in the same way as the W boson does, with the same coupling constants
2. The total width $\Gamma_{W'}$ scales with its mass, being proportional to $\Gamma_W \cdot \frac{M_W'}{M_W}$.
3. The decay channel $W' \to$WZ is suppressed

A summary of the considered signal samples is given in Table 7.3. The LO cross section times branching fraction, $\sigma \times BR(W' \to \mu\nu)$, varies from 6.3 pb for a relatively light W' boson of mass $M_{W'}$ = 600 GeV/c^2 up to 11.5 fb for the heaviest investigated mass of 2 TeV/c^2. Figure 7.2 shows the behaviour of the cross section, falling steeply with the mass of the W' boson. The green band in the figure corresponds to the uncertainty due to the PDF set ($\sim$10%).

Signal samples were generated in LO, but next-to-next-to-leading order corrections on the PYTHIA cross section, known as k-factors, have been applied:

$$k_{NNLO} = \frac{\sigma_{NNLO}}{\sigma_{LO}}$$

They are roughly mass independent, varying from k=1.32 for the lowest mass point considered $M_{W'}$= 600 GeV/c^2 to k=1.26 for $M_{W'}$= 2 TeV/c^2 [74, 75]. They are derived for the process pp$\to V + X$, where V corresponds to a vector boson. For the event counts and the limit calculation the exact k-factors for every W' mass point are used. In Table 7.3 the NNLO cross sections, obtained by multiplying the LO cross-section by the k-factors, are given.

[2] Although Tevatron already excluded the existence of W' bosons with masses below 1 TeV at the time this analysis started, samples of lighter W' bosons were simulated in case a lower exclusion limit was obtained with the LHC data.

Generator	$m_{W'}$ (GeV/c^2)	σ_{LO} (pb)	σ_{NNLO} (pb)	$\Gamma_{W'}$ (GeV/c^2)
PYTHIA	600	6.28	8.29	20.8
PYTHIA	700	3.23	4.26	24.3
PYTHIA	800	1.84	2.43	27.8
PYTHIA	900	1.06	1.39	31.2
PYTHIA	1000	0.64	0.838	34.7
PYTHIA	1100	0.397	0.516	38.3
PYTHIA	1200	0.257	0.334	41.6
PYTHIA	1300	0.167	0.215	45.1
PYTHIA	1400	0.106	0.136	48.5
PYTHIA	1500	0.077	0.0986	52.0
PYTHIA	2000	0.0115	0.0145	69.4

Table 7.3: Summary of signal Monte Carlo samples. The NNLO cross sections for the various W' mass points are calculated with a mass-dependent k-factor ranging from 1.32 (for $M_{W'}$=600 GeV/c^2) to 1.26 (for $M_{W'}$=2 TeV/c^2). The PDF set used is CTEQ6L.

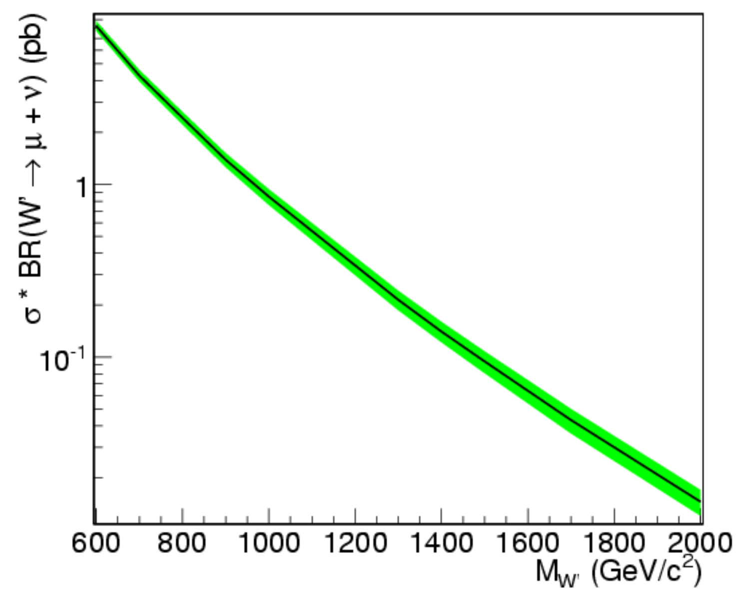

Figure 7.2: Signal cross-section as a function of the W' mass, including the NNLO corrections, the green band corresponds to the uncertainty due to the PDFs.

Figure 7.3 left shows the generated W' mass distribution for three mass points. The asymmetry of the resonance peak is clearly visible, arising from the Breit-Wigner shape in equation 7.9, the low mass tail is enhanced and the high-mass one is suppressed. The invariant mass distribution is not accessible in the measurement due to the unknown momentum of the neutrino in the z-direction, so only the transverse mass (M_T) can be measured, calculated from the muon and the neutrino transverse energies:

$$M_T = \sqrt{2 \cdot E_T^{\mu} \cdot E_T^{\nu} \cdot (1 - \cos\Delta\phi_{\mu,\nu})}$$

where E_T^{μ} is the observed transverse energy of the muon, E_T^{ν} is the transverse energy of the neutrino escaping undetected, observed as missing transverse energy, and $\Delta\phi_{\mu,\nu}$ is the opening azimuthal angle between both leptons. The corresponding distributions, showing a Jacobian peak shape, are shown in figure 7.3, right. These distributions and the next ones in this chapter are obtained at generator level, before being processed through the detector simulation.

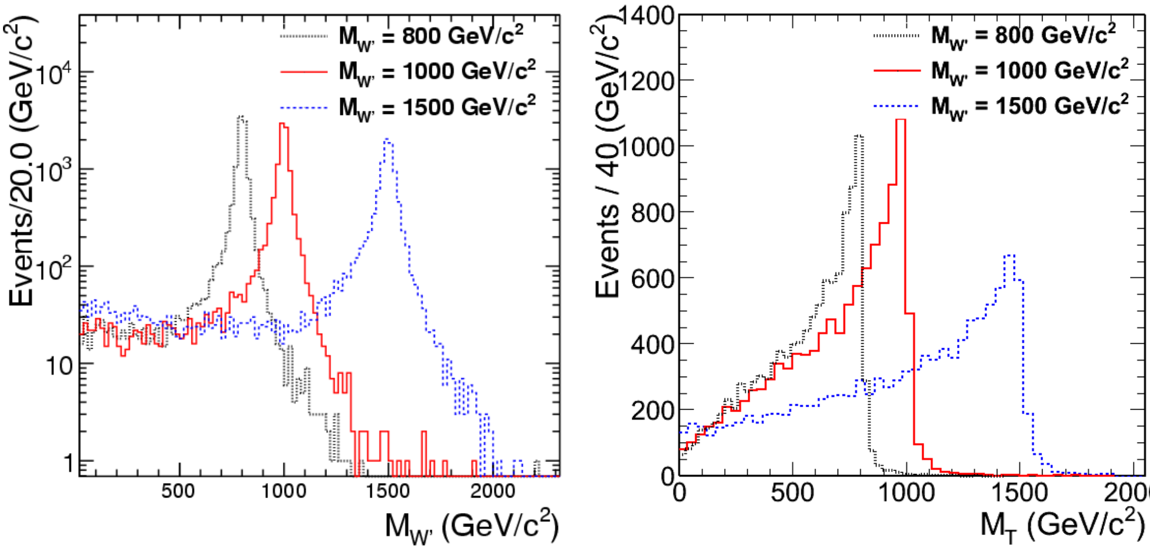

Figure 7.3: Mass (left) and transverse mass (right) distributions of the generated W' bosons for three mass points, 800 GeV/c^2 (dotted black line), 1000 GeV/c^2 (solid red line) and 1500 GeV/c^2 (dashed blue line). Each simulated sample contains 11000 generated events.

The muon transverse momentum and pseudorapidity variables are presented for the same values of W' masses in Figure 7.4. The p_T distributions show a clear peak at about M$_{W'}$/2, which would be experimentally observed smeared, the reason being detector resolution effects. Muons have energies well above ∼100 GeV and they tend to be produced centrally, according to the Figure 7.4 right. For the highest W' mass point displayed, around 95% of the muons are in the region $|\eta| < 2.1$ at generated level. The proportion is smaller for lower masses, but above 90% for the range of W' masses considered.

As illustrated in Figure 7.5, the muon and the neutrino (experimentally measured as the missing transverse energy, E_T^{miss}) are well balanced in the transverse plane, they are back-to-back, expected given the two body decay and that the W' transverse momentum, like the W boson one, tends to low values, peaking its distribution at few GeV/c. This means that the azimuthal angle between them is close to π (left plot). Also the energy carried by each of the leptons is well balanced. Then, the ratio

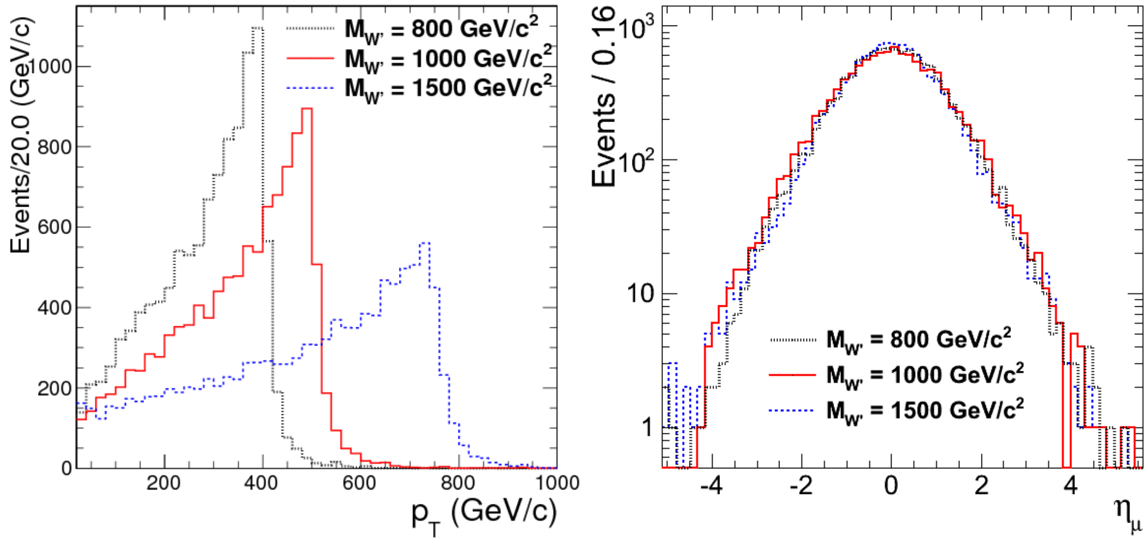

Figure 7.4: Transverse momentum (left) and pseudorapidity (right) distributions of muons from the decay of W' bosons, for three mass points, 800 GeV/c^2 (dotted black line), 1000 GeV/c^2 (solid red line) and 1500 GeV/c^2 (dashed blue line). Each distribution is obtained with 11000 generated events.

between their transverse energy (or momentum as their masses are negligible) shows a pronounced peak around 1 (right plot). These distributions are similar for all the W' mass points.

Based on the properties of the signal (high p_T muon, kinematic distributions, etc.) the selection procedure to reject efficiently the Standard Model background processes while keeping a high signal efficiency is described in the next chapter. Prior to this, the fundamental elements of the analysis, muons and neutrinos, will be further described.

7.3 Object Definitions

The CMS detector is built as described in Chapter 3 with an *onion-like* structure with different types of detectors optimised for the identification and the measurement of energy/momentum of the various particles: electrons, muons, taus, photons, quarks, gluons and neutrinos. The first two generations of leptons, electrons and muons, as well as photons are identified directly, while quarks and gluons are not observed directly, but they can be identified as jets after fragmentation and hadronisation, except for the top quark. The neutrino, as a very weakly interacting particle, escapes detection, but it can be inferred from the missing energy in the transverse plane with respect to the proton beams. Unstable objects as t quarks, τ leptons, W and Z bosons can be identified through known decay channels involving the objects listed above. In order to detect such complex events, sophisticated object reconstruction algorithms with both high efficiency and background rejection power are developed. Since this analysis relies only on the efficient reconstruction of high transverse momentum muons and neutrinos

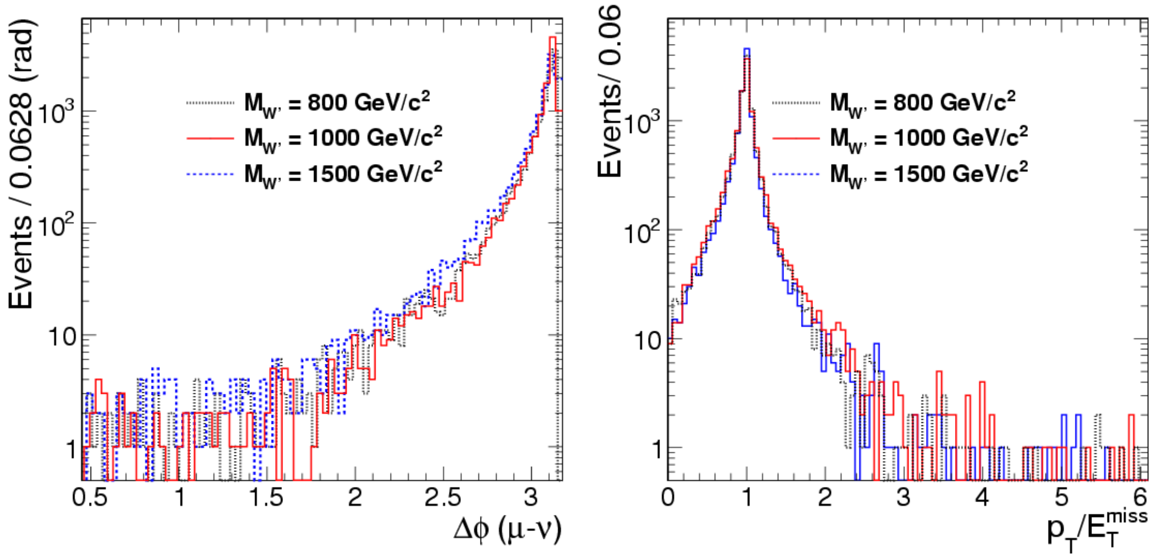

Figure 7.5: Difference in azimuthal angle, $\Delta\phi$, between the muon and the neutrino in the event (left) and ratio of the transverse momentum (right) of both leptons.

(missing transverse energy), the focus is set on their description in this chapter. The identification of taus, electrons and heavy quarks not discussed here, can be found elsewhere [76].

The W' search is performed using the transverse mass spectrum, M_T of the muon-E_T^{miss} system, profiting from the good understanding of the E_T^{miss} with the 2010 data [77, 78]. This strategy provides a good suppression of background from off-shell and boosted W bosons and it was applied in other analyses, see for instance [79] to study the electronic decay channel in the Tevatron experiments.

Similarly to the W boson, the W' would give rise to a Jacobian peak in the M_T distribution, see Figure 7.3 right. Recalling from the previous section, the transverse mass is calculated as

$$M_T = \sqrt{2 \cdot (p_T^{\mu} \cdot c) \cdot E_T^{miss} \cdot (1 - \cos \Delta\phi_{\mu,\nu})}$$

From that expression, the key elements of this analysis are a precise measurement of the muon momentum and of E_T^{miss}. This applies as well for the W boson measurement as the signature is the same, although the kinematic region under study is different due to the different W and W' masses.

The reconstruction of TeV-muons was already described in section 5.2.1, including the description of their performance evaluated with simulated samples and cosmic data. In this section the momentum distributions given by the different reconstructors is shown for data and simulated background and signal samples, once the analysis selection is applied. The available E_T^{miss} reconstruction algorithms in CMS are introduced as well.

7.3.1 High p_T Muons

The reconstruction of the muon tracks has already been addressed in chapter 5. Among the different algorithms to reconstruct high p_T muons, the one chosen for the analysis is the *cocktail* one. For completeness, here its performance with the analysed collision data is compared to the results with the different algorithms. This comparison is limited by the reduced number of high p_T muons in data.

Prior to the results with data, the comparison of the muon p_T distributions is presented for the background and signal Monte Carlo simulation. The p_T distributions of the muons reconstructed with the cocktail algorithm compared to the results using the Picky and tracker algorithms are shown in Figure 7.6. Both of them give similar results. The ratio of these two algorithms and the dedicated TeV algorithms is displayed on the bottom part, for SM simulation and for a simulated W' signal of mass 1.5 TeV/c^2. The maximal difference for the values given by the Picky algorithm is 5%, while for the tracker algorithm the differences are larger, especially at high values of p_T when the resolution of this algorithm worsens. The comparison with the distributions given by the TPFMS algorithm is similar to the Picky one. These results are expected as the cocktail algorithm seldom assigns the muon the p_T measurement given by the tracker, therefore, their difference is larger, while the Picky algorithm is selected about 50% of the cases.

In Figure 7.7 the transverse momentum distributions for the selected data as given by the five algorithms are shown. On the top plot the cocktail algorithm is compared to the resulting p_T distribution measured by the standard tracker and global reconstructors. The latter is in fact the same as the tracker one up to 200 GeV/c. On the bottom plot the cocktail distribution is compared with the TPFMS and Picky reconstructor results. Most of the muons have p_T lower than ∼200 GeV/c, the region where the information only from the tracker is expected to give the most precise measurement. The global and the Picky algorithms may overestimate in some cases the p_T, as it could be the case of the largest p_T measurement, which seems to be off in both cases by ∼100 GeV/c. The cocktail algorithm, on the basis of the χ^2, takes the measurement for that muon given by the tracker muon, similar to the TPFMS value. Taking into account the results in section 5.2.1, where it was seen that the core and the tails of the resolution distribution improve with the cocktail fit, this would indicate that the choice of the algorithm by the cocktail indeed chooses the appropriate momentum.

7.3.2 Missing Transverse Energy

The neutrino is the only stable particle in the Standard Model that does not interact with the detector material and is hence not directly measurable. However, it can be identified indirectly using the momentum conservation in the transverse plane, as aforesaid. The accuracy and precision of this measurement are limited by the energy measurement resolution for all of the deposits, pile-up events and by instrumental problems such as noisy or dead channels. In addition, E_T^{miss} can be mismeasured if

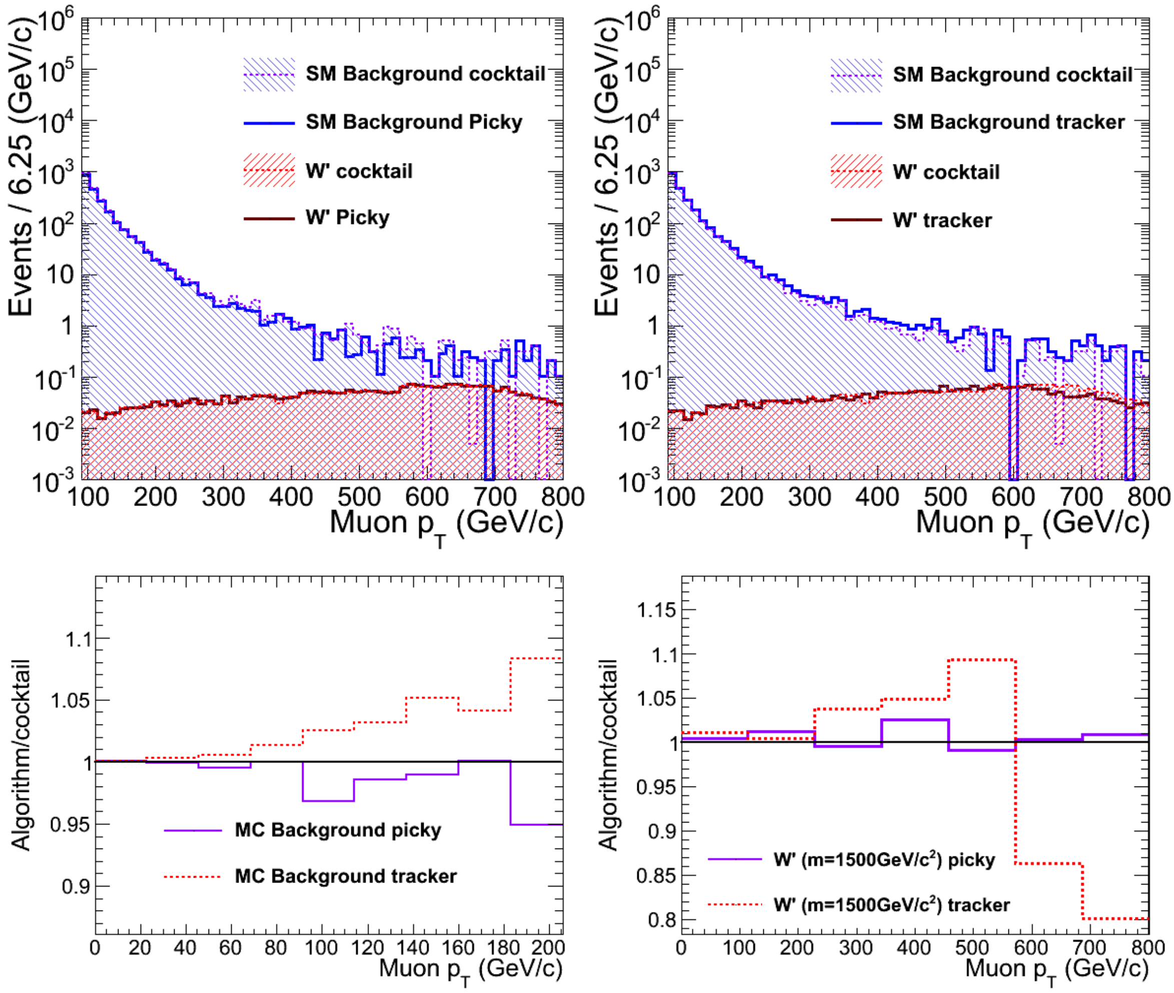

Figure 7.6: Top plots: p_T distributions for simulation of the expected SM background and W' of mass 1500 GeV/c^2, obtained with the cocktail and the Picky reconstruction algorithms (left) and the cocktail and tracker ones (right), for events firing the single muon trigger. Bottom plots: ratio between each of the two algorithms considered and cocktail algorithm, for the background (left) and signal (right) events. Due to the lack of statistics at high p_T, the left plot is only displayed up to 200 GeV/c.

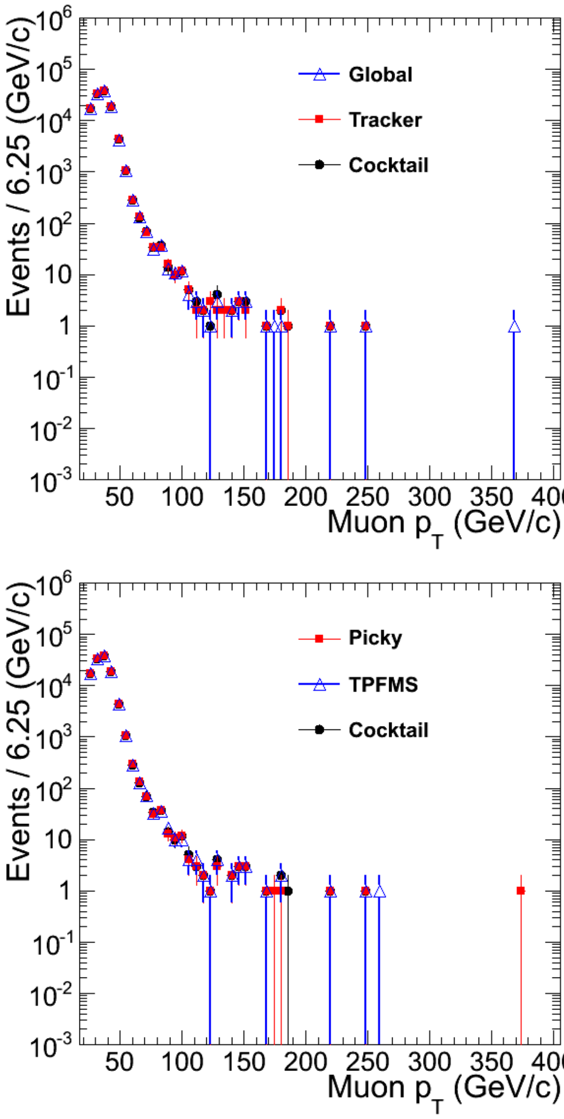

Figure 7.7: Distribution of muon p_T in data as given by the cocktail refit compared with the Global and Tracker algorithms (top) and the Picky and TPFMS ones (bottom), after the selection described in the next section.

other particles pass through poorly instrumented parts of the detector.

There are three algorithms developed within the CMS experiment, involving all of the subdetectors, to ensure the required performance is obtained: calorimeter based E_T^{miss} (caloMET), track-corrected calorimeter E_T^{miss} (tcMET), and particle-flow E_T^{miss} (pfMET).

- CaloMET is the negative vector sum of the transverse energy deposited in calorimeter towers that are above a certain noise threshold [80]. It does not include any information from other detectors besides the electromagnetic and the hadronic calorimeter. In events with muons, a correction removes the muon p_T and adds the small fraction of its energy deposited in the calorimeters (~ 2 GeV).

$$\overrightarrow{E_T}^{miss} = -\sum_{\mathrm{CaloTowers}} \overrightarrow{E_T} - \sum_{\mathrm{muons}} \overrightarrow{p_T}^{\mu} + \sum_{\mathrm{muons}} \overrightarrow{E_T}^{\mu}$$

- The track-corrected E_T^{miss} algorithm starts from caloMET and incorporates tracking information by adding the p_T of reconstructed tracks and subtracting the expected calorimetric energy deposited by that track [81]. This correction is applied to all tracks not identified as muons, which are corrected in the CaloMET calculation, or electrons, already well measured.

$$\overrightarrow{E_T}^{miss} = -\sum_{\mathrm{CaloTowers}} \overrightarrow{E_T} - \sum_{\mathrm{muons}} \overrightarrow{p_T}^{\mu} + \sum_{\mathrm{muons}} \overrightarrow{E_T}^{\mu} - \sum_{\mathrm{good\ tracks}} \overrightarrow{p_T}^{track} + \sum_{\mathrm{good\ tracks}} \overrightarrow{E_T}^{track}$$

- The particle-flow technique aims to reconstruct a complete, unique list of particles in each event using the entire CMS detector [82]: muons, electrons, photons, and charged and neutral hadrons. Then, pfMET is constructed as the negative vector sum of the momentum of all reconstructed particles in the event.

$$\overrightarrow{E_T}^{miss} = -\sum_{\mathrm{AllPF-Particles}} \overrightarrow{p_T}$$

  There is no need to apply any corrections for muons or tracks since their momenta is properly taken into account in this inclusive approach.

The latter algorithm was adopted for this analysis as its performance was found to be the best among all E_T^{miss} calculations [83]. To be consistent in the analysis, the default muon momentum included in the E_T^{miss} calculation (the pfMuon momentum) is replaced by the momentum as measured by the chosen algorithm, the cocktail fit. Otherwise the reconstructed transverse mass would contain p_T measurements coming from different algorithms, in this case, the muon momentum given by the cocktail algorithm and the Particle Flow muon used to reconstruct E_T^{miss}. It is important to avoid failures to reconstruct the muon and subsequent propagation to pfMET as this could fake a signal event.

The distribution of pfMET is displayed in Figure 7.8, showing a relatively good agreement of the selected data with MC.

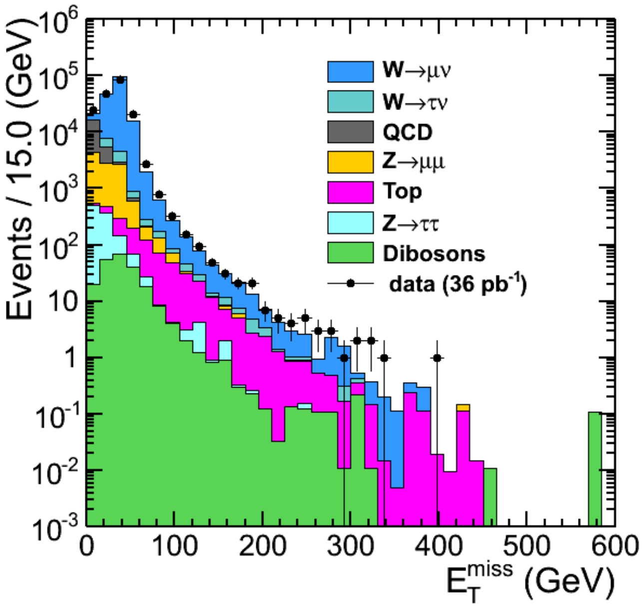

Figure 7.8: Distribution of E_T^{miss} for particle-flow algorithm described in the text, for data and SM background. All selection criteria related to the muon are applied.

Chapter

8

Selection of Signal Events and Background Determination

Once the strategy and the elements of the analysis are established, the next step is the description of the selection procedure, designed to reject efficiently events from the Standard Model backgrounds, keeping a high signal efficiency. Stringent criteria are needed also to reject badly reconstructed events, which could bias the measurement. Hence, the aim of this chapter is to describe the selection steps and show its performance results using data - Monte Carlo comparisons. To accomplish the latter, the simulation is first adjusted for residual discrepancies between data and MC.

8.1 Selection Steps

Most of the requirements used in this analysis have already been discussed in section 6.1 as they all aim to select muons from events rather similar. Thus here they are only briefly reminded, highlighting the few differences with respect to the ones used to obtain the efficiencies for the $W \to \mu\nu$ cross section measurement. The selection is the following:

1. **Trigger selection:** Events selected online by the lowest-threshold unprescaled single muon trigger are kept. This corresponds to events firing three trigger paths: `HLT_Mu9`, `HLT_Mu11` and `HLT_Mu15` depending on the run period. The trigger thresholds are much lower than the kinematic region relevant for a W' search

and the different trigger paths behave similarly, so combining them does not influence the analysis in any way. A detailed discussion on trigger performance and efficiency studies can be found in section 8.3.1.

2. **Muon identification and quality criteria:** The same requirements explained in Chapter 6 are applied. The only difference is the more restrictive transverse impact parameter range selected, $d_0 < 0.02$ cm instead of $d_0 < 0.2$ cm in order to further reduce background from cosmics, discussed in section 8.2.2.

3. Similarly the muon pseudorapidity has to be in the range $|\eta| < 2.1$ matching the trigger acceptance and the minimum p_T is 25 GeV/c.

4. **Only one high-p_T muon** in the event was required to reduce Drell-Yan (and potentially Z') background. In particular events with more than one global muon with p_T>25 GeV/c as measured by the tracker are rejected. In section 8.2.2 the effect of this criterion in cosmic muon rejection is considered.

5. **Isolation:** The threshold in the muon relative isolation variable is fixed at 0.15, instead of the more restrictive 0.1, which was justified to remove QCD. In this analysis this background will be completely negligible in the kinematic region of interest for the search (high M_T), so a looser requirement is sufficient.

6. **Kinematic cuts:** Given that E_T^{miss} is well described and understood, it was possible to use a combination of kinematics cuts involving it, in particular, two dedicated selection criteria based on the ratio of the muon p_T over E_T^{miss} ($p_T/$ E_T^{miss}) and the angular difference between the direction of the muon and E_T^{miss} in the transverse plane. They are designed to select events with the W' signal topology, where the lepton and E_T^{miss} are expected to be almost back-to-back in the transverse plane, see plots at generator level in section 7.2. The requirements are:

   - $0.4 < p_T/E_T^{miss} < 1.5$
   - $\Delta(\phi_{\mu,E_T^{miss}}) > 2.5$

   These criteria are optimised for high signal efficiency and further suppression of the background events. Their combined efficiency is above 90%, after the remaining selection requirements are applied, for any W' signal in the mass range considered (0.6 TeV/c^2 - 2.0 TeV/c^2), whereas it is remarkably lower for all backgrounds, except for $W \to \mu\nu$ due to the similar topology, which is around 80%. It is close to 30% for diboson events and as low as ~10% for $t\bar{t}$ events.

The expected number of signal and background events surviving the various selection steps in a data sample of an integrated luminosity of 36 pb^{-1} are shown in Tables 8.1 and 8.2, respectively. The values are obtained with the p_T given by the cocktail algorithm, they vary slightly using a different algorithm due to the kinematic cuts, however, it is not a relevant change. (For instance, the number of events varies by about 0.1% for the W' mass points considered). The tables contain as well the relative efficiency of each step with respect to the previous one. The final column includes de total efficiency (including the acceptance) after all selection is applied respect to the preselected events, the ones containing a muon with p_T>15 GeV/c is present in the event. The step labelled *Quality Cuts* includes the acceptance conditions, $|\eta|$ <2.1 and p_T>25 GeV/c, and all quality requirements for the muon track as described before. The average efficiency for a W' signal is about 80% being slightly larger for heavier W' bosons: for the two lowest mass points it is a bit below that value, whereas the efficiency is above 81% for the rest.

Before the selection, muons arising from QCD and W events are the dominant contributions. The former dominates the distribution at low p_T, but its contribution falls rapidly with increasing momenta, so they are largely removed by the minimum p_T cut and its expected contribution to the final background sample is negligible, at the per mil level compared to the $W \to \mu\nu$ sample surving all the cuts, also thanks to the isolation requisite. Z decay events are mainly suppressed by the requirement of a single muon, with the exception of those Z events where one of the muons escapes undetected.

The contribution of $W \to \mu\nu$ represents the dominant background over the whole p_T range. The proportion of dibosons events that survive the selections is not negligible, but their total number of events is small because of their much lower cross-section compared for instance to W events. Considering only the region with p_T>100 GeV/c where most of the muons from W' are expected, the remaining background is composed mainly by $W \to \mu\nu$, and to a lower extent by $Z \to \mu\mu$ and top decays.

The comparison between data and simulated background samples predicted by the SM is shown in the following figures as a function of the relevant variables involved in the analysis. In Figure 8.1 the muon pseudorapidity (η) and azimuthal angle (ϕ) distributions are presented for muons before selections. The muon distributions for a potential W' of 1.0 TeVc^2 and 1.5 TeV/c^2 are included. The MC is normalised to the luminosity in data, it describes correctly the data behaviour, even before applying the selection criteria. Both, the background and the signal simulations, are flat as a function of ϕ, while their behaviour differs slightly as a function of η, the signal tends to concentrate more at central values of η (also the W simulation) compared for instance to QCD or Z events.

The relative isolation is presented in Figure 8.2, for muons which pass the muon quality requirements. The effectiveness of rejecting muons with relative isolation greater than 0.15 is clear, especially against QCD events as it reduces its contribution by more than 90%.

The distributions used to optimise the kinematic selection cuts are depicted in Figure 8.3, their goodness as discriminating variables is clear: the signal peaks at p_T/E_T^{miss} ~1, and the angle between the lepton and E_T^{miss} is $\sim \pi$ while the background presents higher tails in both distributions, again except the $W \to \mu\nu$ distribution as a consequence of its similar topology compared to the $W' \to \mu\nu$ process.

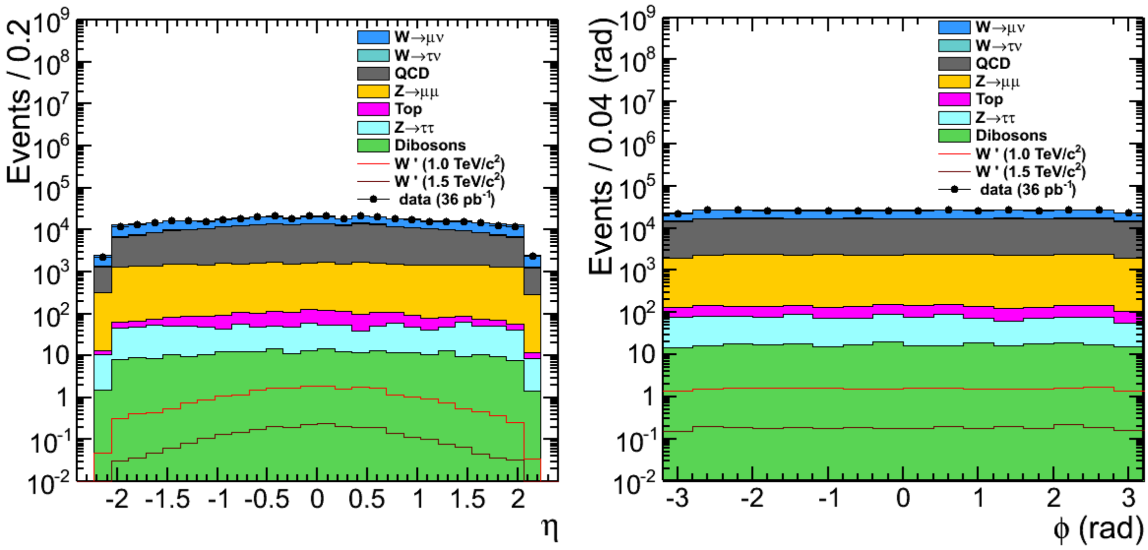

Figure 8.1: η (left) and ϕ (right) distributions of muons before any selection criterion is applied, comparing data to the sum of all expected backgrounds evaluated with MC. The hypothetical distributions for a W' of 1.0 TeV/c^2 and 1.5 TeV/c^2 are included. The different MC samples are listed in the legend in the same order than they are plotted for clarity.

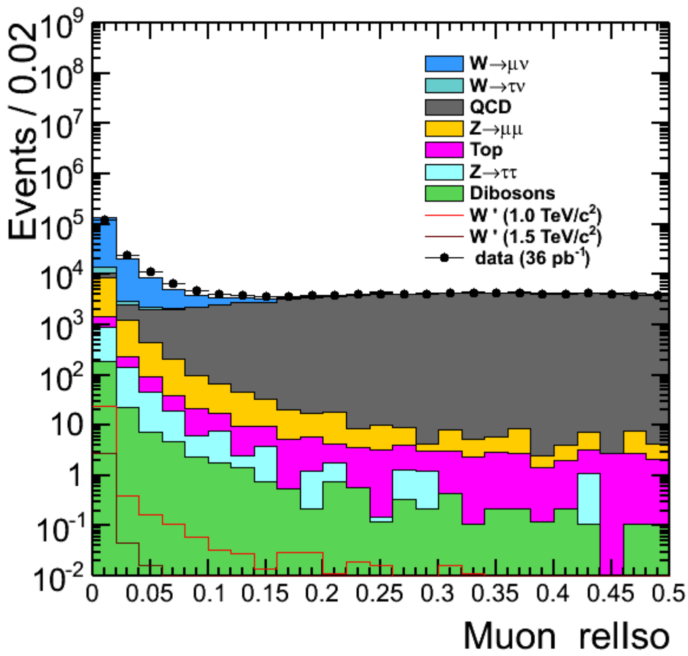

Figure 8.2: Distribution of the muon relative isolation after the quality criteria described in the selection, comparing data to the sum of all expected backgrounds evaluated with MC. The hypothetical distributions for a W' of 1.0 TeV/c^2 and 1.5 TeV/c^2 are included.

W' mass (TeV/c^2)	Presel. p_T>15 GeV/c	HLT	Quality Cuts	Only one global μ	Isolation	Kinematic Criteria
0.6	282.3	256.0 90.7 %	245.2 95.7 %	244.9 99.9 %	242.2 98.9	225.2 ± 2.3 93.0 % (79.8 %)
0.7	145.4	131.1 90.2 %	125.8 94.0 %	125.7 98.6 %	123.9 98.6 %	116.2 ± 1.2 90.9 % (79.9 %)
0.8	83.7	76.2 91.0 %	73.0 95.8 %	73.0 99.9 %	72.1 98.9 %	68.1 ± 0.7 94.4 % (81.4 %)
0.9	47.9	43.5 90.8 %	41.7 95.8%	41.6 99.9%	41.1 98.8%	39.0 ± 0.4 95.0% (81.4 %)
1.0	29.0	26.3 90.7%	25.1 95.3%	25.0 99.8%	24.7 98.8%	23.7 ± 0.2 95.7% % (81.7 %)
1.1	17.9	16.3 91.1 %	15.6 95.6%	15.5 99.8%	15.3 98.6	14.7 ± 0.1 95.9 % (82.3 %)
1.2	11.6	10.4 89.6 %	10.0 95.4%	10.0 99.8%	9.8 98.8	9.4 ± 0.1 96.2% % (81.4 %)
1.3	7.4	6.7 90.3 %	6.4 95.4%	6.4 99.8%	6.3 98.9%	6.1 ± 0.0 96.2 % (82.4 %)
1.4	4.7	4.2 89.4 %	4.1 95.3%	4.1 99.9%	4.0 98.5%	3.9 ± 0.0 97.2 % (81.9 %)
1.5	3.4	3.1 90.6 %	2.9 95.3%	2.9 99.9%	2.9 98.4%	2.8 ± 0.0 96.9 % (81.9 %)
2.0	0.49	0.44 89.8 %	0.42 94.2%	0.42 99.9%	0.42 98,9%	0.40 ± 0.00 96.6 % (81.6 %)

Table 8.1: Expected number of signal events after the different selection steps along with the corresponding efficiencies obtained with MC samples. The first line for each mass point gives the number of events expected for 36 pb^{-1} of integrated luminosity and the second line the efficiency of that selection step with respect to the previous one. In the last column the statistical errors are shown for illustration and the percentage on the right (in brackets) corresponds to the total efficiency times acceptance.

Finally, Figure 8.4 shows the muon p_T distribution and E_T^{miss} in the event after applying the complete selection. The agreement between data and simulation is quite good in p_T while there are some discrepancies in the E_T^{miss} distribution, particularly in the medium-high range. This is not unexpected as the prediction of background events from Monte Carlo processes needs to be adjusted for residual discrepancies between data and MC, accounting for effects that the full detector simulation is not capable to describe sufficiently.

In the following part of the chapter the corrections implemented to model adequately the background are addressed. This includes an independent evaluation of the cosmic muon contamination, which is not described by MC. Another aspect to consider is the correction factor arising from the different efficiency in data and simulation, previously discussed in Chapter 6. In this chapter the focus is only set on

Sample	Presel. p_T>15 GeV/c	HLT	Quality Cuts	Only one global μ	Isolation	Kinematic Criteria
$W \to \mu\nu$	243149	213001 87.6 %	154134.3 72.4 %	154059 99.9 %	152336 98.9 %	116683 ± 204 76.9 % (48.0 %)
QCD	$2.626{\times}10^6$	$2.373{\times}10^6$ 90.4 %	228039 9.6 %	226302 99.2 %	4945 6.6 %	135 ± 1 0.9 % (0.0 %)
$t\bar{t}$	1592	1446 90.8 %	967 65.9 %	888 91.8 %	719.3 81.0 %	78.3 ± 0.6 10.8 % (4.9 %)
$Z \to \mu\mu$	35078	32700 93.2 % %	22320 71.0%	9185 28.1 %	9080 98.9 %	3846 ± 20 42.3 % (11.0 %)
$Z \to \tau\tau$	3152.2	2741.4 86.7 %	941.9 34.3 %	924.7 98.2 %	916.6 99.1 %	133.2 ± 2.2 42.3 % (4.2 %)
$W \to \tau\nu$	17237	14906 86.4 %	4759 31.9 %	4741 99.6 %	4693 99.0 %	2652 ± 18 56.5 % (15.3 %)
ZZ	17.1	15.8 92.5%	11.7 74.0 %	5.5 47.0 %	4.6 83.6 %	0.6 ± 0.0 13.0 % (3.5 %)
WW	274.7	243.9 68.1%	187.2 76.7 %	177.1 9.6 %	172.3 97.3 %	51.7 ± 1.0 30.0 % (18.8 %)
WZ	88.7	79.0 89.1 %	78.0 98.7 %	48.5 62.1 %	46.1 95.1 %	13.6 ± 0.5 29.5 % (15.3 %)

Table 8.2: Expected number of background events after different selection steps, and corresponding efficiencies. The first line gives the number of events (normalised to 36 pb^{-1}) for each background process, and the second line the efficiency with respect to the previous condition. In the last column the statistical error is included, the second value (in brackets) of the efficiency is the total cumulative efficiency.

the efficiency measurement results on the scope of the W' search. Once these corrections are obtained and applied to the analysis, the final distribution and the estimation of background events are presented.

8.2 Background Estimation

The evaluation of the background contamination in the signal region is crucial for understanding and quantifying any potential deviation in the data from the SM predictions. The aspects studied, regarding the MC prediction, to describe more accurately the data are a correction to the electroweak backgrounds, to account for the difference in E_T^{miss} between the simulation and data, and a correction for the difference in efficiency of the simulated samples with respect to data.

Up to now, only the Standard Model backgrounds have been considered, however high p_T cosmics ray muons may constitute an additional source of background which has to be considered. The majority of cosmic ray muons are removed by the requirement that the transverse impact parameter with respect to the beamspot is less than 0.02

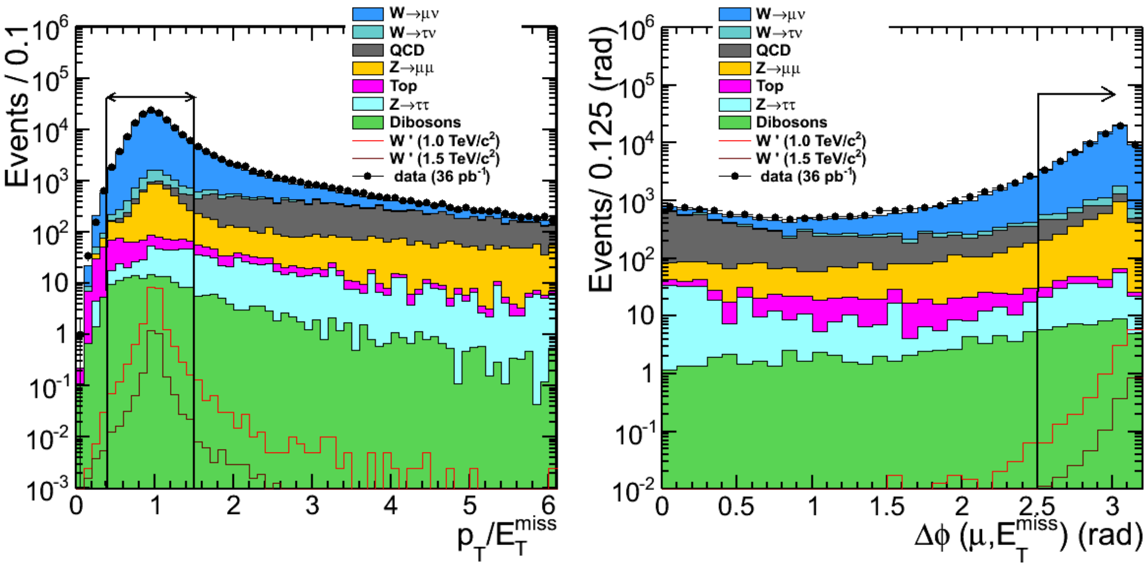

Figure 8.3: Distributions of the p_T over E_T^{miss} ratio (left) and azimuthal angle between lepton and E_T^{miss} (right), which have been used to optimise the kinematic selection. All selection criteria are applied except from the discussed ones.

cm. To quantify the remaining background, a dedicated studied has been performed and will be detailed in section 8.2.2.

The contribution of multi-jet QCD is the background component with the largest uncertainty on the cross section, found to be is 25%-40% higher than the Monte Carlo prediction [84], which should in principle be considered. However, after the kinematic cuts the QCD contribution to the total background is negligible, as seen in Figure 9.2, so this correction factor to the normalisation does not affect the analysis. For the other SM backgrounds the prediction from MC without further corrections is used.

8.2.1 E_T^{miss} Resolution Correction from Data

The production of W bosons is well understood theoretically and the general kinematic of the event is properly reproduced by Monte Carlo generators. So the distributions predicted in simulation are expected to model successfully the data. The muon momentum scale and resolution determined in data are in very good agreement with the prediction from MC simulation [42]. However, a correction on E_T^{miss} needs to be applied due to imperfections in the simulation of calorimetric response and resolution [83]. This argument also applies to other electroweak processes, but the correction is negligible due to their small contribution to the total background.

This correction is determined from a control sample of Z events, profiting from the similar kinematics of W and Z events. Z events have no physical source of E_T^{miss} besides detector related resolution effects or mismeasured particles. So a clean $Z \to \mu\mu$ sample can be used to model E_T^{miss} response and resolution with data and then incorporate that information to the construction of the hadronic recoil for the W Monte Carlo

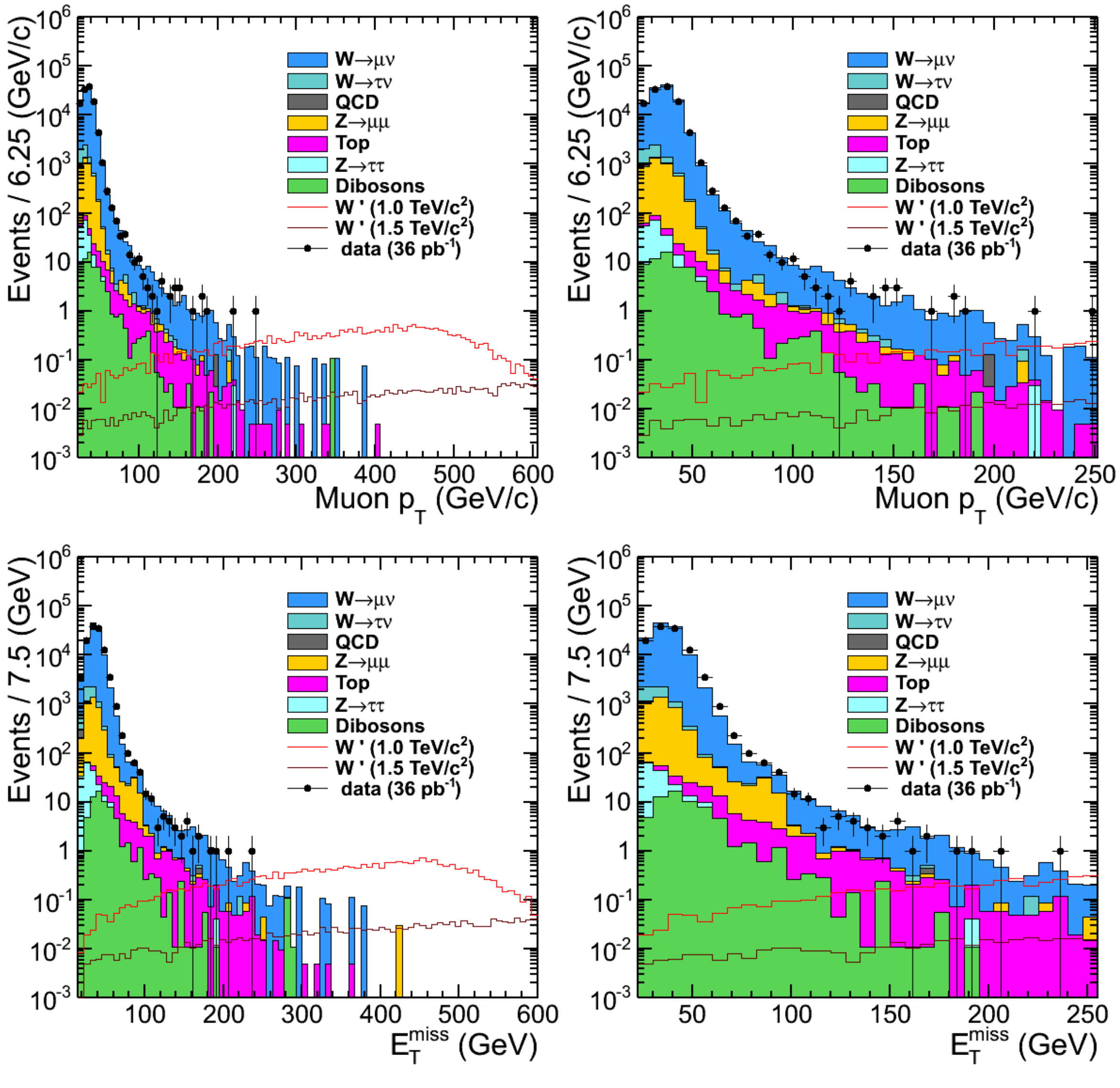

Figure 8.4: Distributions of the muon p_T (top) and E_T^{miss} (bottom) for MC and data after all selection. Right plots show the variables restricted to the low p_T and E_T^{miss} regions.

events. The method has been employed in CMS in the measurement of the inclusive W cross section and is described in detail in reference [85].

Z events selected consist in muon pairs of opposite charge with an invariant mass between 60 and 120 GeV/c^2; one muon passing the selection criteria reported in section 8.1, and a second muon passing a looser selection. In Z events the momentum of the vector boson can be reconstructed by using the muon momenta. The hadronic recoil, which corresponds to E_T^{miss} without the muon contribution, is defined as

$$\vec{U}_T = -\left(\vec{E}_T^{miss} + \vec{p}_T^{Z}\right). \tag{8.1}$$

It does not only depend on the hadronic activity associated with the vector boson but also on the underlying event and pile-up. The latter is contained in the data, an increasing amount according to the peak luminosity, but not in the reference Monte Carlo sample chosen.

The procedure is the following: for a given value of the boson p_T an experimental missing transverse energy distribution from $Z \to \mu\mu$ data is obtained. This distribution is used to sample a realistic E_T^{miss} value for a W Monte Carlo event of that boson p_T.

The method samples the hadronic recoil into two components, parallel (U_1) and perpendicular (U_2) to the vector boson momentum. The parallel component is due to initial state gluons radiated from the quarks which produced the Z boson. This emission balances the p_T of the boson so the average U_1 is expected to increase with the Z boson momentum. The perpendicular component is caused by multiple interactions and remnants of the proton involved in the Z production. The distribution of U_2 is then centred at zero, showing only resolution effects and being roughly constant as a function of Z p_T. Figure 8.5 shows the distributions of the parallel (U_1) and perpendicular (U_2) components as a function of Z p_T , illustrating the previously described behaviour, and the projection of each of them.

The hadronic recoil in the W Monte Carlo simulation is replaced using the results derived from the Z events in data on an event-by-event basis. This results in a correction of E_T^{miss} using $\vec{E}_T^{miss} = -\left(\vec{U}_T + \vec{p}_T^{Z}\right)$, and hence in a corrected M_T distribution.

The effect of this correction is displayed in Figure 8.6 for the shape of the W transverse mass distribution. The original Monte Carlo distribution is compared to the corrected one and to the data. The correction shifts essentially events from the W peak at higher values, as the E_T^{miss} resolution in data is broader than the simulated one. After the recoil correction, the agreement between MC and data is improved, in particular in the region around M_T ~80-150 GeV/c^2. This can be clearly viewed in Figure 8.7 where the ratio between the uncorrected and corrected simulations and data is depicted. The range of the ratio is restricted to the region where the the amount of data is enough not to be dominated by statistical fluctuations. For high values of M_T, the estimated number of W boson events increases with respect to the non-corrected MC prediction, see Table 8.3. In the table the number of MC W events after different transverse mass thresholds is shown, for the corrected $W \to \mu\nu$ MC sample and the default one.

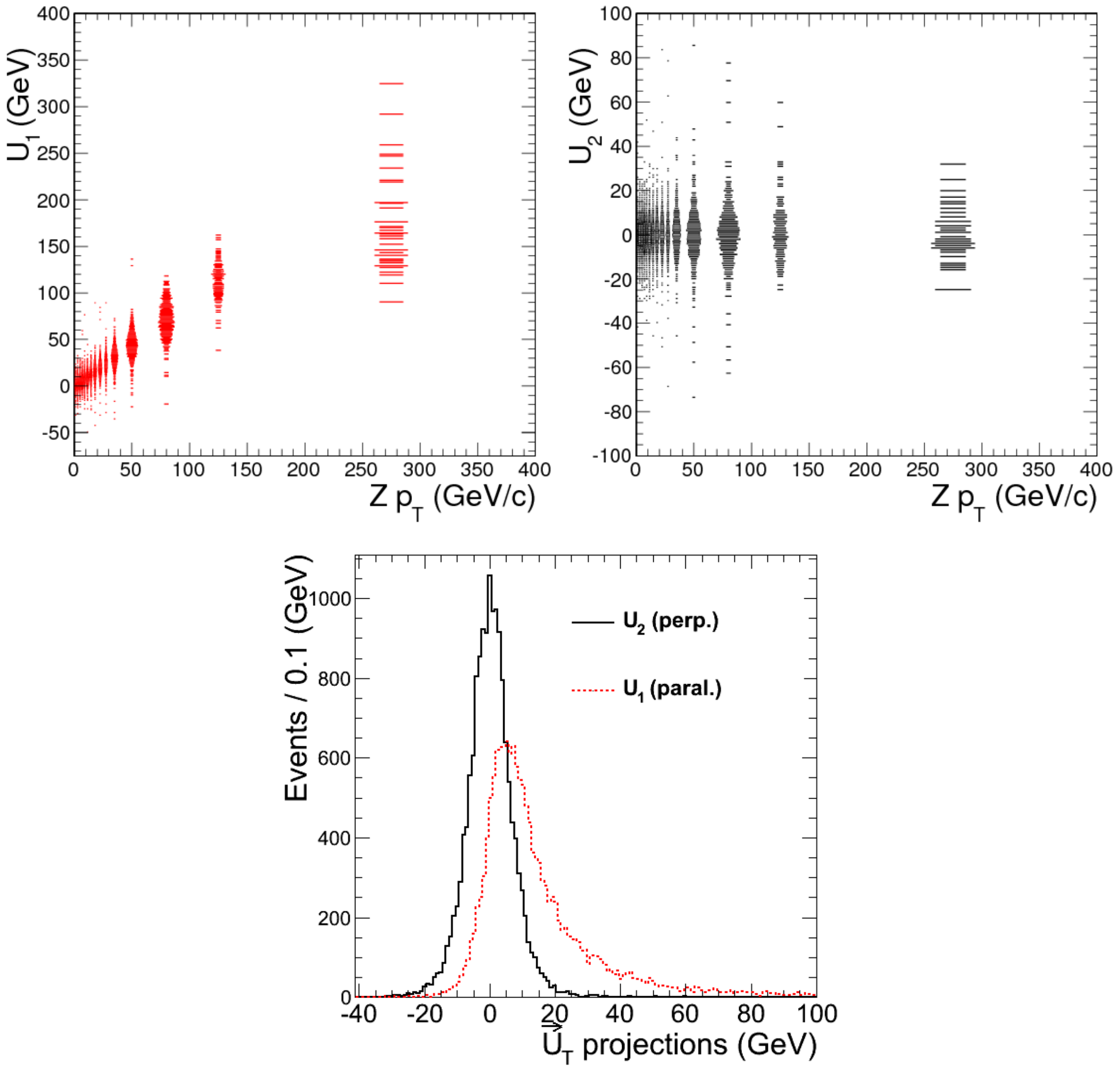

Figure 8.5: Top plots: Hadronic recoil components, U_1, left, and U_2, right, as a function of the vector boson p_T with the 36 pb^{-1} of data selecting $Z \to \mu\mu$ events. The bottom plot corresponds to the projections of U_1 and U_2.

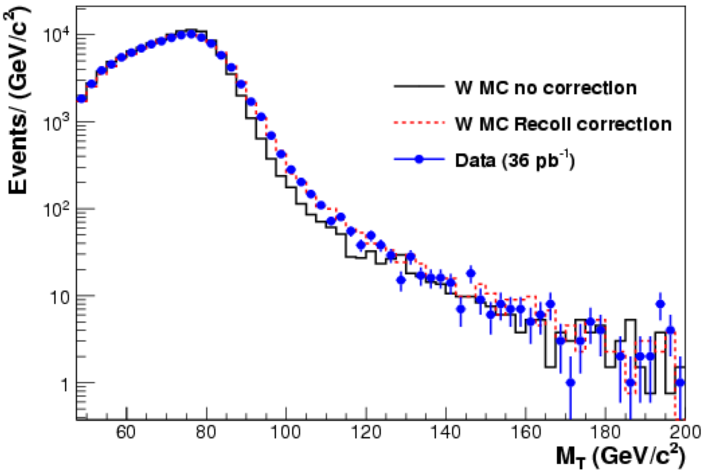

Figure 8.6: Transverse mass distribution before (black solid) and after (red dashed) recoil correction for simulated W MC sample compared to data (dots).

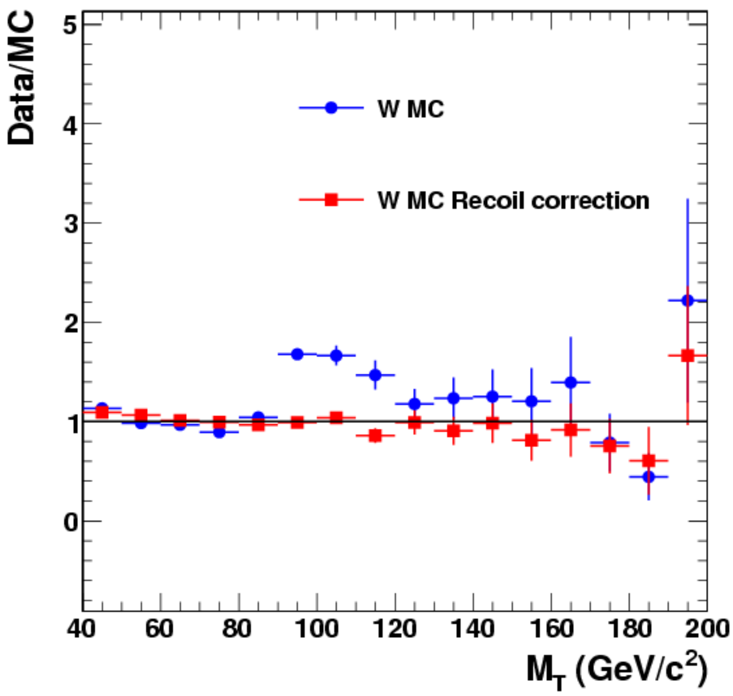

Figure 8.7: Data-to-MC ratio of the transverse mass distributions before (dots) and after (squares) the hadronic recoil correction.

$W \to \mu\nu$ with muon p_T> 25 GeV/c					
Events	After selection	$M_T > 300$ (GeV/c^2)	$M_T > 400$ (GeV/c^2)	$M_T > 500$ (GeV/c^2)	$M_T > 600$ (GeV/c^2)
without recoil	116665	11.17	2.86	0.94	0.38
with recoil	113328	11.14	3.58	1.44	0.61

Table 8.3: Impact of the hadronic recoil correction on the estimation of the number of selected simulated $W \to \mu\nu$ events. Events are essentially shifted from the W peak into the tail of the M_T distribution.

8.2.2 Cosmic Rays Background Estimation

The background due to cosmic rays is not described by the simulation and has been studied therefore separately with data. The main variable used to reject cosmic rays is the transverse impact parameter with respect to the interaction point (d_0), as it was already mentioned. A second relevant requirement against cosmic background is the selection of events with exactly one global muon with p_T above 25 GeV/c. In this way, events with two well reconstructed muons, that may come in fact from a single track crossing both halves of the detector passing close to the interaction point, are discarded.

The distribution of cosmic muons as a function of the impact parameter is expected to be flat for any range of d_0 considered. Figure 8.8 shows the impact parameter spectrum in data after all the selection steps excluding the impact parameter cut itself and the distribution with the W MC sample for comparison. According to the simulation, there is no expected contribution from the collision data in the region $|d_0| > 0.05 - 0.1$ cm. So at the region sufficiently far from the expected collision data one, the observed events correspond only to cosmic muons. Thus, the events in data in that region can be used to determine the background due to cosmic rays in the selected range, $|d_0| < 0.02$ cm. The number of events with $0.1 < |d_0| < 2$ cm is counted, obtaining 87±9 cosmic muons in data, for the whole data sample, this is the 36 pb^{-1} analysed. Extrapolating, the number of expected cosmic muons in the region $|d_0| < 0.02$ cm results then 0.92±0.10. If the quantity is obtained in a more restrictive range $0.2 < |d_0| < 2$ cm, to ensure that there is indeed no collision data at all, the values are 84±9 in the control region and 0.93±0.10 in the signal region. This check is intended to probe that the number is not influenced by the range chosen, as far as it is outside the expected one for collision data. The latter result will be used to estimate the contamination in the high M_T search window. The cosmic contribution is completely negligible compared to the total number of selected muons in the whole M_T spectrum, being approximately 10^{-5} times smaller.

However, its impact is more relevant for the high M_T region, the region of interest, where the SM background component falls steeply while the cosmic component diminishes at a much slower pace. This is illustrated in Figure 8.9. The M_T distributions for events with muons reconstructed in different impact parameter

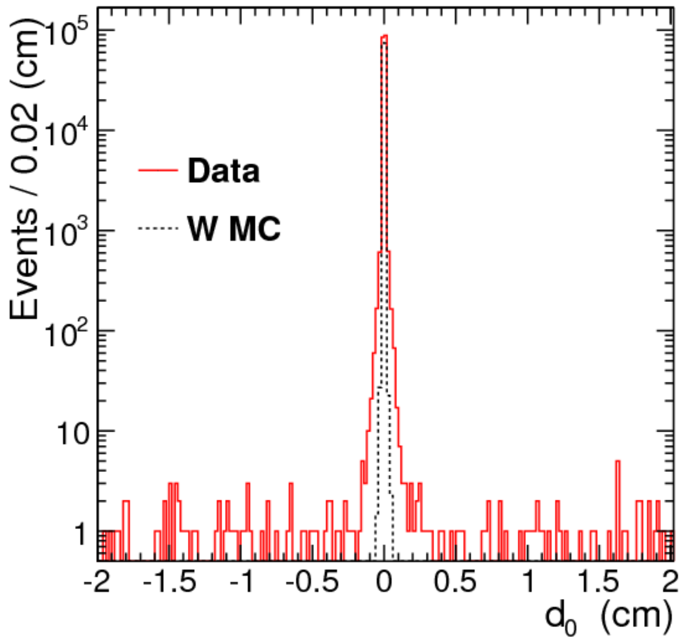

Figure 8.8: Impact parameter distribution after selection excluding the impact parameter itself for data (red histogram) and $W \to \mu\nu$ simulation (dotted line), shown for comparison.

regions are shown for all M_T values and the M_T <400 GeV/c^2 region.

Table 8.4 summarises the cosmic background estimate for different M_T ranges, compared with the contribution estimated from the SM simulation (the hadronic recoil correction is already applied). For M_T > 100 GeV/c^2 the cosmic contamination corresponds only to 0.5% of the total background, while it amounts to ∼7% for M_T > 500 GeV/c^2. The estimated combined background will be used for the exclusion limit.

M_T (GeV/c^2)	SM background	Cosmic background	Relative contribution
$M_T > 100$	1531	0.64 ± 0.09	0.005
$M_T > 300$	12.2	0.32 ± 0.06	0.026
$M_T > 400$	3.80	0.13 ± 0.04	0.035
$M_T > 500$	1.50	0.11 ± 0.03	0.073
$M_T > 600$	0.72	0.10 ± 0.03	0.137

Table 8.4: Estimated SM background, cosmic ray one and relative contribution of the latter to the total background for different M_T thresholds, obtained by extrapolating the number of cosmic muons in the region $0.2 < |d_0| < 2.0$ cm.

This contamination of cosmic rays can be further reduced, tightening the requirement on the presence of additional muons in the event to exclude events with

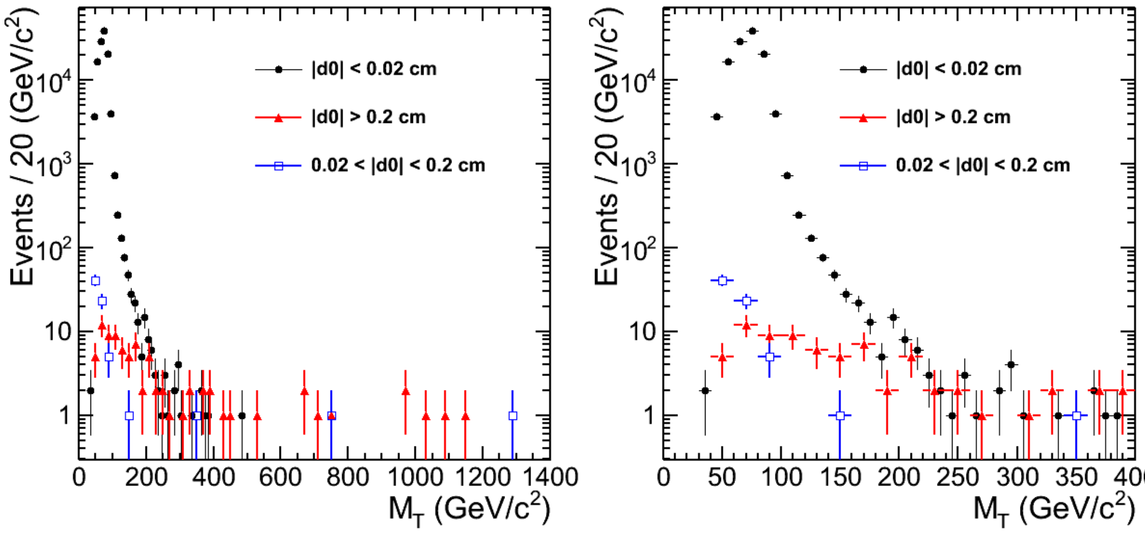

Figure 8.9: The M_T distributions for events in different impact parameter ranges, after all selection cuts, the lower M_T region is shown in the right plot.

a second muon with p_T>25 GeV/c reconstructed by any algorithm instead of a global muon. In Table 8.5 the number of events rejected by the criterion on the second muon reconstructed by the different standard CMS algorithms, is presented for the region $|d_0|$ >0.02 cm, where most of the SM background is excluded, in order to study the effect on cosmic muons. The complete selection criteria on the first muon is required, however to have more statistics the kinematics cuts are not applied. The first raw of the table corresponds to the total number of events before applying the cut on the second muon. The next ones show the number of events rejected by requiring that the second muon is reconstructed by the different algorithms. Note that this only applies to the second muon, the selection criteria on the first one is unchanged. Excluding events with a second muon reconstructed as a tracker muon instead of a global one reduces the cosmic contamination by ∼25% in the region $|d_0|$ >0.02 cm. Extrapolating this result, one would expect a similar reduction of the cosmic contamination for the selected $|d_0| < 0.02$ cm region. A second factor to consider is the effect on the signal efficiency. The number of events rejected from the W' sample with $M_{W'} = 1500$ GeV/c^2 with the different cuts is presented in the last column of the table. Considering the statistics, signal efficiency is not affected significantly by the algorithm used to identify the second muon.

8.3 Muon Reconstruction and Trigger Efficiencies

The next step in the analysis is the determination of the muon reconstruction and identification efficiency in order to infer the number of events that were really produced. The efficiency will be factorised into three main categories, discussed before on this thesis:

	Data ($\|d_0\|$ >0.02 cm)	W' events ($M_{W'}$ = 1.5 TeV/c^2)
Total (no cuts)	1161	808
Second muon p_T >25 GeV/c	Data Rejected ($\|d_0\|$ >0.02 cm)	Signal Rejected (all $\|d_0\|$)
Any	180	5
Tracker only	166	0
StandAlone	140	5
Global	125	3

Table 8.5: Number of data events rejected by requiring that there is no second high p_T muon in the event, depending on the reconstruction algorithm used. The number of signal events rejected from a hypothetical W' of mass M_T = 1500 GeV/c^2 is also given.

1. The efficiency of the offline muon reconstruction
2. The efficiency of the muon selection process, including identification and isolation criteria
3. Trigger efficiency: the combined L1 and HLT online selection efficiency

Simulated samples are adjusted to the resolution observed in data and the same muon reconstruction algorithms are applied to data and Monte Carlo events. However slightly different reconstruction and identification efficiencies in both cases are observed, see Chapter 6. Hence correction factors are obtained and applied to simulated samples in the analysis to reproduce correctly the efficiency observed in data.

The method was described in Chapter 6: muon efficiencies are determined with a Tag and Probe method in a clean sample of $Z \to \mu\mu$ events both in data and MC to measure and compare their efficiencies. The same background extraction technique is applied here. The only caveat of this method is the small statistics available for the high p_T muon region: only ∼60 *probe* muons with p_T> 100 GeV/c pass the whole selection. This fact is not significant for EWK analysis as most of the muons have lower p_T values, nevertheless, it is relevant for the W' search because the signal muons are expected to have much higher p_T. Therefore, the efficiency measured with data with muons from $Z \to \mu\mu$ decays has to be extrapolated to the high p_T region, which will be discussed later in this section.

The *tag* muon satisfies the trigger criteria and all identification and isolation requirements according to the muon selection for this analysis, see section 8.1. The other muon candidate, the *probe*, is required to pass specific criteria which define the particular efficiency under study. Each efficiency term is defined as the fraction of *probe* muons satisfying the selection criteria.

In the following, the efficiency of the different steps involved in the selection for this analysis is calculated, although for the measurement a global correction factor accounting for all of them is extracted. These various terms are defined as:

1. ϵ_{track}, the reconstruction efficiency of the inner tracker detector, which is extracted independently with this method. It was explained in detail in section 6.4.4. To measure $\epsilon_{\mathrm{track}}$, the *probe* muon is defined as a good-quality stand-alone muon and to be efficient it must have an associated inner track.

2. ϵ_{Mu}, the reconstruction efficiency of a good quality muon. To measure it, the *probe* muon is defined as a tracker track. It will pass the test if it is reconstructed as a muon satisfying the following:

   - it must be reconstructed both as a global and tracker muon
   - it must fulfil the requirements on the number of hits in the muon and tracker detectors

3. ϵ_{sel}, the muon selection requirements in terms of χ^2 and $|d_0|$. To measure ϵ_{sel}, the *probe* muon is defined as a global plus tracker muon satisfying all tight muon criteria except for the χ^2 and d_0 requirements, which must pass to be considered efficient. This and the previous factor correspond to the factor ϵ_{rec} in Chapter 6.

4. ϵ_{isol}, for the isolation requirement. The *probe* muon is defined as a good-quality global muon passing all the previous conditions.

5. ϵ_{trig} corresponds to the trigger selection, the efficiency that the offline muon fires the trigger, so it is associated to an HLT muon. This factor encompasses both L1 and HLT efficiency. To measure this term, the *probe* muon is defined as a global plus tracker muon satisfying all previous criteria including isolation except for the HLT.

This section is organised as follows: first, the trigger efficiency is obtained; secondly the offline reconstruction and selection is discussed; and finally, the extrapolation of the results obtained to higher values of p_T is addressed.

8.3.1 Muon Trigger Efficiency

The trigger efficiency is separated into different run ranges, corresponding to different unprescaled muon trigger paths being present on the trigger menu. The unprescaled path with the lowest muon p_T threshold was taken for each run. During the period Run2010A only the `HLT_Mu9` was used. For the Run2010B also `HLT_Mu11` and `HLT_Mu15` were present. The summary of the results on trigger efficiency from the Tag and Probe method is given in Table 8.6, separated in two muon p_T bins: p_T>25 GeV/c and p_T>50 GeV/c, well above the rising region of the turn-on curve. The integrated luminosity for each period is given. Figure 8.10 shows the trigger efficiency for the three relevant muon paths as a function of *probe* p_T, as measured by the cocktail algorithm described before. All efficiencies are essentially flat versus muon momentum. For the Run2010B running period, all triggers have roughly the same efficiency.

Trigger Path	p_T>25 GeV/c	p_T>50 GeV/c	Luminosity
Run2010A			
HLT_Mu9	0.88±0.01	0.89±0.02	3.1 pb^{-1}
Run2010B			
HLT_Mu9	0.919±0.008	0.936±0.013	5.0 pb^{-1}
HLT_Mu11	0.926±0.003	0.925±0.010	9.4 pb^{-1}
HLT_Mu15	0.929±0.003	0.930±0.007	18.3 pb^{-1}

Table 8.6: Single muon trigger efficiency measured with the Tag and Probe technique for the unprescaled lowest threshold muon paths in different run ranges.

The higher trigger efficiency during Run2010B is due to improvements made to the L1 configuration, as well as the switch to a new HLT algorithm. During Run2010A standalone muon tracks were matched to tracker tracks using an "Outside-In" approach, wherein the standalone track is propagated to the outer tracker surface to seed the tracker track reconstruction. Additionally during Run2010B, an "Inside-Out" algorithm, wherein tracker tracks were seeded by pixel pairs or triplets in a region around the standalone state, was run when the "Outside-In" approach failed to produce a tracker track. This improved the robustness of the HLT, especially in cases where the standalone track was of poor quality, for instance, for muons which develop a shower in the outer muon system. The average efficiency as a function of p_T for the

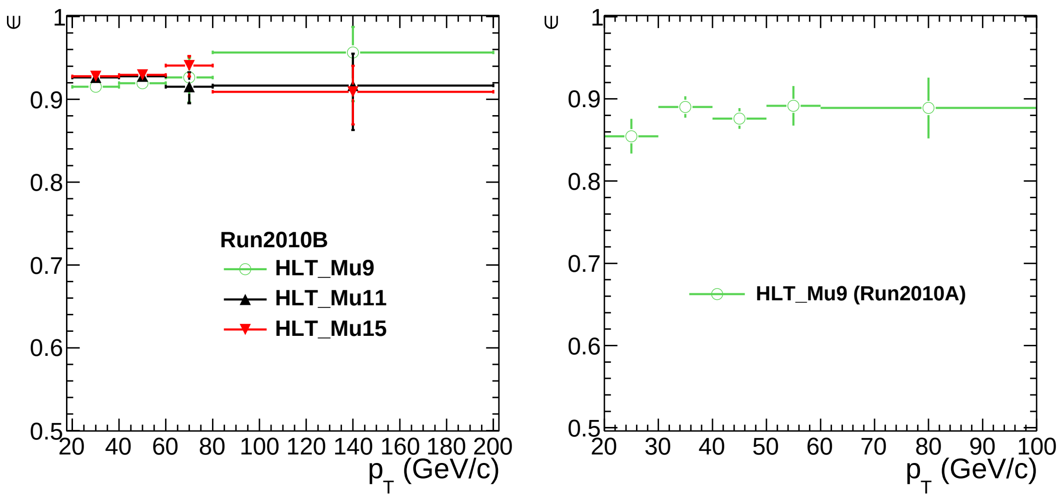

Figure 8.10: Single muon trigger efficiency as measured using Tag and Probe for the relevant trigger paths used in the analysis, versus muon *probe* p_T, as measured by the cocktail algorithm. On the left figure the plotted efficiency for the HLT_Mu9 corresponds only to the Run2010B. The efficiency for that path during Run2010A is shown on the right.

whole data (Run2010A and Run2010B) is presented in Figure 8.11 compared to the $Z \to \mu\mu$ Monte Carlo sample. For the trigger efficiency in MC the HLT_Mu11 path is used as a reference. The difference between the efficiency obtained in data and with the simulation is about 3% for the whole p_T spectrum.

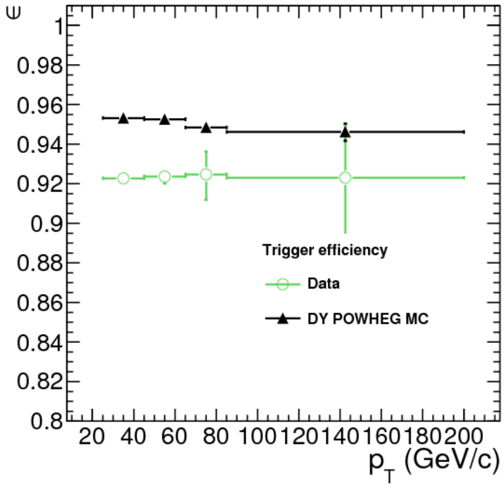

Figure 8.11: Trigger efficiency as measured using Tag and Probe in data and in the reference DY sample. The efficiencies are plotted versus the muon *probe* p_T from the cocktail algorithm.

8.3.2 Muon Reconstruction and Selection Efficiency

In this section the results for the other efficiency factors (muon reconstruction and selection, quality requirement and isolation) are presented. Table 8.7 summarises the results for all of them for data and the $Z \rightarrow \mu\mu$ MC sample, including the average correction factor, $\rho = \epsilon_{Data}/\epsilon_{MC}$, which will be incorporated in the W' analysis to obtain the correct number of simulated background and signal events. The errors are only statistical. The difference between the efficiency in data and simulation is ~0.2% for each factor, being significantly smaller than the difference in the trigger efficiency.

Figure 8.12 shows each term as a function of muon *probe* p_T, both for data and $Z \rightarrow \mu\mu$ Monte Carlo. The value of the efficiency term ϵ_{Mu} corresponds to the corrected value to account for the background present in the Tag and Probe preselection. This is obtained with the reweighting procedure presented before. The fitting function and the factors to reweight the *probe* muons were calculated using the reference MC and specific selection used for this analysis. The sample was split in the same p_T ranges as in Chapter 6, that is $p_T \geq$ 35 GeV/c and $p_T <$ 35 GeV/c.

Finally, in Table 8.8 the total efficiency excluding the trigger one,

$$\epsilon_{Mu+sel+isol+track} = \epsilon_{Mu} \times \epsilon_{sel} \times \epsilon_{isol} \times \epsilon_{track},$$

the trigger efficiency and the total one

$$\epsilon_{TOTAL} = \epsilon_{Mu+sel+isol+track} \times \epsilon_{trig}$$

Efficiency	Data	Simulation	Data/Simulation
ϵ_{Mu}	0.971±0.001	0.9726±0.0002	0.998±0.001
ϵ_{sel}	0.9943±0.0006	0.9962±0.0002	0.9981±0.0008
ϵ_{isol}	0.983±0.001	0.9863±0.0002	0.997±0.001
ϵ_{track}	0.9976±0.0004	0.9991±0.0001	0.9985±0.0006

Table 8.7: Single muon efficiency, divided into four factors, obtained in data and simulation by using the Tag and Probe technique on a clean Z $\rightarrow\mu\mu$ sample. The efficiencies are given for p_T>25 GeV/c.

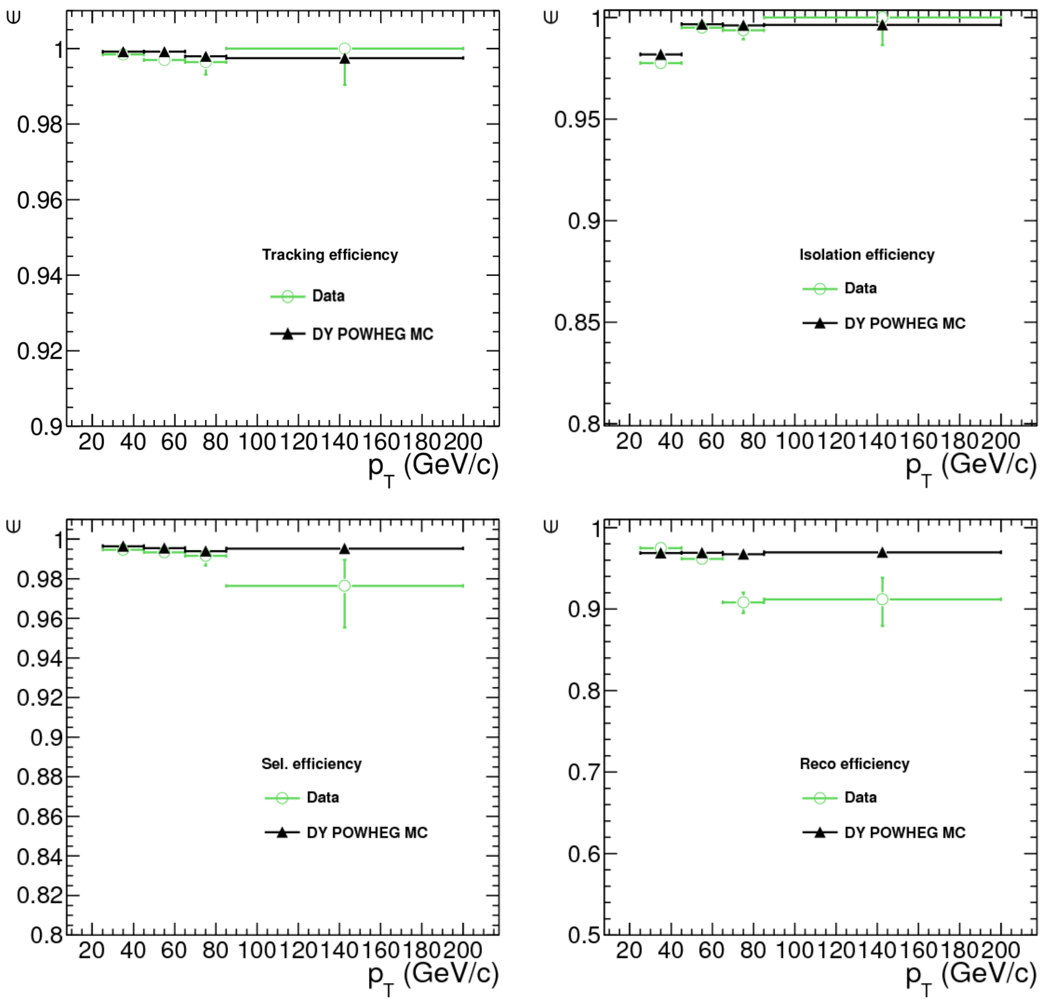

Figure 8.12: From left to right and from top to bottom: tracking, isolation, selection, muon identification and reconstruction efficiencies measured using the Tag and Probe method in a $Z \rightarrow \mu\mu$ sample from data compared to Monte Carlo, versus muon *probe* p_T, as measured by the tracker.

Efficiency	Data	Simulation	Data/Simulation
$\epsilon_{Mu+sel+isol+track}$	0.948±0.002	0.9557±0.0003	0.992±0.003
ϵ_{trig}	0.923±0.002	0.9529±0.0003	0.968±0.002
ϵ_{TOTAL}	0.874±0.002	0.9098±0.0003	0.960±0.002

Table 8.8: Total muon identification efficiencies in data compared with the values obtained with a high statistics $Z \to \mu\mu$ simulated sample. The errors quoted correspond to the statistical ones, the total error including the statistical error from the fit and the systematic error from the method amounts to 0.008, see Chapter 6.

are given, together with the resulting correction factors. The global factor applied to correct the normalisation of the MC samples is 0.96. As already mentioned, the largest contribution to the final correction factor comes from the difference in the trigger efficiency, while the total contributions of the rest of the terms is less than 1%.

The efficiencies with the Tag and Probe technique are robustly measured up to p_T ~100 GeV/c and found to be roughly flat for the whole range considered. The trigger efficiency was cross-checked with a second method using a sample of jet-triggered data [42] which enables the single muon trigger efficiency measurement up to $p_T \sim$ 250 GeV/c the highest p_T values recorded during 2010. Only muons up to that p_T from pp collisions during 2010 have been recorded. Both methods agree within 1%. The total efficiency is not expected to depend on p_T despite the fact that the showering probability in the iron yoke increases with the muon energy. This assumption, checked with cosmic muons up to 1 TeV [41], is a consequence of the redundancy of the muon system.

For completeness, efficiency studies for muons with p_T of the order of 500 GeV/c are done with simulated W' samples to extrapolate the efficiencies obtained with data and Monte Carlo with the Tag and Probe method to higher p_T. The aim of the comparison, presented in the following section, is not only to have a hint of the validity of the results at high p_T but also to be able to establish a realistic systematic uncertainty associated to the measurement.

8.3.3 Comparison with Monte Carlo Based Efficiencies

The Monte Carlo based efficiencies are obtained in the same way as in section 6.3. The efficiency is defined as the number of reconstructed muons associated to generated ones that survive the requirements under study over the total number of generated muons in the selected kinematics phase space. The Tag and Probe results are compared to the efficiency of the $W \to \mu\nu$ POWHEG sample, covering the same kinematic region, and the efficiency of the W' signal PYTHIA samples covering a higher p_T range. In particular, the comparison is done for two samples of simulated W' bosons, with masses of 1.1 TeV/c^2 and 1.5 TeV/c^2.

Figure 8.13 top shows the trigger efficiency (left) and the efficiency related to the selection and reconstruction of the muon (right) for the two W' samples as a function of the generated muon momentum. Both efficiency factors are stable as a function of p_T for the region with significant statistics and are similar for the samples compared. The bottom plots of the figure correspond to the comparison of the efficiency of muons from W decays compared to the expected efficiency from muons coming from the W' sample with mass of 1.5 TeV/c^2, the difference in efficiency between both samples can be clearly seen, especially in the reconstruction and identification efficiency term.

Table 8.9 shows the average trigger and global muon reconstruction Monte Carlo efficiency for the W and W' samples and the Tag and Probe efficiency with the $Z \to \mu\mu$ sample. The latter correctly predicts the efficiency for the W sample, whereas it seems to overestimate the efficiency for the W' sample by 2%, compared to the corresponding MC truth values. Also the trigger efficiency is slightly lower, ∼93%, flat over the whole p_T spectrum.

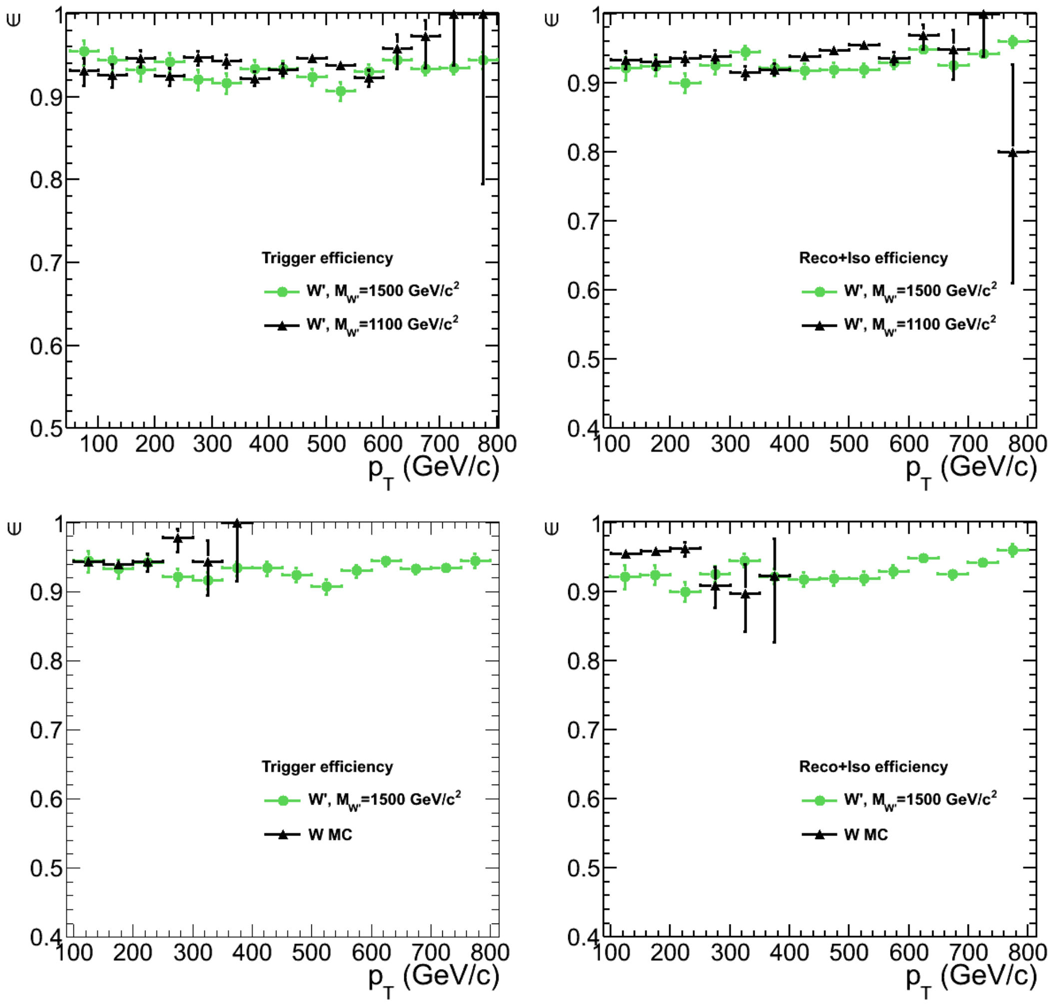

Figure 8.13: Top: trigger efficiency measured in MC samples as a function of the generated muon p_T (left) and muon reconstruction, identification and isolation efficiency (right) for two W' samples with masses 1500 GeV/c^2 and 1100 GeV/c^2. Bottom: same comparison between the simulated W' of $M_{W'}$=1500 GeV/c^2 and the W samples.

Efficiency	Tag and Probe (W MC)	MC truth (W)	MC truth (W' , $M_{W'}$=1.5 TeV/c^2)
$\epsilon_{\mathrm{Mu+SEL+iso}}$	0.9557±0.0003	0.9465±0.0003	0.929±0.001
$\epsilon_{\mathrm{Trigg}}$	0.9529±0.0003	0.9484±0.0003	0.930±0.001

Table 8.9: Comparison of the efficiency obained with MC using the Tag and Probe method on a Z $\rightarrow\mu\mu$ sample and the pure MC efficiency obtained for a W and a W' samples. The efficiency is split into two factors, trigger efficiency, and muon reconstruction and identification. The efficiencies are given for p_T>25 GeV/c.

Taking into account all these results, the correction factor obtained in this section between data and Monte Carlo efficiencies was taken as a global value, without splitting in different η regions like it was done for the $W \rightarrow \mu\nu$ analysis, which is indeed a precision measurement. This approximation is justified by the fact that the kinematics of the signal events differ from the region studied with data, and from the Monte Carlo studies the difference in the efficiency could amount to the few percent level. In other words, the expected improvement using different correction factors lies within the error. This difference will be considered in the systematic uncertainty associated with the muon efficiency, discussed in the next section.

8.4 Systematic Uncertainties

Several sources of systematic uncertainties have been evaluated to estimate the total uncertainty on the expected number of signal and background events, which are summarised in the following:

- Luminosity determination.
- Muon p_T scale and resolution.
- E_T^{miss} resolution.
- Trigger and reconstruction efficiencies.
- Cross section uncertainty

The uncertainties on the effective luminosity or the muon efficiency corrections affect only the normalisation, while the ones on muon energy scale and resolution or the hadronic component of E_T^{miss} affect the shape of the distributions.

8.4.1 Uncertainty on Luminosity

The uncertainty on the absolute value of the integrated luminosity was estimated in CMS to be 4% [44, 86], which affects both background and signal estimations. The luminosity is obtained from a measurement of the event rate of a given process observed when compared to the visible cross section, $L(t) = N(t)/\sigma_{vis}$. CMS uses signals registered by the forward hadronic (HF) calorimeters to determine the instantaneous luminosity in real time. This result is cross-checked with an offline analysis of the data. The absolute normalisation of the luminosity estimation is obtained through a method known as Van der Meer scans to determine the size of the colliding beams [44].

8.4.2 Muon p_T Scale and Resolution

The transverse mass has two components, p_T and E_T^{miss}. If E_T^{miss} in an event has any contribution from muons, which is the case of this analysis, a mismeasurement of the muon momentum has a direct impact on its computation, which then is propagated to M_T (besides the effect on the p_T itself). The measurement of charged particles crossing the detector was well simulated in the 2010 MC production, taking into account the energy losses and change of the trajectory suffered by the particle as functions of the alignment of the tracking system, the inactive material along the path and the magnetic field the particles are subject. However there could be effects of residual misalignment in the tracker, inaccurate magnetic field or inactive material simulation still missing due to the lack of high p_T muons from collision at the time of generating the samples.

The impact of such effects on the measurement of the momentum scale and resolution of the muons was studied [42, 87, 56] with medium p_T muons from collision data and from TeV muons with the collected cosmic muon data. From detailed studies of the $Z \to \mu\mu$ invariant mass distribution, scale shifts above 0.4% for muons with ~40 GeV/c can be excluded at the level of one standard deviation. Alignment studies using TeV muons show that this upper limit on the scale shift is also valid in the high momentum region. Studies using cosmic muons have also set upper limits on the uncertainty of the curvature offset. From all these studies, upper limits on the uncertainty in the muon momentum scale and resolution have been obtained.

In order to estimate the effect on the final number of expected background events in the signal region, the muon p_T is distorted (scaled and smeared), according to the values obtained from those studies, which are in fact conservative upper limits. The reconstructed muon momentum is thus replaced by:

- Muon momentum scale: $\frac{1}{p'_T} = \frac{1}{p_T} + 0.113\ (\mathrm{TeV}/c)^{-1}$
- Resolution: $\frac{1}{p'_T} = \frac{1}{p_T} + 0.14 \times \mathrm{G}(0,1)\ (\mathrm{TeV}/c)^{-1}$

with G(0,1) being a Gaussian distributed random number with mean 0 and width 1. These values are quite conservative with the aim of setting an upper limit to the effect in the transverse mass. The missing transverse energy is recomputed and finally a distorted transverse mass is obtained [88].

In Figure 8.14 the *distorted* transverse mass distribution is shown together with the original one for all SM background samples. The global effect is not significant. The effect was studied as well for high values of M_T, where the data sample is reduced and a shift in the distribution would have a larger impact. This corresponds also to higher values of p_T more affected by the uncertainty. The results obtained are listed in Table 8.10. For the signal region, where higher values of p_T should be considered, a conservative value of ~10% has been assigned as systematic uncertainty due to this effect.

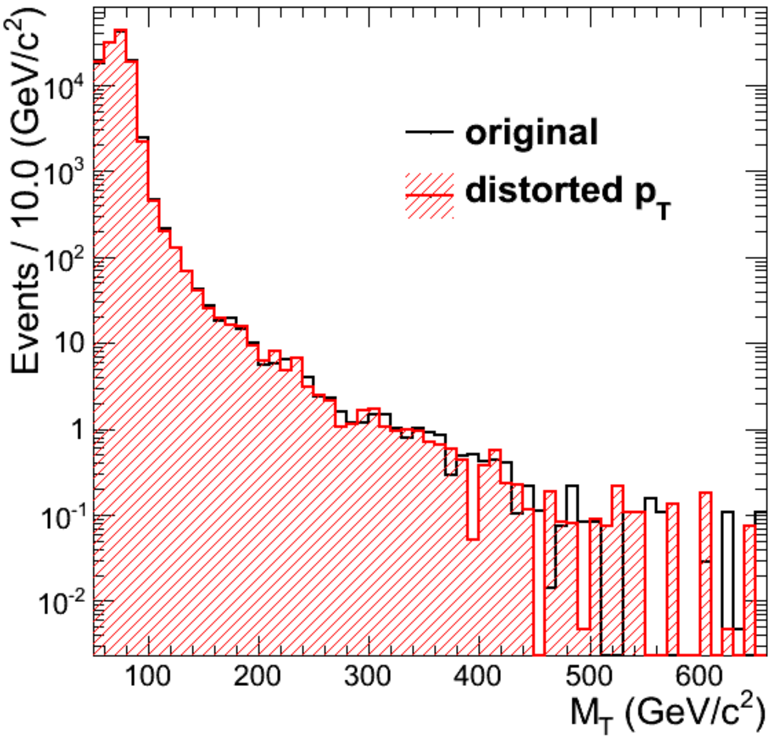

Figure 8.14: M_T distribution for all background samples and *distorted* M_T. The hadronic recoil correction is not applied in this distribution.

M_T threshold	200 GeV/c^2	300 GeV/c^2	500 GeV/c^2	600 GeV/c^2
Default	48.55	12.1	1.06	0.50
Distorted p_T	48.54	11.2	1.17	0.44
Rel. difference	0.02%	~8%	~9%	~12%

Table 8.10: Expected number of events from SM processes selected above a certain M_T threshold according to the original MC and the one where the p_T has been distorted.

8.4.3 E_T^{miss} Resolution

The hadronic component of E_T^{miss} is obtained directly from a data sample for the dominant $W \to \mu\nu$ background, so the simulation should already describe the data correctly. However, at high values of E_T^{miss} the statistics of the data $Z \to \mu\mu$ sample is reduced and to account for a possible fluctuation an uncertainty of 10% on the hadronic component of the E_T^{miss} resolution was considered. This factor was used to smear the x and y components of the reconstructed E_T^{miss} in all the MC samples, in a similar way as it was done with the muon p_T. The smeared M_T distribution for the background compared to the original one is shown in Figure 8.15. The number of events from SM processes above several M_T thresholds given by the original simulation and the one with the smeared E_T^{miss} can be seen in Table 8.11. The effect for low masses is negligible, at the permil level, while due to the lack of statistics affects more the high M_T region, being the difference about 15% for 500 GeV/c^2.

For the W' signal, for which E_T^{miss} comes solely from MC prediction, the same smearing was applied, the impact on the number of events is found to be below 0.3% for all the masses considered.

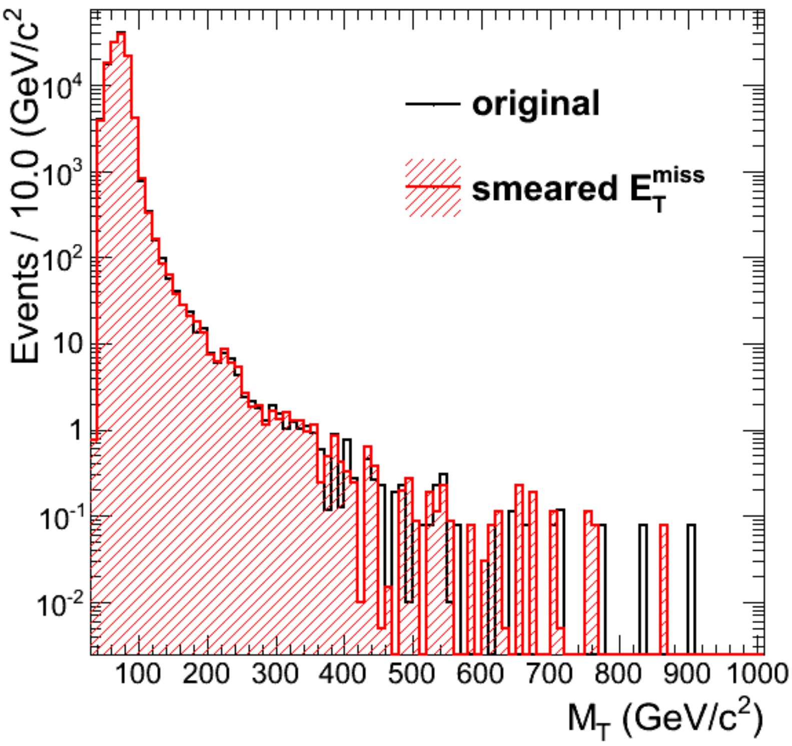

Figure 8.15: Final M_T distribution for all background samples and *smeared* M_T, considering a 10% uncertainty on the hadronic component of the E_T^{miss} resolution .

8.4.4 Efficiencies

- **Reconstruction and selection efficiencies:** Efficiencies and their uncertainties are determined from a sample of Z→ $\mu\mu$ events using the Tag and Probe method, as discussed in Section 8.3. The statistical uncertainty on the correction

M_T threshold	200 GeV/c^2	300 GeV/c^2	500 GeV/c^2
Default	54.2	12.5	1.61
smeared E_T^{miss} resolution	55.8	13.4	1.78
Rel. difference	∼3%	∼16%	∼15%

Table 8.11: The number of events for various M_T thresholds compared with the default and the smeared E_T^{miss}, where the hadronic component of the distribution is smeared according to a 10% resolution uncertainty.

factor, the ratio between the efficiency obtained with data and the reference MC, yields 0.3%. The use of Z events limits the sensitivity of the method to momenta up to ∼200 GeV/c, given the small statistics. The extrapolation to higher p_T was studied with W' samples in comparison to simulated W boson events (see Table 8.9). The variation on the combined efficiency, $\epsilon_{Mu+sel+isol+track}$, from these studies amounts to 3% (covering the systematic error associated to the Tag and Probe method). This value is used as the systematic uncertainty on the muon efficiency, including all factors (reconstruction, identification, selection and isolation) except for the trigger, and applied to the estimation of signal events.

- **Trigger efficiency:** The trigger efficiency yields values of ∼92% for the Run2010B data and ∼88% for the Run2010A data, being the correction factor between data and simulation ∼0.97, which is applied to the expected number of signal events and background events from MC. This value is in agreement with the results obtained with the same technique [42]. A second method using jet-triggered samples presented in that document gives a 1.5% lower efficiency. This value was taken as a conservative uncertainty on the trigger efficiency for signal yield estimations. The decision is also motivated by the fact that the MC trigger efficiency obtained with the W and W' samples differ approximately by the same amount.

8.4.5 Cross Section Uncertainties

For the W' signal an uncertainty of 10% in the predicted cross section is assigned, due to PDF uncertainties. This value is obtained by reweighting each event using all the elements of the CTEQ6 PDF set (used for the generation of the sample).

According to Ref. [73], the uncertainty on the di-bosons (WW, ZZ, WZ) production cross section is smaller than 5% and it is about 5% on $Z \to \mu\mu$ and W $\to \mu\nu$, including the uncertainty due to PDF, α_S and factorisation/renormalisation scales. The uncertainty on the theoretical prediction for $t\bar{t}$ cross-section is around 15% [73].

A summary of the systematic uncertainties and their impact on the signal and background event yield is presented in Table 8.12. For the background estimation two ranges have been considered, the total M_T region and the signal region, where the efficiencies are extrapolated and due to the lack of statistics resolution effects could have a larger impact on the final number of events.

Source of systematic error	Signal	Background (all M_T)	Background Signal region
Integrated luminosity	4%	4%	4%
Trigger efficiency	1.5%	1.5%	1.5%
Reconstruction and selection efficiency	3.0%	1.0%	3.0%
Muon p_T resolution and scale	1.0%	0.3%	10.0%
E_T^{miss} resolution	0.3%	0.2%	15 %
Theoretical cross section	10%	∼5%	∼5%
Total (lumi not included)	10.5%	5.3%	20%

Table 8.12: Systematic uncertainties due to the different sources on the signal and background event yields. For the signal two regions are considered, the whole spectrum where the resolution effects are negligible and the high M_T region, to estimate a realistic systematic for the total number of events in the search window.

Chapter

9

Results of the $W' \to \mu\nu$ Analysis

In this chapter, the selected data are compared to the background prediction and to the expectation of hypothetical W' signals, once the simulation includes the corrections described previously. Distributions and numbers for both are discussed. Since no significant excess is found in the data and the selected events agree well with the expected contribution from known SM processes, upper limits on the production cross section times branching fraction for the production of hypothetical W' bosons decaying into muon and neutrino pairs are derived. The statistical method used for the limit calculation is briefly reviewed.

9.1 Final Distributions

After applying the corrections discussed in the previous chapter (hadronic recoil correction and efficiency correction factor), a very good agreement between data and background prediction (PYTHIA and POWHEG Monte Carlo samples) can be observed, see Figure 9.1. The following distributions are shown: muon ϕ, η and muon transverse momentum, missing transverse energy in the event, angular difference between muon and E_T^{miss} and ratio p_T/E_T^{miss}. Like in the previous plots, in Chapter 8, the data and background distribution are shown along with the signal for two hypothetical W' bosons with masses $M_{W'} = 1500$ GeV/c^2 and $M_{W'} = 1000$ GeV/c^2. The individual composition of the backgrounds after all selection steps correspond to the samples listed in Table 8.2.

The full spectrum of the transverse mass M_T reconstructed from the muon and

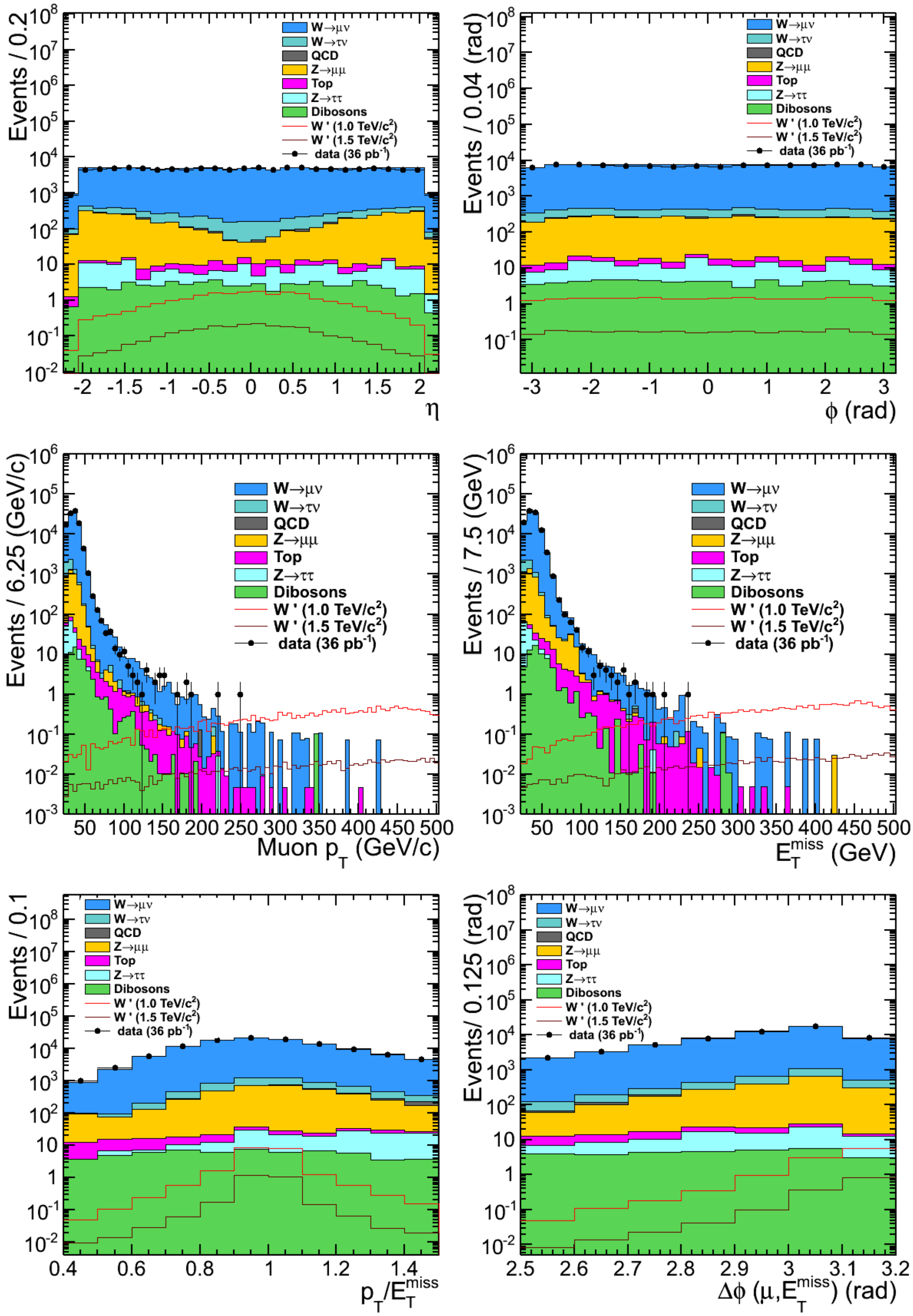

Figure 9.1: From top to bottom and from left to right, muon pseudorapidity, η, azimuthal angle, ϕ, and transverse momentum and kinematic variables related to the event: transverse missing energy, ratio p_T/E_T^{miss} and angular difference $\Delta\phi$ for data, background simulation and two W' mass points.

E_T^{miss} is presented in Figure 9.2. The dominant background process up to high transverse masses is $W \to \mu\nu$, given its almost identical signature to the W' signal. Smaller contributions are due to $Z \to \mu\mu$ (where one muon escapes detection) and top events. Diboson decays yielding a single high p_T muon and E_T^{miss} can contribute with a few events, even at large M_T. The cumulative plot is shown in Figure 9.3.

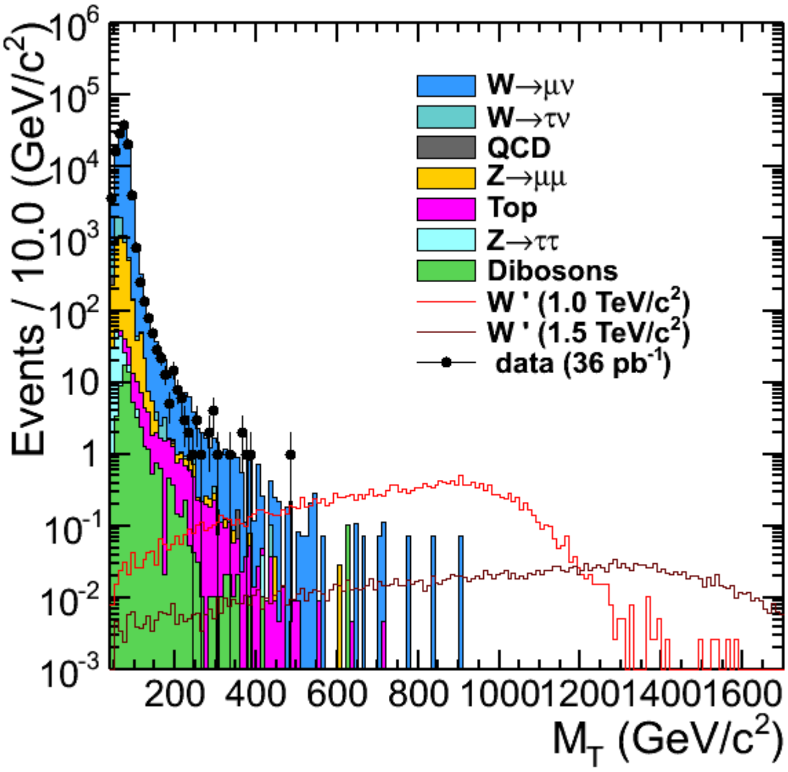

Figure 9.2: M_T distribution after all the selection steps and corrections are applied to the simulation. The MC backgrounds and 2010 data are shown along with two hypothetical W' signals.

The agreement between data and the expected background estimation from simulation in the whole M_T region is good, there is a small excess in the MC background prediction, nonetheless, the number of events is compatible within the errors.

The highest transverse mass event observed with 2010 collision data has $M_T = 487$ GeV/c^2. It is displayed in Figure 9.4 to illustrate how a expected signal event would look like in the detector. The transverse view is presented on the left and the longitudinal one on the right figure. The muon is represented by a red line, it is reconstructed in the central part of the detector, the barrel. The muon chambers containing hits are darker than the rest. E_T^{miss} is represented by a blue arrow. The longitudinal component of the direction of the neutrino is unknown, so the arrow indicates only the direction in the transverse plane. Charged particles tracks (light yellow lines) accompanying the process and the deposited energy (red towers) in the calorimeter cells are also displayed.

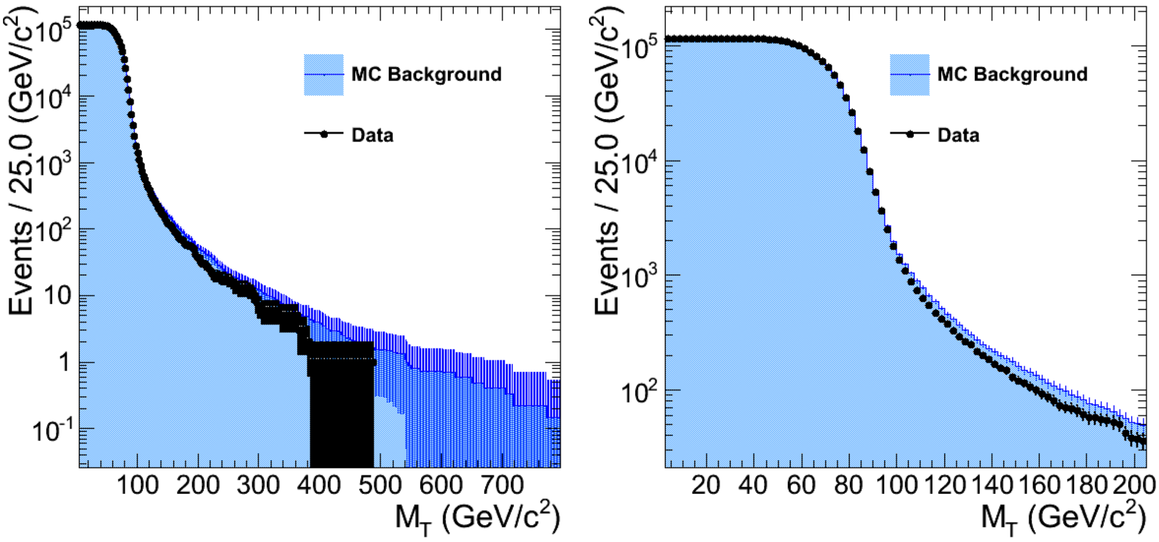

Figure 9.3: The cumulative distribution of the transverse mass after all selection steps, for the whole spectrum and zoomed to M_T <200 GeVc/c^2.

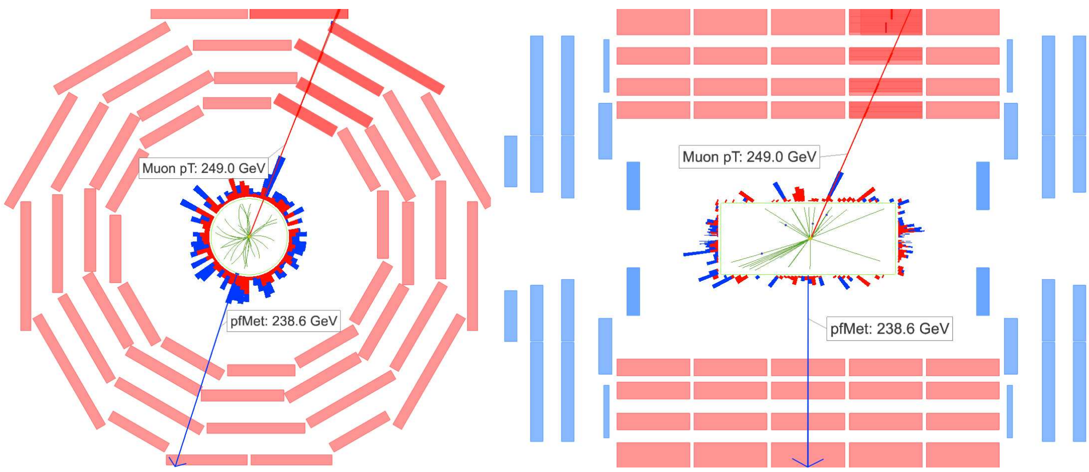

Figure 9.4: Display of the highest M_T event with 2010 data as measured by CMS. The transverse view is shown on the left and the longitudinal one on the right. The four barrel muon stations are shown in red, the forward muon stations in blue. Charged particle tracks as well as the deposited energy per calorimeter cell are displayed. The muon is symbolised by a red line, and the E_T^{miss} (pfMET) by a blue arrow. The values for muon p_T and E_T^{miss} are given.

The data sample contains 114064 events, compared to an expected number of 115481 ± 250 (stat) ± 5774 (sys) background. The total relative systematic uncertainty on the background event numbers is dominated by the uncertainties in the luminosity and the cross sections used for normalisation (∼4% each), followed by the uncertainty on the muon reconstruction and trigger efficiency correction (∼2% for both of them).

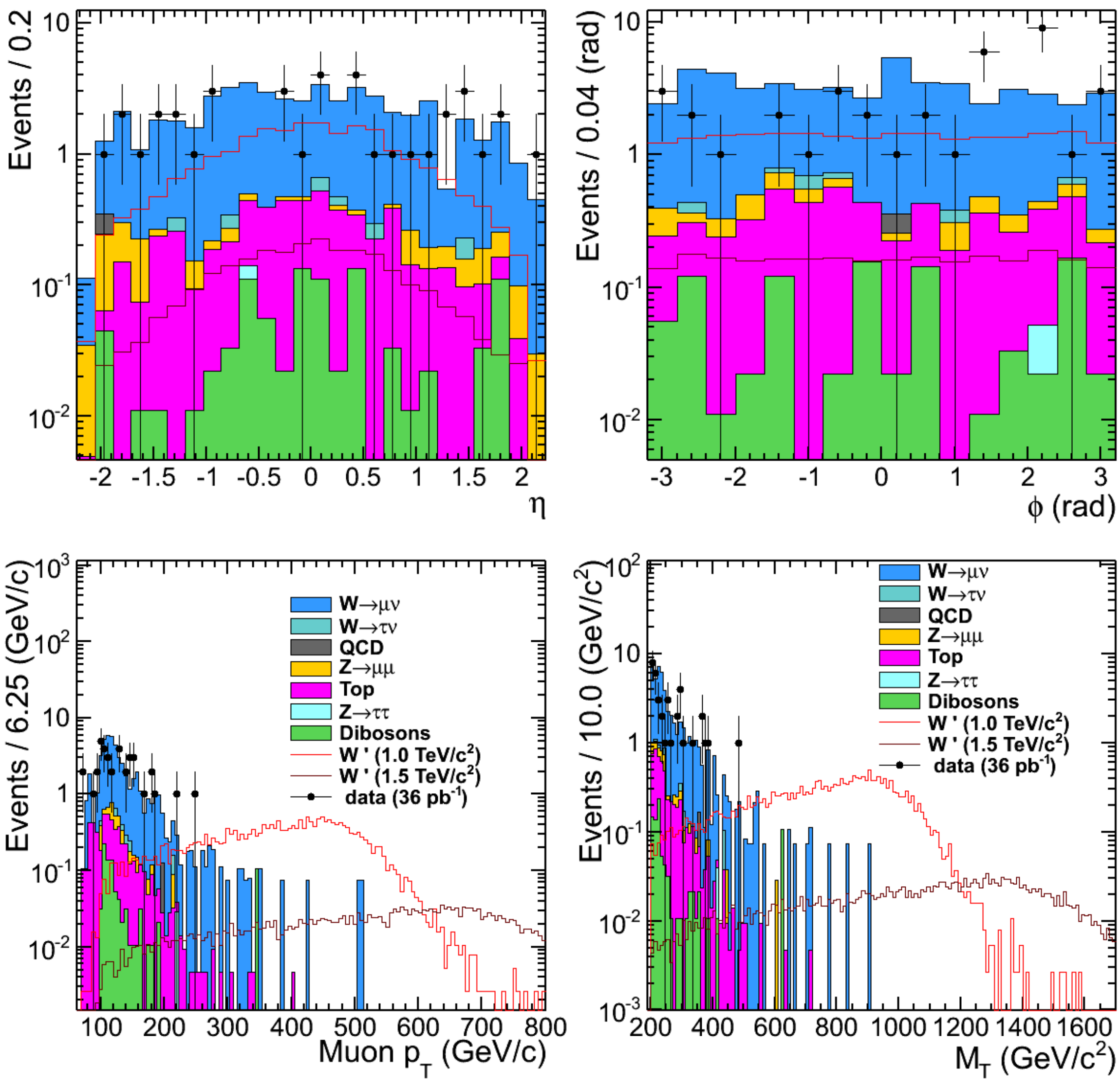

Figure 9.5: From top to bottom and from left to righ, muon variables, η, ϕ and p_T, and M_T of the event, for the ones fulfilling M_T >200 GeV/c^2 .

In Figure 9.5 the kinematic variables of the muon η and ϕ, together with the transverse momentum and transverse mass distribution for events with $\mathrm{M}_T > 200$ GeV/c^2 can be viewed, for data and signal and background simulated samples. The MC prediction agrees with the data distributions in all variables also for events in the tail of the M_T distribution. The threshold is set in 200 GeV/c^2 in order to keep reasonable statistics in data to perform the comparison between data and simulation. Table 9.1 summarises the number of events after all selection procedure for different M_T ranges for data, SM background and signal simulation. The simulated samples are corrected with the factors already explained. The number of events of two W' mass points are included to have an estimate of the proportion between the expected signal compared to the background events. At high M_T, the systematic error associated to the background estimation is dominated by the error associated to the resolution and scale of the muon and E_T^{miss}.

Minimum M_T	100 GeV/c^2	200 GeV/c^2	400 GeV/c^2	500 GeV/c^2
N_{data}	1360	37	1	0
N_{Bckg} (MC)	1531 ± 52	49.5 ± 1.9	3.86 ± 1.07	1.54 ± 0.64
W' $M_{W'}$=1000 GeV/c^2	22.6 ± 2.3	21.3 ± 2.1	20.0 ± 2.0	18.4 ± 1.8
W' $M_{W'}$=1500 GeV/c^2	2.56 ± 0.27	2.52 ± 0.26	2.39 ± 0.24	2.26 ± 0.24

Table 9.1: Number of events for various M_T windows, data, background events (only SM) and the expected number of events for two W' mass points. Simulation samples are normalised to the luminosity of the data sample, 36 pb^{-1}. The error associated to the signal events come mainly from the uncertainty in the PDFs.

To ensure that the choice of a certain muon algorithm for the p_T determination does not bias the results, the expected number of events for several mass windows was extracted as well with the rest of the available algorithms. The results are listed in Table 9.2. The background prediction is similar with the rest of the algorithms. Although according to the Picky and TPFMS algorithms one data event would survive up to $M_T > 500$ GeV/c^2, this is compatible with the SM background prediction.

Algorithm	$M_T > 200$ GeV/c^2		$M_T > 300$ GeV/c^2		$M_T > 400$ GeV/c^2		$M_T > 500$ GeV/c^2	
	Data	SM MC	Data	SM MC	Data	SM MC	Data	SM MC
Cocktail	**37**	**49.5 ± 1.9**	**7**	**12.0 ± 1.4**	**1**	**3.86± 1.07**	**0**	**1.54 ± 0.64**
Tracker	37	51.8 ± 2.0	6	12.1 ± 1.4	1	3.94 ± 1.09	0	1.60 ± 0.66
TPFMS	38	50.4 ± 1.4	7	11.8 ± 1.4	2	3.78 ± 1.05	1	1.47 ± 0.61
Picky	38	50.6 ± 1.4	8	11.9 ± 1.4	2	3.74 ± 1.04	1	1.55 ± 0.64

Table 9.2: Number of events for various M_T windows, data, background events for several muon algorithms.

Since there is no observed excess of data at the high M_T region beyond the Standard Model background prediction, an upper limit can be set on the W' production cross section times branching fraction, which can be translated as a lower limit on the mass of the potential W'. The background events are obtained with the Monte Carlo once the necessary corrections to the simulation using data based methods are applied, so that it reproduces the data adequately.

In the $W' \to \mu\nu$ analysis an alternative approach was employed to estimate the expected number of background events in the search region, based on the extraction of the total background contamination from the data using the sidebands of the

M_T spectrum, which is expected to provide a reliable estimate of the background events. This second method, chosen for the publication [84], is presented in the Appendix A profiting for the developed tools, as a cross-check of the approach chosen in this thesis.

9.2 Statistical Procedure for the Limit Setting

The limit is set in the framework of the Reference Model [66], described in Chapter 7. As the potential W' signal would peak at large values of transverse mass, a high threshold on the transverse mass is set to reduce the amount of background in the search window without significantly affecting the signal yield.

The underlying statistical method is based on counting the number of data events above an optimised M_T threshold (the *search window*) and comparing it to the expected number of signal and background events including all systematic uncertainties. In other words, the aim is to quantify the level of agreement of the number of data events d with the sum of the different background processes b_i and a potential signal s with cross section σ.

The upper limit on the cross section for the production of a boson W' is calculated as a function of the boson mass, using a *Bayesian technique*, and it is later on translated into a lower limit in the mass, as aforesaid. A brief review of the method follows.

The probability of observing D data events is given by *Poisson statistics* for a given mean value d. This is

$$P(D|d) = \frac{e^{-d} \cdot d^D}{D!}, \tag{9.1}$$

where the mean d is given by the sum of the signal, s, and N background samples b_i

$$d = s + \sum_{i=1}^{N} b_i = \sigma \cdot \mathcal{L} \cdot \mathcal{A} + \sum_{i=1}^{N} b_i = \sigma \cdot A + B \equiv d(\sigma, A, B) \tag{9.2}$$

where A stands for the product of the luminosity and the signal acceptance and B for the sum of all backgrounds. In general a conditional probability can be inverted according to the *Bayes theorem*

$$P(Y|X) = \frac{P(X|Y)P(Y)}{P(X)} \tag{9.3}$$

where P(Y) and P(X) are the *prior probabilities* of Y and X, the latter acts as a normalising constant, and P(Y|X) is the conditional probability of Y given X, also called the *likelihood function*, L. It is a conditional probability function considered as a function of its second argument, with the first one fixed, then

$$L \quad : \quad y \mapsto P(X|Y = y) \quad \Rightarrow L(y) \quad \propto P(X|Y = y). \tag{9.4}$$

Then, Bayes theorem can be written using the likelihood function as

$$P(Y|X) \propto L(y)P(Y). \tag{9.5}$$

This can be applied in order to derive P(d|D) from equation 9.1

$$P(d|D) = \frac{L(D|d)\pi(d)}{\mathcal{N}} \equiv \frac{L(D|\sigma, A, B)\pi(\sigma, A, B)}{\mathcal{N}} \tag{9.6}$$

where $\mathcal{N}$ ensures proper normalisation. $\pi(d)$ corresponds here to the *prior probability* of d, which depends on the signal σ, acceptance A and the total background B. The *posterior probability density* P(σ| D) for the signal cross section, σ, given the observed number of events D is obtained by integration over the parameters A and B:

$$P(\sigma|D) = \frac{1}{\mathcal{N}} \int \int L(D|\sigma, A, B)\pi(\sigma, A, B)dAdB \tag{9.7}$$

with $\mathcal{N} = \int P(\sigma|D)d\sigma$. The prior probability density $\pi(\sigma, A, B)$ can be disentangled under the assumption that any prior knowledge of A and B is independent of the signal cross section:

$$\pi(\sigma, A, B) = \pi(\sigma) \cdot \pi(A, B) \tag{9.8}$$

The following flat prior is used for the signal cross section

$$\pi(\sigma) = \begin{cases} \frac{1}{\sigma_{max}} & \text{for} \quad 0 < \sigma < \sigma_{\max} \\ 0 & \text{otherwise} \end{cases} \tag{9.9}$$

The upper bound on the cross section σ_{max} is chosen such that the posterior probability is negligible for $\sigma > \sigma_{max}$. Finally the Bayesian upper limit on the cross section at a certain confidence level, CL, is obtained by solving this expression

$$CL = \int_0^{\sigma_{CL}} P(\sigma|D)d\sigma \tag{9.10}$$

with CL=0.95, using the posterior probability

$$P(\sigma|D) \propto \int L(D|\sigma, a, B) \cdot \pi(A, B)dAdB. \tag{9.11}$$

The technical implementation in this analysis is done with the BATCalculator tool interfacing RooStats [89] (a joint project between the LHC experiments and the ROOT [90] team to provide validated suite of statistical tools within ROOT) with BAT [91] (Bayesian Analysis Toolkit, a tool for data analysis) to calculate the limits with the help of Markov Chain Monte Carlo methods.

Systematic uncertainties described in the previous chapter are incorporated in the limit setting procedure by treating them as nuisance parameters. A log-normal prior shape is used to integrate over these parameters.

The number of expected and observed events, including all the background sources discussed are detailed in Table 9.3, along with the search window (optimised for the best expected limit) and the expected and observed limits. The expected limit is obtained as the average limit of a large number of background-only pseudo-experiments where all the parameters (efficiencies, number of estimated background events, luminosity) take random values within their uncertainties. Figure 9.6 presents the expected limit

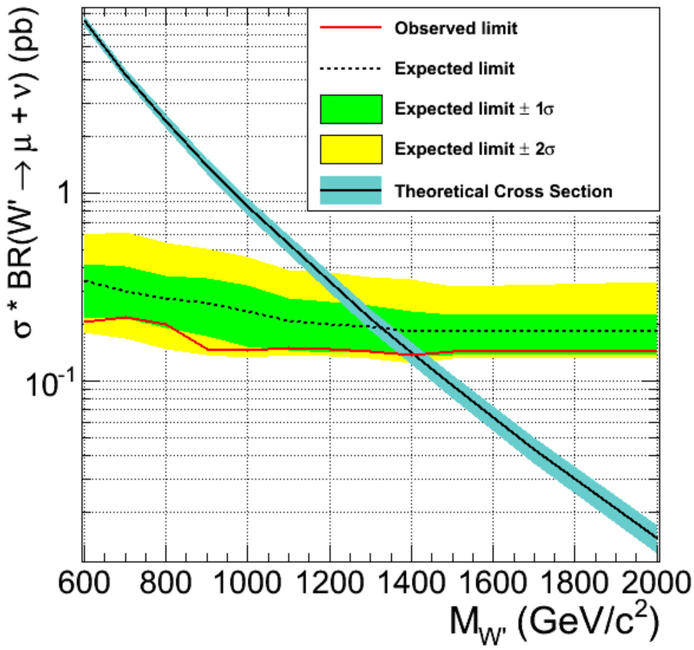

Figure 9.6: Expected and observed limit on $\sigma\times$BR for the channel $W' \rightarrow \mu\nu$ using a Bayesian method for a counting experiment. The background expectation is derived from the MC prediction and the small contribution of cosmic ray muons.

(with the one and two sigma bands showing its variation), the observed limit and the theoretical cross section for the production of a W' boson decaying into muon-neutrino as a function of $M_{W'}$. The intersection between the observed limit and the theoretical cross section determines the lower limit on the W' mass. Then, the existence of a W' boson with Standard Model-like couplings with a mass below 1.40 TeV/c^2 can be excluded at a 95% confidence level. This result is in agreement with the one published by the CMS collaboration.

The calculation of the limit was repeated without including the systematic uncertainty, the limit results unaffected, because the expected background is a fraction of an event in the search windows for the W' signals close to the mass where the limit is set, and no events are observed.

9.2.1 Limit as a Function of the Neutrino Mass

The limit obtained in the previous section is valid, as aforementioned, also in the case of a right handed W' decaying into a very light right handed neutrino. If the decay products were a muon and a heavy stable neutrino, not decaying in the detector, the signature of the process would be the same, a high p_T muon plus missing transverse energy. Then, the same analysis procedure could be applied. Note that if the neutrino decays, its products would be a charged lepton and an off-shell W^*, which would subsequently decay into a pair of quarks that hadronize into jets, so the signature to look for would be $W_R \rightarrow l_1 N_l \rightarrow l_1 l_2 jj$, as it is done in [92]. Thus, we restrict to the

$M_{W'}$ (GeV/c^2)	M_T (GeV/c^2)	N_{sig} (Events)	N_{bkg} (Events)	N_{data} (Events)	σ_{NNLO} (pb)	Expected limit (pb)	Observed limit (pb)
600	390	151.87 ± 16.10	4.12 ± 1.11 ± 0.83	1	8.290	0.340	0.203
700	450	78.34 ± 8.30	2.19 ± 0.78 ± 0.44	1	4.264	0.300	0.215
800	470	48.74 ± 5.18	2.06 ± 0.75 ± 0.42	1	2.426	0.276	0.200
900	500	29.00 ± 3.09	1.64 ± 0.67 ± 0.33	0	1.389	0.261	0.147
1000	530	17.78 ± 1.89	1.41 ± 0.63 ± 0.28	0	0.849	0.234	0.145
1100	590	10.83 ± 1.15	0.83 ± 0.49 ± 0.17	0	0.516	0.208	0.148
1200	610	7.09 ± 0.75	0.80 ± 0.46 ± 0.16	0	0.334	0.199	0.147
1300	630	4.66 ± 0.50	0.60 ± 0.35 ± 0.12	0	0.214	0.193	0.144
1400	630	3.05 ± 0.32	0.60 ± 0.35 ± 0.12	0	0.141	0.182	0.137
1500	680	2.12 ± 0.23	0.48 ± 0.29 ± 0.10	0	0.094	0.182	0.143
2000	690	0.31 ± 0.03	0.47 ± 0.29 ± 0.10	0	0.014	0.184	0.145

Table 9.3: W' mass point and the minimum M_T requirement for its search window, expected number of signal and background (including cosmics) events, along with expected and observed upper limit on the cross section for each W' signal sample. The NNLO cross section for each W' signal is also shown. The exclusion limit is determined using a Bayesian method.

hypothesis that the heavy neutrino is stable.

Pythia Parameter	Meaning
MSUB(354)	Switch W_R production
PMAS(352,1)	W_R mass
PMAS(349,1)	muon ν_R mass
PMAS(348,1)	electron ν_R mass
PMAS(350,1)	tau ν_R mass
MWID(349)= 0	stable ν_R

Table 9.4: Parameters to generate $W_R \to$ events with PYTHIA event generator

The aim of this section is to expand the limit extraction for different values of the neutrino mass, set a limit on the $(M_{W'}, M_{\nu_R})$ plane. Signal samples for this process were not simulated centrally for by the MC generator group in CMS, so they were produced privately. The W' samples were generated with PYTHIA, see the specific parameters to define the process in Table 9.4, assigning the same value of the neutrino mass to the three leptonic families. Assuming the strict LR symmetric model, the coupling constant and the CKM matrix elements are the same as the Standard Model ones. The W' mass points generated ranges between 800 GeV/c^2 and 1400 GeV/c^2 in steps of 100 GeV/c^2 and neutrino masses between 100-700 GeV/c^2. The idea lying behind this limit extraction is the similarity of the signature after the selection criteria, as aforementioned, and the feasibility of reconstructing the transverse mass in a similar way. The peak of the M_T distribution for a certain W' mass point is displaced towards lower values as the neutrino mass increases. This is illustrated in Figure 9.7, where the transverse mass for a W' signal of $M_{W'} = 1400$ GeV/c^2 is compared to the distributions obtained for a right-handed W' decaying into a neutrino of mass 200 GeV/c^2 and 500 GeV/c^2.

The cross section of the process varies if a heavy neutrino is produced instead of

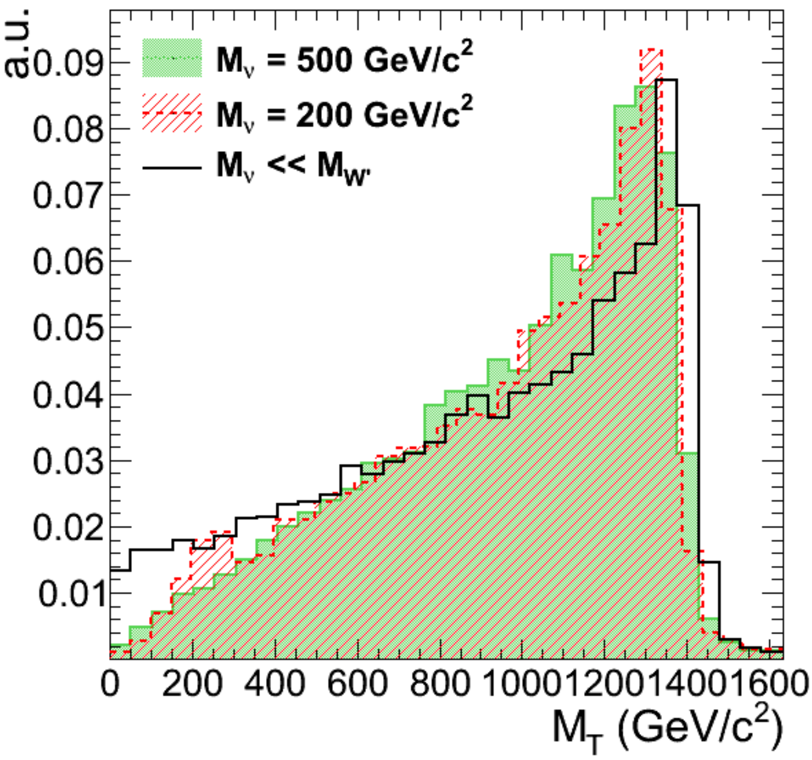

Figure 9.7: Transverse mass of a W' signal of $M_{W'}$ = 1400 GeV/c^2 with M_ν <<$M_{W'}$ (black histogram), M_{ν_R}=200 GeV/c^2 (full red histogram) and M_{ν_R}=500 GeV/c^2 (green histogram). The distributions are obtained at generator level.

a light one, decreasing as the neutrino mass increases. For the example considered of a W' of mass 1400 GeV/c^2, the cross section is 7% and 50% lower in the case of a heavy neutrino with M_ν=200 GeV/c^2 and M_ν=500 GeV/c^2 respectively, compared to the cross section of the W' signal listed in Table 9.3. Since QCD does not distinguish between left- and right-handed particles, the same k-factors ($\sigma_{NNLO}/\sigma_{LO}$) are applied.

The trigger efficiency and the muon reconstruction and selection ones are assumed to be similar for a W_R of the same mass to the one obtained with the left-handed particle generated with Pythia. In the selection procedure the variables that can be affected are the ones involving both the muon and E_T^{miss} , so the $\Delta\phi$ and p_T $/E_T^{miss}$ criteria. In Figure 9.8 those distributions are compared to the reference W' signal of $M_{W'}$ = 1400 GeV/c^2 and the W_R considering right-handed neutrinos of masses 200 GeV/c^2 and 500 GeV/c^2. The angle between the leptons $\Delta\phi$ is nearly unaffected while the $p_T/$ E_T^{miss} distribution is more spread and tends to lower values for higher values of the ratio between the neutrino and the W' masses, due mainly to the smaller momentum of the muon produced. In the light of these results, no dependence as a function of $\Delta\phi$ can be assumed, while the condition p_T $/E_T^{miss}$ is affected differently depending on the mass.

To obtain the number of events for each point in the mass plane $(M_{W'}, M_{\nu_R})$ instead of applying the analysis chain to all new samples, the number of signal events obtained

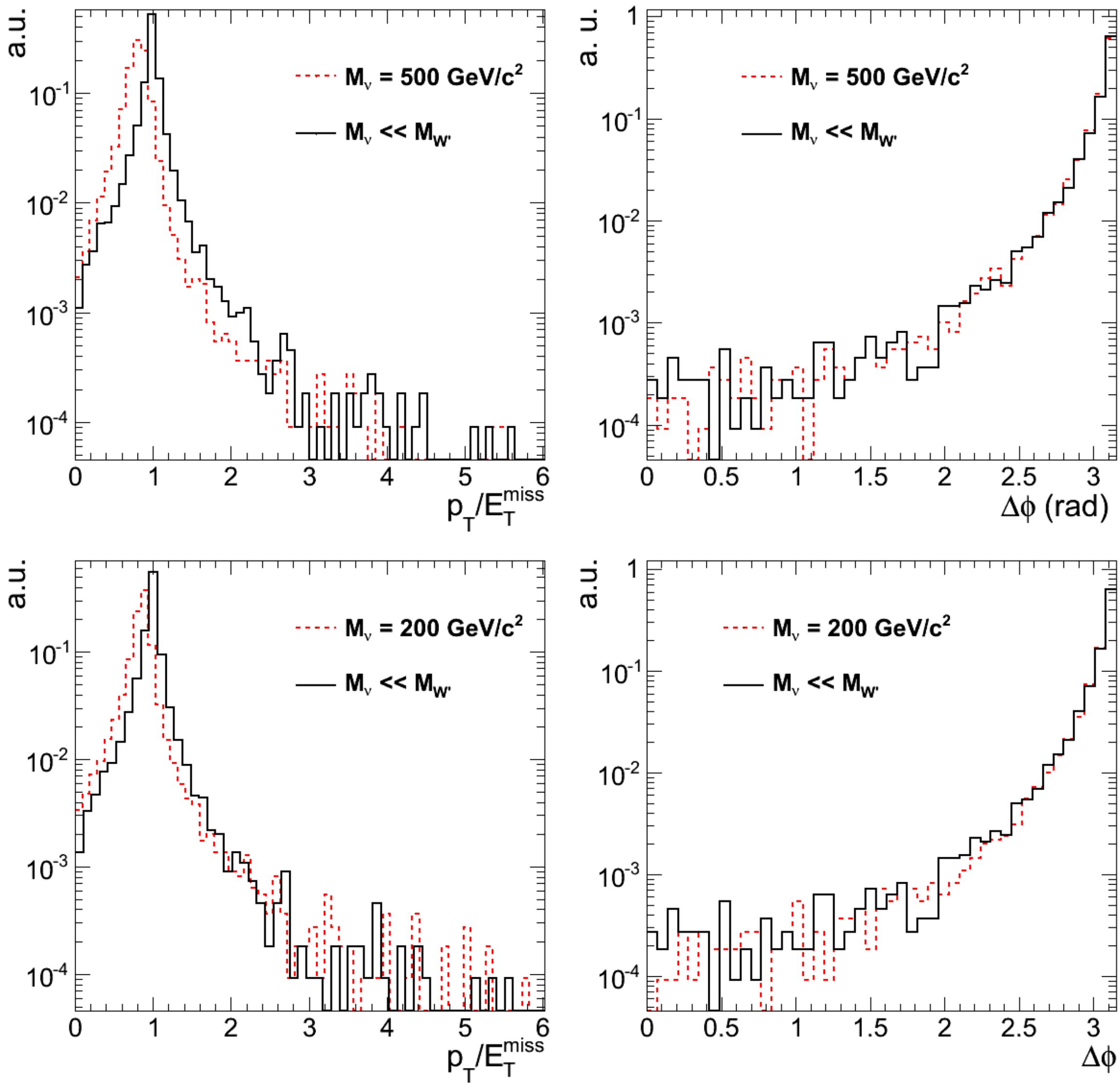

Figure 9.8: Ratio p_T/E_T^{miss} and angular difference between the leptons, $\Delta\phi$, for a W' signal of $\mathrm{M}_{W'} = 1400$ GeV/c^2 with M_ν <<$\mathrm{M}_{W'}$ (black histogram), M_{ν_R}=500 GeV/c^2 (top row, red dashed histogram) and M_{ν_R}=200 GeV/c^2 (bottom row, red dashed histogram). The distributions are obtained at generator level, normalised to area.

in the search region for each W' mass point was employed. This value was reweighted by the ratio of the number of events of W_R over W' in the $(M_T, p_T/E_T^{miss})$ plane in the selected region $(M_T^{thr}, 0.4 < p_T/E_T < 1.5)$, which are the two relevant variables affected by the neutrino mass. This weight is normalised to the ratio of the cross section between the two W' processes. The possible differences due to the rest of the cuts is considered negligible or at least small compared to the error associated to the expected signal events.

Evaluating the limit for each point in the the grid of W' masses and neutrino masses the exclusion region can be seen in Figure 9.9. The values are obtained with the same statistical method described above. The current and most stringent W' mass limit obtained by the DO Collaboration at Tevatron [93] is included in the figure.

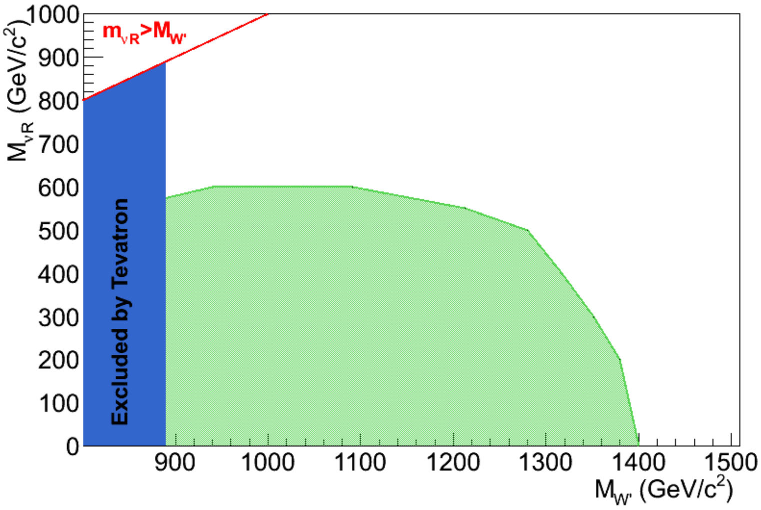

Figure 9.9: 95% CL excluded W_R mass region as a function of the right-handed neutrino mass, assuming $g_L = g_R$ and $V_L = V_R$. The diagonal line corresponds to the kinematic limit for the $W_R \to \mu\nu_R$ decay. The W' mass exclusion limit given by Tevatron [93] is included.

9.3 Combined Limit

For completeness, in this section the results obtained studying the $W' \to \mu\nu$ channel are combined with those from the electron one, $W' \to e\nu$ which has also been analysed by the CMS collaboration [94]. Since the latter is outside the scope of the work presented in this thesis, only the more relevant details for the combination are given. The individual limit for the electron channel excludes the existence of W' boson with masses below 1.36 TeV/c^2 at 95% CL, obtained as well with a Bayesian approach. This result superseded the previous limit obtained studying the same channel by the Tevatron experiments [68, 67]. Like in the muon case, no events are seen at high transverse masses. The details concerning the search window, the observed limit in the $\sigma \times BR$ in the electron channel and the observed limit combined with the muon channel are shown in Table 9.3.

Assuming lepton universality, the cross sections (at NNLO) for the signals used for both channels are the same. The luminosity uncertainty is assumed to be fully correlated between both channels, the rest of the systematic sources are considered as fully uncorrelated. With these premises, the limits for the two individual channels as well as the limit obtained by combining them are shown in Figure 9.10.

Using this method the existence of a W' boson with Standard Model-like couplings with masses below 1.58 TeV/c^{2}at the 95% confidence limit.

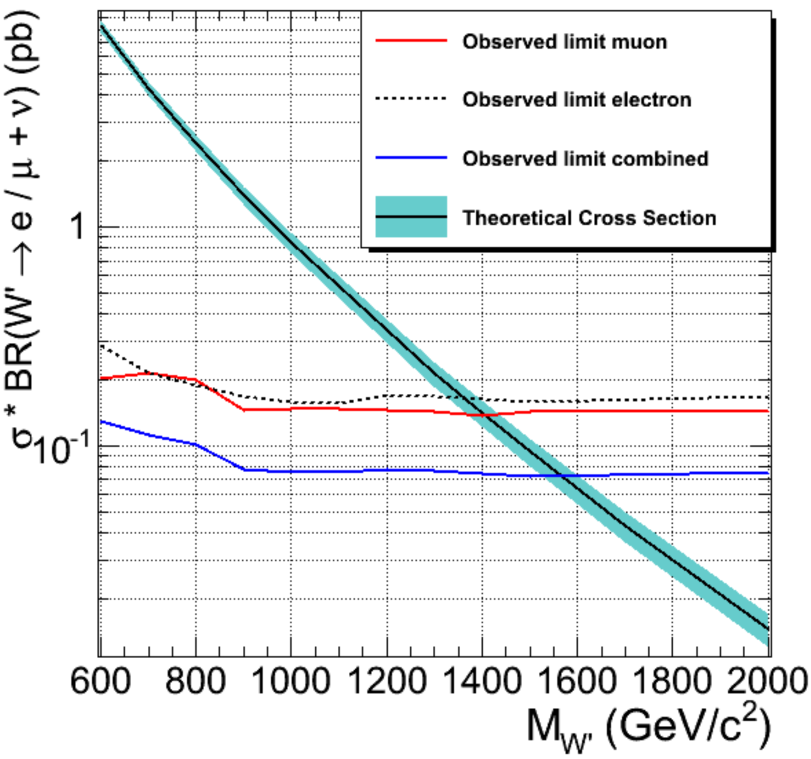

Figure 9.10: Individual limits on the cross section times branching fraction for the electron and the muon channels (red: electron, black dotted line: muon) and their combination (blue line) using a Bayesian technique.

$M_{W'}$ (GeVc^2)	σ_{NNLO} (pb) per channel	$\mathrm{M_T}$ (e) (GeVc^2)	Obs. limit e (pb)	$\mathrm{M_T}$ (μ) (GeVc^2)	Obs. limit μ (pb)	Obs. limit comb. (pb)
600	8.290	400	0.289	390	0.203	0.135
700	4.264	500	0.215	450	0.215	0.116
800	2.426	500	0.188	470	0.200	0.105
900	1.389	500	0.168	500	0.147	0.078
1000	0.849	500	0.159	530	0.145	0.076
1100	0.516	500	0.157	590	0.148	0.076
1200	0.334	650	0.170	610	0.147	0.078
1300	0.214	675	0.168	630	0.144	0.077
1400	0.141	675	0.164	630	0.137	0.076
1500	0.094	675	0.159	680	0.143	0.073
2000	0.014	675	0.167	690	0.145	0.078

Table 9.5: Search window, channel independent theoretical NNLO cross section for various W' mass points, excluded cross section times branching fraction for the electron channel, muon channel and combined. Numbers for the electron channel are from [94], with an integrated luminosity of 36 pb^{-1}.

Chapter

10

Conclusions

The work described in this dissertation focuses on the different aspects related to the muon performance relevant for the analysis. The muon reconstruction and identification was thoroughly studied, to ensure a good understanding of its performance, which is a basic step towards any physics measurement.

The focus was set on the performance of the muon trigger, from the local Barrel trigger up to the Level 2 in the High Level Trigger system. The performance of the local trigger was studied before the first collision data arrived, profiting from the large amount of cosmic data collected during 2008 and 2009. Cosmic data studies allowed the muon detector to be perfectly ready and commissioned for the collision data. The results obtained with these analyses show a good correlation between the information from the L1 trigger and the offline reconstruction in terms of position and direction of the segments. The resolution of the trigger is in agreement with the design performance. Moreover, this work helped to spot few problems, solved for the collision data taken. The parameters used in the seeding of the L2 step of the HLT were carefully evaluated, showing that the current implementation was good enough to reach the required muon resolution without the need of further optimisation.

Regarding the offline muon reconstruction, the performance of the dedicated high p_T muon reconstructors was analysed as it was fundamental for the W' search, guaranteeing that no misreconstructed muons appear in the tail of the distributions, which would affect the limit calculation. The chosen algorithm was checked to be the optimal one for the analysis with simulated and cosmic muon data samples, given the lack of statistics of high-p_T muons in the 2010 collision data. The results also indicate that the algorithm performs well with collision data.

A great effort was put on the single muon efficiency measurement, developing a data driven method based on a sample of $Z \to \mu\mu$ events, keeping in mind the fundamental aspects of the analysis the efficiencies were aimed for. The method takes into account the presence of background processes in the selected control data sample to obtain an unbiased efficiency. The efficiency was studied as a function of the muon kinematic variables p_T and η, showing a constant behaviour with muon p_T in the range where the muon statistics is significant. As a function of η, the efficiency decreases in the transition region between the Barrel and the EndCap subdetectors and it shows variations along the whole η range due to real effects of the detector. A relevant outcome was the different efficiency observed between negative and positive charged muons. This method was applied to determine the efficiencies for the $W \to \mu\nu$ cross section measurement and extended to the high muon p_T region for the $W' \to \mu\nu$ search analysis, for which the former process is the main background. In practice, a correction factor between the MC efficiency and the efficiency measured in data, around 4% lower, was applied to the yield of the simulated samples.

Finally a search for the production of heavy charged gauge bosons and their decay into muon and neutrino is presented in this thesis. The data analysed corresponds to the full pp collision data set collected during 2010 by the CMS experiment at a centre of mass energy of 7 TeV, which amounts to an integrated luminosity of 36 pb^{-1}.

The potential new bosons are predicted by many extensions of the Standard Model. Here a general approach is considered: the W' appears as a heavy copy of the Standard Model W boson. The couplings to quarks and leptons of the electroweak interaction are identical to the Standard Model couplings, while the interaction with other gauge bosons is suppressed as well as interactions with other heavy gauge bosons as the hypothetical Z'.

The transverse mass spectrum of the muon and neutrino pairs was investigated for deviations with respect to the SM predictions, however no excess in data over the background expectation was observed. Moreover, the agreement between the background prediction and data is good. Thus an upper limit at 95% CL on the production cross section times branching ratio, $\sigma \times \mathcal{B}(W' \to \mu\nu)$, was set. Comparing the observed limit with the theoretical predictions, a lower limit on the W' boson mass is obtained:

$$M_{W'} > 1.40 \text{ TeV/c}^2 \text{ (at 95\% CL)}$$

in agreement with the published result.

In this dissertation, the search was extended to a generic search for a W' decaying into a muon and a heavy stable right-handed neutrino, a process with the same signature, setting limits to the W' mass as a function of the hypothetical neutrino mass.

CMS performed the search of the W' boson in the electronic channel as well, excluding the existence of a W' boson with a mass below 1.36 TeV/c^2 at 95% CL. Combining it with the result presented in this thesis yields a lower mass limit of

$$M_{W'} > 1.58 \text{ TeV/c}^2 \text{ (at 95\% CL).}$$

To conclude, CMS collected 36 pb^{-1} in 2010 at centre of mass energy of 7 TeV. This data was analysed not only to measure the known SM processes thanks to the excellent performance of the detector, but also to search for new particles, one of them being the analysis presented in this thesis. Many of them, despite the reduced luminosity, already surpassed the previous limits. With the fast increasing amount of data collected by the LHC experiments, physics beyond the SM will hopefully come into reach.

Appendix

A

Background Estimation from Sidebands in the Transverse Mass Spectrum

The basis of this method is to fit the data behaviour in a background-dominated M_T region (sideband region) and to extrapolate the fitting function to the region of interest (search region), the high transverse mass region, hence, to evaluate the number of background events from the fit in data instead of the MC prediction. This method is purely based on data and does not rely on the MC prediction. However, to asses its validity the fit was repeated with the simulated samples to compare the results with the actual number obtained with MC.

The total pp background contamination in the signal region is estimated using the control region, selected to be the range $180 < M_T < 350$ GeV/c^2 of the M_T spectrum. A relativistic Breit-Wigner function is used as an ad-hoc empirical shape to fit the sideband, both in the data and the MC, a region which is dominated by $W \to \mu\nu$. This function is expected to describe correctly the tail of the M_T spectrum, since it is basically made of off-peak W events. Once the background is modelled in the control region, the fitting function is used to calculate the number of expected background events in the different M_T search windows.

The choice of the sideband lower and upper limits was optimised with MC to minimise the contribution from a hypothetical W' signal and to find a region that gives reliable extrapolations of the background in the signal region. According to the MC prediction, 70.6±8.2 events are expected in the sideband region including all SM backgrounds for an integrated luminosity of 36 pb^{-1}. In that region the expected number of events of a potential W' ranges from 1.6 for a W' of $M_{W'}=$ 1000 GeV/c^2, to 0.8 with $M_{W'}=$ 1100 GeV/c^2 and to 0.12 events for a signal with mass of 1500 GeV/c^2. These numbers translate into a relative contamination of 2%, 1.1% and 0.1%, respectively. Taking into account that W' masses below 1.1 TeV/c^2 are already excluded [68, 67], the potential contamination would be in any case smaller than 1%, therefore the sideband region chosen can be safely considered to be fully composed of background events. In data the same sideband region contains 52 events, consistent with the MC prediction within the systematic uncertainties discussed previously.

The results of the fit to the data and MC are presented in Figure A.1, in both cases the fit describes correctly the data: the normalised χ^2/ndof is 0.57 for data and 0.19 for MC.

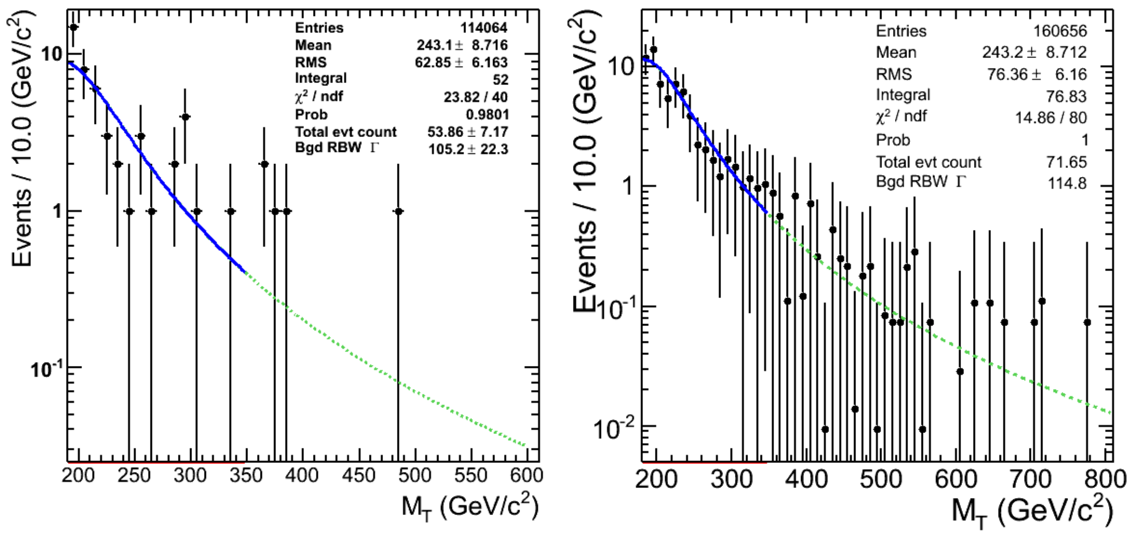

Figure A.1: Fits on the sidebands region of the M_T spectrum, 180<M_T <350 GeV/c^2, for data (left) and MC (right). The fits in that range describe well the distributions and can be used to evaluate the expected number of background events in the tail.

The values obtained with the fit for the sideband region and several M_T regions can be found in Table A.1. The errors quoted correspond to the statistical error given by the fit. The comparison shows that the numbers from the fits in the sideband region agree with the histogram entries in the corresponding bins both in data and simulation, which is a first hint of the goodness of the method. The background extrapolation in the $M_T >$ 400, 500 and 600 TeV/c^2 regions correctly predicts the number of background events in the MC, therefore the extrapolation in data is expected to perform well also. The expected number of background events in MC and data, as determined by the fit, agrees within 1.0 to 1.5 sigma.

The robustness of the sidebands region fit and the uncertainty in the number of background events in the signal region obtained from the fit was studied by varying the binning of the M_T distribution, see Table A.2. The highlighted values correspond to

	180 <M_T < 350 GeV/c^2	M_T > 400 GeV/c^2	M_T > 500 GeV/c^2	M_T > 600 GeV/c^2
MC (corrected)				
# of evts	70.6 ± 8.2	3.8 ± 1.07	1.54 ± 0.64	0.73 ± 0.43
Fit	71.7 ± 8.2	3.3 ± 0.8	1.52 ± 0.36	0.82 ± 0.20
Data				
# of evts	52	1	0	0
Fit	53.9 ± 7.2	2.2 ± 0.6	1.02 ± 0.28	0.55 ± 0.20

Table A.1: Expected number of background events according to the simulation (normalised to 36 pb^{-1}) and number of data events observed in different M_T regions. They are compared with the extrapolation obtained from the fit.

the binning chosen as a reference. The prediction of number of events in the sideband region is stable, the largest difference being of the order of 0.2%. The effect in the extrapolated region is about 3.7%, negligible compared to the statistical error coming from the fit (not smaller than 25%).

The effect of choosing different M_T interval ranges (lower, upper limits) defining the sideband region was also studied, the results can be seen Table A.3. The lower limit has little influence on the extrapolated number of events, while the upper limit affects more due to the larger statistics involved. In any case, the variation in the number of events with respect to the chosen sideband range lays within the statistical precision, not being larger than 10-13% depending on the minimum M_T.

Bin size (GeV/c^2) (GeV/c^2)	180<M_T < 350 (GeV/c^2)	M_T > 400 (GeV/c^2)	M_T > 500 (GeV/c^2)	M_T > 600 (GeV/c^2)
2.5	53.9±7.2	2.22±0.62	1.02±0.28	0.55±0.20
5	53.9±7.2	2.18±0.61	1.00±0.28	0.55±0.20
10	**53.9±7.2**	**2.23±0.62**	**1.02±0.28**	**0.55±0.20**
20	54.0±7.2	2.14±0.61	0.98±0.28	0.53±0.15

Table A.2: Robustness test of the sideband fit method. The number of extrapolated background events in the data is calculated by varying the binning of the M_T distribution and the interval range defining the sideband region. Reference values, with the binning of 10 GeVc^2, are shown in bold font.

The systematic uncertainty assigned in the extrapolation of the background in the signal region is the difference between the predicted number with data and with MC , as given by the fit. This systematic effect is about ∼25% for the high-M_T bins. Due to lack of events surviving above M_T =500 GeV/c^2, the expected background in the signal region with a better accuracy cannot be quantified. However, this effect has no impact on the search sensitivity and the exclusion limit because no events are observed and the expected number is a fraction of an event for the highest mass search windows.

The limit on $\sigma \times BR$ was calculated with the number of background events obtained from the fit to the sideband region in data, following the same statistical procedure as in Chapter 9. The result is shown in Figure A.2 together with the observed limit

Sideband region (GeV/c^2)	$M_T > 400$ (GeV/c^2)	$M_T > 500$ (GeV/c^2)	$M_T > 600$ (GeV/c^2)
180-350	**2.23 ± 0.62**	**1.02 ± 0.28**	**0.55 ± 0.20**
200-350	2.16 ± 0.77	0.97 ± 0.35	0.52 ± 0.19
150-350	2.37 ± 0.45	1.12 ± 0.21	0.62 ± 0.12
150-300	2.37 ± 0.45	1.12 ± 0.21	0.62 ± 0.12
180-380	2.16 ± 0.59	0.99 ± 0.27	0.53 ± 0.15
180-330	2.16 ± 0.59	0.99 ± 0.27	0.53 ± 0.15

Table A.3: Estimated number of data obtained with the sideband fit in data, varying the interval range (lower, upper limits) defining the sideband region.

m(W') (GeV/c^2)	M_T (GeV/c^2)	N_{bkg} - fit (Events)	N_{bkg} (Events)	Observed - fit limit (pb)	Observed limit (pb)
600	390	2.37 ± 0.65 ± 1.19	4.12 ± 1.11 ± 0.83	0.211	0.203
700	450	1.42 ± 0.39 ± 0.72	2.19 ± 0.78 ± 0.44	0.222	0.215
800	470	1.22 ± 0.34 ± 0.62	2.06 ± 0.75 ± 0.42	0.208	0.200
900	500	1.02 ± 0.28 ± 0.56	1.64 ± 0.67 ± 0.33	0.148	0.147
1000	530	0.81 ± 0.22 ± 0.41	1.41 ± 0.63 ± 0.28	0.147	0.145
1100	590	0.57 ± 0.16 ± 0.29	0.83 ± 0.49 ± 0.17	0.147	0.148
1200	610	0.51 ± 0.14 ± 0.26	0.80 ± 0.46 ± 0.16	0.143	0.147
1300	630	0.45 ± 0.12 ± 0.23	0.60 ± 0.35 ± 0.12	0.142	0.144
1400	630	0.45 ± 0.12 ± 0.23	0.60 ± 0.35 ± 0.12	0.140	0.137
1500	680	0.35 ± 0.10 ± 0.18	0.48 ± 0.29 ± 0.10	0.145	0.144
2000	690	0.33 ± 0.09 ± 0.27	0.47 ± 0.29 ± 0.10	0.147	0.145

Table A.4: Minimum M_T requirement for search window, expected number of background events extrapolated with the sideband fit to data and obtained from the MC prediction, along with the observed limit for each hypothetical W' mass.

obtained with the background prediction from MC. There is no significant difference, in both cases W' bosons are excluded below 1.40 TeV/c^2. Table A.4 contains the number of expected background events given by the extrapolation of the fit to data and the MC prediction, with the statistical and systematical errors, and the resulting observed limits.

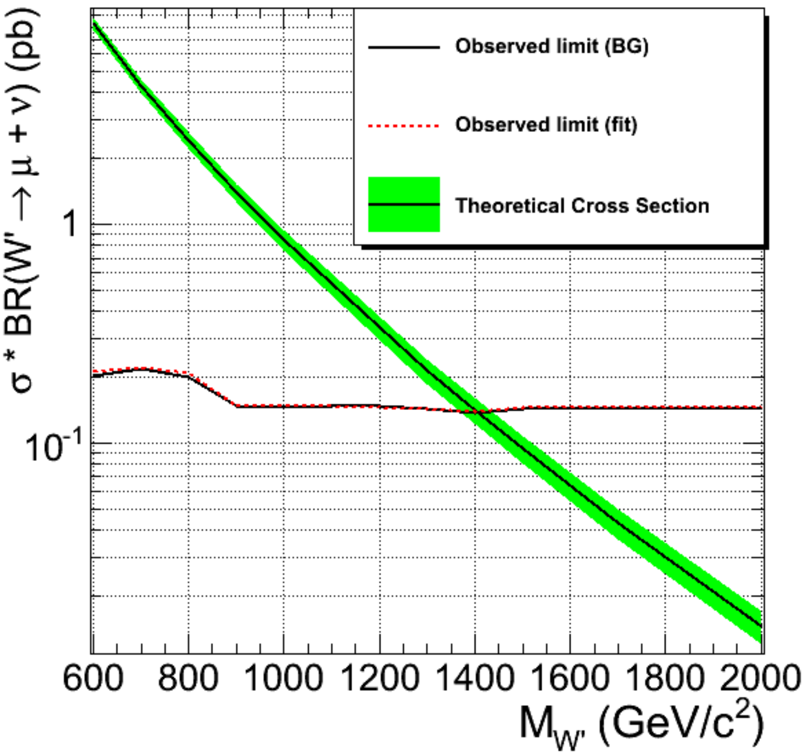

Figure A.2: Limits on the W' cross section times branching ratio, with the SM background predicted by the sideband fit method applied to the data (red dashed line) an the one using the prediction from the simulation (black line).

References

[1] S. L. Glashow. **Partial Symmetries of Weak Interactions**. *Nucl. Phys.*, **22**:579–588, 1961.

[2] A. Salam and J. C. Ward. **Electromagnetic and weak interactions**. *Phys. Rev. Lett.*, **13**:168–171, 1964.

[3] Steven Weinberg. **A Model of Leptons**. *Phys. Rev. Lett.*, **19**(21):1264–1266, Nov 1967.

[4] S. L. Glashow, J. Iliopoulos, and L. Maiani. **Weak Interactions with Lepton-Hadron Symmetry**. *Phys. Rev. D*, **2**(7):1285–1292, Oct 1970.

[5] F. Halzen and A. D. Martin. *Quarks and Leptons.* Wiley, 1984.

[6] Daniel V. Schroeder Michael E. Peskin. *An Introduction to Quantum Field Theory.* Addison-Wesley Advanced Book Program, 1995.

[7] C. Amsler et al. **Review of particle physics**. *Phys. Lett.*, **B667**, 2008.

[8] LEP Electroweak Working Group, http://lepewwg.web.cern.ch/LEPEWWG/.

[9] CMS publications, http://cdsweb.cern.ch/collection/CMS%20Papers?ln=en.

[10] CMS Collaboration. **Measurement of the $t\bar{t}$ production cross section and the top quark mass in the dilepton channel in pp collisions at $\sqrt{s}$ =7 TeV.** *oai:cds.cern.ch:1354581*, May 2011.

[11] ALEPH, DELPHI, OPAL, SLD, LEP Collaborations. **Precision electroweak measurements on the Z resonance.** *Phys. Rept. 427:257*, 2006.

[12] R. Barate et al. **Search for the standard model Higgs boson at LEP**. *Phys. Lett.*, **B565**:61–75, 2003.

[13] Stephen P. Martin. **A Supersymmetry Primer**. *arXiv:hep-ph/9709356v5*, 2008.

[14] CMS Collaboration. **A search for excited leptons in pp Collisions at $\sqrt{s} = 7$ TeV**. *oai:cds.cern.ch:1366774*, Jul 2011.

[15] O.S. Bruning et al. **The LHC design report v.1: the LHC Main Ring**. *CERN-2004-003-V-1*, 2004.

[16] O.S. Bruning et al. **The LHC design report v.2 : the LHC Infrastructure and General Services**. *CERN-2004-003-V-2*, 2004.

[17] B. Benedikt et al. **The LHC design report v.3 : the LHC Infrastructure and General Services**. *CERN-2004-003-V-3*, 2004.

[18] ATLAS Collaboration. **The ATLAS Experiment at the CERN Large Hadron Collider**. *JINST 3 S08003*, 2008.

[19] CMS Collaboration. **The CMS experiment at the CERN LHC**. *JINST 0803:S08004*, 2008.

[20] CMS Collaboration. **CMS technical proposal**. *CERN-LHCC-94-38*, **http://cdsweb.cern.ch/record/290969.**

[21] LHCb Collaboration. **LHCb technical design report: Reoptimized detector design and performance**. *CERN-LHCC-2003-030*, 2003.

[22] ALICE Collaboration. **ALICE: Technical proposal for a large ion collider experiment at the CERN LHC**. *CERN-LHCC-95-71*, 1995.

[23] CMS Collaboration. **Precise Mapping of the Magnetic Field in the CMS Barrel Yoke using Cosmic Rays**. *JINST*, **5**:T03021, 2010.

[24] CMS Collaboration. **The Tracker Technical Design Report**. *CERN-LHCC-98-6*, 1998.

[25] CMS Collaboration. **Tracking and Primary Vertex Results in First 7 TeV Collisions**. *CMS Physics Analysis Summary TRK-10-005*, 2010.

[26] CMS Collaboration. **The CMS electromagnetic calorimeter project : Technical Design Report**. *CMS-TDR*, (CERN-LHCC-97-033; CMS-TDR-004), 1997.

[27] CMS Collaboration. **CMS Physics Technical Design Report Volume 1: Detector Performance and Software**. *CMS-TDR*, (CERN-LHCC-2006-001, CMS-TDR-008-1), 2006.

[28] CMS Collaboration. **The CMS hadron calorimeter project : Technical Design Report**. *CMS-TDR*, (CERN-LHCC-97-031; CMS-TDR-002), 1997.

[29] CMS Collaboration. **The CMS muon project : Technical Design Report**. *CMS-TDR*, (CERN-LHCC-97-032; CMS-TDR-003), 1997.

[30] CMS Collaboration. **CMS The TriDAS Project Technical Design Report, Volume 1: The Trigger Systems**. *CMS-TDR*, (CERN-LHCC-2000-38; CMS TDR 6.1.), 2000.

[31] CMS Collaboration. **CMS The TriDAS Project Technical Design Report, Volume 2: Data Acquisition and High-Level Trigger**. *CMS-TDR*, (CERN-LHCC-2002-26; CMS TDR 6.2.), 2002.

[32] CMS Collaboration. **Alignment of the CMS Silicon Tracker during Commissioning with Cosmic Rays**. *JINST*, **5**:T03009, 2010.

[33] CMS Collaboration. **Aligning the CMS Muon Chambers with the Muon Alignment System during an Extended Cosmic Ray Run**. *JINST*, **5**:T03019, 2010.

[34] Carlo Battilana. *Drift Tubes Trigger System of the CMS Experiment at LHC : Commissioning and Performances. oai:cds.cern.ch:1328965.* PhD thesis, Bologna, U., Bologna, 2009. Presented 2009.

[35] CMS Collaboration. **Performance of the CMS Drift-Tube Local Trigger with Cosmic Rays**. *J. Instrum.*, **5**(arXiv:0911.4893. CMS-CFT-09-022):T03003. 33 p, Nov 2009.

[36] P. Arce et al. **Bunched beam test of the CMS drift tubes local muon trigger**. *Nucl. Instrum. Methods Phys. Res., A*, **534**:441–485, 2004.

[37] R. Fruhwirth. **Application of Kalman filtering to track and vertex fitting**. *Nucl. Instrum. Meth.*, **A262**:444–450, 1987.

[38] A. Everett et al. **Muon High-Level Trigger in CMS**. *CMS Note AN-2010/234*, 2010.

[39] CMS Collaboration. **Performance of muon identification in** pp **collisions at** $\sqrt{s}$**= 7 TeV**. *CMS Physics Analysis Summary MUO-10-002*, 2010.

[40] CMS Collaboration. **Search for High-Mass Resonances Decaying to Muon Pairs with 35 pb**$^{-1}$. *CMS Note AN-2010/317*, 2010.

[41] CMS Collaboration. **Performance of CMS Muon Reconstruction in Cosmic-Ray Events**. *J. Instrum.*, **5**(arXiv:0911.4994. CMS-CFT-09-014):T03022 . 47 p, Nov 2009.

[42] CMS Collaboration. **Performance of muon identification in 2010 data**. *CMS Physics Analysis Summary MUO-10-004*, 2011.

[43] CMS Collaboration. **Measurement of the Inclusive W and Z Production Cross Sections in pp Collisions at sqrt(s) = 7 TeV**. *Submitted to JHEP, arXiv:1107.4789*, Jul 2011.

[44] N. Adam et al. **Absolute Calibration of Luminosity Measurement in CMS**. *CMS Note AN-2011/093*, **2011/093**, 2011.

[45] S. Agostinelli et al. **GEANT4: A simulation toolkit**. *Nucl. Instrum. Methods*, **A506**:250., 2003.

[46] John Allison et al. **Geant4 developments and applications**. *IEEE Trans. Nucl. Sci.*, **53**:270, 2006.

[47] T. Sjostrand, S. Mrenna, and P. Skands. **PYTHIA 6.4 Physics and Manual**. *JHEP*, **05**:026, 2006.

[48] Simone Alioli, Paolo Nason, Carlo Oleari, and Emanuele Re. **NLO vector-boson production matched with shower in POWHEG**. *JHEP*, **07**:060, 2008.

[49] P. Nason. **A new method for combining NLO QCD with shower Monte Carlo algorithms**. *JHEP*, **11**:040, 2004.

[50] S. Frixione, P. Nason, and C. Oleari. **Matching NLO QCD computations with Parton Shower simulations: the POWHEG method**. *JHEP*, **11**:070, 2007.

[51] VBTF TWiki,Reference Monte Carlo Samples.

[52] C. Balázs and C.-P. Yuan. **Soft gluon effects on lepton pairs at hadron colliders**. *Phys. Rev. D*, **56**(9):5558–5583, Nov 1997.

[53] J.C. Collins, D.E. Soper, and G. Sterman. **Transverse momentum distribution in Drell-Yan pair and W and Z production**. *Nucl. Phys. B*, **250**(199), 1985.

[54] F. James and M. Roos. **Minuit: A System for Function Minimization and Analysis of the Parameter Errors and Correlations**. *Comput. Phys. Commun.*, **10**:343–367, 1975.

[55] C. J. Clopper and S. Pearson. **The use of confidence or fiducial limits illustrated in the case of the binomial**. *Biometrika*, **26**:404–413, 1934.

[56] M. De Mattia, R. Castello, J. Alcaraz, and J. Santaolalla. **Muon Momentum Scale and Resolution from $Z \to \mu\mu$**. *CMS Note AN-2011/166*, 2011.

[57] Hung-Liang Lai et al. **New parton distributions for collider physics**. *Phys. Rev.*, **D82**:074024, 2010.

[58] Richard D. Ball, Luigi Del Debbio, Stefano Forte, Alberto Guffanti, Jose I. Latorre, et al. **A first unbiased global NLO determination of parton distributions and their uncertainties**. *Nucl.Phys.*, **B838**:136–206, 2010.

[59] CMS Collaboration. **Measurements of Inclusive W and Z Cross Sections in pp Collisions at $\sqrt{s}$=7 TeV**. *JHEP*, **1101**:080, 2011.

[60] Hsin-Chia Cheng, Christopher T. Hill, Stefan Pokorski, and Jing Wang. **The standard model in the latticized bulk**. *Phys. Rev.*, **D64**:065007, 2001.

[61] Masako Bando, Taichiro Kugo, and Koichi Yamawaki. **Nonlinear Realization and Hidden Local Symmetries**. *Phys. Rept.*, **164**:217–314, 1988.

[62] Jogesh C. Pati and Abdus Salam. **Lepton Number as the Fourth Color**. *Phys. Rev.*, **D10**:275–289, 1974.

[63] G. Senjanovic and Rabindra N. Mohapatra. **Exact Left-Right Symmetry and Spontaneous Violation of Parity**. *Phys. Rev.*, **D12**:1502, 1975.

[64] Rabindra N. Mohapatra and Jogesh C. Pati. **Left-right gauge symmetry and an 'isoconjugate' model of CP violation**. *Phys. Rev.*, **D11**(3):566, 1975.

[65] R. N. Mohapatra and J. C. Pati. **"Natural" left-right symmetry**. *Phys. Rev. D*, **11**(9):2558–2561, May 1975.

[66] G. Altarelli, B. Mele, and M. Ruiz-Altaba. **Searching for New Heavy Vector Bosons in $\mathrm{p\bar{p}}$ Colliders**. *Z. Phys.*, **C45**:109, 1989.

[67] D0 Collaboration. **Search for W' bosons decaying to an electron and a neutrino with the D0 detector**. *Phys. Rev. Lett.*, **100**:031804, 2008.

[68] CDF Collaboration. **Search for a new heavy gauge boson W' with event signature electron and missing transverse enery in $p\bar{p}$ collisions at $\sqrt{s}$ = 1.96 TeV**. *Phys. Rev.*, **D83**:031102, 2011.

[69] T. Aaltonen et al. **Search for the Production of Narrow t anti-b Resonances in 1.9 fb-1 of p anti-p Collisions at s**(1/2) = 1.96-TeV**. *Phys.Rev.Lett.*, **103**:041801, 2009.

[70] PDG mass limits, http://pdg.lbl.gov/2011/listings/rpp2011-list-heavy-bosons.pdf.

[71] PDG W' BOSON SEARCHES, http://pdg.lbl.gov/2011/reviews/rpp2011-rev-wprime-searches.pdf.

[72] JOHAN ALWALL ET AL. **MadGraph/MadEvent v4: the new web generation**. *JHEP*, **09**:028, 2007.

[73] https://twiki.cern.ch/twiki/bin/viewauth/CMS/StandardModelCrossSections, https://twiki.cern.ch/twiki/pub/CMS/GeneratorMain/ShortXsec.pdf.

[74] R. HAMBERG, W.L. VAN NEERVEN, AND T. MATSUURA. **A complete calculation of the order α_s^2 correction to the Drell-Yan K-factor**. *Nucl. Phys. B*, **359**:343, 1991.

[75] R. HAMBERG, W.L. VAN NEERVEN, AND T. MATSUURA. **Erratum to a complete calculation of the order α_s^2 correction to the Drell-Yan K-factor (vol B359, pg 343, 1991)**. *Nucl. Phys. B*, **644**:403, 2002.

[76] CMS COLLABORATION. **CMS technical design report, volume II: Physics performance**. *J. Phys.*, **G34**:995–1579, 2007.

[77] CMS COLLABORATION. **On measuring missing transverse energy with the CMS detector in pp collisions at $\sqrt{s} = 7$ TeV**. *to be published in JINST*, 2011.

[78] CMS COLLABORATION. **Missing Transverse Energy Performance in Minimum-Bias and Jet Events from Proton-Proton Collisions at $\sqrt{s}$=7**. *CMS Physics Analysis Summary JME-10-004*, 2010.

[79] CARSTEN MAGASS. *Search for New Heavy Charged Gauge Boson. ISBN 978-3836485968*. PhD thesis, RWTH, Aachen, 2007.

[80] CMS COLLABORATION. **Missing ET Performance in CMS**. *CMS Physics Analysis Summary JME-07-001*, 2007.

[81] CMS COLLABORATION. **Track-corrected Missing Transverse Energy in CMS**. *CMS Physics Analysis Summary JME-09-010*, 2009.

[82] CMS COLLABORATION. **Particle-Flow Event Reconstruction in CMS**. *CMS Physics Analysis Summary PFT-09-001*, 2009.

[83] CMS COLLABORATION. **CMS MET Performance in Events Containing Electroweak Bosons from pp Collisions at $\sqrt{s}$=7 TeV**. *CMS Physics Analysis Summary JME-10-005*, 2010.

[84] CMS COLLABORATION. **Search for a W' boson decaying to a muon and a neutrino in pp collisions at $\sqrt{s}$=7 TeV**. *Physics Letters B*, **701**(2):160 – 179, 2011.

[85] J. Alcaraz et al. **Measurement of the inclusive W and Z Cross Sections in** ***pp*** **collisions at 7 TeV with fixed templates**. *CMS Note AN-2011/053*, 2011.

[86] CMS Collaboration. **Absolute luminosity normalization**. *CMS DP-2011/002*, 2011.

[87] CMS Collaboration. **Measurement of Momentum Scale and Resolution using Low-mass Resonances and Cosmic Ray Muons**. *CMS Physics Analysis Summary TRK-10-004*, 2010.

[88] M. Cepeda, C. Diez Pardos, J. Santaolalla, J. Alcaraz, B. de la Cruz, I. Josa, and M. Soares. **Studies on Missing Transverse Energy for events with muons**. *CMS Note AN-2010/197*, 2010.

[89] L. Moneta et al. **The RooStats Project**. *ACAT2010 Conference Proceedings*, 2010.

[90] R. Brun and F. Rademakers. **Root - an object oriented data analysis framework**. *Nuclear Inst. Meth. in Phys. Res. A 389*, **81**, 1997.

[91] A. Caldwell, D. Kollar, and K. Kröninger. **BAT - The Bayesian Analysis Toolkit**. *Computer Physics Communications*, **180**, 2009.

[92] CMS Collaboration. **Search for a heavy neutrino and right-handed W of the left-right symmetric model in** ***pp*** **collisions at sqrt(s) =7 TeV**. *CMS Physics Analysis Summary EXO-11-002*, 2011.

[93] Victor Mukhamedovich Abazov et al. **Search for $W' \to$tb resonances with left- and right-handed couplings to fermions**. *Phys. Lett.*, **B699**:145–150, 2011.

[94] CMS Collaboration. **Search for a W' boson decaying to a electron and a neutrino in** ***pp*** **collisions at $\sqrt{s} = 7$ TeV**. *Phys. Lett. B*, **698**:21, 2011.

List of Associated Publications

The work reported in this thesis has been presented by the author in the following papers, conference reports, CMS public analysis summaries, and CMS analysis notes. This following list comprises the most relevant publications and the directly related ones to the thesis topic.

Papers:

- CMS Collaboration, *Search for a W' boson decaying to a muon and a neutrino in pp collisions at* $\sqrt{s}$*=7 TeV*, Physics Letters B", 701(2):160-179, 2011
- CMS Collaboration, *Measurement of the Inclusive W and Z Cross-Sections in pp Collisions at* $\sqrt{s} = 7$ *TeV*, submitted to J. High Energy Phys, oai:cds.cern.ch:1370079, (Jul. 2011)
- CMS Collaboration, *Measurement of the Inclusive W and Z Cross-Sections in pp Collisions at* $\sqrt{s} = 7$ *TeV*, Journal of High Energy Physics, 2011:140, 2011. 10.1007/JHEP01(2011)080.
- CMS Collaboration, *Performance of the CMS Drift-Tube Local Trigger with Cosmic Rays*, Journal of Instrumentation, 5:T03003, 2009.

  10.1088/1748-0221/5/03/T03003

Conference Reports:

- Carmen Diez Pardos (on behalf of the CMS Collaboration), *Search for leptonic resonances at CMS*, Physics at the LHC (Perugia, Italy) 2011 Proceedings to be published

- Carmen Diez Pardos (on behalf of the CMS Collaborations), *First searches for physics beyond the Standard Model at CMS*, Proceedings of First Results from the LHC and Their Physics Interpretation, IHEP, Protvino (Russia), 19-21 October 2010, CMS CR-2010/295 (2010)
- Carmen Diez Pardos *et al.*, *Estudio del funcionamiento del sistema local del Trigger de Muones de las cmaras de deriva del experimento CMS del LHC*, Proceedings of XXXII Bienal de la Real Sociedad de Física Española, (2009)

CMS Analysis Notes:

- T. Bose, E. Carrera Jarrin, C. Diez Pardos, S. Goy López, A. Gueth, J. Hauser, T. Hebbeker, K. Hoepfner, C. Jarvis, C. Leonidopoulos, D. Sperka, S. Thuuer, *Search for a W' boson decaying to a muon and a neutrino in pp collisions at* $\sqrt{s}$*=7 TeV*, CMS AN-2010/315 (2010)
- J. Alcaraz, M. Cepeda, B. de la Cruz, C. Diez Pardos, D. Domínguez, M.I. Josa, J. Santaolalla, M. Soares, *Measurement of the inclusive* $W\mu\nu$ *cross section in pp collisions at 7 TeV*, CMS AN-2011/053 (2011)
- J. Alcaraz, *et al.*, *Updated measurements of the inclusive W and Z cross sections at 7 TeV*, CMS AN-2010/264 (2010)
- M. Cepeda, C. Diez Pardos, J. Santaolalla, J. Alcaraz, B. de la Cruz, I. Josa, M. Soares *Studies on Missing Transverse Energy for events with muons*, CMS AN-2010/197 (2010)
- C. Diez Pardos *et al.*, *Establishing the method to measure the single muon efficiency from events with the first data*, CMS AN-2010/233 (2010)
- A. Everett *et al.*, *Muon High-Level Trigger in CMS*, CMS AN-2010/233 (2010)
- C. Diez Pardos, B. de la Cruz, *DT L1 Trigger Performance with CRAFT Data*, CMS IN-2009/019 (2009)